DESIGN & EXPERIMENTAL STUDY OF A DUAL VIRCATOR MICROWAVE SOURCE

A Thesis presented to the Faculty of the Graduate School

at the University of Missouri-Columbia

In Partial Fulfillment of the Requirements for the Degree

Master of Science

---

by

KELTON R. CLEMENTS

Dr. Randy Curry, Thesis Supervisor

DECEMBER 2012

The undersigned, appointed by the Dean of the

Graduate School, have examined the thesis entitled:

DESIGN & EXPERIMENTAL STUDY OF A

DUAL VIRCATOR MICROWAVE SOURCE

Presented by Kelton R. Clements

A candidate for the degree Master of Science

And hereby certify that, in their opinion, it is worthy of acceptance.

_____

Dr. Randy Curry

_____

Dr. Robert Druce

_____

Dr. Carmen Chicone

ACKNOWLEDGEMENTS

First, I would like to thank Dr. Randy Curry for all of the opportunities and support that he has given me throughout the last few years. I would not have been introduced to the fields of pulsed power and directed energy without Dr. Curry's influence.

I would also like to thank Dr. Robert Druce and Dr. Carmen Chicone not only for participating as a part of my thesis committee, but also for acting as guiding forces during my studies. Their advice and support has been vast.

I am also thankful for all of the fellow graduate students that I have worked with. In particular, I thank Dr. Peter Norgard for sharing his own knowledge gained through experience as well as Kevin O'Connor for always being willing to listen and provide his insights.

Multiple staff members who have worked at the Center for Physical and Power Electronics are also owed thanks, particularly Scott Booska, Matt Wieberg, and Matt Kovac for helping with the system and for soaking numerous articles of clothing in transformer oil. Multiple outside sources have also provided support throughout this project including Dr. James Benford who supported the design and testing of the HPM source as well as Dr. Ken McDonald who aided in bringing the pulsed power system online. Last but not least, I thank the undergraduate assistants who lent a hand whenever asked, particularly Matt Cook who has been of great assistance in performing a great number of experiments.

Finally, I extend my thanks to my family and friends for their support and my fiancé Karissa Felten for her patience while spending numerous hours writing this thesis.

TABLE OF CONTENTS

LIST OF FIGURES

Figure **Page**

LIST OF TABLES

Table **Page**

Chapter 1 — Introduction and Project Motivation

1.1 Project Rationale and Motivation

This report discusses a system that utilizes two virtual cathode oscillator (vircator) high power microwave (HPM) sources that are powered by a single pulsed power source. It is the purpose of this system to generate two simultaneous microwave signals with independent and tunable microwave frequencies. This system serves as a test stand for electron beam research in which the parallel vircators permit the study of numerous parameters of the system. Among these system parameters are material properties and current sharing effects between the vircators. This test stand will serve as a system to advance the understanding of high power microwave effects and vircator operation.

1.2 Project Overview

Applications utilizing HPM sources include directed energy weapons (DEW), communications, and space travel. As a result of this interest, several HPM sources, and their accompanying pulsed power excitation circuitry, are currently being investigated [1], [2], [3], [4], [5], [6], [7], [8], [9]. Multiple means for driving HPM devices are also available with most having a basis in pulsed power. Due to the growing interest and need for HPM sources, an HPM source was constructed at the University of Missouri—Columbia (UMC) based on a vircator to enable a diverse range of experiments and testing.

In this report, the design and construction of the pulsed power driving system, the dual vircator HPM source, and the accompanying suite of system diagnostics are described in detail. The pulsed power system was used to drive the vircator microwave

source and can provide over 3 GW of peak power in a 250 kV, 70 ns pulse. This system consisted of a thyratron-switched modulator, a pulse forming line (PFL), and a high pressure oil switch. The modulator was used to pulse charge the PFL through a step-up pulse transformer. A square pulse was created by the discharge of the PFL through the high pressure oil switch. This output pulse was then stepped up through an inductive voltage adder and used to power the dual vircator load. The HPM source consisted of two vircators driven in parallel by the same source whose frequencies were independently tunable. All construction and experimentation was performed at the Center for Physical and Power Electronics at the University of Missouri. A simple flow chart representation of the full system is shown in Figure 1.1.

Figure 1.1—System flow chart

For the design of the pulsed power system, SPICE, a circuit simulation software that originated at UC-Berkeley, was used to perform circuit simulations to examine system performance and to determine the necessary component specifications. A lumped-element model was utilized, and the parameters of the model were adjusted based upon experimental results. Several simulations were also executed in the design of the vircator HPM system using various computer simulation packages. These included electrostatic simulations in CST Particle Studio®, which optimized the electric field shaping, and particle-in-cell (PIC) simulations that were performed in both MAGIC and CST Particle Studio® to analyze virtual cathode formation as well as the frequency of the output signal produced by the HPM system. Several parameters in the vircator geometry

were examined in both simulation packages. The results of these simulations were used as a basis for the original design and construction of the vircator and were later compared to experimental data.

1.3 Introduction and Overview of High Power Microwave Sources

The field of high power microwaves has a broad impact across engineering, communications, remote sensing, health care, and other fields. A timeline of HPM devices and supporting technologies is shown in Figure 1.2, which points out vircator research becoming prominent in the 1970s.

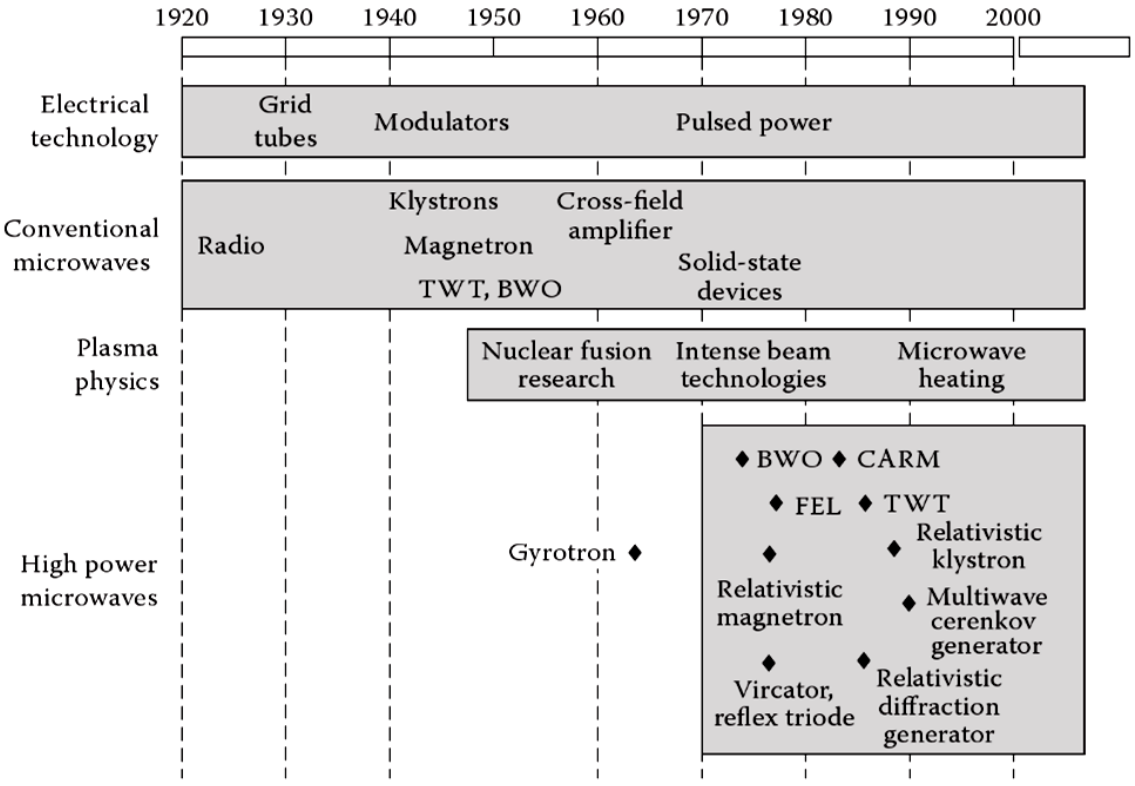

Figure 1.2—Timeline of HPM sources and supporting technologies from [10]

The definition of an HPM is somewhat ambiguous, but it is generally accepted that HPM devices have very high peak powers (several tens of megawatts to over 100 MW) with coherent, or narrowband, frequency operation in the range of 1 GHz to

300 GHz [9], [10], [11]. HPM sources have also been defined by their pulse energy instead of the peak power, whereby an HPM source would have a radiated pulse energy of one joule or more per pulse [8]. Inherent to these systems, due to high peak powers in the megawatts and gigawatts regimes, is a pulsed power driving system [3], [4], [9], [12]. Some common examples of pulsed power systems used to drive HPM sources include, but are not limited to, Marx generators, pulse forming lines (PFLs), and pulse forming networks (PFNs) [2], [3], [4], [5], [10]. The background of pulsed power is discussed in more detail in section 2.2.

The research and utilization of HPM sources have ramifications on a vast number of fields. Some of these areas are radar, communications, and directed energy. The use of HPM sources in radar and communication systems would allow for increased detection and contact range [10]. A great deal of research is being conducted for the use of HPM sources in the areas of electronic warfare, nonlethal weapon applications, and electronic susceptibility [1], [2], [7], [10], [13], [14], [15]. The feasibility of using HPM in space applications including propulsion has also been explored in some detail [10], [16]. These space-related applications include launch to orbit from the earth and launch from orbit to deep space. These applications utilize an HPM source to create a thrust through heat exchange [10], [16]. These applications and others are shown in Figure 1.3 and correspond with the areas shown in [8].

The design of HPM sources requires several areas to be considered in order to make a practical system. Among these are size limitations, the type of HPM source, the antenna used to radiate the signal, the power necessary for the application, and the efficiency of the system [10], [15]; however, these areas are extremely interdependent.

For example, if system efficiency is low, higher input power is needed and larger system sizes are necessary.

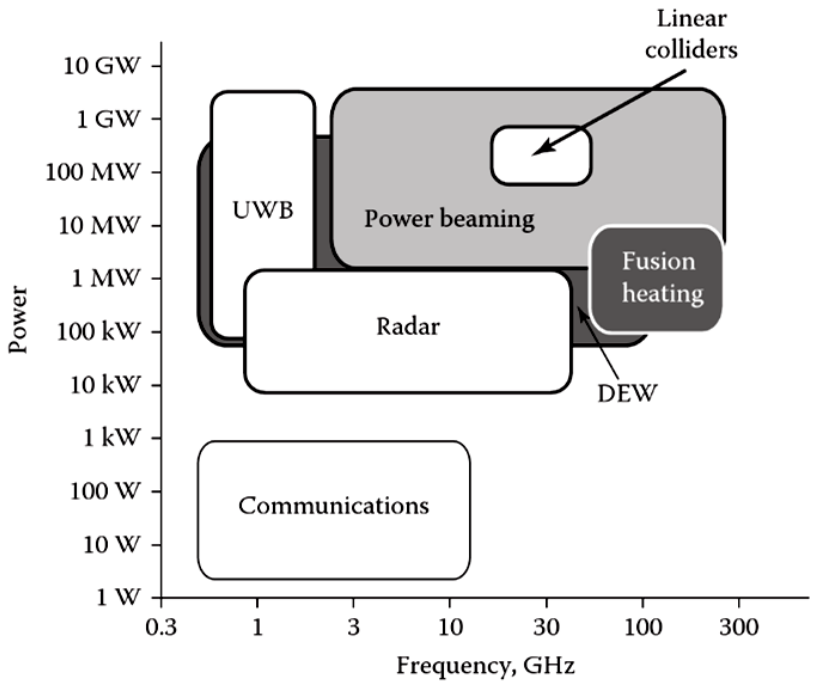

Figure 1.3—HPM application areas [10]

The size design constraint for the pulsed power system and HPM system is relatively easy to understand. The system must be designed to fit in a given vehicle desired for the application, and if the system is not properly designed, it becomes impractical. The antenna size is related to different antenna properties, most significantly directivity. In order to apply the maximum field on target, the directivity of the radiating antenna must be very high. However, to achieve high directivities, the size of an antenna must often be increased. Another concern pertaining to size is maneuverability. Large system sizes often inhibit system agility and maneuverability [15].

Various applications might require different forms of power, i.e. peak power versus average power. Often, the average power is severely limited in HPM systems due to heating and material degradation [10], [15]. A relationship of the peak and average

power for different microwave devices is shown in Figure 1.4. Nonetheless, very few, if any, applications require high peak and high average powers concurrently [10].

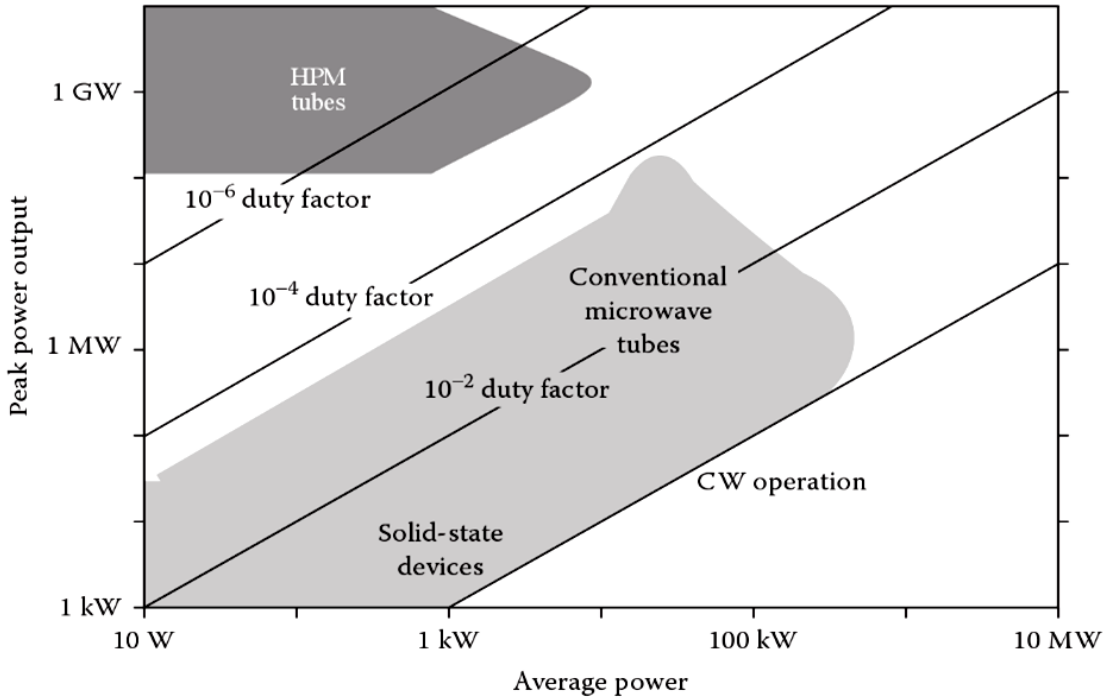

Figure 1.4—Relationship of peak and average power for various sources [10]

Another limiting factor of current HPM systems is efficiency. This parameter has a significant impact on other system parameters. The HPM systems are typically quite inefficient in their energy conversion from electrical to radiated energy with power efficiencies typically around 10%, while energy efficiencies are typically much lower due to various effects such as resonances and pulse shortening [10].

1.4 Rationale for Vircator Source

After investigation of several HPM systems, a vircator was chosen to create HPM signals across a wide range of tunable frequencies. Vircators have several advantages over other HPM systems that make them an attractive choice. Compared to other HPM devices, vircators are very simple in both design and construction [10], [15], [17], [18].

Vircators also do not require any external magnetic fields for operation although there have been studies examining the effects of an external magnetic field on the performance of a vircator [10], [15], [19]. Another advantage of a vircator is that its operation frequency is tunable as it is related to the anode-cathode gap [10], [15], [17], [18]. For the applications being explored at the University of Missouri, it was desirable to have an HPM source that allowed for the tuning over a wide range of frequencies. Due to the traditional method for tuning a vircator, this was a major factor in choosing to implement a vircator based system. Another advantage in choosing to implement a vircator source is that current hardware available for the pulsed power system allowed for the relatively simple transition to a vircator system. This allowed for a reduced cost of implementation by utilizing existing hardware.

Vircators also have several disadvantages. Most significantly they are very inefficient in converting input electrical power to radiated power with typical values around 1%-2% [3], [10], [15]. Comparing this efficiency to other systems, conventional and relativistic magnetrons have typical efficiencies around 50% and 30%, respectively, magnetically-insulated line oscillators have efficiencies less than 10%, and klystrons and reltrons have typical efficiencies around 40% to 50% [10]. Several experiments have been performed to investigate methods to improve the efficiency of vircators. Some of these experiments are discussed in Chapter 2. Another issue with vircators is that the operational frequency tends to chirp meaning that the frequency changes over time. A chirped signal has a relatively broadband spectrum. This broadband spectrum can be caused by pulse shortening and impedance collapse caused by gap closure [10], [15], [17], [18]. Chapter 2 discusses the relationship between the operating frequency and the

gap between the anode and cathode. This relationship indicates that when the gap closes due to plasma, the output frequency also changes. Finally, due to material limitations, pulse repetition rates and burst lengths are greatly limited due to heating and anode and cathode destruction [4], [10], [17], [18]. Despite the disadvantages of the vircator design, no other source can match the simplicity of design and the ability to tune the output frequency that comes with implementing a vircator HPM source.

References for Chapter 1

[1] S. Azam and Q. Wahab, "The present and future trends in High Power Microwave and Millimeter Wave Technologies," in *Advanced Microwave and Millimeter Wave Technologies Semiconductor Devices Circuits and Systems*.: Intech, 2010.

[2] V. G. Baryshevsky et al., "A compact high power microwave (HPM) source," in *2009 IET European Pulsed Power Conference*, 2009, pp. 1-4.

[3] Y. Chen, "Compact, Repetitive Marx Generator and HPM Generation with the Vircator," Texas Tech University, Master's Thesis 2005.

[4] See for example M. Elfsberg, T. Hurtig, A. Larsson, C. Moller, and S. Nyholm, "Experimental Studies of Anode and Cathode Materials in a Repetitive Driven Axial Vircator," *IEEE Transactions on Plasma Science*, vol. 36, no. 3, pp. 688-693, June 2008.

[5] S. H. Gold and G. S. Nusinovich, "Review of high-power microwave source research," *Review of Scientific Instruments*, vol. 68, no. 11, 1997.

[6] C. Moller, M. Elfsberg, A. Larsson, and S. E. Nyholm, "Experimental Studies of the Influence of a Resonance Cavity in an Axial Vircator," *IEEE Transactions on Plasma Science*, vol. 38, no. 6, pp. 1318-1324, June 2010.

[7] United States Air Force, "High-Power Microwaves," AFRL, Kirtland AFB, NM, 2002.

[8] University of Maryland, "High Power Microwave Technology and Effects," 2005.

[9] E. Schamiloglu, "High Power Microwave Sources and Applications," in *2004 IEEE MTT-S International Microwave Symposium Digest*, 2004, pp. 1001-1004.

[10] J. Benford, J. A. Swegle, and E. Schamiloglu, *High Power Microwaves*, 2nd ed.: CRC Press, 2007.

[11] R. J. Barker and E. Schamiloglu, Eds., *High Power Microwave Sources and Technologies*. New York: IEEE Press/J. Wiley & Sons, 2001.

[12] K. E. Hackett, "Directed Energy Applications for High Power Vacuum Electronics," in *IEEE International Vacuum Electronics Conference*, Monterey, 2006, pp. 11-13.

[13] E. M. Walling, "High Power Microwaves: Strategic and Operational Implications for Warfare," USAF, 2000.

[14] G. Ni, B. Gao, and J. Lu, "Research on High Power Microwave Weapons," in *Asia-Pacific Microwave Conference Proceedings*, 2005.

[15] Sandia National Laboratories, "A Brief Technology Survey of High-Power Microwave Sources," Sandia National Lab, Albuquerque, NM, 2001.

[16] J. Benford, "Space Applications of High-Power Microwaves," *IEEE Transactions on Plasma Science*, vol. 36, no. 3, pp. 569-581, June 2008.

[17] L. E. Thode and C. M. Snell, "Virtual Cathode Microwave Devices - Basics," Los Alamos National Laboratory, Los Alamos, 1991.

[18] D. Price, D. Fittinghoff, J. Benford, H. Sze, and W. Woo, "Operational Features and Microwave Characteristics of the Vircator II Experiment," *IEEE Transactions on Plasma Science*, vol. 16, no. 2, pp. 177-184, April 1988.

[19] See for example P. A. Lindsay, W. K. Toh, and X. Chen, "The influence of an axial magnetic field on the performance of a coaxial vircator," *IEEE Transactions on Plasma Science*, vol. 30, no. 3, pp. 1186-1195, June 2002.

Chapter 2 — Background

2.1 Basic Electromagnetic Fields Background

In electronics, the transfer of energy from a source to a load is the fundamental basis of a system. This can be accomplished in several different ways such as through transmission lines, wires, or through free-space. In a high power microwave system, energy can be transferred through free-space in the form of electromagnetic waves [1], [2]. There are many different subsets of electromagnetic waves, with microwaves being one specific type of electromagnetic wave. The electromagnetic spectrum is shown in Figure 2.1, where the various types of electromagnetic waves are divided into subsets based upon ranges of the wavelength of the wave [2], [3], [4]. In this figure, microwaves fall between 300 MHz to just over 100 GHz.

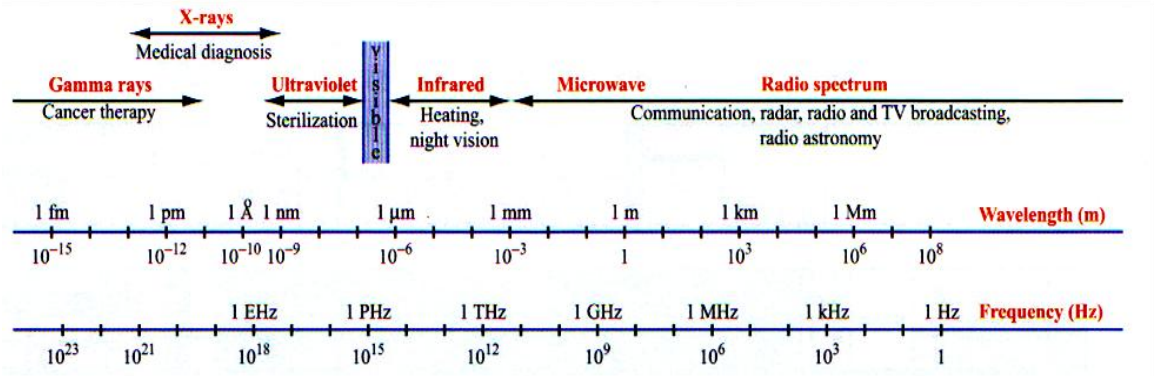

Figure 2.1—Electromagnetic spectrum [3]

Electromagnetic wave behavior can be described through Maxwell's equations. Maxwell's equations show an interdependence between electric and magnetic fields, the existence and propagation of electromagnetic waves, and a relationship between the

speed of the electromagnetic wave in free space and the speed of light [2]. The electromagnetic field equations are shown in equation 2.1 through equation 2.4:

$$\nabla \times \mathbf{E} = -\frac{\partial \mathbf{B}}{\partial \mathrm{t}} \tag{2.1}$$

$$\nabla \times \mathbf{H} = \mathbf{J} + \frac{\partial \mathbf{D}}{\partial \mathrm{t}} \tag{2.2}$$

$$\nabla \cdot \mathbf{D} = \rho_{\mathrm{v}} \tag{2.3}$$

$$\nabla \cdot \mathbf{B} = 0 \tag{2.4}$$

where $\boldsymbol{E}$ is the electric field intensity vector in V/m, $\boldsymbol{B}$ is the magnetic flux density vector in tesla, t is time in seconds, $\boldsymbol{H}$ is the magnetic field intensity vector in A/m, $\boldsymbol{D}$ is the electric flux density in C/m^2, $\boldsymbol{J}$ is the current density vector in A/m^2, and ρ_v is the volume charge density in C/m^3 [2], [3], [4]. In order to further relate the parameters in these equations, the electric field intensity is related to the electric flux density via the medium permittivity and the magnetic field intensity is related to the magnetic flux density via the medium permeability, or:

$$\mathbf{D} = \epsilon \mathbf{E} \tag{2.5}$$

$$\mathbf{B} = \mu \mathbf{H} \tag{2.6}$$

where ϵ is the permittivity of the medium in which the fields are located with units of F/m and μ is the permeability of the medium in H/m. All parameters in these equations are both time- and space-dependent.

In examining Equation 2.1 and 2.2, it is apparent that the electric and magnetic fields are related. Even more so, the time-varying signals of each are related to the spatially varying signals of the other. In other words, as the electric field changes with time or space, the magnetic field changes with space or time, and vice versa. It is in this way that electromagnetic waves are formed [2], [3]. Waves are spatially-directed and

time-varying signals which propagate at finite speeds through a medium, transporting energy from one place to another [2].

The simplest electromagnetic wave to analyze is a uniform plane wave. A uniform plane wave is a wave whose intensities are directed in a fixed direction with a constant amplitude and phase for a given position in space. The intensities in an electromagnetic plane wave are the electric and magnetic field; these fields exist in planes that are perpendicular to the direction of propagation [2]. Solving Maxwell's equations assuming that the electric field is oriented along the x-axis and the wave is traveling in the z-direction gives electric and magnetic fields of:

$$E_x(z,t) = E_0^+ \cos(\omega t - kz + \phi) \tag{2.7}$$

$$H_y(z,t) = \frac{E_0^+}{\eta}\cos(\omega t - kz + \phi) \tag{2.8}$$

where E_0^+ is the amplitude of the forward traveling wave in V/m, ω is the angular frequency in rad/s, k is the spatial frequency in rad/m, ϕ is a phase constant in radians, and η is known as the intrinsic impedance of the medium in Ω. The intrinsic impedance varies by material and is equal to [2], [3], [4]:

$$\eta = \frac{E_x}{H_y} = \sqrt{\frac{\mu}{\epsilon}} \tag{2.9}$$

As mentioned before, waves are used to transport energy from one point to another. In electromagnetic waves, the power flow of the wave is given as a power density vector and is related to the electric and magnetic fields through the Poynting vector:

$$\boldsymbol{S} = \boldsymbol{E} \times \boldsymbol{H} \tag{2.10}$$

where $\boldsymbol{S}$ is the Poynting vector in W/m^2 [2], [3], [4]. The Poynting vector not only defines the power density at a particular point in space but it also defines the direction of power flow.

A method for efficiently containing electromagnetic waves and transferring their energy from one point to another is necessary due to the spherical spreading of energy of waves in free space. This is often accomplished through the utilization of a waveguide. As their name suggests, waveguides are used to guide electromagnetic waves. This allows for the containment of all of the energy of the transmitted signal so that it might be fully transferred from a source to a load. Different forms of waveguides exist, but only rectangular waveguides are described here.

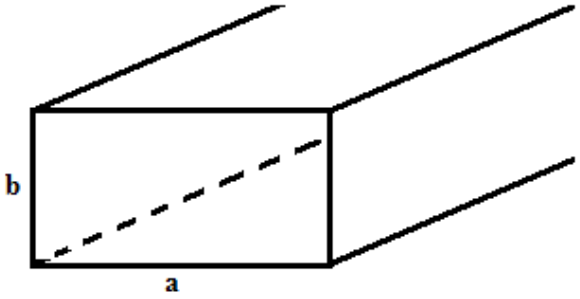

Figure 2.2—Rectangular waveguide cross section

A diagram of a rectangular waveguide is shown in Figure 2.2. In this figure, the long dimension has a length of a, and the short dimension has a length of b. In a rectangular waveguide, the boundary conditions at the conductor determine the possible propagating modes available for transferring energy. Different modes include transverse electromagnetic (TEM) modes where both the electric and magnetic fields are perpendicular to the direction of propagation, transverse magnetic (TM) modes where just the magnetic field is perpendicular to the direction of propagation, and transverse electric (TE) modes where just the electric field is perpendicular to the direction of

propagation [2]. In a rectangular waveguide, TEM waves cannot be supported due to the boundary conditions [4]. The dominant mode in a rectangular waveguide, or the mode capable of supporting the lowest frequency signal is the TE_{10} mode [2]. The 1 and 0 denote a mode of propagation in the waveguide. Waveguides are designed with a particular operating frequency in mind and have a cutoff frequency below which no signal will traverse through the waveguide for a particular mode [2], [4]. The cutoff frequency for a rectangular waveguide for a mode numbered *m,n* can be calculated through the following [2], [4]:

$$f_{c,mn} = \frac{1}{2\pi\sqrt{\mu\epsilon}}\sqrt{\left(\frac{m\pi}{a}\right)^2 + \left(\frac{n\pi}{b}\right)^2} \tag{2.11}$$

where a and b are in meters and are designated in Figure 2.2.

2.2 Pulsed Power Background

Pulsed power, in its most basic definition, is the field of electrical engineering in which systems are designed to deliver energy to a load such that the energy is delivered in a short time packet or pulse with very high peak power. This energy delivery in a short amount of time allows for the creation of signals with very high peak power being delivered to the load. There are many different topographies and methods to design a system to deliver a pulsed output to a load. Pulsed power systems typically utilize energy storage devices and switching mechanisms to discharge the stored energy in the form of a pulse. Some of the basic components used in pulsed power systems are described in order to provide a basis of understanding for the driving system for the high power microwave source described in this report. Some common pulsed power topologies are also introduced.

One component that is utilized in several forms of pulsed power systems is a transmission line. Transmission lines are commonly used to carry electrical signals. However, pulsed power systems also utilize them for their transient behavior [5]. A transmission line can be modeled using resistors, capacitors, and inductors to form an equivalent circuit. An example of this can be seen in Figure 2.3 representing an infinitesimally small section of a transmission line.

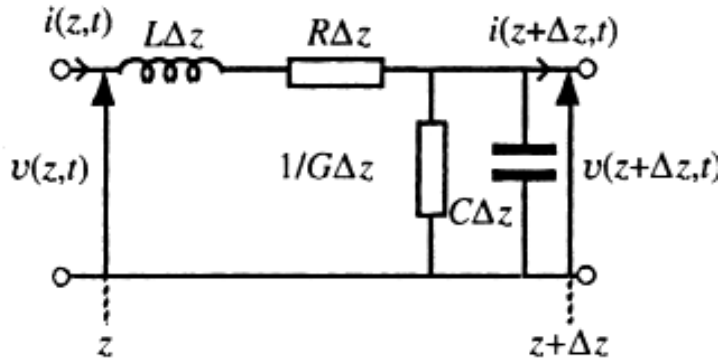

Figure 2.3—Model of infinitesimally small section of transmission line [5]

If it is assumed that the transmission line is lossless, the two lossy parameters of the transmission line model, namely R and G, go to zero. Using the line parameters from this model, a characteristic impedance of the transmission line can be determined. In a lossless line, the characteristic impedance is equal to:

$$Z_0 = \sqrt{\frac{L'}{C'}} \tag{2.12}$$

where Z_0 is the characteristic impedance in Ω, L' is the inductance per unit length in H/m, and C' is the capacitance per unit length in F/m [2], [3], [5]. Matching the transmission line impedance to the load is important for efficient energy transfer. If the transmission line is connected to a load with an impedance different than the impedance of the transmission line, a discontinuity is created, and the electrical signal is reflected at this

point. A reflection coefficient is related to the ratio of the voltage amplitude delivered to the connected load V_L and the input voltage amplitude V_{in}. This reflection coefficient is equal to:

$$\Gamma = \frac{V_L}{V_{in}} - 1 = \frac{Z_L - Z_0}{Z_L + Z_0} \tag{2.13}$$

where Z_L is the load impedance in Ω and Z_0 is the transmission line characteristic impedance in Ω [3], [5]. Transmission lines can also be used to create a pulse and deliver it to a load. This output pulse can be created by charging a transmission line up to a voltage V_0 treating the transmission line as an energy storage device. Transmission lines used in this fashion are typically called pulse forming lines (PFLs) [5]. A simple PFL circuit is shown in Figure 2.4.

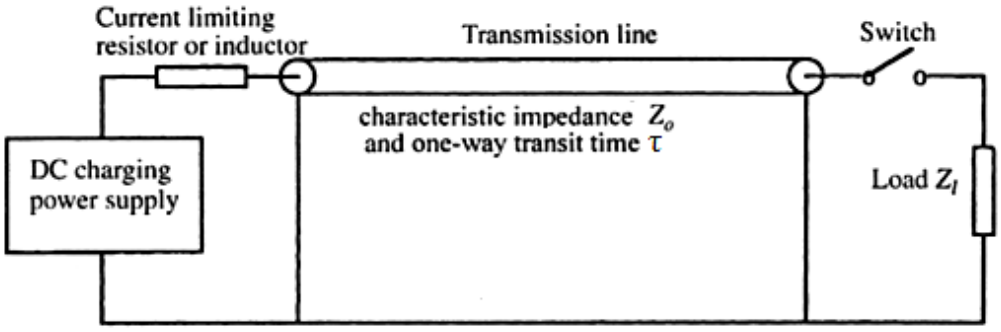

Figure 2.4—Simple PFL circuit [5]

Once the PFL is charged, its output can be switched into a load. If the load impedance matches the line impedance, the output pulse has an amplitude of $\frac{V_0}{2}$ and has a pulse width of 2τ where τ is the one-way transit time of the line. The one-way transit time is related to the line parameters by:

$$\tau = \sqrt{LC} \tag{2.14}$$

where L is the inductance of the line in henries, and C is the capacitance of the line in farads [3].

Pulsed power systems utilize energy storage devices that are rapidly discharged in the form of a pulse. One common energy storage device is a simple capacitor, or a bank of capacitors in parallel. The energy stored in a capacitor is proportional to the capacitance and can be calculated as follows:

$$W = \frac{1}{2}CV^2 \tag{2.15}$$

where W is the stored energy in joules, C is the capacitance in farads, and V is the voltage that the capacitor is charged to in volts [6]. In a simple switching circuit, capacitors can be used to create a voltage pulse. An example capacitive discharge circuit is shown in Figure 2.5. In this figure, a capacitor discharges its initially stored energy into a load resistor through an inductance.

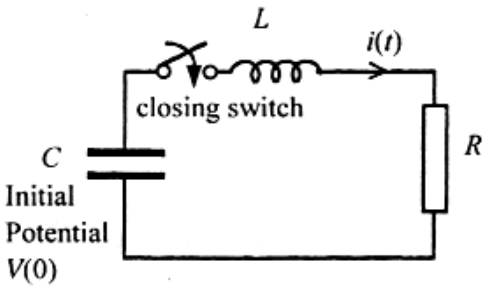

Figure 2.5—Simple capacitive discharge circuit [5]

A slightly more advanced discharge circuit is one which utilizes a capacitor and inductor to resonantly charge a second capacitor. This is known as a CLC resonant charging circuit. The pulsed power system used to drive the HPM source discussed in this paper operates on the principle of a CLC resonant topology. A basic CLC circuit schematic shown is in Figure 2.6.

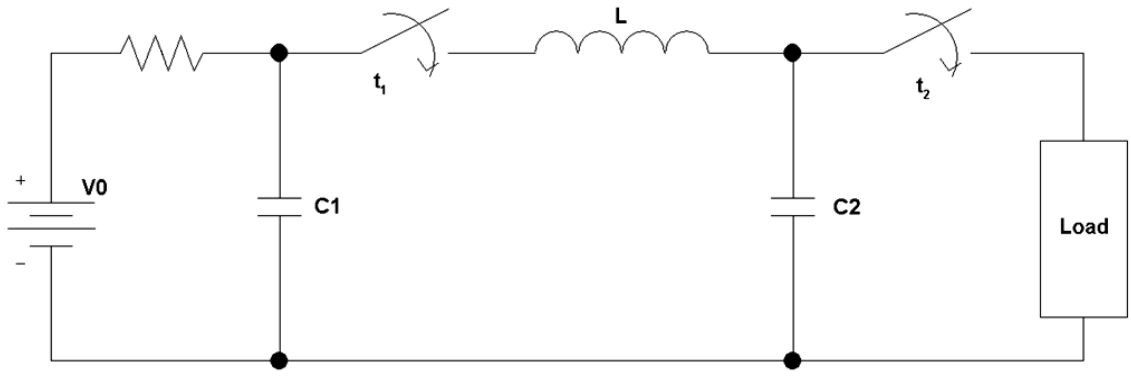

Figure 2.6—Basic CLC resonant charging circuit

The capacitor C_1 is charged to an initial voltage V_0 by the DC voltage source. When this capacitor is switched at time t_1, the capacitor C_2 is charged through the inductor L with a waveform described in the equation [5], [7]:

$$v_2(t) = \frac{C_1 V_0}{C_1 + C_2}(1 - \cos(\omega_d t)) \tag{2.16}$$

In this equation, C_1 is the initially charged capacitance in farads, ω_d is the resonant frequency of the CLC discharge in rad/s, t is time in seconds, and C_2 is the capacitance in farads that is charged up by the pulse. The resonant frequency of the CLC network is calculated as:

$$\omega_d = \sqrt{\frac{1}{L}\left(\frac{C_1 + C_2}{C_1 C_2}\right)} \tag{2.17}$$

where L is the CLC network inductance in henries [5], [7]. The capacitor C_2 can be charged up to a maximum of twice the original charge voltage, given the proper choices of C_1 and C_2. A second switch can be triggered at time t_2 to output this higher voltage pulse.

High voltage DC power supplies usually are capable of outputting tens of kilovolts. Depending on the system, this voltage amplitude might need to be increased. One method of accomplishing a voltage gain for an output pulse is through the use of a

pulse transformer. Transformers are often used in continuous AC operation, but the design for pulsed operation is more complex, especially for high voltage pulses with fast rise-times. A transformer is essentially a circuit component with separate windings, typically a primary and a secondary winding, that are coupled through the use of a magnetic core. A magnetic core concentrates the magnetic field lines created when the primary winding receives an input signal. The change in the magnetic flux coupling into the secondary winding induces a voltage across its terminals. This voltage is proportional to the input voltage by the turns ratio, ignoring losses. The turns ratio n is the ratio of the number of turns on the secondary winding N_2 to the number of turns on the primary winding N_1. A practical transformer has various parasitic components representing the capacitance between turns, the winding resistance, core losses due to conduction, and stray inductances created by a non-ideal coupling between windings [5]. An equivalent circuit for a practical pulse transformer is shown in Figure 2.7.

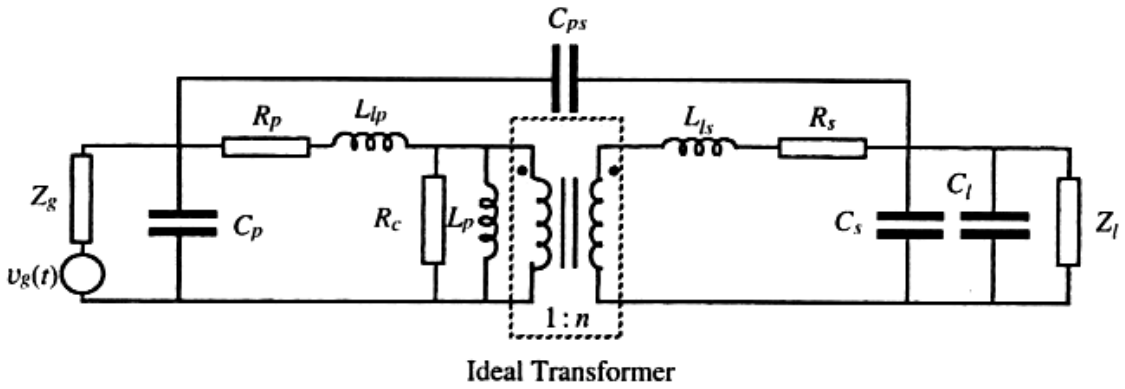

Figure 2.7—Practical pulse transformer model [5]

Pulse transformers typically use a magnetic core to increase the coupling between windings and maintain a reduced system size. An issue with magnetic cores is the saturation of the magnetic material. This saturation is observable by examining the B-H

loop for a magnetic core, an example of which is shown in Figure 2.8. In a pulsed power system, the maximum linear range for the magnetic permeability is usable by implementing a reset circuit to move to the opposite quadrant of the B-H loop [8].

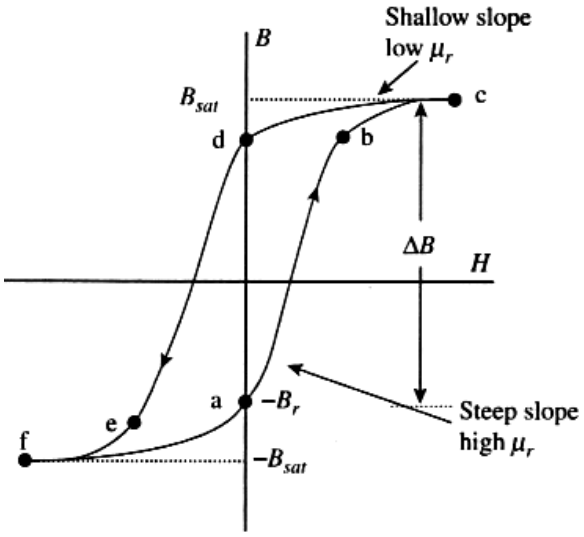

Figure 2.8—Example BH hysteresis loop showing all four quadrants [5]

2.3 Electron Beam Background

High power microwave sources are able to produce strong microwave signals by converting the kinetic energy of electrons into microwave energy [1], [9]. Multiple methods exist for creating electron emission. The most common are explosive emission, thermionic emission, and photoemission [1]. In HPM systems, the most common cathode emission type is explosive emission [1]. This emission type is discussed in detail.

Explosive electron emitter materials include metal cathodes, velvet, carbon fibers, and cesium iodide (CsI) doped carbon fibers [1], [10]. The electric fields in these explosive emitter materials are enhanced at very fine points on the emitter surface [1], [10]. Because the fields at these points are so much higher, large currents flow through

these points until they heat up and vaporize, forming plasmas [1], [10]. This vaporization and subsequent ionization leads to plasma formation across the cathode surface, allowing for the production of high current densities [1], [10]. Various issues exist for explosive emission cathodes. One of these issues is gap closure between the anode and cathode due to localized plasma "jets" forming on the cathode moving towards the anode [1]. Another problem, particularly in microwave systems, is that the nonuniformity of the electron emission across the cathode can affect microwave generation [1]. Explosive emission materials also tend to "outgas" during operation because of the burning and destruction of cathode particles. This outgassing limits the system repetition rate as this it creates molecules that can be ionized, causing arcing and diode closure [1].

When the electrons are emitted and an electron beam is formed between an anode and a cathode, the amount of current between the two electrodes is governed by the boundary conditions of the electron beam diode. Parameters influencing the boundary conditions, and consequently the limiting current, include the potential between the two electrodes and the distance between the electrodes. Solving for a parallel-plate electron beam diode assuming equilibrium, the current is governed by the Child-Langmuir equation and can be calculated through the following equation:

$$J_{CL} = \frac{4}{9}\epsilon_0\sqrt{\frac{2e}{m}}\,\frac{{V_0}^{3/2}}{d^2} \tag{2.18}$$

where J_{CL} is the current density in A/m^2, ϵ_0 is the permittivity of free space in F/m, e is the charge of an electron in coulombs, m is the mass of an electron in kg, V_0 is the voltage across the diode in volts, and d is the anode-cathode (AK) gap in meters [11], [12], [13], [14].

Vircators receive their classification because the high power microwave signals are generated by the oscillations of a virtual cathode. The virtual cathode is created by an electron beam current exceeding the space-charge-limited current in a cylindrical drift tube [1], [15]. For a drift tube with grounded walls, current flows through the anode foil until it exceeds the space-charge-limited current beyond the anode foil given by the formula:

$$I_{SCL} = \frac{17}{G}\left(\gamma_0^{2/3} - 1\right)^{3/2} \tag{2.19}$$

where I_{SCL} is the space-charge-limited current in kA, G is determined by the beam geometry, and γ_0 is determined by the diode voltage V_0 as follows:

$$G = \begin{cases} 1 + 2\ln\left(\frac{r_g}{r_b}\right), & solid\ beam \\ 2\ln\left(\frac{r_g}{r_b}\right), & thin\ annular\ beam \end{cases} \tag{2.20}$$

$$\gamma_0 = 1 + \frac{eV_0}{mc^2} \tag{2.21}$$

where r_g is the drift tube, or guide radius in centimeters, r_b is the beam radius in centimeters, V_0 is the diode voltage in volts, e is the elementary electron charge in coulombs, m is the mass of an electron in kg, and c is the speed of light in m/s [1], [9], [15]. When the space-charge-limited current given by equation 2.19 is exceeded in the drift tube, the electrons form a potential barrier which reflects electrons and disallows them from passing further into the drift tube. This potential barrier is the virtual cathode [1].

Electron beams operate in a vacuum. This reduces the chance of electrical breakdown between electrodes due to the reduced number of molecules to ionize. In order to achieve vacuum conditions, insulators are used to seal the interface between the

vacuum and atmosphere. They are also used to maintain conductor separation. Insulators provide a surface for secondary electron emission which increases the chances of flashover. In vacuum electronics, the triple point, or the point where the vacuum, dielectric, and conductive interfaces all meet, is one of the critical points for vacuum design in high voltage systems since this is often the initial point for vacuum breakdown [16], [17], [18]. Minimizing any field enhancement factors as well as minimizing the electric field at this triple point is crucial. To minimize the chances for secondary emission along an insulator's surface and minimize the field at the triple point, the insulator can be designed to slant at an optimal angle depending on the dielectric material to prevent secondary emission, and the electric fields at the triple point can be shaped to reduce the field strength at this point [16], [17], [18].

2.4 Theory of Vircator Operation

High power microwave sources are typically classified according to the wave-particle interaction that occurs to create microwaves. Classification of several HPM sources can be seen in Table 2.1 [1].

Table 2.1—HPM source classification [1]

	Slow Wave	Fast Wave
O-Type	Backward wave oscillator	Free-electron laser
	Traveling wave tube	Optical kystron
	Surface wave oscillator	Gyrotron
	Relativistic diffraction generator	Gyro-BWO
	Relativistic klystron	Gyro-TWT
	Dielectric & Plasma Cerenkov maser	Gyroklystron
M-Type	Relativistic magnetron	Rippled-field magnetron
	Cross-field amplifier	
	Magnetically insulated line oscillator	
Space-Charge	**Vircator**	
	Reflex Triode	

In this table, "O-type" devices are ones in which the electrons traverse parallel to an external magnetic field. The "M-type" devices have the electrons travel perpendicularly to crossed electric and magnetic fields. "Space-charge" devices are ones in which microwaves are directly related to a space-charge interaction due to the system geometry and may or may not utilize an external magnetic field [1].

Electron beam theory and pulsed power combine to form the foundation of vircator high power microwave sources, since vircators fall in the classification of space-charge devices [1]. A vircator's operation depends on the formation of a virtual cathode caused by a space-charge phenomenon produced by an electron beam diode [1], [9], [15], [19], [20], [21]. In a vircator, an electron beam is formed by a cathode that emits the electrons and an anode that is semitransparent. This transparency in the anode material allows electrons to pass through to the evacuated drift space beyond the anode. The electron-beam current density is governed by the Child-Langmuir current for a space-charge-limited diode as shown in Equation 2.18 [11], [12], [13]. The actual current can be written as:

$$I_b = SJ_{CL} \tag{2.22}$$

where I_b is the beam current in amps, S is the surface area of the cathode emission surface in m^2, and J_{CL} is the current-density of the electron beam in A/m^2 [11], [12], [13]. Beyond the anode in the drift tube, a different set of boundary conditions exist. A virtual cathode is formed when the beam current through the anode exceeds the drift tube's space-charge-limited current threshold given in equation 2.19 [1], [15]. This phenomenon is due to a strong potential created at the leading edge of the beam. This potential is strong enough to reflect electrons back toward the anode [1], [15]. Since no

equilibrium state exists in the creation of this virtual cathode, it oscillates along the axis of the electron beam. This oscillation of the virtual cathode creates radiation at a microwave frequency proportional to the square root of the beam current density [1], [15].

Two radiation phenomena in vircators create two distinct frequencies that can be used in the design and experiments of a vircator: the reflexing frequency and the virtual cathode frequency [1], [15], [22]. The virtual cathode frequency is related to the beam plasma frequency [1], [9], [15], [20], [37], [24]. This frequency is largely dependent on the AK gap and the beam current density [1], [15]. The ability to alter the AK gap and its relation to the virtual cathode frequency gives vircators their main advantage: they are tunable over a relatively large range of frequencies compared to other HPM sources [1], [25].

The reflexing frequency component originates from electrons that are being reflected back and forth between the actual cathode and the virtual cathode whereas the virtual cathode frequency is created by the oscillations of the virtual cathode itself [1], [15], [22], [26], [27], [28]. In general, the virtual cathode frequency is greater than the reflexing frequency [1]. This is not always the case, however [29]. The most significant characteristic pertaining to both of these signals is that they are both dependent on the AK gap in a similar way. Both are inversely proportional to the AK gap:

$$f \propto \frac{1}{d}. \tag{2.23}$$

The plasma frequency of the electron beam, and an approximation of the virtual cathode frequency, can be calculated using the following equations:

$$f_{VC} \approx f_P = \frac{1}{2\pi}\left(\frac{n_b e^2}{\varepsilon_0 m \gamma_0}\right)^{1/2} \text{ [Hz]}. \tag{2.24}$$

The plasma frequency is given as:

$$f_P = 4.10\left[\frac{J_b}{\beta\gamma_0}\right]^{1/2}\ [\text{GHz}] \tag{2.25}$$

where n_b is the electron density of the beam in cm^{-3}, β is the speed of the electrons relative to the speed of light, and J_b is the beam current density in kA/cm^2 [1], [15]. This equation only provides an approximation for the virtual cathode frequency. Simulations and experiments have shown that the center frequency of vircator operation can be in the range [15], [30]:

$$f_p < f_{VC} < f_p\sqrt{2\pi}. \tag{2.26}$$

Other approximations have been published, based upon experimental data sets. One such empirical formula for determining the dominant frequency is given in the following equation [20]:

$$f_{vc} = \frac{4.77}{d\ (cm)}\ln\left[\gamma_0 + (\gamma_0{}^2 - 1)^{1/2}\right] \tag{2.27}$$

where f_{vc} is the virtual cathode frequency in GHz. This formula agrees very well with the results of four independently published experimental results.

While both the reflexing frequency and the virtual cathode frequency share an inversely proportional relationship to the AK gap, the functional forms of the two frequencies are very different. The reflexing frequency is determined by the transit time of the electrons between the cathode and the virtual cathode [1]. This oscillation leads to the production of microwaves [1]. The period of the oscillation is related to the transit time between the cathode and virtual cathode [1]. With the assumption that the virtual cathode is approximately the same distance from the anode as the actual cathode is, the reflexing frequency can be written as [1]:

$$f_r = \frac{1}{4T} = \frac{1}{4\int_0^{d} \frac{dz}{v_z}}. \tag{2.28}$$

where T is the transit time from the cathode to the virtual cathode in seconds and v_z is the axial velocity between the cathode and virtual cathode in m/s [1]. For a non-relativistic beam, this equation can be approximated by [1]:

$$f_r = \frac{2.5\beta}{d} \tag{2.29}$$

where f_r is the reflexing frequency in GHz, β is the speed of the electrons relative to the speed of light, and d is the AK gap in cm [1]. The value for β is given as:

$$\beta = \sqrt{1 - 1/\gamma^2} \tag{2.30}$$

2.5 Previous Research Utilizing Vircators

Numerous studies have been performed on vircator HPM systems. These studies include materials studies for the semi-transparent anode and for the cathode emission surface, various cavity effects on the microwave output, and several geometrical variations of vircator systems implemented in the attempt to increase output efficiency. Some of these research studies are discussed in the following.

Materials play a role in microwave power and efficiency, microwave bandwidth, frequency jitter, and system durability and lifetime [1], [27], [31]. Cathode emitter materials and anode materials have the most significant effect on these parameters. Common cathode materials include velvet, graphite, carbon fibers, and chemically etched metallic surfaces [27], [31]. The choice of material for the cathode can be limited by the driving system, since metallic cathodes often require much higher voltages to operate due to the lack of field-enhancement [22]. The material used for the cathode has been shown to strongly affect the output power and bandwidth of the output microwave signal. For

example, velvet generally creates higher peak power outputs with longer pulse widths, whereas graphite and metallic cathodes produce microwave signals with narrower bandwidths [9], [27], [31]. Anode materials also vary and may include very thin foils and transparent meshes made of materials including, but not limited to, aluminum, molybdenum, stainless steel, titanium, and copper [1], [31]. Transparency is closely related to microwave power output, since, to some extent, higher transparency typically provides higher output power [31]. One of the most significant concerns for the anode material is lifetime, especially when operating at a repetition rates of 10 Hz or more since melting of the anode material causes degeneration of the screen and, in turn, system performance [31]. For example, molybdenum wire was shown to survive more pulses under repetitive pulse tests than stainless steel [31]. The microwave output also varied less from pulse to pulse for the molybdenum anode, during the repetitive pulse tests [31].

The most significant disadvantage of a vircator HPM source relative to other HPM devices is its very low efficiency. One of the causes of this inefficiency is the multitude of frequency components in the microwave signal typically output by a vircator. Ideally, all of the microwave energy would be radiated at a single frequency. To remove this spread of frequencies, the drift tube can form a resonant cavity by using an adjustable cavity wall. This limits the modes that are capable of forming in the drift tube cavity [1], [19]. This in turn removes different spectral components and increases the microwave output at the dominant frequency. Another role of this cavity wall is the reduction in the spectral bandwidth of the output signal. Both of these functions allow for the increase in efficiency and spectral purity [1], [19], [22]. The use of a resonant cavity has been shown to reduce the spectral bandwidth of the output signal while

simultaneously maximizing the peak microwave signal by positioning the cavity in an optimized position [19].

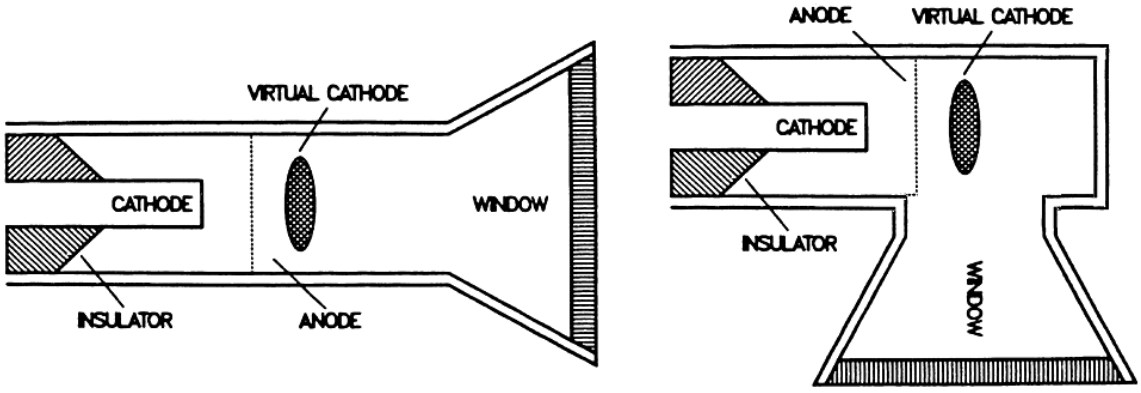

Figure 2.9—Basic extraction geometries: axial (left) and radial (right) [1], [9], [15]

There are several geometries that have been used in vircator experiments. Two of the simplest and most common geometries are shown in Figure 2.9. In the axial extraction geometry, the microwave signals are extracted from the end of the drift tube. The microwaves in this setup form TM modes that are typically extracted through a cylindrical waveguide that serves as a continuation of the drift tube [1], [24]. In the radially extracted vircator geometry, microwaves are typically extracted using a rectangular waveguide with the small dimension parallel with the axial axis of the vircator [1], [22]. However, there have been cases where a circular waveguide has been used in radial extraction [19], [31]. When using a rectangular waveguide, more than 90% of microwave output is carried by the TE_{10} mode meaning that the electric and magnetic field profiles can be predicted to travel in this mode [1].

These traditional extraction methods have yielded low microwave efficiencies. Because of this, various geometries have been explored in the attempt to increase the system efficiency [1], [9], [37], [28], [29], [32], [33], [34], [35], [36]. There have been

other attempts to maximize microwave output by using both axial and radial extraction [30]. By doing this, the extraction area was increased to allow for enhanced microwave extraction. The results from this experiment showed peak power efficiencies of about 2% [30]. Other geometries include, but are not limited to, the reflex triode geometry, the double-anode vircator, and the coaxial vircator. These three geometries are shown in Figure 2.10, Figure 2.11, and Figure 2.12, respectively.

The reflex triode geometry is similar to a traditional geometry with radial extraction. The main difference, however, is that the high voltage pulsed power system drives the anode rather than the cathode. This geometry has had reports showing an efficiency of 12%, although these results are somewhat controversial [37]. Typical efficiencies were in the 1% to 2% range [9], [21].

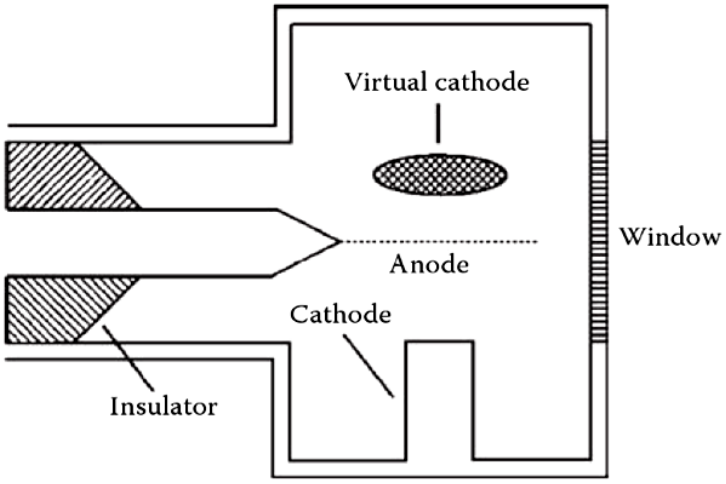

Figure 2.10—Reflex triode vircator geometry [1], [9]

The double-anode geometry uses two anode screens with an optimized separation. This separation increases the distance that the electrons traverse between the cathode and virtual cathode. Experimental results have shown that this allows the reflexing frequency and virtual cathode frequency to be matched, eliminating the competition between the

two microwave generation mechanisms, increasing microwave efficiency to between 1% and 2% as well as improving spectral purity [1], [28], [33], [38].

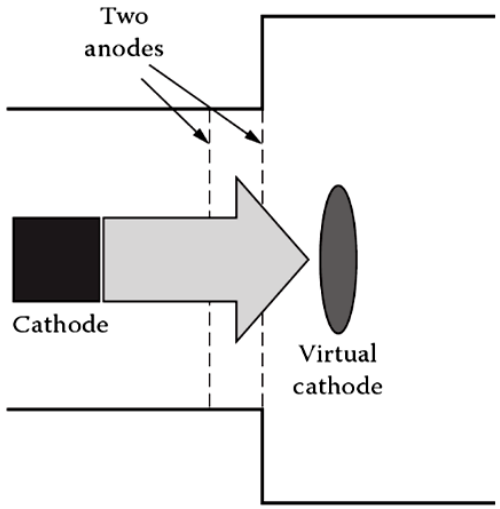

Figure 2.11—Double-anode vircator geometry [1], [28]

The coaxial vircator, as the name suggests, utilizes a coaxial geometry formed by the cathode and anode screen. The virtual cathode is formed in the center, and the microwaves are extracted axially [1], [37]. This geometry has shown improved efficiencies with peak efficiencies around 4% to 5.5% [37], [36].

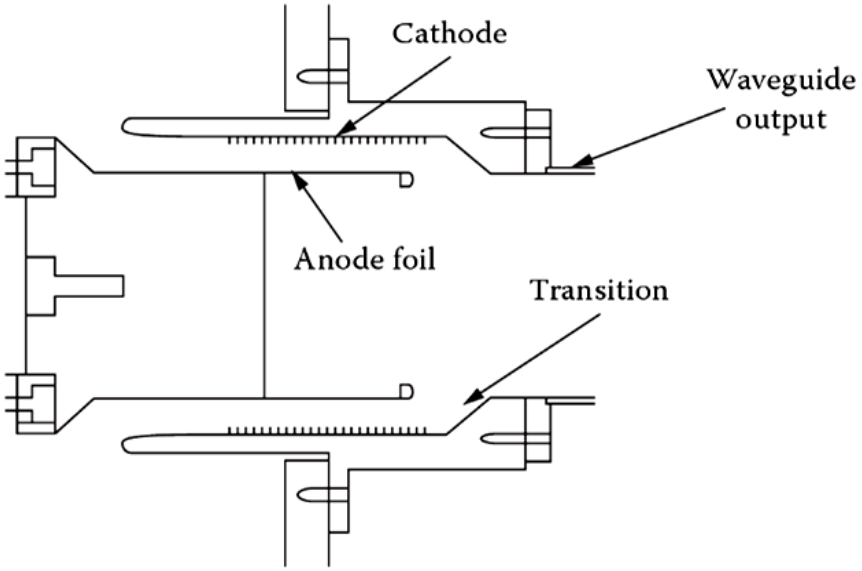

Figure 2.12—Coaxial vircator geometry [1]

The research performed at the Center for Physical and Power Electronics at the University of Missouri utilized two vircator HPM sources that were powered by a single pulsed power source. These vircators were capable of being independently tunable. This was accomplished by altering the AK gap to which each is set independently of each other. These two independent vircators were used to create multi-frequency high power microwave signals in a radially extracted geometry. The current and power sharing between the vircators was studied as well as the frequency independence between the two HPM sources.

References for Chapter 2

[1] J. Benford, J. A. Swegle, and E. Schamiloglu, *High Power Microwaves*, 2nd ed.: CRC Press, 2007.

[2] N. Ida, *Engineering Electromagnetics*, 2nd ed. New York: Springer-Verlag New York, LLC, 2004.

[3] F. T. Ulaby, E. Michielssen, and U. Ravaioli, *Fundamentals of Applied Electromagnetics*, 6th ed.: Pearson Education, Inc., 2010.

[4] C. A. Balanis, *Advanced Engineering Electromagnetics*.: John Wiley & Sons, Inc., 1989.

[5] P. W. Smith, *Transient Electronics: Pulsed Circuit Technology*.: John Wiley & Sons Ltd., 2002.

[6] J. W. Nilsson and S. A. Riedel, *Electric Circuits*, 8th ed., 2008.

[7] R. J. Adler, "Pulse Power Formulary," North Star Research Corporation, 1989.

[8] D. Bortis, J. Biela, and J. W. Kolar, "Optimal Design of a DC Reset Circuit for Pulse Transformers," in *APEC 2007 - 22nd Annual IEEE Applied Power Electronics Conference*, 2007, pp. 1171-1177.

[9] Y. Chen, "Compact, Repetitive Marx Generator and HPM Generation with the Vircator," Texas Tech University, Master's Thesis 2005.

[10] R. B. Miller, "Mechanism of explosive electron emission for dielectric fiber (velvet) cathodes," *Journal of Applied Physics*, vol. 84, no. 7, pp. 3880-3889, October 1998.

[11] C. D. Child, *Phys. Rev.*, no. 32, p. 492, 1911.

[12] I. Langmuir, "The effect of space charge and residual gases on thermionic currents in high vacuum," *Phys. Rev.*, no. 2, p. 450, 1913.

[13] J. W. Luginsland, Y. Y. Lau, R. J. Unstattd, and J. J. Watrous, "Beyond the Child-Langmuir Law: A review of recent results on multidimensional space-charge-limited flow," *Physics of Plasmas*, vol. 9, no. 5, pp. 2371-2376, May 2002.

[14] R. B. Miller, *An Introduction to the Physics of Intense Charged Particle Beams*. New York, United States of America: Plenum Press, 1982.

[15] L. E. Thode and C. M. Snell, "Virtual Cathode Microwave Devices - Basics," Los Alamos National Laboratory, Los Alamos, 1991.

[16] A. Watson, "Pulsed Flashover in Vacuum," *Journal of Applied Physics*, vol. 38, no. 5, p. 2019, April 1967.

[17] O. Milton, "Pulsed Flashover of Insulators in Vacuum," *IEEE Transactions on Electrical Insulation*, vol. EI-7, no. 1, p. 9, March 1972.

[18] J. P. Shannon, S. F. Philp, and J. G. Trump, "Insulation of High Voltage Across Solid Insulators in Vacuum," *Journal of Vacuum Science and Technology*, vol. 2, no. 5, p. 234, September 1965.

[19] C. Moller, M. Elfsberg, A. Larsson, and S. E. Nyholm, "Experimental Studies of the Influence of a Resonance Cavity in an Axial Vircator," *IEEE Transactions on Plasma Science*, vol. 38, no. 6, pp. 1318-1324, June 2010.

[20] W. -Y. Woo, "Two-dimensional features of virtual cathode and microwave emission," *Phys. Fluids*, vol. 30, no. 1, pp. 239-244, January 1987.

[21] D. J. Sullivan, "High power microwave generation from a virtual cathode oscillator (Vircator)," *IEEE Transactions on Nuclear Science*, vol. 30, no. 4, pp. 3426-3428, August 1983.

[22] D. Price, D. Fittinghoff, J. Benford, H. Sze, and W. Woo, "Operational Features and Microwave Characteristics of the Vircator II Experiment," *IEEE Transactions on Plasma Science*, vol. 16, no. 2, pp. 177-184, April 1988.

[23] K. S. Woolverton, "High-Power, Coaxial Vircator Geometries," Texas Tech

University, PhD Dissertation 1998.

[24] E. -H. Choi et al., "High-Power Microwave Generation from an Axially Extracted Virtual Cathode Oscillator," *IEEE Transactions on Plasma Science*, vol. 28, no. 6, pp. 2128-2134, December 2000.

[25] Sandia National Laboratories, "A Brief Technology Survey of High-Power Microwave Sources," Sandia National Lab, Albuquerque, NM, 2001.

[26] B. V. Alyokhin et al., "Theoretical and Experimental Studies of Virtual Cathode Microwave Devices," *IEEE Transactions on Plasma Science*, vol. 22, no. 5, pp. 945-959, October 1994.

[27] J. Mankowski, Y. Chen, J. Dickens, and A. Neuber, "A Low-Cost Metallic Cathode for a Vircator HPM Source," in *IEEE Pulsed Power Conference*, Monterey, 2005, p. 66.

[28] A. Shlapakovski et al., "Double-Gap Vircator Operation at Sub-Microsecond Pulse Duration," in *IEEE International Vacuum Electronics Conference*, Rome, 2009, pp. 66-67.

[29] See for example S. C. Burkhart, R. D. Scarpetti, and R. L. Lundberg, "A Virtual-Cathode Reflex Triode for High-Power Microwave Generation," *J. Appl. Phys.*, vol. 58, no. 1, pp. 28-36, 1985.

[30] H. Sze, J. Benford, T. Young, D. Bromley, and B. Harteneck, "A Radially And Axially Extracted Virtual-Cathode," *IEEE Transactions on Plasma Science*, vol. 13, no. 6, pp. 492-497, December 1985.

[31] See for example M. Elfsberg, T. Hurtig, A. Larsson, C. Moller, and S. Nyholm, "Experimental Studies of Anode and Cathode Materials in a Repetitive Driven Axial Vircator," *IEEE Transactions on Plasma Science*, vol. 36, no. 3, pp. 688-693, June 2008.

[32] X. Chen et al., "Microwave Frequency Determination Mechanisms in a Coaxial Vircator," *IEEE Transactions on Plasma Science*, vol. 32, no. 5, pp. 1799-1804, October 2004.

[33] P. Poulsen, P. A. Pincosy, and J. J. Morrison, "Progress toward steady-state, high-efficiency vircators," in *Proc. SPIE*, 1991, pp. 172-182.

[34] See for example P. A. Lindsay, W. K. Toh, and X. Chen, "The influence of an axial magnetic field on the performance of a coaxial vircator," *IEEE Transactions on Plasma Science*, vol. 30, no. 3, pp. 1186-1195, June 2002.

[35] J. Walter, J. Dickens, and M. Kristiansen, "An "Energy Efficient" Vircator-Based HPM System," in *IEEE Pulsed Power Conference*, 2011, pp. 658-661.

[36] W. Jiang, K. Woolverton, J. Dickens, and M. Kristiansen, "High Power Microwave Generation by a Coaxial Virtual Cathode Oscillator," *IEEE Transactions on Plasma Science*, vol. 27, no. 5, pp. 1538-1542, October 1999.

[37] A. N. Didenko et al., in *Proc. of the 3rd Intl Top. Conf. on High Power Electron and Ion Beam Research and Technology*, 1979, p. 683.

[38] B. V. Alekhin et al., "Effective pulsed-repetitive vircator with double anode grid," in *Intl. Conf. on High-Power Particle Beams (BEAMS 2004)*, 2004, pp. 544-547.

Chapter 3 — Pulsed Power System

3.1 Overview of System

High power microwave systems require powerful electrical systems to allow for high power microwave generation. Because HPM devices require very high power levels, pulsed systems are often used in order to reduce the average power and system heating [1], [2]. Examples of pulsed power systems include Marx generators and power conditioning systems utilizing a modulator and pulse forming line (PFL) to create square high voltage pulses [1], [3], [4], [5], [6]. Some of the basic components that form pulsed power systems were introduced in Section 2.2. A power modulator and PFL were used for the dual vircator system described in this report. The simulation and diagnostics of the pulsed power system are discussed in Chapters 4 and 6, respectively.

The repetitive high voltage pulse generator designed and built at the Center for Physical and Power Electronics at the University of Missouri—Columbia is capable of generating pulses with peak powers over 3 GW to drive an HPM load. A schematic of the pulsed power circuit is shown in Figure 3.1 [7].

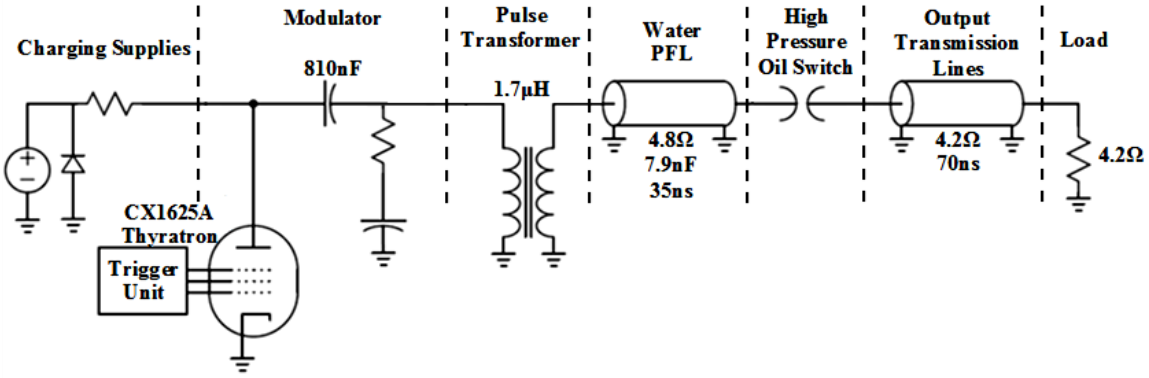

Figure 3.1—Pulsed power system schematic [7]

This system utilizes a modulator which pulse charges a PFL up to 250 kV [8]. The PFL is a water transmission line with an impedance of 4.8 Ω and a 35 ns one way transit time. The energy stored in this line is discharged as a rectangular pulse through a high pressure oil switch. The following sections discuss each piece of the pulsed power driving circuit in detail.

3.1.1 Modulator

The pulsed power system utilized in this project was previously used as a test stand for experimenting with various high pressure liquid dielectric switch geometries and fluids [7]. The modulator was refurbished and rebuilt using components from this system to create a pulsed power system for driving the vircator HPM source. A photo of the modulator is shown in Figure 3.2 with the capacitor bank and thyratron switch labeled. These components are discussed in detail later in this section.

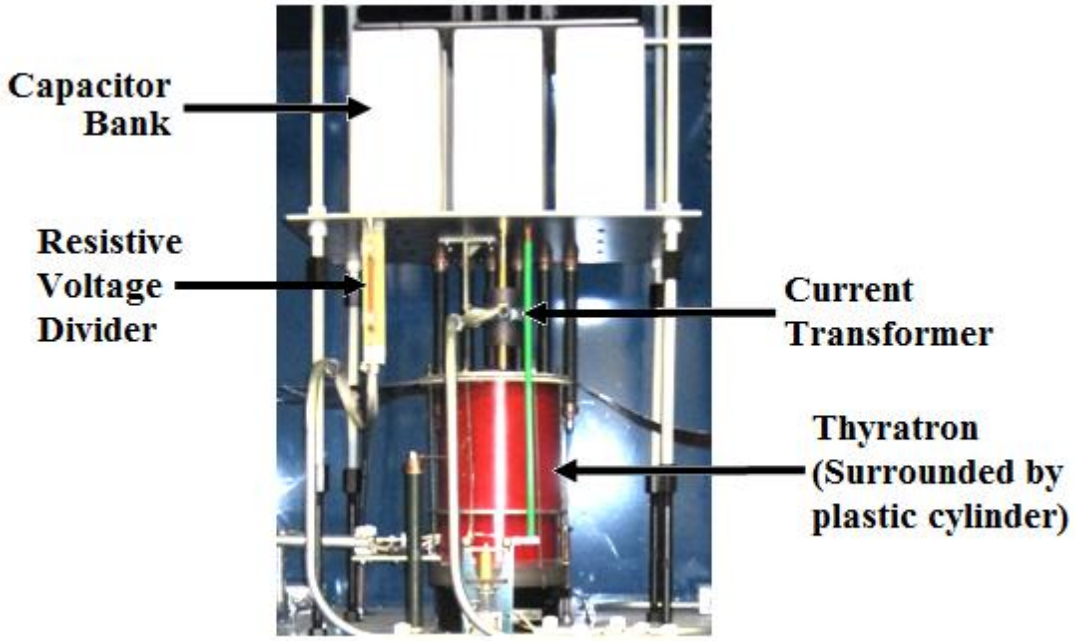

Figure 3.2—Upper (driven) section of pulse modulator

The modulator, as defined in this thesis, consisted of a switch and a capacitor bank. The capacitor bank was made up of nine 90-nF capacitors (General Atomic, Model 31662) connected in parallel, forming an equivalent capacitance of 810 nF. At 25 kV, the energy stored in the capacitor bank was approximately 250 J. Further specifications for the capacitors are shown in Table 3.1 [9]. The capacitor bank is shown in Figure 3.2.

Table 3.1—High voltage capacitor specifications

Parameter	Value
Manufacturer	General Atomics
Part Number	31662
Capacitance	90 nF
Equivalent Series Inductance	80 nH
Max Voltage	40 kV
Peak Current	25 kA
RMS Current	25 A

The power supplies used to charge the capacitors were 30-kV power supplies (TDK-Lambda, Model ALE 302S). Six of these supplies operated in parallel to rapidly charge the capacitor bank. While a single power supply would be capable of charging the system, using multiple supplies in parallel allows the system to operate at a much higher repetition rate. The connection network for each individual supply consisted of the power supply, a resistor to isolate the supply from the other supplies and to reduce current transients during discharge, and a diode network to provide reversal protection. An example schematic of this protection circuit is shown in Figure 3.3. The specifications for the power supplies are shown in Table 3.2 [10].

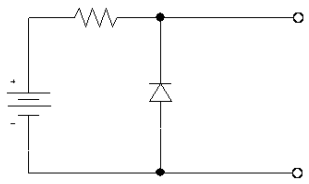

Figure 3.3—Power supply protection schematic

Table 3.2—Specifications for individual charging power supplies

Parameter	Value
Manufacturer	Applied Laser Electronics
Model Number	ALE 302S
Max Voltage	30 kV
Average Power	3 kW
Peak Power	4 kW

To generate the output pulse from the charged capacitor bank, the capacitor bank was switched with a hydrogen thyratron. A thyratron acts as a high voltage switch which closes through a controlled plasma discharge. It has multiple connection points: the anode, cathode, and control grids [11], [12]. Voltage pulses applied to the control grids generate a controlled plasma column which connects the anode and cathode and allows current to flow. The thyratron used in this system was a CX1625A thyratron manufactured by E2V Technologies. A schematic of the thyratron connections is shown in Figure 3.4. In the case of this project, the grid resistors had values of: $R_1 = 82\ \Omega$, $R_2 = 820\ \Omega$, and $R_3 = 75\ \Omega$

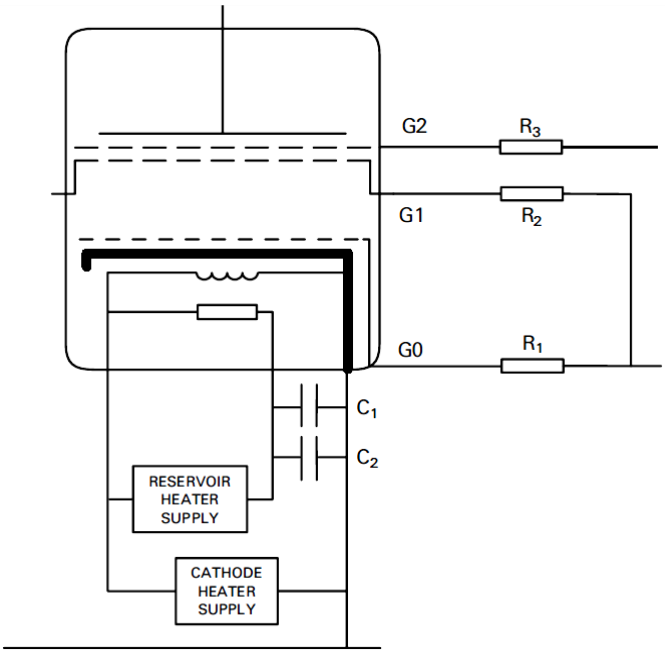

Figure 3.4—Thyratron connection schematic [11]

The thyratron had three separate control grids for switching the thyratron. This thyratron was capable of handling 15 kA of peak anode current, 5 A of average current, and 35 kV of forward anode voltage [11]. The top electrode is the anode, and the bolded electrode is the cathode in Figure 3.4.

A double-pulse scheme was used to trigger the thyratron, which minimizes the switch jitter and improves the lifetime of the thyratron [12]. In this setup, grids 0 and 1 were triggered by the same pulse but with a current division ratio of 10:1, respectively. Grid 2 was driven with a separate pulse delayed from the first pulse by about 1 μs. The open-circuit trigger generator pulses are shown in Figure 3.5. The thyratron trigger generator characteristics into an open load are shown in Table 3.3.

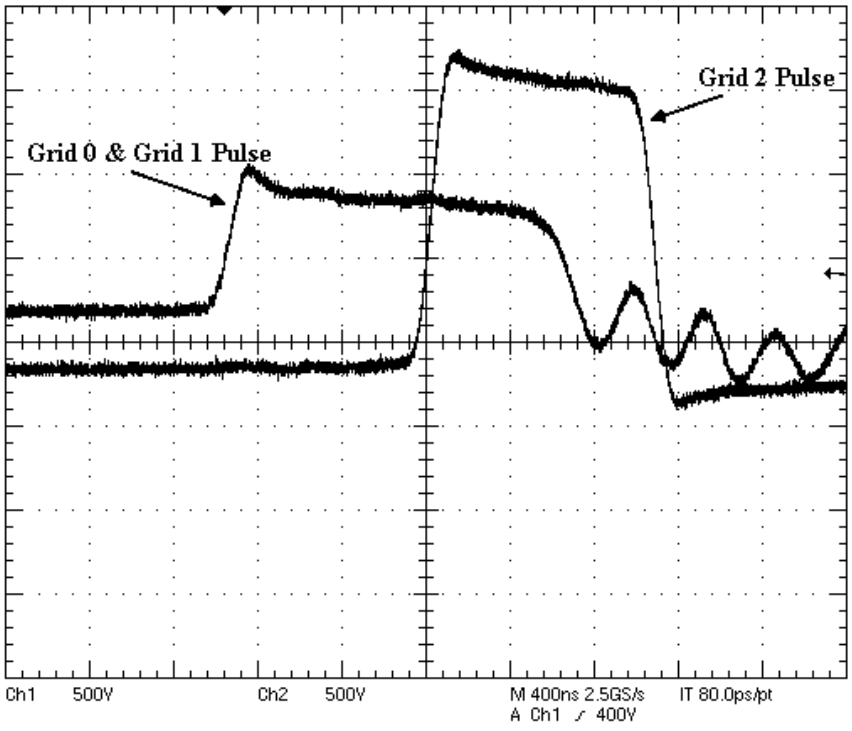

Figure 3.5—Thyratron trigger generator open-circuit grid pulses: Ch1 500 V/div, Ch2 500 V/div, 400 ns/div

Table 3.3—Thyratron trigger generator unloaded characteristics

Parameter	Grid 0/1	Grid 2
Voltage Amplitude, kV	0.8	1.5
Driver Impedance, Ω	75	75
Bias Voltage, V	0	-200
Pulse Length, μs	1.6	1
Pulse Delay, μs	0	1
Pulse Overlap, μs	0.5	
Rate of Rise, kV/μs	5	7.5

The output from the capacitor bank on the modulator was delivered to a pulse transformer via twelve RG-217 cables that were each ten meters in length. The length of these cables created an impedance mismatch, which, in the absence of filter circuitry, creates a voltage overshoot with an amplitude much higher than the charge voltage. In order to limit the possibility of breakdown induced by this voltage ringing, an RC snubber/filter network was implemented in the system. An RC snubber is one of the most commonly used transient suppressors in power circuits and in circuits with solid-state switches. Its main purpose is to remove voltage spikes that occur because of an inductive "kick" when a switch opens or closes [13]. This RC network consisted of a resistor and capacitor in series that filtered out high frequency signals. The resistor used in this project was a high energy ceramic composite disk resistor manufactured by HVR Advanced Power Electronics. The specifications for this resistor are shown in Table 3.4 [14]. The capacitor was a high-voltage 3.3-nF ceramic capacitor that was capable of holding off 40 kV_{DC} [15]. Eight of the series RC networks were connected in parallel. Eight were placed in parallel in order to achieve the correct RC time constant for filtering out the resonant signal created by the cable inductance. Figure 3.6 is a photo of the RC snubber attached to the high voltage input plate of the pulse transformer, with an enlarged view of an individual RC network shown in Figure 3.7.

Table 3.4—High energy ceramic carbon disk resistor specifications

Parameter	Value
Manufacturer	HVR Advanced Power Electronics
Part Number	W0508C500L
Resistance	50 Ω ± 20%
Outer Diameter	50 mm
Inner Diameter	19 mm
Height	25.4 mm
Max Energy	12 kJ

Figure 3.6—RC snubber circuit

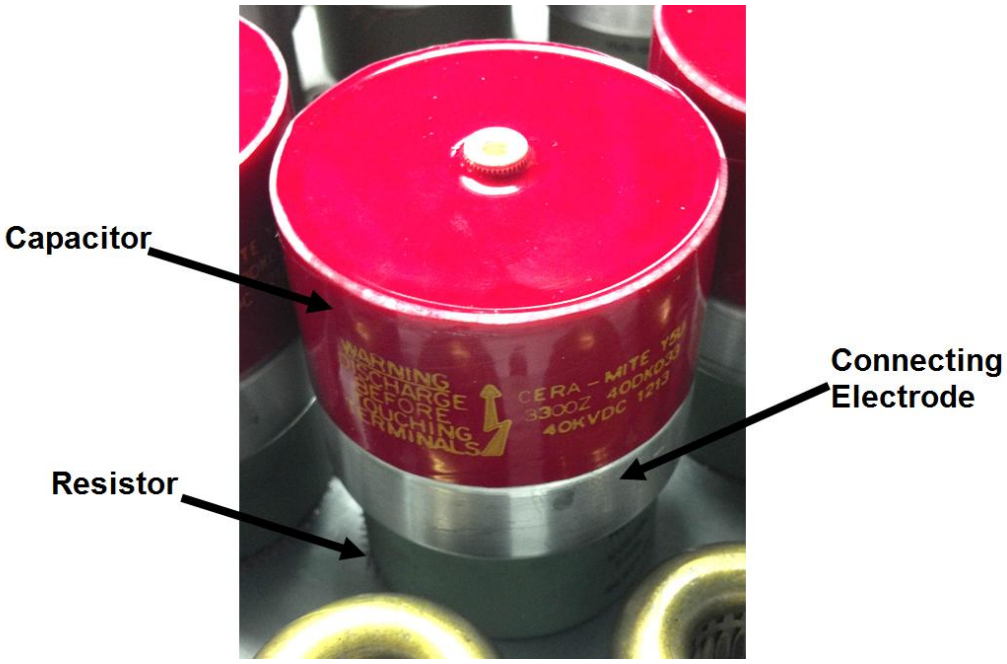

Figure 3.7—Single series RC network

The modulator also incorporated a safety mechanism to protect the operator. Since the capacitors were designed to be low loss and store energy through high voltage, dangerous amounts of energy could be stored for long periods of time. To dissipate this energy, a shorting relay was used to short out the capacitor bank. The relay was a Ross EA-40NC relay capable of holding off 40 kV [16]. The contacts of this relay are normally closed without power so that if power was disconnected, the relay would close and dissipate the energy stored in the modulator's capacitor bank.

3.1.2 Pulse Transformer

The modulator was limited to a 30-kV charge and discharge as this was the limiting voltage of the power supplies. It was necessary to convert this low-voltage pulse into a high-voltage pulse in order to break down the oil switch at the output of the pulse forming line. To accomplish this task, a pulse transformer with an approximate voltage step-up ratio of 1:10 was used to increase the voltage from 30 kV to a maximum 300 kV at the output of the transformer. The transformer also provided the dominating inductance in the CLC discharge circuit described in Section 2.2.

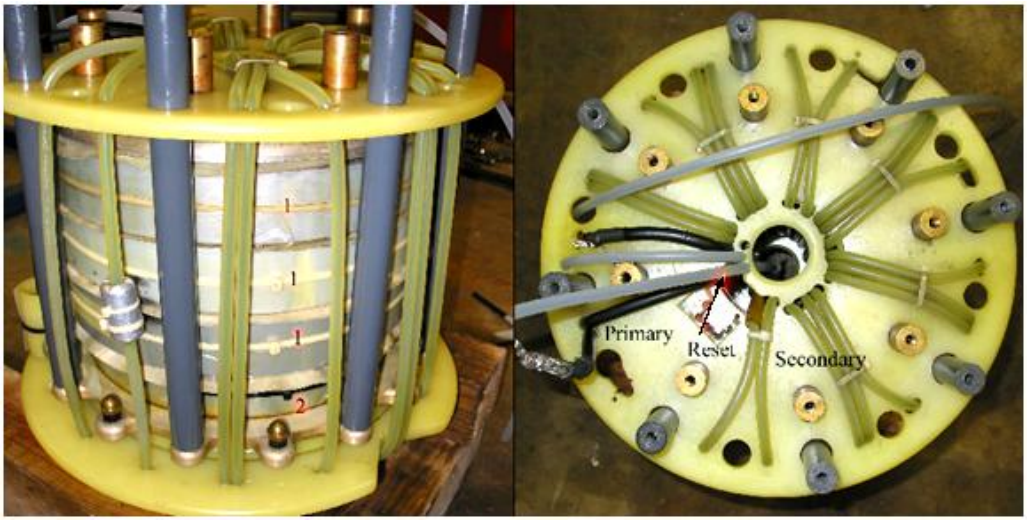

Figure 3.8—Pulse transformer with core and winding labels [7]

In order to achieve high coupling between the primary and secondary of the transformer, and maximize the possible voltage gain through the transformer, a magnetic core was used, which is made of Metglas 2605CO. The properties for this material can be seen in Table 3.5 [17]. The pulse transformer itself is shown in Figure 3.8.

Table 3.5—Magnetic core properties [17]

Parameter	Value
Manufacturer	Allied Signal
Material	Metglas 2605CO
Saturation Flux	1.8 T
Remanent Flux	1.7 T
Coercive Force	3.2 A/m

We measured the various inductances of the pulse transformer: primary, secondary, and leakage inductances. From these measurements, the primary and secondary inductances were found to be 76 μH and 7.4 mH, respectively. To determine the leakage inductance of the transformer, the windings can be shorted [18]. Using this technique, as well as resonant time constants from measured diagnostic signals, the leakage inductance was found to be approximately 1.7 μH.

Since a nonlinear magnetic core was being used, a DC reset circuit was used in order to operate in the linear regime of the magnetic material. This DC reset of the magnetic core allowed for the maximum utilization of the linear regime of the magnetic core. The design equation for a reset circuit utilizing a DC supply is as follows:

$$I \geq \frac{Hl_m}{N} \tag{3.1}$$

where I is the DC current needed to reset the cores in amps, l_m is the magnetic length of the cores in meters, H is the coercive force in A/m, and N is the number of turns used for the reset circuit [19]. The magnetic length was approximated to be 0.658 m, and the reset circuit utilized 2 turns around the cores. Using the value for the coercive force from

Table 3.5 as the value for *H* and substituting the other values into equation 3.1, one can calculate the minimum current required to be 1.053 A. A schematic of the reset circuit is shown in Figure 3.9.

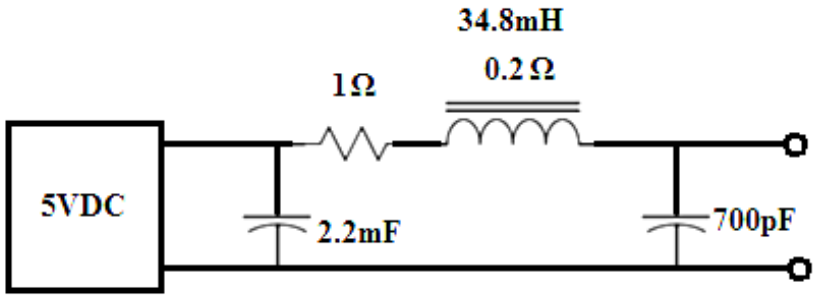

Figure 3.9—Pulse transformer reset circuit

To perform simulations, an accurate model of the transformer was necessary. To model the transformer including the nonideal characteristics of the transformer, a T-model representation was used [20]. A schematic is shown in Figure 3.10. The actual parameters used in the circuit simulations are shown in Table 3.6. The primary and secondary inductances and resistances were experimentally measured, while the leakage inductance and mutual inductance were calculated both from experimental measurements, including inductance measurements and time constants from diagnostic waveforms.

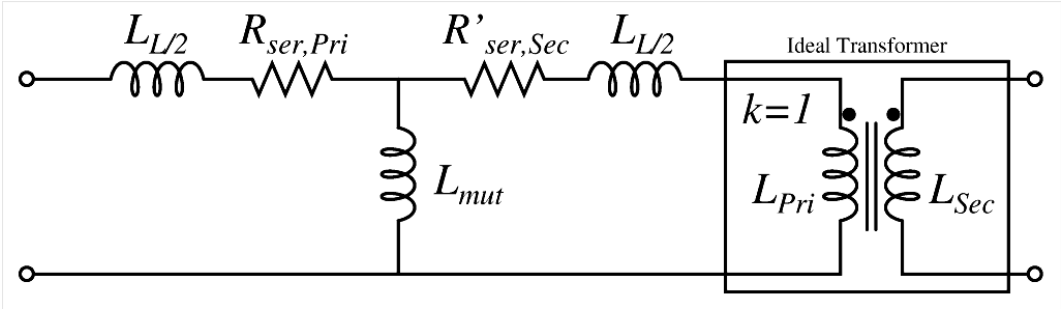

Figure 3.10—T-model equivalent of pulse transformer [7]

Table 3.6—T-model parameters used in simulations

Parameter	Value
L_L	1.703 μH
L_{mut}	75.6 μH
$R_{ser,Pri}$	15.9 mΩ
$R^*_{ser,Sec}$	15.9 mΩ
L_{Pri}	75 μH
L_{Sec}	7.5 mH

3.1.3 Water PFL

The pulse transformer stepped up the voltage from the modulator pulse by a factor of ten to charge the water pulse forming line. The PFL was essentially a water-filled coaxial transmission line. The line is made of stainless steel and acts as an energy storage device. The physical properties of the PFL are shown in Table 3.7. A photo of the line can be seen in Figure 3.11.

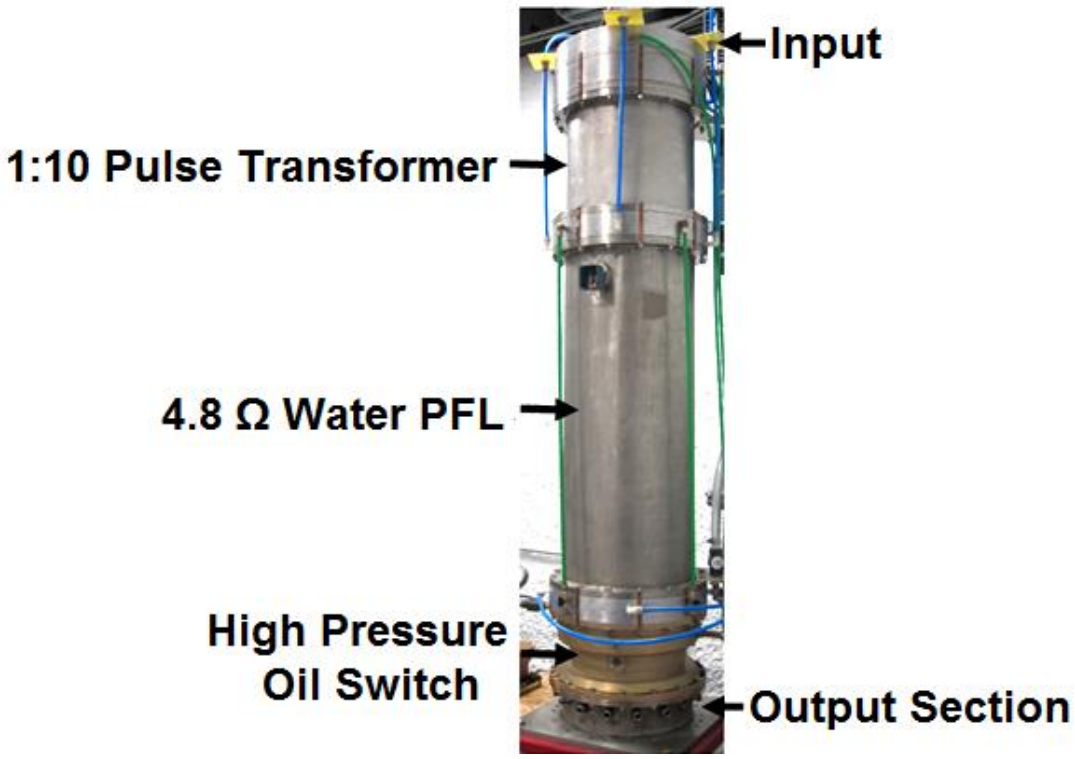

Figure 3.11—35 ns, 4.8 Ω pulse forming column showing various sections

Table 3.7—PFL properties

Parameter	Value
Inner Conductor Diameter	20.8 cm
Outer Conductor Diameter	42.5 cm
Length	1.171 m
Relative Permittivity ϵ_r	80

In order to maximize energy efficiency, the impedance of the modulator and PFL should be matched. Before the PFL impedance could be calculated, the line's constitutive parameters were determined. Ignoring the resistance of the conductors and the conductance losses in the dielectric, the impedance of the pulse forming line is:

$$Z = \sqrt{\frac{L}{C}} \tag{3.2}$$

where L is the inductance of the line in henries, C is the capacitance of the line in farads, and Z is the impedance of the line in Ω [20], [21]. The inductance and capacitance were calculated using equation 3.3 and 3.4 as derived from Gauss's Law and Ampere's Law for a coaxial line [20], [21]:

$$L = l\frac{\mu}{2\pi}\ln\left(\frac{b}{a}\right) \tag{3.3}$$

$$C = l\frac{2\pi\epsilon}{\ln\left(\frac{b}{a}\right)} \tag{3.4}$$

where l is the coaxial line length in meters, μ is the permeability of the insulator in H/m ($\mu = \mu_r\mu_0$), ϵ is the permittivity of the insulator in F/m ($\epsilon = \epsilon_r\epsilon_0$), a is the radius of the center conductor in meters, and b is the radius of the outer conductor in meters. Using the parameters from Table 3.7, the inductance and capacitance of the pulse forming line were found to be 167.3 nH and 7.293 nF. The line impedance was then calculated to be 4.79 Ω. Again, assuming that the lossy parameters of the pulse forming line are

negligible, the transit time, τ, of the PFL can be determined from the inductance and capacitance as follows [20], [21]:

$$\tau = \sqrt{LC}. \tag{3.5}$$

The one-way transit time of the PFL was calculated to be 34.9 ns. When the energy stored in the PFL was discharged through the high-pressure oil switch, the output pulse length was equal to twice the one-way transit time at half the voltage [20]. This means that the pulse width was approximately 69.9 ns.

Table 3.8—PFL electrical parameters

Parameter	Value
Inductance	167.3 nH
Capacitance	7.293 nF
Output Pulse Length	69.9 ns
Line Impedance	4.79 Ω

To deliver the output pulse from the pulse forming line, twelve parallel high voltage transmission line cables were connected to the output plate on the switch as shown in Figure 3.12.

Figure 3.12—Twelve parallel high voltage output cables at the base of the PFL structure

The cables were RG-218 cables with a characteristic impedance of 50 Ω [22]. In parallel, the cables had an impedance of approximately 4.167 Ω. This created an impedance mismatch between the PFL and the output cables. The reflection coefficient at this interface was, $\Gamma = -0.0706$ [21]. This means that the amplitude of the output pulse

delivered to the output cables was actually 0.4647 times the charge voltage on the PFL. In other words, the output pulse for a charge voltage of 250 kV would be approximately 116 kV as opposed to 125 kV for a matched load. To provide isolation between the switch and any reflections that might occur due to load mismatches, the one-way transit time of the cables was 70 ns. This was on the order of the width of the output pulse so that reflections that traverse back toward the switch are incapable of passing through the switch due to their decreased voltage amplitude making it improbable that the reflections would cause breakdown.

In order to reduce the losses that occur from conduction in the water acting as the insulating material in the PFL, the water was deionized. The conductivity of tap water is much too high to act as a good insulator due to various ions and metals in the liquid. To reduce the conductivity, the water flowed through a resin-based deionizing filter. A water conductivity probe was placed in line with the water feedlines to show whether the conductivity was below a certain threshold. When the resistivity was higher than 2 MΩ-cm, a green LED indicated that an acceptable level had been reached. This is shown in Figure 3.13. In addition to the deionizing filter, the water was filtered with a standard particulate filter, similar to a swimming pool filter, to remove any particles in the water. During operation, the water flowed continuously through the water PFL.

Figure 3.13—Water conductivity meter

3.1.4 High-Pressure Oil Switch

The pulse generator utilized a high pressure oil switch for the improved jitter performance, increased switch lifetime, and higher breakdown voltage shown in previous studies to switch the water PFL [7], [23], [24], [25]. The output pulse from the water pulse forming line was generated when the voltage on the PFL caused the oil flowing through the switch to break down. The arc generated during the breakdown closed the switch and delivered the voltage in the form of a 70 ns pulse to the load through the high voltage output cables. The switch was designed and developed at the Center for Physical and Power Electronics at the University of Missouri [7]. A photo of the switch can be seen in Figure 3.14.

Figure 3.14—High pressure oil switch

In this photo, the inflow port for the oil and the charging side of the switch is at the bottom while the outflow port and output side of the switch is at the top. During testing, the switch was in an inverted orientation to that shown in Figure 3.14, and the hydraulic oil pump is continuously flowing oil through the switch. This continuous flow removed the byproducts created during the arc discharge. The oil used in the switch was a polyalphaolefin-based synthetic fluid, namely Brayco Micronic 889, manufactured by

Castrol Limited, meeting the military specification number MIL-PRF-87252C. A side cutaway of the switch is shown in Figure 3.15. The maximum pressure before mechanical failure of the switch is 2500 psig. To adjust the mean breakdown voltage, and thus the mean output pulse amplitude, the output electrode is adjustable to gaps greater than 5 mm.

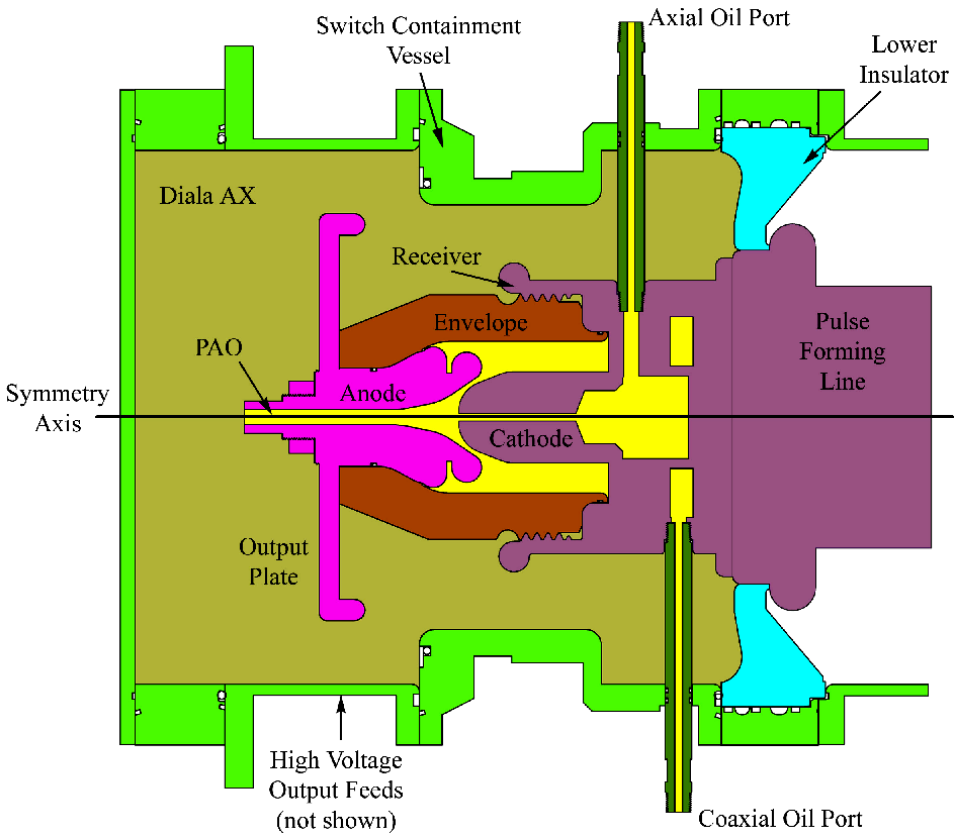

Figure 3.15—Side cutaway of the switch and PFL output [7]

Another side-cut view of the switch can be seen in Figure 3.16 [26]. The electrode gap is adjusted by turning the outflow port on the switch assembly. This portion is threaded (28 threads per inch) and adjusts the uncharged electrode while the charged electrode is stationary. The gap between the electrodes is related to the axial distance that the outflow port is adjusted by the following equation:

$$d_{act} = d_{axial} \cos(56°) \tag{3.6}$$

where d_{act} is the actual distance increase between the electrodes in mm and d_{axial} is the axial distance in mm that the outflow port moves when adjusted.

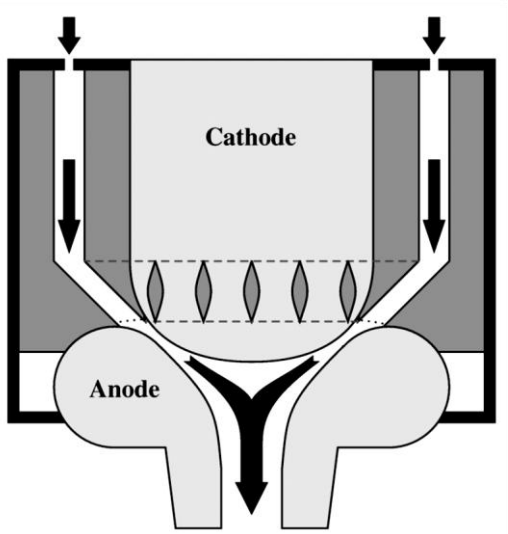

Figure 3.16—Side-cut diagram of the high-pressure oil switch

Several diagnostics were used to maintain parameters related to the oil dielectric passing through the switch in order to provide consistency between tests. The parameters that were controlled include the pressure of the oil in the switch and the flow rate of the oil through the switch. Both of these parameters were independently variable. Oil pressure was controlled through the use of a needle valve that restricted the return flow of the oil. In-line pressure gauges were placed both at the inlet of the switch and at the outlet side near the hydraulic pump. The maximum measurable pressure on these gauges was 3000 psi, which was higher than the maximum allowed pressure limited by the mechanical properties of the switch.

The flow rate of the oil was controlled by a valve on the hydraulic pump. Two separate gauges were used to verify the oil flow rate. A variable-area-orifice flow sensor was placed in-line with the inlet flow path. This sensor was a Hedland Flow Meters part number H601-A-010-RF with a flow rate range of 1 to 15 gallons per minute (gpm) [27].

The second sensor used to measure the flow through the oil return line was a turbine flow sensor with higher precision than the variable-orifice flow sensor. The turbine sensor was a Cox Instruments AN-10 turbine flow sensor with a range of 2-20 gpm [28]. This flow meter required the use of a flow computer to convert its output signal into a readable flow rate. This computer was a Hoffer Flow Controls 163 flow computer that can display flow rates with a precision of 0.01 gpm [29]. The flow rate of the oil for this project was set to 5 gpm.

3.1.5 Inductive Voltage Adder

To achieve electron emission from the cathode in a planar Child-Langmuir diode, high field strengths are required. While the field is enhanced by the pointed tips on cathode fibers and surfaces used as the emission surface, higher voltage levels are required for the large anode-cathode gap spacings necessary to achieve lower microwave frequencies. To obtain higher voltages, an inductive voltage adder was used to double the output voltage from the pulse forming line. The inductive adder fundamentally consists of two transformers whose primary connections are connected in parallel while the secondary connections are connected in series so that the voltages on the output of each transformer add together. To increase the coupling, magnetic cores were used to increase the permeability and focus the magnetic field lines. To reset the cores to maintain linear operation, a DC reset circuit was utilized to maximize the magnetic flux swing on the B-H curve of the magnetic material. The inductive adder was placed in a tank that was filled with transformer oil to prevent breakdown from occurring within the inductive voltage adder. The oil in this tank was filtered, and after filtering, a small pump was used to flow the oil in areas where air bubbles were likely to be caught. This

was done to remove the air bubbles and thus decrease the chances of early breakdown in the adder system.

Magnetic cores were used to maximize the coupling between the primary input and the secondary output. The magnetic cores were Ceramic Magnetics, Inc. CN20 Nickel-Zinc ferrite cores. Each "turn" of the inductive adder had seven cores. A photograph of the adder is displayed in Figure 3.17. The properties for CN20 are displayed in Table 3.9 [30].

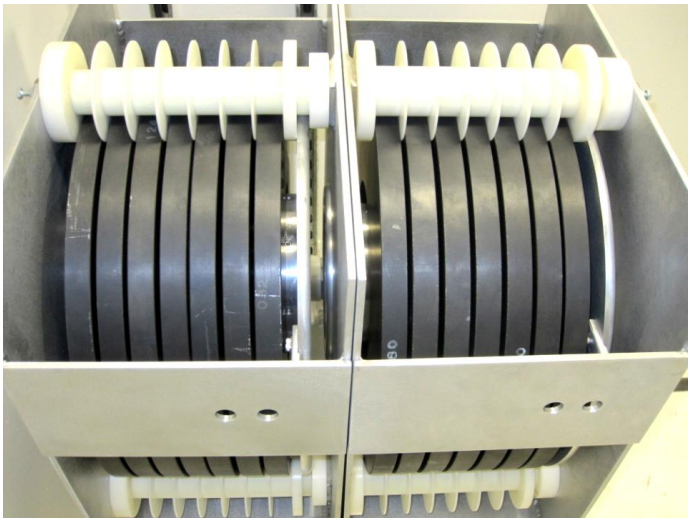

Figure 3.17—Inductive voltage adder

Table 3.9—CN20 magnetic core properties

Parameter	Value
Manufacturer	Ceramic Magnetics, Inc.
Material	CN20 Nickel-Zinc Ferrite
Saturation Flux	0.4 T
Remnant Flux	0.26 T
Coercive Force	15.9 A/m
Initial Permeability, μ_r	925

The T-model used for the inductive voltage adder is shown in Figure 3.18. The value for primary inductance was measured to be approximately 25 µH at a frequency of 1 MHz. The specifications for the magnetic cores are shown in Appendix D.

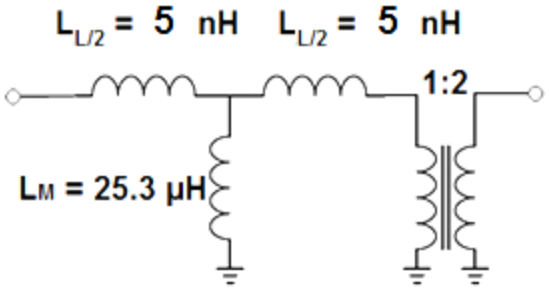

Figure 3.18—T-model of inductive voltage adder

In order to take full advantage of the linear permeability range on the B-H curve for the magnetic cores, a DC reset circuit was used to reset the position on the curve. The design equation for a reset circuit utilizing a DC supply was shown in equation 3.1. The magnetic length for the inductive adder was approximated to be 1.09 m. The reset circuit was electrically connected to the primary turns. Using the value for the coercive force from Table 3.9 as the value for H, one can calculate the minimum current required to be 17.3 A to utilize the full flux swing on the B-H loop. The actual magnetic flux swing can be calculated from Faraday's law of induction:

$$\int v(t)dt = NA\,\Delta B \tag{3.7}$$

where ΔB is the flux swing in tesla, N is the number of turns, A is the core cross-sectional area in m^2, and $v(t)$ is the time-varying voltage inducing the magnetic field in volts [31]. The integral of the voltage with respect to time is typically referred to as the volt-seconds product. Assuming a rectangular pulse of amplitude of 250 kV with a pulse width of 70 ns, the volt-seconds product of the pulse is 17.5 mV-s. The number of turns in this case was one and the cross-sectional area of each individual core was 0.00344 m^2, making the total area with 7 cores per turn equal to 0.0241 m^2. The flux swing from the pulse is 0.726 T, which is less than the maximum flux swing in the linear regime of the

B-H loop with a DC reset, $2B_{sat} = 0.8\,T$. A schematic of the reset circuit is shown in Figure 3.19.

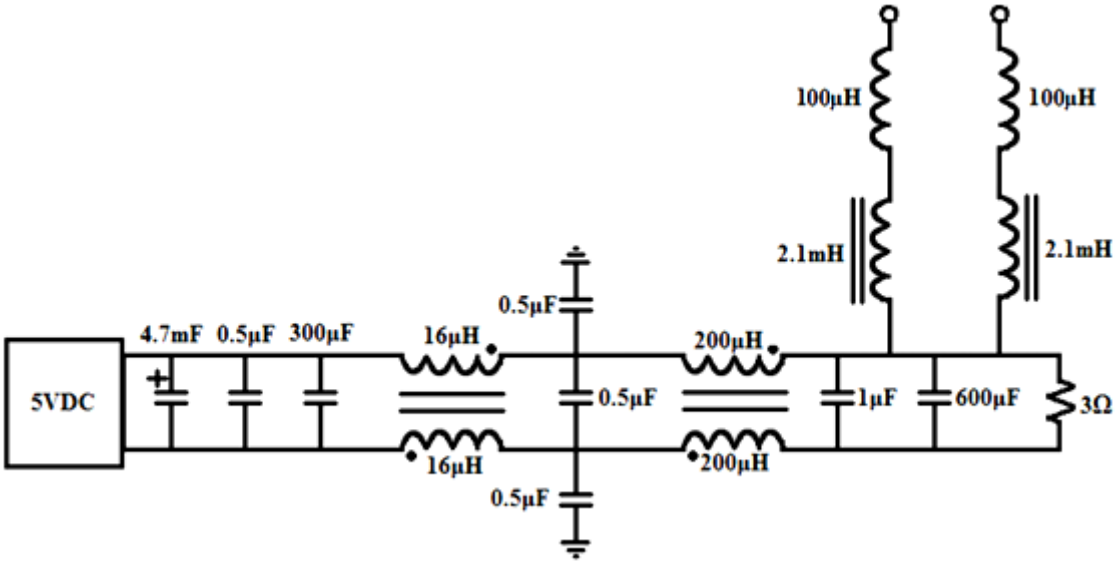

Figure 3.19—Inductive voltage adder reset circuit

Simulations including the inductive adder were performed along with the simulations of the modulator and PFL into a dummy load. The ideal SPICE model of the inductive adder without the leakage inductances is shown in Figure 3.20. The inductive adder is essentially two 1:1 transformers with the primaries driven in parallel and the secondary outputs connected in series, creating a 1:2 voltage step up.

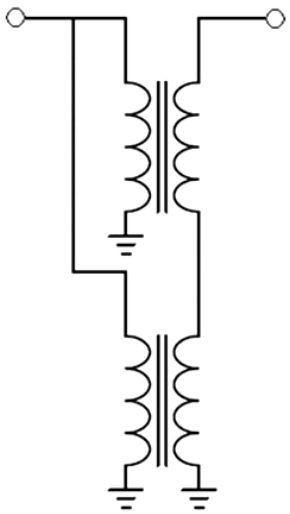

Figure 3.20—Ideal inductive voltage adder SPICE model

3.1.6 Load Resistors

In order to test the modulator and pulse generator system, dummy loads were used: one for the output of the pulse forming line and another for the output of the inductive adder. Both water resistor loads use copper sulfate crystals ($CuSO_4 \cdot 5H_20$) as the solute to adjust the resistance. The design of both loads is described later in this section.

The first load was a low inductance water resistor with solution flowing capabilities. A photo of this load resistor before assembly is shown in Figure 3.21. On the left in this figure, the solution containment vessel along with the electrodes in the bottom of the containment before connection are shown. On the right, the high voltage connection plates are shown with twelve grounding terminals for the cable shields of the twelve high voltage cables from the pulse forming line. This resistor had the capability of flowing the solution to cool the solution for sustained high repetition-rate applications. The resistor was based on a previous design used with this high voltage system [7]. The physical specifications of the resistor used for solution concentration calculations are shown in Table 3.10.

Figure 3.21—Pulse generator load resistor before assembly

Table 3.10—Pulse generator load resistor physical specifications

Parameter	Value
Electrode Area	123.49 cm^2
Electrode Spacing	10.16 cm
Desired resistance	4.2 Ω

The load for the inductive voltage adder was formed by two cylindrical water resistors in parallel. Two resistors were used to allow for the testing and characterization of each vircator individually before connecting the two in parallel. One of these water resistors is shown in Figure 3.22. One side of the resistor is connected to an aluminum plate which acts both as a sealing plate for the oil-filled tank that houses the inductive adder and as an electrical connection to the oil tank, which is grounded. The physical specifications for this resistor are shown in Table 3.11. The output impedance of the inductive voltage adder is approximately 16.67 Ω. To achieve this equivalent impedance, two resistors with resistances of approximately 33.3 Ω are necessary.

Figure 3.22—Single high voltage load resistor for adder output

Table 3.11—Inductive voltage adder load resistor physical specifications

Parameter	Value
Electrode area	20.27 cm^2
Electrode spacing	18.42 cm
Desired resistance	33.3 Ω

In order to obtain the desired resistance for the water resistor loads, the concentration of the solution used in the water resistor had to be altered depending on the

resistor geometry to achieve the necessary solution resistivity. The resistance is related to the resistor geometry and resistivity by the equation [32]:

$$R = \frac{\rho l}{A} \tag{3.8}$$

where R is the resistance in Ω, l is the resistor length or the electrode spacing in cm, ρ is the solution resistivity in Ω-cm, and A is the electrode area in cm^2. The solution is typically made with deionized water and various salt solutes such as copper sulfate, sodium thiosulfate, and others [32]. By trying different solution concentrations in a controlled setup, an empirical curve fit can be found relating the resistivity to the concentration through the equation:

$$\rho = aC^b \tag{3.9}$$

where C is the solution concentration in g/L and a and b are curve fitting coefficients. From [32], the coefficients a and b for a copper sulfate solute have been found to be 1553 and -0.7465, respectively. The concentrations necessary for both loads can be found by substituting the values shown in Table 3.10 and Table 3.11 into equations 3.8 and 3.9. The resistivity needed for the pulse generator load was 51.05 Ω-cm. This corresponds with a copper sulfate concentration of 97.02 g/L. After adding the solution to the resistor's containment vessel, the resistance was measured at 4.3 Ω instead of the 4.2 Ω that was used in the design. The resistivity needed for the inductive adder load was 36.64 Ω-cm. This corresponds with a copper sulfate concentration of 151.3 g/L. The resistors used in the inductive voltage adder load were found to have values of 33 Ω and 35 Ω, forming an equivalent parallel resistance of approximately 17 Ω, slightly greater than the matched impedance of 16.67 Ω.

References for Chapter 3

[1] J. Benford, J. A. Swegle, and E. Schamiloglu, *High Power Microwaves*, 2nd ed.: CRC Press, 2007.

[2] E. Schamiloglu, "High Power Microwave Sources and Applications," in *2004 IEEE MTT-S International Microwave Symposium Digest*, 2004, pp. 1001-1004.

[3] Y. Chen, "Compact, Repetitive Marx Generator and HPM Generation with the Vircator," Texas Tech University, Master's Thesis 2005.

[4] See for example M. Elfsberg, T. Hurtig, A. Larsson, C. Moller, and S. Nyholm, "Experimental Studies of Anode and Cathode Materials in a Repetitive Driven Axial Vircator," *IEEE Transactions on Plasma Science*, vol. 36, no. 3, pp. 688-693, June 2008.

[5] S. H. Gold and G. S. Nusinovich, "Review of high-power microwave source research," *Review of Scientific Instruments*, vol. 68, no. 11, 1997.

[6] A. Roy et al., "Influence of Electron-Beam Diode Voltage and Current on Coaxial Vircator," *IEEE Transactions on Plasma Science*, vol. 40, no. 6, pp. 1601-1606, June 2012.

[7] P. Norgard, "Development of a Gigawatt Repetitive Pulse Modulator and High-Pressure Test Stand and Results from High-Pressure Switch Tests," University of Missouri - Columbia, Master's Thesis 2006.

[8] D. L. Birx, S. A. Hawkins, S. E. Poor, L. L. Reginato, and M. W. Smith, "Technology of Magnetically Driven Accelerators," *IEEE Transactions on Nuclear Science*, vol. 32, no. 5, pp. 2743-2747, October 1985.

[9] General Atomics Electronic Systems, "Pulse Discharge Capacitors," Data Sheet 2007.

[10] A.L.E. Systems, Inc., "Model 302 capacitor charging power supplies," Data sheet 2003.

[11] E2V Technologies, "CX1625A, CX1625AX Air Cooled, Hollow Anode, Metal/Ceramic Pentode Thyratrons," October 2002.

[12] E2V Technologies, "Hydrogen Thyratrons Preamble," Technical Brief 2002.

[13] Illinois Capacitor, Inc., "RC Snubbers (SMPS)," Technical Brief 2011.

[14] HVR Advanced Power Components, Inc., "High energy disc resistors," Tonawanda, Data sheet 2010.

[15] Vishay, "715C.DK Vishay Cera-Mite: High voltage disc capacitors, screw terminal mounting," Data Sheet 2009.

[16] Ross Engineering Co., "EA series relays," Data sheet 2002.

[17] G. A. Mesyats,. New York: Springer Science+Business Media, Inc., 2005, ch. 20, p. 359.

[18] Rhombus Industries, Inc., "Testing Inductance," Huntington Beach, Technical Brief 1998.

[19] D. Bortis, J. Biela, and J. W. Kolar, "Optimal Design of a DC Reset Circuit for Pulse Transformers," in *APEC 2007 - 22nd Annual IEEE Applied Power Electronics Conference*, 2007, pp. 1171-1177.

[20] P. W. Smith, *Transient Electronics: Pulsed Circuit Technology*.: John Wiley & Sons Ltd., 2002.

[21] F. T. Ulaby, E. Michielssen, and U. Ravaioli, *Fundamentals of Applied Electromagnetics*, 6th ed.: Pearson Education, Inc., 2010.

[22] Pasternack Enterprises, Inc., "RG218/U," Irvine, Data Sheet 2009.

[23] R. Curry et al., "The development and testing of subnanosecond-rise, kilohertz oil switches for the generation of high frequency impulses," *IEEE Trans. Plasma Sci.*, vol. 20, no. 3, pp. 383-392, June 1992.

[24] J. Leckbee, R. Curry, K. McDonald, R. Cravey, and A. Grimmis, "An advanced model of a high pressure liquid dielectric switch for directed energy applications," in *Proc. IEEE 14th Int'l Pulse Power Conf.*, 2003, pp. 1389-1393.

[25] J. Leckbee et al., "Design and testing of a high pressure, rep-rate, liquid dielectric switch for directed energy applications," in *Proc. IEEE 26th Int'l Power Modulator Conf.*, 2004, pp. 193-196.

[26] P. Norgard and R. D. Curry, "An In-depth Investigation of the Effect of Oil Pressure on the Complete Statistical Performance of a High-pressure Flowing Oil Switch ," *IEEE Transactions on Plasma Science*, vol. 38, no. 10, pp. 2539-2547, October 2010.

[27] Hedland Flow Meters, "3500/6000 PSI Flow Meters: For Petroleum Fluids," Data

Sheet 2006.

[28] Cox Instruments, "Precision Turbine Flow Meters—AN Series," Scottsdale, Data Sheet 2009.

[29] Hoffer Flow Controls, Inc., "Model 163 Digital Flow Rate Indicator," Elizabeth City, User's Manual 1995.

[30] Ceramic Magnetics, Inc., "CN20: Moderate Frequency Ni-Zn Ferrite," Fairfield, Data Sheet 2012.

[31] Texas Instruments, "Section 2: Magnetic Core Characteristics," Dallas, Technical Brief 2000.

[32] R. E. Beverly III and Associates, "Application Notes for Aqueous-Electrolyte Resistors," Application Note 2008.

Chapter 4 — Pulsed Power System Simulations

Circuit simulations of the pulsed power system were performed in LTSPICE. The simulations included a complex lumped-element model used to provide a representative response of the pulse generator system (the modulator, the pulse transformer, the pulse forming line) and the high pressure oil switch. Simulations were also performed on the system response when connected to a dummy load through a simple model for the inductive voltage adder, and finally, simulations were performed utilizing a voltage dependent current source and parallel capacitance representing the vircator load. These simulations were used to determine accuracy and to validate the system diagnostics.

4.1 Pulse Generator

An LTSPICE model for the corresponding components of the pulsed power system was developed to perform simulations. The different components of the pulse generator include the modulator consisting of the thyratron, capacitor bank, the RC snubber, the pulse transformer, the PFL, and the high-pressure oil-filled switch. Cables connecting each major block of the system were included in the simulation as were other parasitic components such as the equivalent series inductance of the capacitor bank in order to produce accurate simulations. The values of these components were altered in order to match experimental results. Each major block is discussed in the subsequent sections.

The SPICE model for the modulator component of the pulse generator is shown in Figure 4.1. In this diagram, L_thy is the inductance of the arc in the thyratron and was

set to 70 nH, S_thy is the thyratron switch, C_bank and L_bank are the capacitance and inductance of the capacitor bank and were set to 810 nF and 10 nH, respectively, T_FL1 represents the 12 parallel RG-217 transmission lines that carry the modulator pulse to the primary on the pulse generator, and R_Snub and C_Snub are the resistor and capacitor values used in the RC snubber and were set to 6 Ω and 26.4 nF, respectively. A small inductance is included in the snubber circuitry to model an equivalent inductance. This inductance was set to 10 nH.

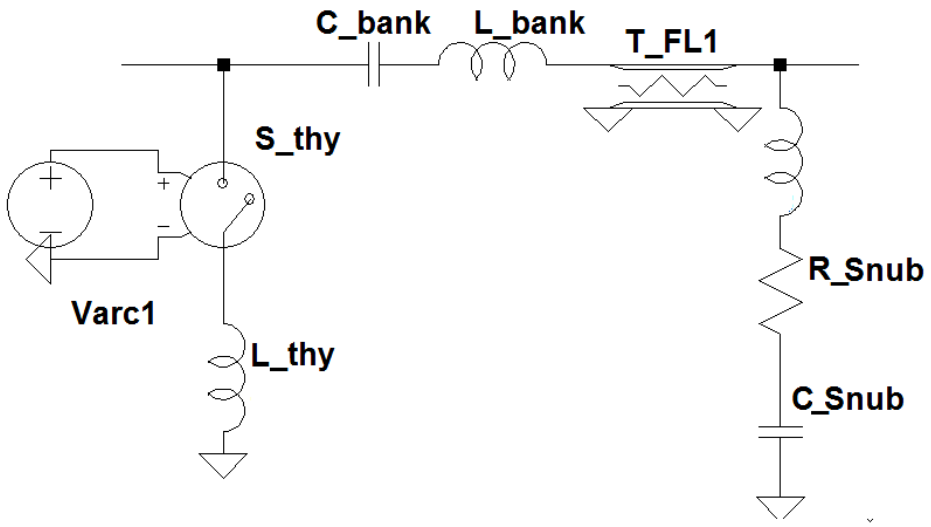

Figure 4.1—Modulator SPICE model

Initially, no RC snubber was included in the circuit. The length and inductance of the transmission lines carrying the modular pulse caused the voltage to ring, and the voltage greatly exceeded the charge voltage. This can be seen in Figure 4.2 which shows the voltage at the output of the feedlines for an initial capacitor bank charge voltage of 30 kV. An RC snubber was added with an equivalent capacitance and resistance of 26.4 nF and 6 Ω. This addition reduced the ringing and overshoots significantly with insignificant voltage losses on the output of the pulse transformer secondary as a result of

the RC snubber. The modulator pulse with an RC snubber in place is shown in Figure 4.3.

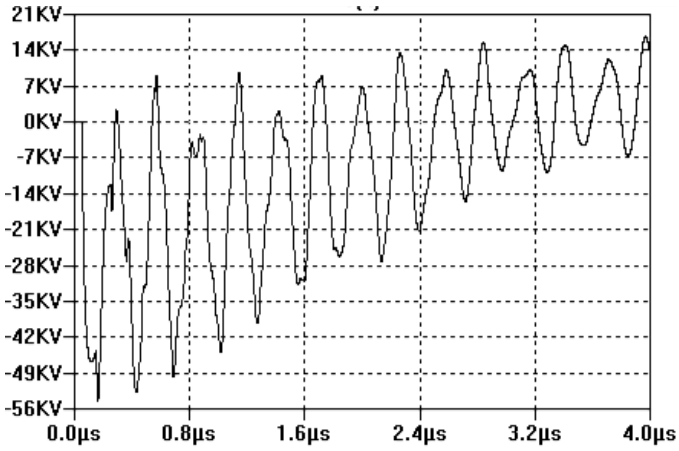

Figure 4.2—Simulated pulse transformer primary input without RC snubber with a charge voltage of 30 kV

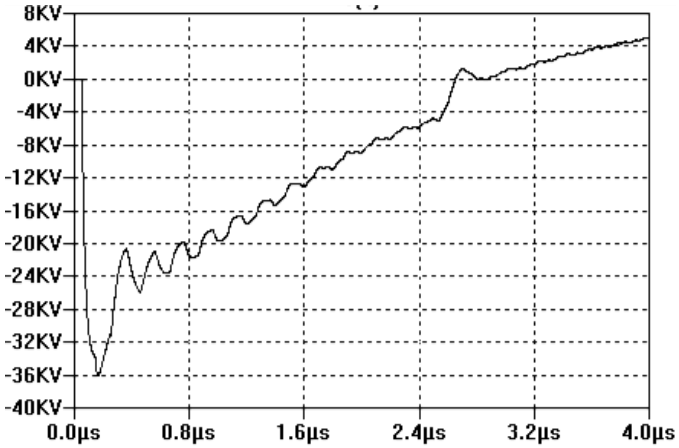

Figure 4.3—Simulated pulse transformer primary input with RC snubber with a charge voltage of 30 kV

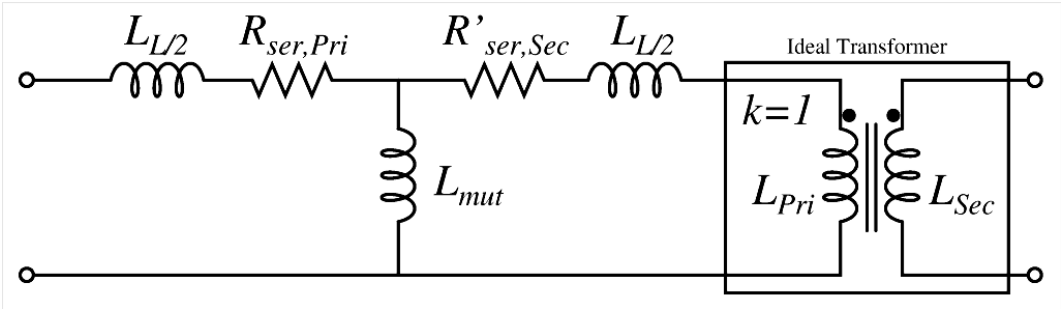

Figure 4.4—T-model equivalent of pulse transformer [1]

Table 4.1—T-model parameters used in simulations

Parameter	Value
L_L	1.703 μH
L_{mut}	75.2 μH
$R_{ser,Pri}$	15.9 mΩ
$R^*_{ser,Sec}$	15.9 mΩ
L_{Pri}	100 μH
L_{Sec}	10 mH

As a review, the model schematic and parameters for the pulse transformer are shown in Figure 3.10 and Table 3.6, respectively. The water PFL was modeled as a transmission line with a transit time of 35 ns and an impedance of 4.8 Ω. The charging waveform at the input of the pulse forming line is shown in Figure 4.5. The oil switch is triggered at 2.5 μs. At the output, the voltage drops to approximately 0.4647 times the peak charge voltage due to the reflection coefficient at the interface of the switch output and the high voltage transmission lines for the length of the output pulse, or twice the one-way transit time of the PFL.

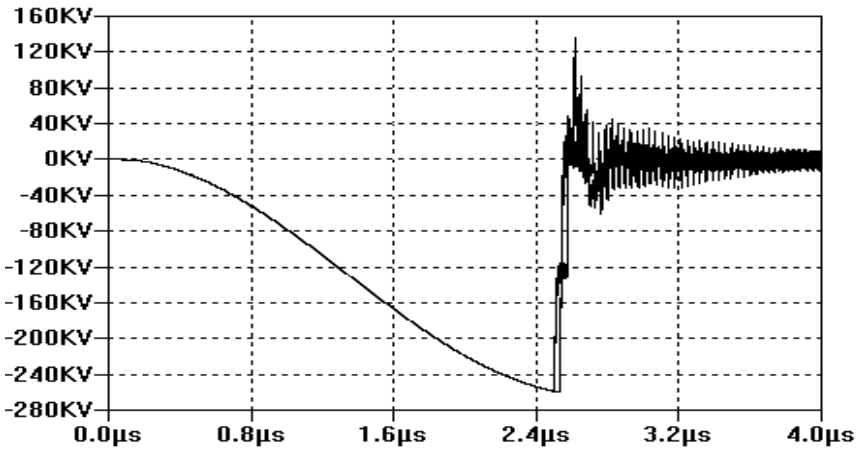

Figure 4.5—Simulated PFL charging waveform at input and output with a charge voltage of 30 kV

An equivalent model for the high pressure oil switch can be seen in Figure 4.6. In this figure, C_{ak} is the capacitance between the anode and cathode of the switch which is

dependent upon the electrode gap spacing and was set to 78.1 pF, C_{kg} is the capacitance between the cathode and the grounded outer conductor of the PFL and was set to 74.1 pF, C_{ag} is the capacitance between the anode and the ground of the PFL and was set to 79.3 pF, L_{arc} is the inductance of the arc column and was set to 3 nH, S_{ArcMod} is a voltage-controlled switch with a small resistance when triggered, and V_{arc} is a pulsed voltage source that switches the model of the oil switch into a conducting regime. These stray components were added to provide a more accurate model of the switch. The values were varied until a proper representation of the system behavior from experimental data was obtained. The input to this section comes from the output of the PFL, and the output connects to a transmission line which models the twelve parallel high voltage output cables. The output from the switch is shown in Figure 4.7. There are some reflections and oscillations that occur and are superimposed on the pulse. These are the result of the complex network of inductance and capacitance added to the model to reproduce the experimental results. The simulated 10-90% risetime of this output pulse was approximately 19.6 ns.

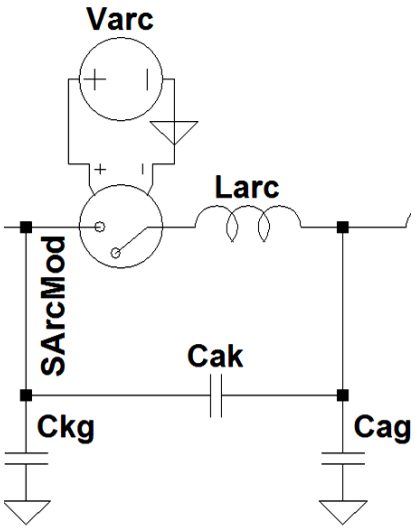

Figure 4.6—SPICE model of high pressure oil switch

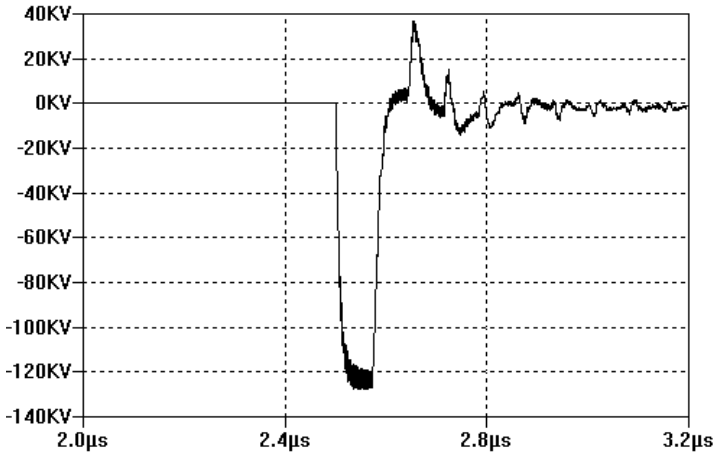

Figure 4.7—Simulated output pulse from high voltage switch with a charge voltage of 30 kV

4.2 Pulse Generator with Inductive Voltage Adder

The SPICE model representation for the inductive voltage adder is shown in Chapter 3. The coupling between the primary and secondary for each transformer was set to 0.9995 in the simulation. As a load, two resistors representing the water resistors were used with resistor values of 33 Ω and 35 Ω. The output pulse for this added component is shown in Figure 4.8 and is delayed by about 70 ns from the pulse from the high voltage switch due to the one-way transit time of the output transmission lines.

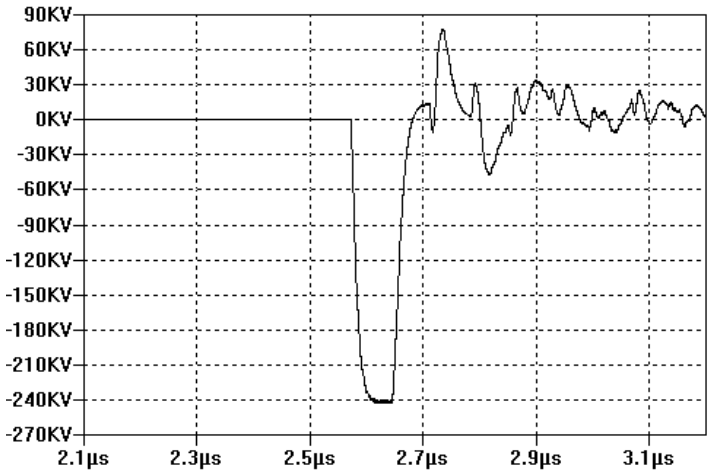

Figure 4.8—Simulated inductive voltage adder output with dummy load with a charge voltage of 30 kV

4.3 System with Dual Vircator Load

Circuit simulations were also performed using a circuit model for the parallel vircator load. The circuit model is shown in Figure 4.9, where the voltage dependent current source is a source governed by the Child-Langmuir equation, and the capacitor is the inherent capacitance of the parallel plate separation created by the cathode and the anode screen.

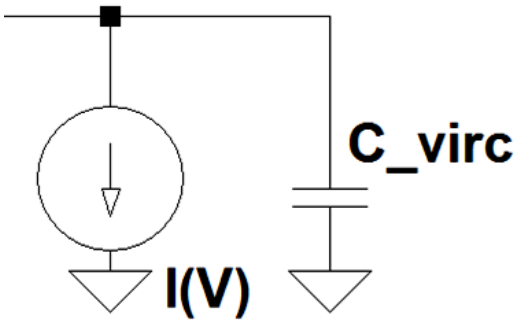

Figure 4.9—SPICE model of electron diode representing a single vircator

Two circuits for the vircator diodes were simulated. In the first case, both cathodes conducted, and the vircators both generate an electron beam. The second simulation shows the results of what would happen if only one vircator were to emit and the other vircator were not operational, representing a fault mode. This situation is very possible, especially in the system state in which one vircator might have a larger anode-cathode gap spacing than the other, creating a large impedance mismatch in the circuit. The voltage pulse for the simulation in which both vircators emit and no faults occur is shown in Figure 4.10. Both vircators in this case were modeled using equal AK gaps of 1.74 cm. The voltage is very similar to that found with just a simple resistive load. The voltage pulse for the simulation in which one vircator faults and the other emits is shown in Figure 4.11. In both situations, voltage reversals occur which is a concern as it would

decondition the cathode and increase the chances of vacuum flashover. In the case in which one vircator faults, the voltage of the pulse increases due to the higher impedance of the load. While this voltage increase could be useful, the impedance mismatch reduces energy efficiency in the system.

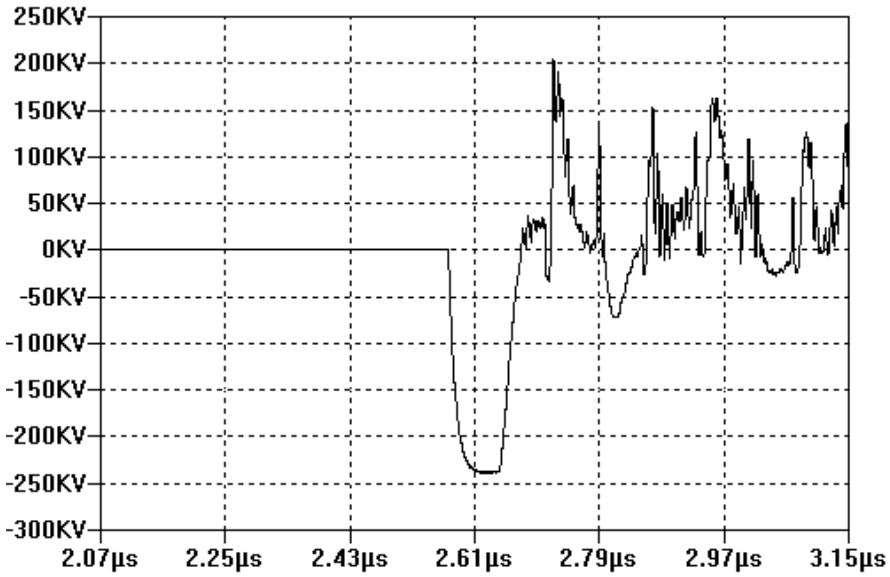

Figure 4.10—Simulated vircator input voltage pulse for non-fault mode with a charge voltage of 30 kV

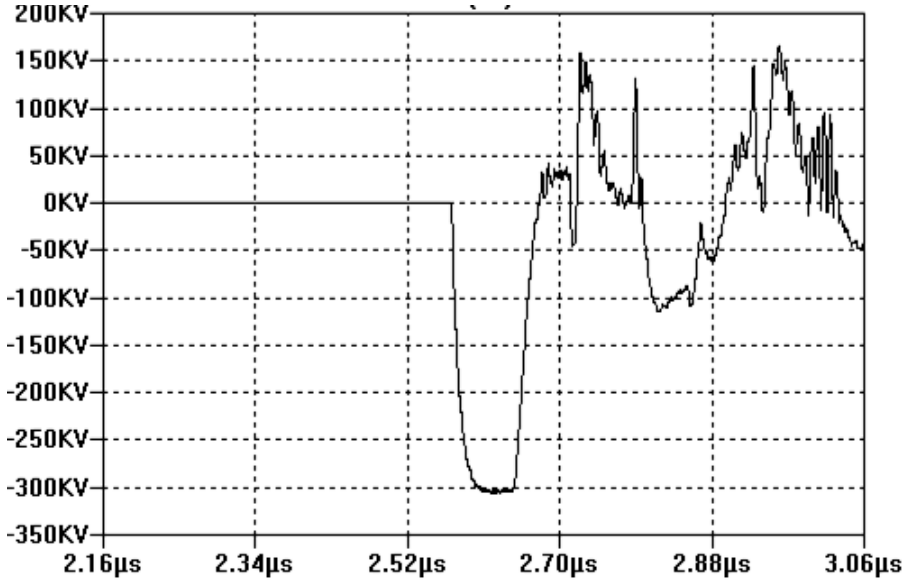

Figure 4.11—Simulated vircator input voltage pulse for single-fault mode with a charge voltage of 30 kV

References for Chapter 4

[1] P. Norgard, "Development of a Gigawatt Repetitive Pulse Modulator and High-Pressure Test Stand and Results from High-Pressure Switch Tests," University of Missouri - Columbia, Master's Thesis 2006.

Chapter 5 — Vircator Design & Simulations

5.1 Overview of System

Virtual cathode oscillators utilize space-charge effects in order to convert kinetic energy from the electron beam to microwave energy [1], [2], [3], [4], [5]. The theory of vircator operation is described in Chapter 2. The vircator system built at the University of Missouri produces a high power microwave signal with a spectrum consisting mainly of the virtual cathode frequency. This frequency is related to the beam plasma frequency given in equation 2.25. The virtual cathode frequency lies within a range of frequencies, determined through experimental results given by equation 2.26. An empirical formula, equation 2.27, has been developed based upon multiple sets of data from published vircator experimental results.

In designing a vircator system, the most significant parameter for the given application must be determined, i.e. the frequency or range of frequencies was the most significant design parameter for the system described here. This is most relevant if low frequencies are desired. For low frequencies, much larger systems are typically necessary to achieve adequate output power levels [1], [6]. To obtain low frequencies, larger anode-cathode (AK) gaps are necessary since the output frequency is inversely proportional to the gap spacing. Inherent in this reduction of frequency with an increase in the gap spacing is the reduction of the current in the electron beam. From the Child-Langmuir equation, an increase in the AK gap results in a reduction in the current. Emission is also dependent upon the electric field between the anode and the cathode

depending on the material used as the emitter [1], [7], [8]. Depending on the voltage and the AK gap, emission may or may not take place with traditional emitter surfaces.

The pulsed power system described in Chapter 3, while capable of being charged to 300 kV, was operated to produce a max output of 250 kV at the inductive voltage adder (125 kV output from the pulse forming line), safely below its rating of 300 kV. Using this output voltage, the space charge limited current can be calculated for a planar Child-Langmuir diode using equation 2.18 and 2.22. As an initial design point, the AK gap spacing for the base design is chosen such that the impedance is matched to the output impedance of the pulse forming line, which is the impedance of the twelve high voltage output cables, or 4.167 Ω (16.67 Ω on the secondary of the inductive voltage adder). The impedance of the space-charge limited diode is simply the voltage divided by the current, or:

$$Z_{CL} = \frac{9}{4}\frac{1}{S\epsilon_0}\sqrt{\frac{m}{2e}}\ \frac{d^2}{{V_0}^{1/2}} \approx \frac{1}{2.33*10^{-6}}\frac{1}{S}\frac{d^2}{V_0^{1/2}} \tag{5.1}$$

where Z_{CL} is the diode impedance in Ω, ϵ_0 is the permittivity of free space in F/m, e is the charge of an electron in coulombs, m is the mass of an electron in kg, V_0 is the voltage across the diode in volts, and d is the AK gap in meters. The pulsed power system used for driving the HPM load was designed to produce an average voltage output from the inductive adder of 200 kV into a matched load. For a voltage of 200 kV and a cathode emission diameter of 10.16 cm (4 inches), the gap necessary to achieve a matched load across the two vircators in parallel is approximately 1.68 cm.

In order for a virtual cathode to be formed, the beam current passing through the anode screen must exceed the space-charged-limited current in the drift tube section given by equation 2.19. With the voltage, gap spacing, and beam diameter chosen, the

drift tube radius can be determined such that the space-charge limited current in the drift tube is exceeded by the beam current. The drift tube diameter was 25.4 cm (10 inches). The side-cut view from a CAD drawing of one vircator is shown in Figure 5.1.

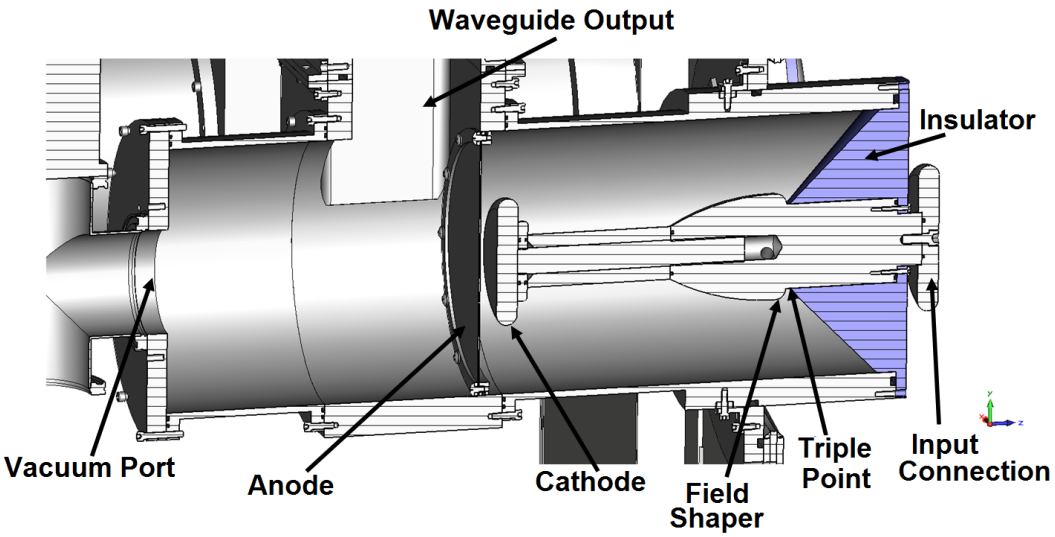

Figure 5.1—Side-cut CAD illustration of one vircator

5.2 Simulations

5.2.1 Electrostatic Simulations

Electrostatic simulations were performed in CST Particle Studio® to examine the electric field strengths in the vacuum system. These simulations were used to design the conductors in the vacuum system and reduce the probability of flashover. The most significant interface in a vacuum system when looking at flashover is the insulator interface. This interface is the most probable place for flashover to occur, since this interface can have secondary electron emission. The triple point, or the point where vacuum, conductor, and dielectric all meet at one point, is often the point where flashover initiates. The probability of breakdown can be reduced by decreasing the electric field at this point. Decreasing the electric field at the triple point can be accomplished by

shaping the electric fields and altering the equipotentials by hiding the triple point with a conductor [9]. In the vircator system, the cathode portion that comes into contact with the dielectric has been shaped so as to hide the triple point. This field shaper is also rounded so as to minimize the field enhancement factor created by the corner of the conductor. The field shaping point and equipotential plot can be seen in Figure 5.2.

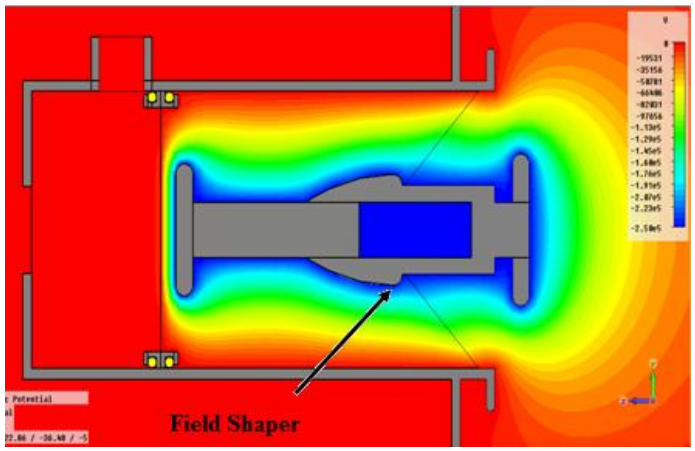

Figure 5.2—Calculated equipotential plot for Vircator from CST Particle Studio®

Without the field shaper on the inner conductor, the electric field at the inner triple point would be approximately 50 kV/cm for a diode voltage of 250 kV. With the addition of the conductive field shaper, the electric field at the inner triple point was reduced to approximately 19 kV/cm, a 60% improvement.

5.2.2 MAGIC PIC Simulations

Particle-in-cell (PIC) simulations were performed in MAGIC PIC Simulation software from Alliant Tech Systems, LLC as this software has previously been used with success in modeling vircator systems [74]. The simulations were performed using an explosive electron emission model with a 200 kV diode voltage with a rise time of 20 ns, matching the actual vircator system. The anode screen had a transparency of 90%, cathode emission diameter was 10.16 cm. The simulation space in MAGIC can be seen

in Figure 5.3. In this figure, half of the cathode, anode foil, and drift tube can be seen. To complete the system, the software uses axial symmetry. A waveguide extends upward and matches the dimensions of the waveguide used for microwave extraction. A plastic insulator models the point where the vacuum section in the actual vircator system is separated from the atmospheric section in the waveguide.

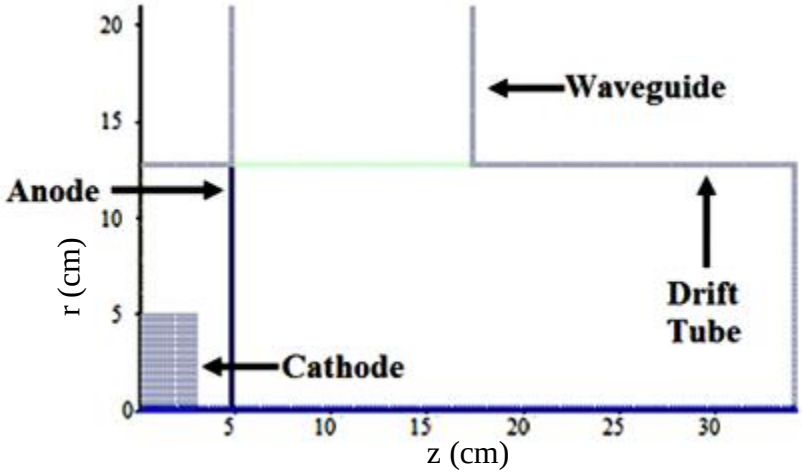

Figure 5.3—MAGIC simulation space

Several outputs were recorded in the simulations. The input voltage, beam current, and diode impedance were all recorded as a function of time. The electric field and magnetic flux density were measured at a similar location as the measurement point of actual B-dot probe. These measurements provided both a time trace and a frequency-domain trace. Various phase-space plots were also calculated, including the energy of the particles along the z-axis, the momentum of the particles along the z-axis, and the relativistic coefficient of the particles along the z-axis.

A sample of the simulation results are displayed in Figure 5.4 through Figure 5.12 for a gap spacing of 1.68 cm. Figure 5.4 and Figure 5.5 show the input voltage waveform and the resulting emitted current that is based upon an explosive emission model space-charge limited diode. Theoretically, for a voltage of 200 kV, an AK gap of 1.68 cm, and

a cathode diameter of 10.16 cm (4 inches), the Child-Langmuir equation predicts a diode current of approximately 6 kA. The current waveform in Figure 5.5 oscillates around 5.4 kA when the voltage has reached 200 kV. This is slightly lower than the expected current predicted by the Child-Langmuir equation. This also results in a larger diode impedance than expected. The impedance versus time trace can be seen in Figure 5.6. The expected impedance is 33.35 Ω. The simulation impedance oscillates around 37 Ω.

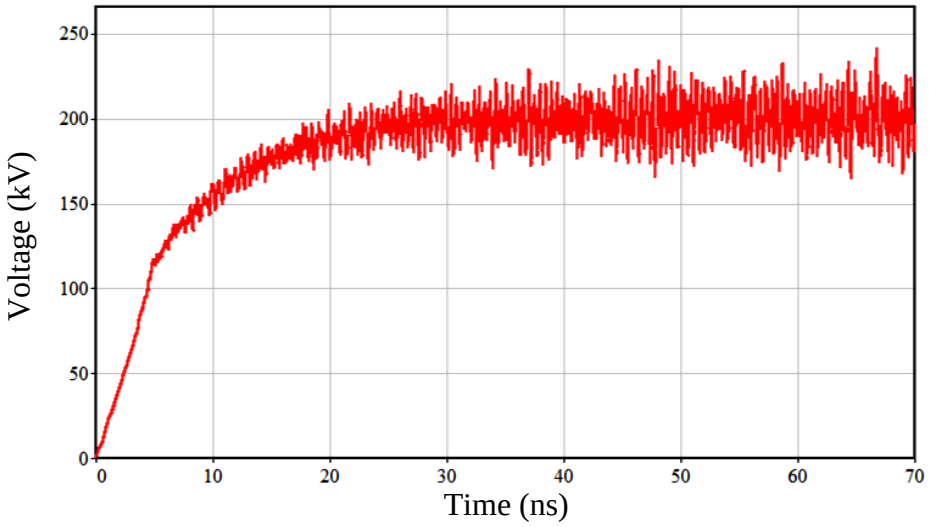

Figure 5.4—MAGIC simulation input voltage waveform for 200 kV input and 1.68 cm AK gap with a calculated dominant frequency of 2.086 GHz

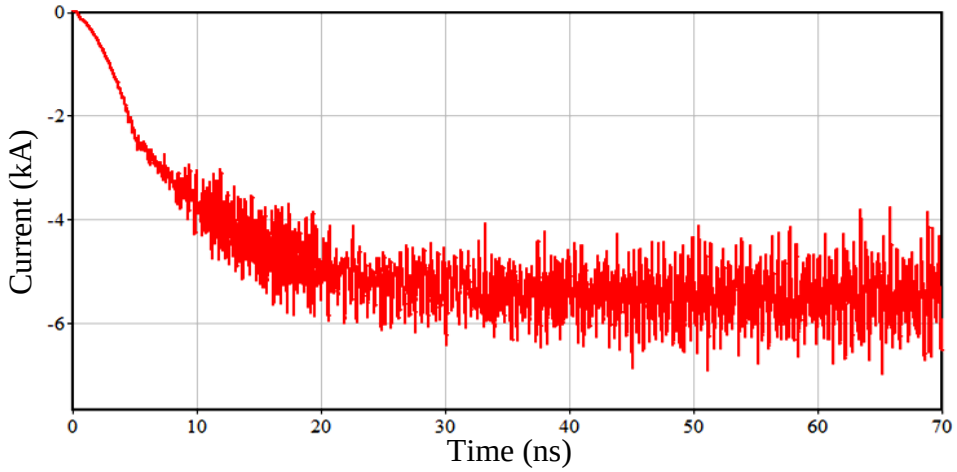

Figure 5.5—MAGIC simulation emitted current waveform for 200 kV input and 1.68 cm AK gap with a calculated dominant frequency of 2.086 GHz

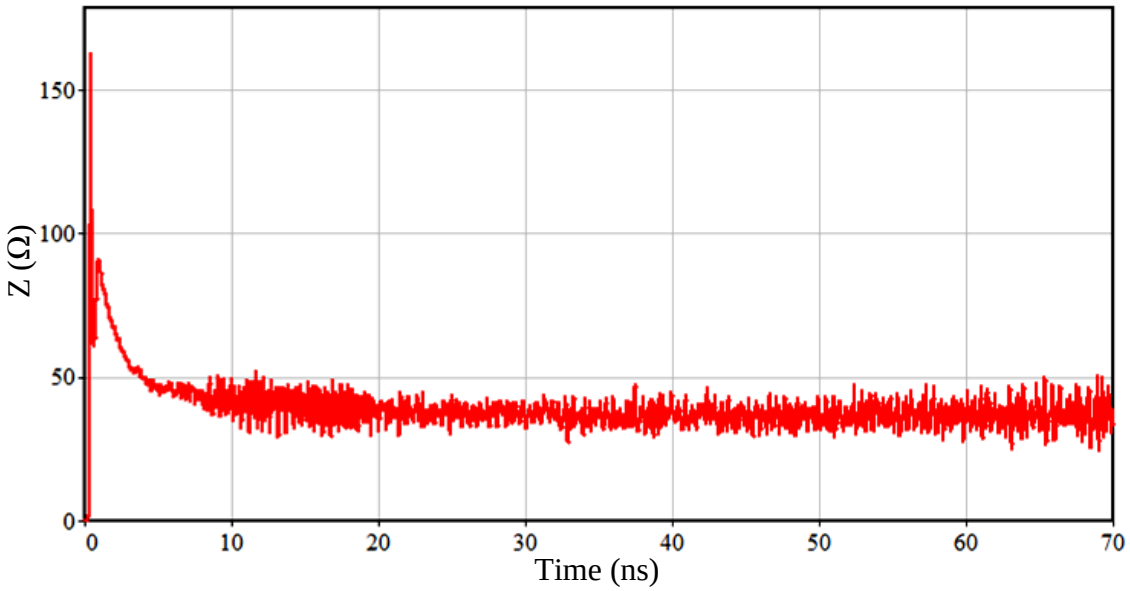

Figure 5.6—Calculated impedance versus time from MAGIC simulation for 200 kV input and 1.68 cm AK gap with a calculated dominant frequency of 2.086 GHz

Field measurements were also taken in the simulation in order to determine what frequency could be expected for the input parameters to the simulation. The time-dependent fields, both electric and magnetic, were measured at a point in the waveguide area of the simulation space similar to the position that the actual B-dot probe used for microwave measurements was set up. At the point in the waveguide where the B-dot probe was positioned for a TE_{10} mode wave, the only two components in this mode are the E_z and H_ϕ components, where z and ϕ are the vector directions based on the simulation coordinate system. The z-direction is the horizontal axis of Figure 5.3 and the ϕ-direction is into the figure. The time-dependent electric field signal is shown in Figure 5.7. A fast Fourier transform (FFT) is applied to this signal in the MAGIC code to obtain the magnitude spectrum of the electric field signal. This is shown in Figure 5.8 for a frequency range from 500 MHz to 6 GHz. A dominant peak is prevalent at a frequency of 2.086 GHz.

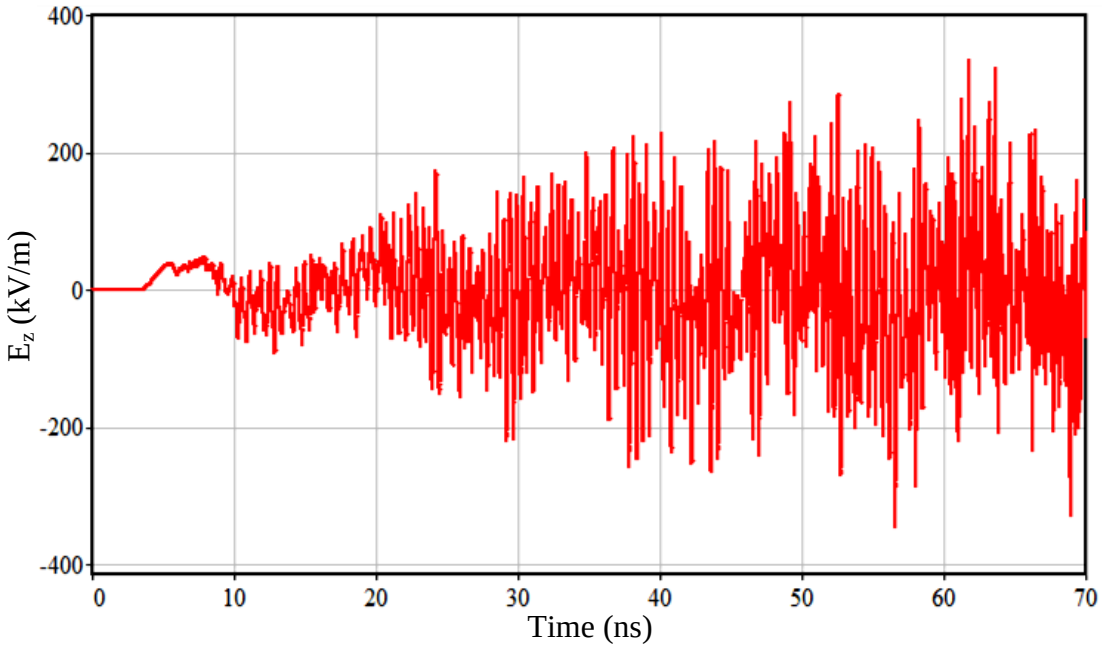

Figure 5.7—Calculated electric field waveform in waveguide from MAGIC for 200 kV input and 1.68 cm AK gap with a calculated dominant frequency of 2.086 GHz

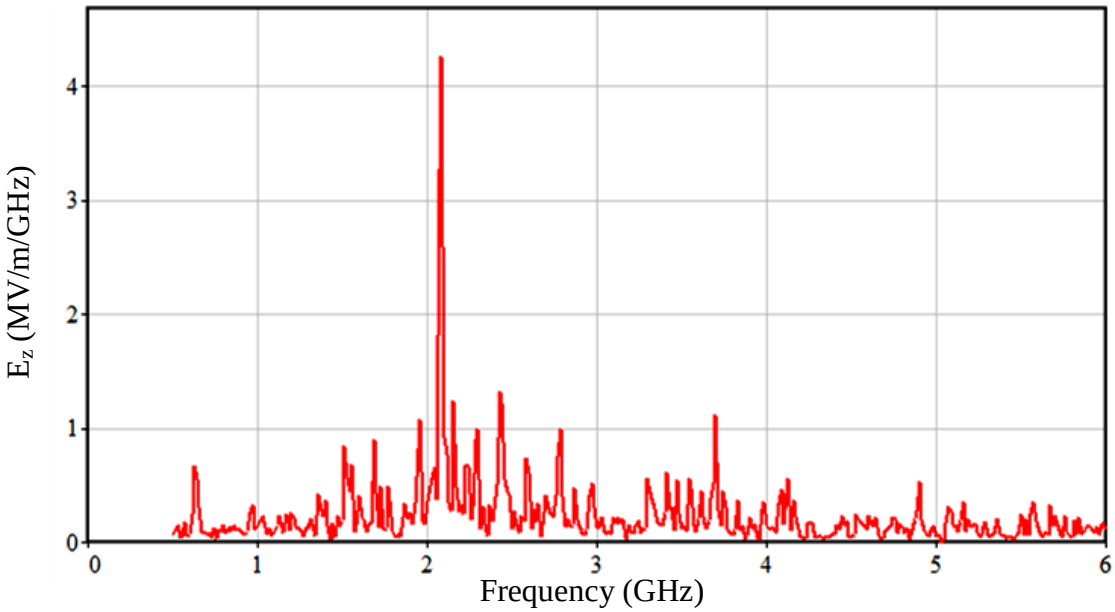

Figure 5.8—Spectrum of calculated electric field shown in Figure 5.7 for 200 kV input and 1.68 cm AK gap with a calculated dominant frequency of 2.086 GHz

The particle positions of the emitted electrons and the various properties of these electrons were also captured in the MAGIC simulations. This was done to examine the virtual cathode formation. In order to visualize the oscillation of the virtual cathode

during the pulse, the electron positions were captured at 10 ns intervals from 10 ns to 60 ns. This time evolution is shown in Figure 5.9 with the virtual cathode marked for the plot showing the particle positions at 20 ns.

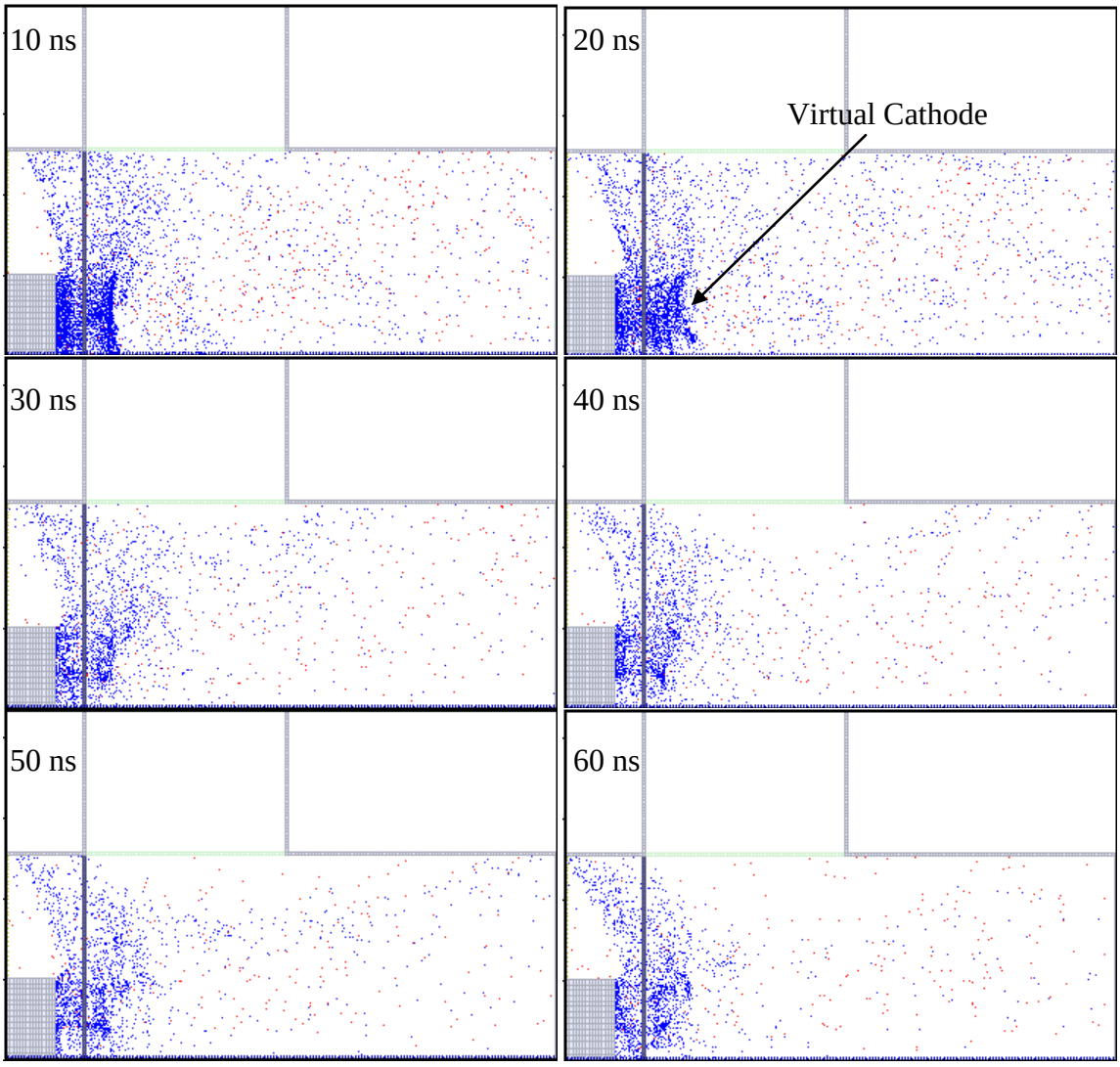

Figure 5.9—Time evolution of electron positions from 10 ns to 60 ns for 200 kV input and 1.68 cm AK gap with a calculated dominant frequency of 2.086 GHz

A virtual cathode is formed when the space-charge-limited current in the drift tube section is exceeded. A strong potential is created at the leading edge of the beam that is strong enough to reflect electrons back toward the anode. This means that the energy and velocity of the electrons at the virtual cathode are approximately zero. Figure

5.10 through Figure 5.12 show the particle energy, particle momentum, and relativistic coefficient, respectively. These all provide illustrations of the point at which the virtual cathode is formed computed at 60 ns into the simulation.

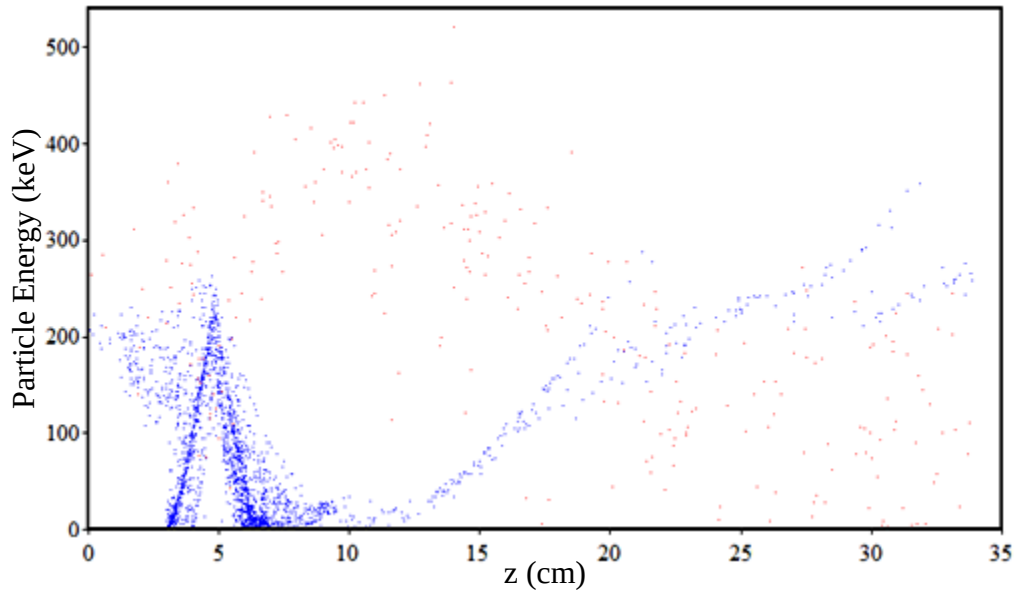

Figure 5.10—Calculated particle energy versus distance at a simulation time of 60 ns for 200 kV input and 1.68 cm AK gap with a calculated dominant frequency of 2.086 GHz

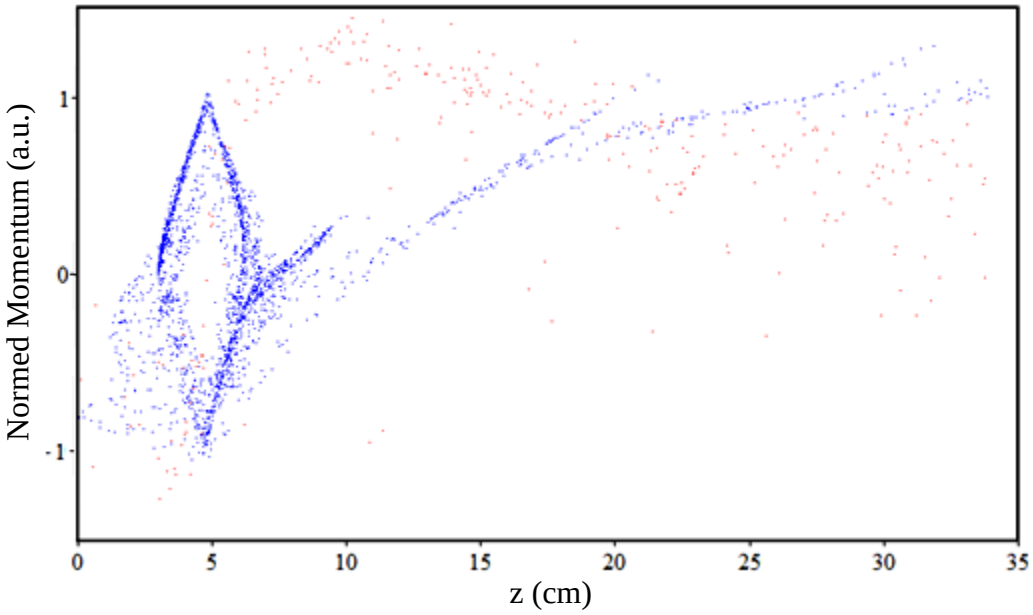

Figure 5.11—Calculated normed particle momentum versus distance at a simulation time of 60 ns for 200 kV input and 1.68 cm AK gap with a calculated dominant frequency of 2.086 GHz

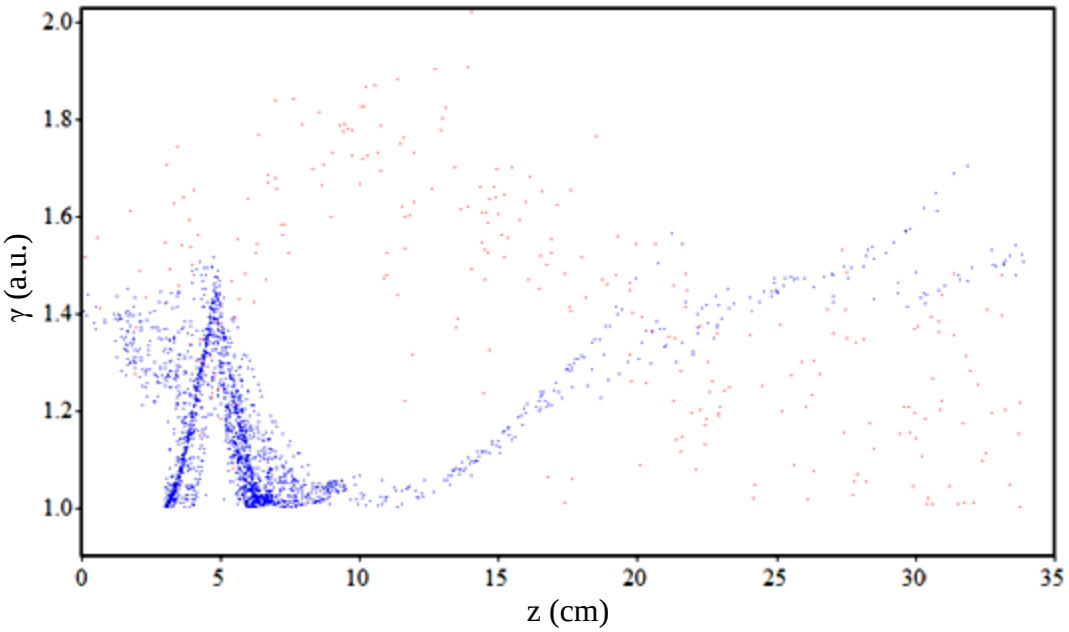

Figure 5.12—Calculated particle relativistic coefficient versus distance at 60 ns for 200 kV input and 1.68 cm AK gap with a calculated dominant frequency of 2.086 GHz

All of the data sets discussed above were recorded for a sweep of the AK gap from 1.00 cm to 2.54 cm to look at the tunability of the vircator as a function of the AK gap spacing as well as the virtual cathode formation. A parameter sweep of the input voltage was also performed in MAGIC for voltages from 100 kV to 300 kV to examine the frequency dependence of the vircator output on voltage. The voltage for the AK gap sweep was kept constant at 200 kV while the AK gap for the voltage sweep was kept constant at 1.68 cm. The dominant frequency from each spectrum in the AK gap iteration is recorded and is plotted in Figure 5.13. The simulated data points are marked with square markers. The points are fitted with a curve relating the gap spacing to the frequency. The two solid lines show the boundaries for the range of possible virtual cathode frequencies showing that the dominant frequencies from the simulations do in fact lie in this range. The fitted curve shows an AK gap dependence for the frequency as follows:

$$f_{vc} \propto 1/d^{1.283}$$

where d is the AK gap and f_{vc} is the virtual cathode frequency. The expected relationship is $f_{vc} \propto 1/d$. Regardless, the frequency is inversely related to the AK gap.

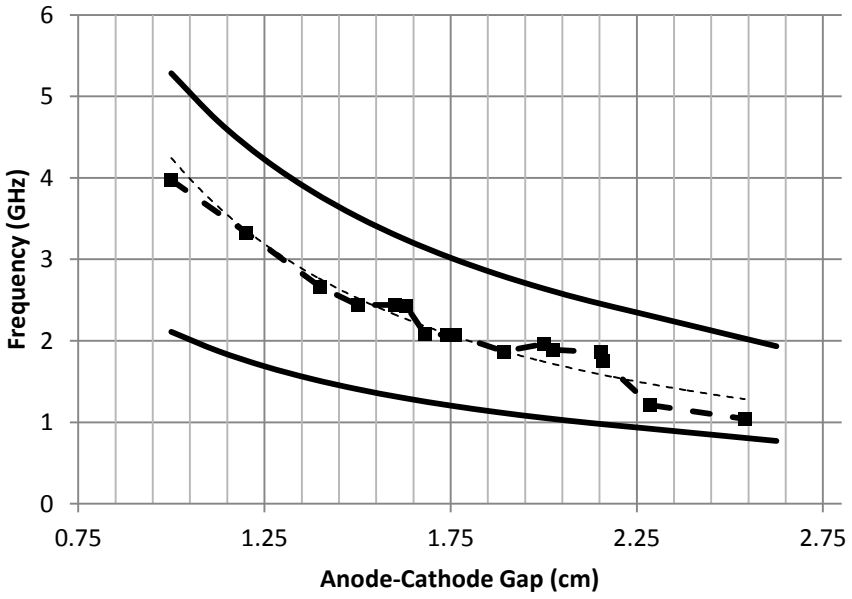

Figure 5.13—Dominant frequency versus AK gap as calculated in MAGIC with a voltage amplitude of 200 kV

The dominant frequency from each spectrum in the voltage sweep is recorded and is plotted in Figure 5.14. The data points are marked with square markers. The points are fitted with a curve relating the voltage to the frequency. The two solid lines show the boundaries for the range of possible virtual cathode frequencies, again showing that the dominant frequencies from the simulations are in this theoretical range. The fitted curve shows a voltage dependence for the frequency as follows:

$$f_{vc} \propto V^{0.578}$$

where V is the diode voltage and f_{vc} is the virtual cathode frequency. The expected relationship is $f_{vc} \propto V^{0.5}$ meaning the simulation results show a dependency nearly equal to the expected voltage dependence [1].

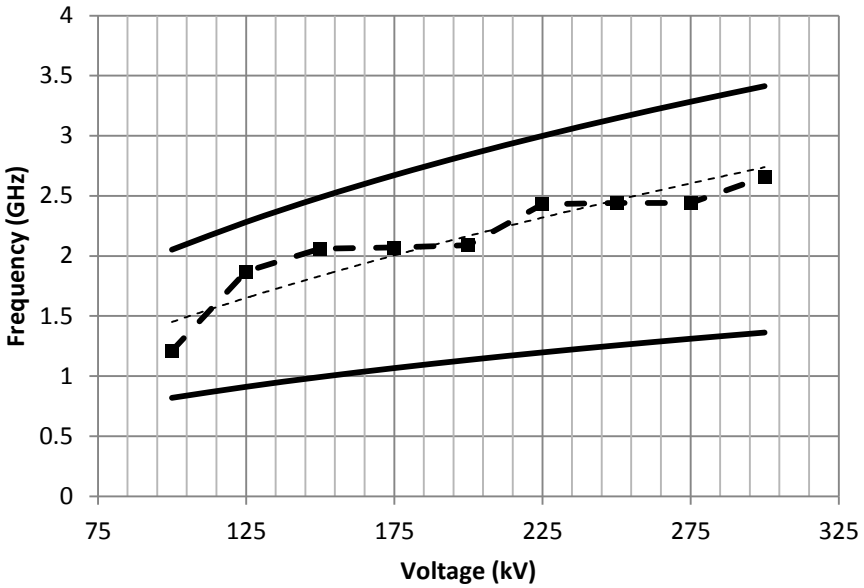

Figure 5.14—Dominant frequency versus input voltage as calculated in MAGIC with an AK gap of 1.68 cm

5.2.3 CST Particle Studio® PIC Simulations

Particle-in-cell (PIC) simulations were also performed in CST Particle Studio®. Simulations were performed using an explosive electron emission model with a 200 kV diode voltage with a rise time of 20 ns, matching the actual vircator system. The anode transparency was set to 90%, and the cathode emission diameter was 10.16 cm.

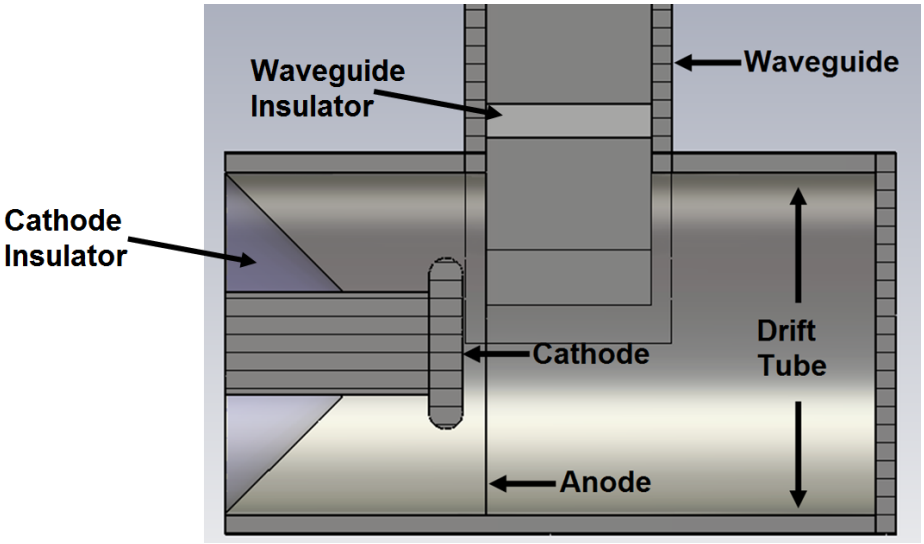

Figure 5.15—Cross section of the CST Particle Studio® simulation space

The simulation space can be seen in Figure 5.15. The model in CST is a three-dimenional CAD-based model. In this figure, the cathode, anode foil, and drift tube can be seen. A waveguide extends upward, modeling the waveguide used for microwave extraction. A plastic insulator models the point where the vacuum section in the actual vircator system is separated from the atmosphere. An insulator at the input side of the cathode also models the angled insulator which seals the vacuum section from the oil in the inductive voltage adder tank.

Several outputs were recorded in the simulations, similar to the results generated by the MAGIC simulations. The input voltage, beam current, and diode impedance were all recorded as a function of time. The electric field and magnetic field were measured at a location similar to the measurement point of the B-dot probe, providing both a time-domain trace as well as a frequency-domain trace. A waveguide port was also used to capture the output waveform for the TE_{10} mode passing through the waveguide, allowing for the determination of the microwave signal occupying this waveguide mode. Various phase-space plots were also captured, including the energy of the particles along the z-axis, the momentum of the particles along the z-axis, and the relativistic coefficient of the particles along the z-axis. All of these data sets were recorded for a sweep of the AK gap from 1.00 cm to 2.30 cm. This parameter iteration was utilized to examine the effect that the AK gap had on the output frequency as a comparison to both the MAGIC simulation results and experimental results described in Chapter 7.

A sample of the simulation results are displayed in Figure 5.16 through Figure 5.24 for a gap spacing of 1.68 cm. All time-based axes are in units of nanoseconds. Figure 5.16 and Figure 5.17 show the input voltage waveform and the

resulting emitted current, which is based upon an explosive emission model, space-charge limited diode, with units of volts and amperes, respectively. Theoretically, for a voltage of 200 kV, the current, as determined by the Child-Langmuir equation, should be approximately 6 kA. The current waveform in Figure 5.17 oscillates around 5.3 kA when the voltage has reached 200 kV. This is slightly lower than the expected current predicted by the Child-Langmuir equation. The impedance-versus-time trace can be seen in Figure 5.18 which is simply obtained by dividing the time-dependent voltage by the time-dependent current. The unit of the y-axis in this plot is Ω. The expected impedance was 33.35 Ω, but the simulation impedance oscillates around 38 Ω, higher than expected but nearly equal to that predicted by MAGIC. In both cases, reflexing electrons between the anode and cathode likely disrupted the electric field in this area and reduced the emitted current.

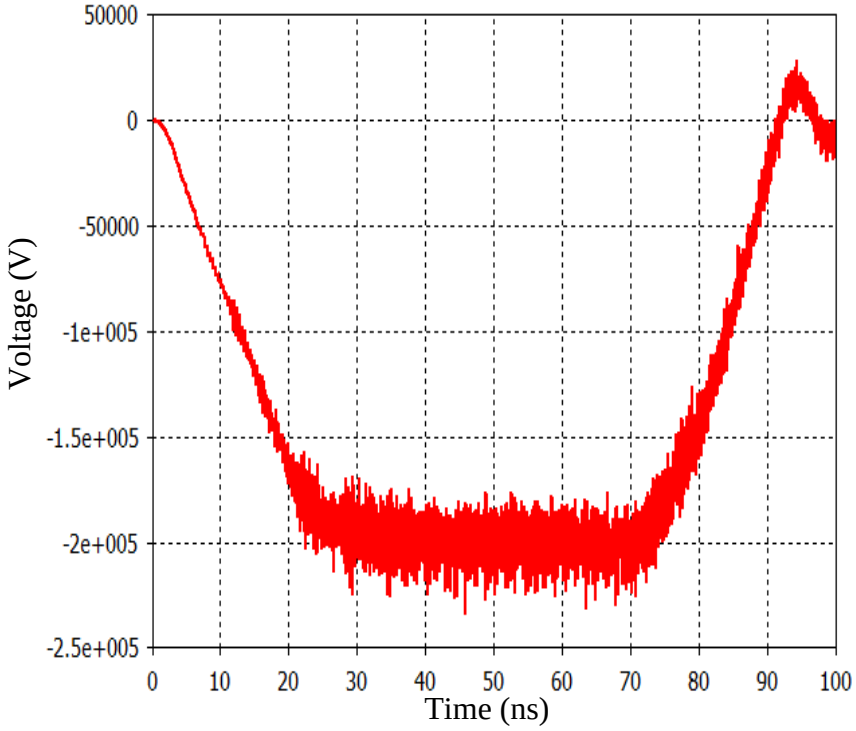

Figure 5.16—CST simulation input voltage waveform versus time for 200 kV input and 1.68 cm AK gap with a calculated dominant frequency of 2.71 GHz

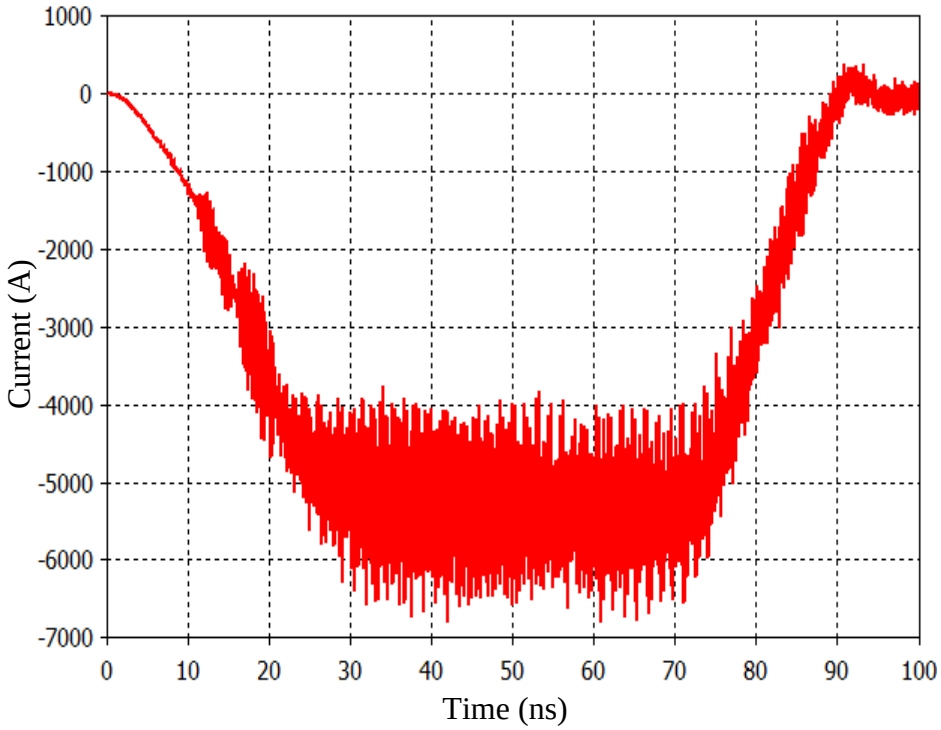

Figure 5.17—CST simulation emitted current waveform versus time for 200 kV input and 1.68 cm AK gap with a calculated dominant frequency of 2.71 GHz

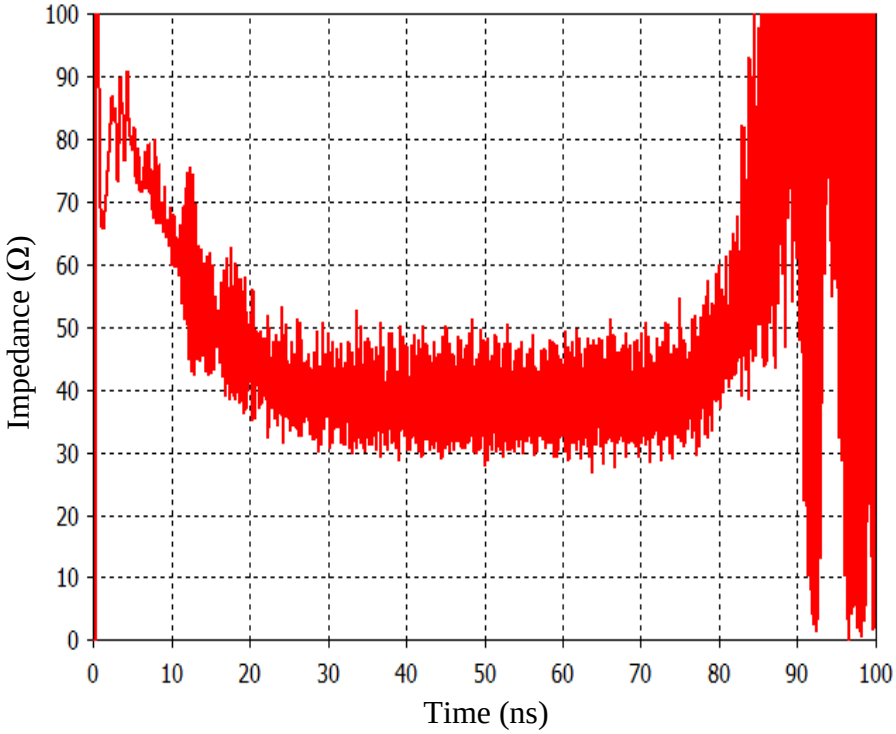

Figure 5.18—Calculated impedance versus time from CST simulation for 200 kV input and 1.68 cm AK gap with a calculated dominant frequency of 2.71 GHz

Field intensities were also calculated in the simulation in order to determine what frequency could be expected for input parameters to the simulation. The output waveform from of the signal traveling through the waveguide was captured by a waveguide port. This port only outputted the TE_{10} mode waveform and absorbed all other signals traveling in different modes. The time-dependent microwave signal for the TE_{10} mode in the waveguide is shown in Figure 5.19. A fast Fourier transform (FFT) is applied to this signal in the CST simulation to obtain the magnitude spectrum of the microwave signal. This is shown in Figure 5.20 for a frequency range from 0 Hz to 6 GHz. A dominant peak is prevalent at a frequency of 2.71 GHz, higher than the frequency predicted in MAGIC which was 2.086 GHz. However, this frequency still lies within the theoretical range from equation 2.26.

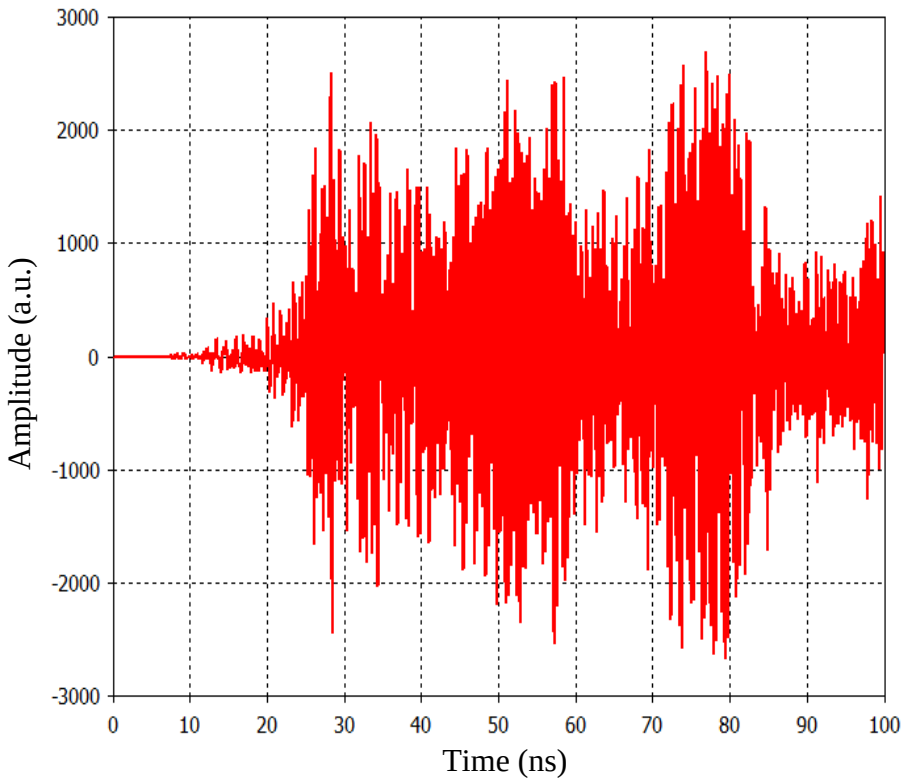

Figure 5.19—Calculated waveguide port output for TE_{10} mode in CST for 200 kV input and 1.68 cm AK gap with a calculated dominant frequency of 2.71 GHz

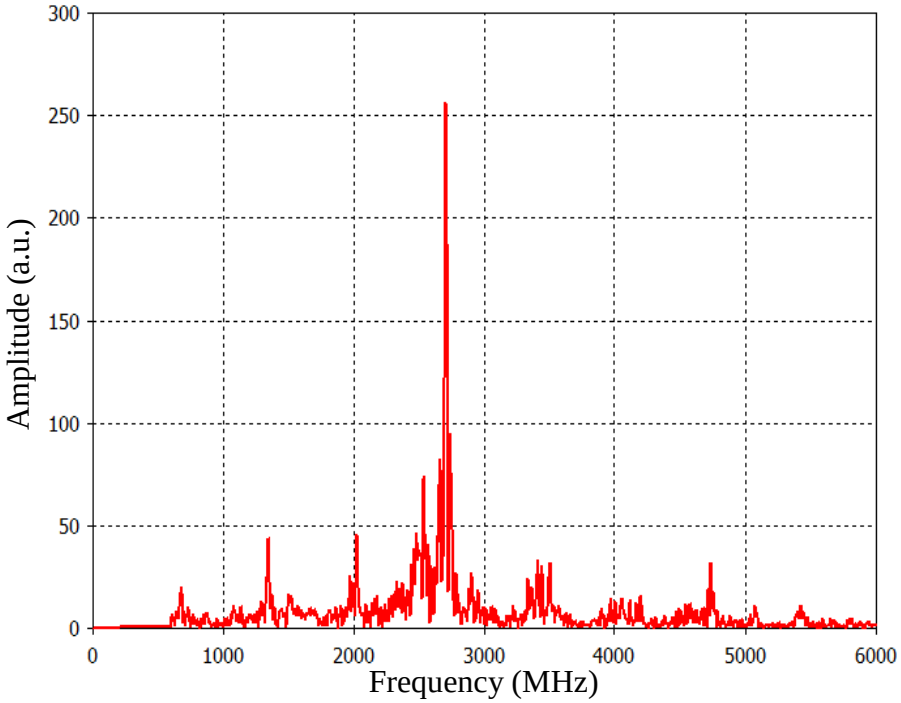

Figure 5.20—Spectrum of calculated electric field shown in Figure 5.19 for 200 kV input and 1.68 cm AK gap with a calculated dominant frequency of 2.71 GHz

The particle positions of the emitted electrons and properties of these electrons were also captured in the CST Particle Studio® simulations to explore the time evolution of the particle positions and virtual cathode formation. The electron positions were captured at 10 ns intervals from 10 ns to 60 ns. These plots can be seen in Figure 5.21. In these figures, the electrons are depicted as a color gradient from blue to red. This color can represent different particle properties such as energy, momentum, velocity, etc. In the case of this figure, the color represents the parameter denoted β. This parameter is the ratio of the velocity of the particles to the speed of light. The blue color represents electrons that are moving slowly while the red represents faster moving electrons. The position of the virtual cathode is easily realizable as the cloud of slow moving (blue) particles on the right side of the anode screen in the figure.

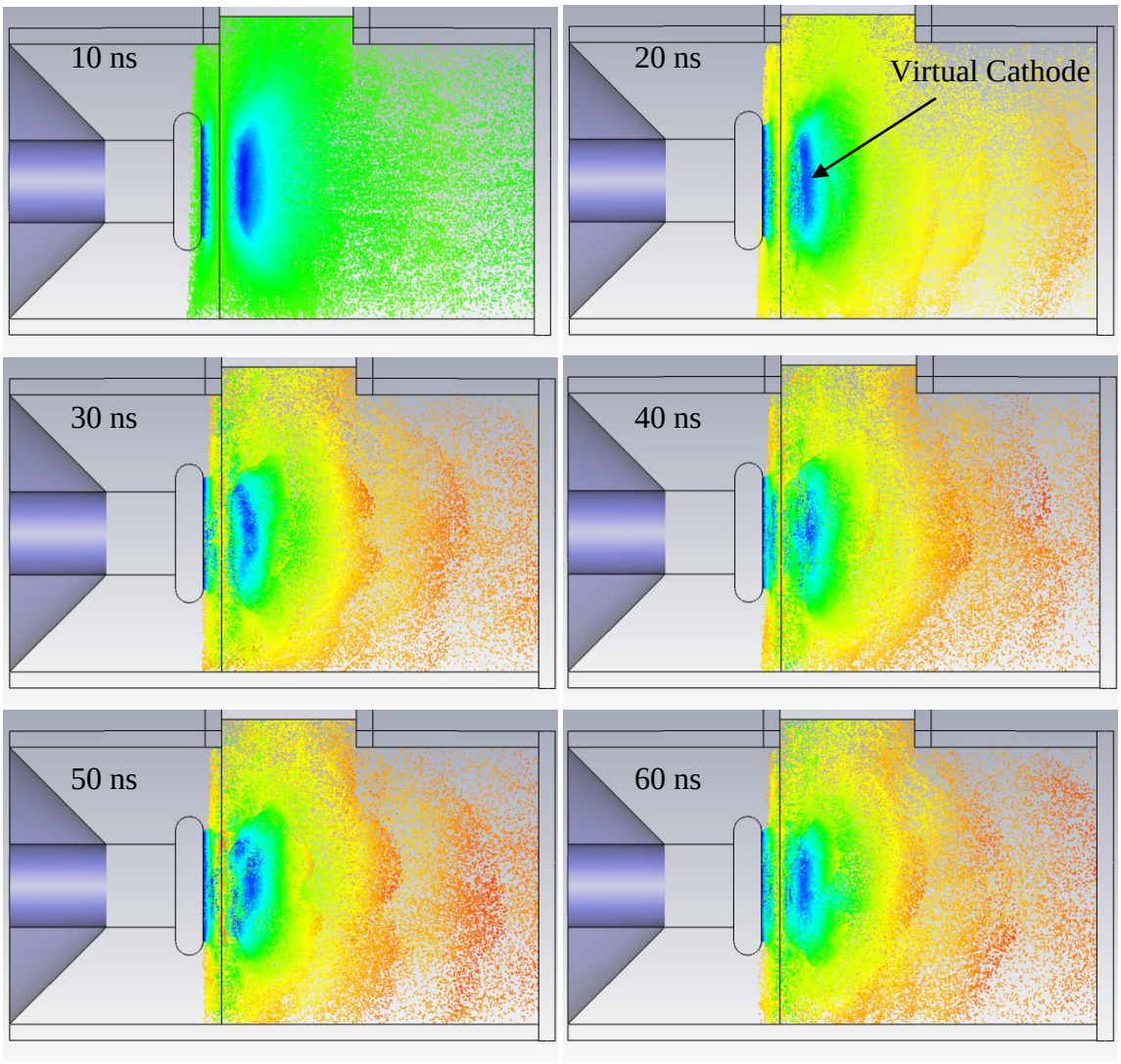

Figure 5.21—Time evolution of electron positions from 10 ns to 60 ns for 200 kV input and 1.68 cm AK gap with a calculated dominant frequency of 2.71 GHz

As has been discussed, a virtual cathode is formed when the space-charge-limited current in the drift tube section is exceeded. The electrons traveling towards this potential are reflected backwards toward the anode screen, meaning that the velocity, and thus kinetic energy, of the electrons at the virtual cathode is approximately zero, as can be seen in Figure 5.21. Other phase-space plots were acquired in the simulation depicting the properties of the particles as a function of distance along the drift tube axis. Figure 5.22 through Figure 5.24 show the particle energy, particle momentum, and

relativistic coefficient, respectively. These all provide an illustration of the point at which the virtual cathode is formed computed at 60 ns into the simulation.

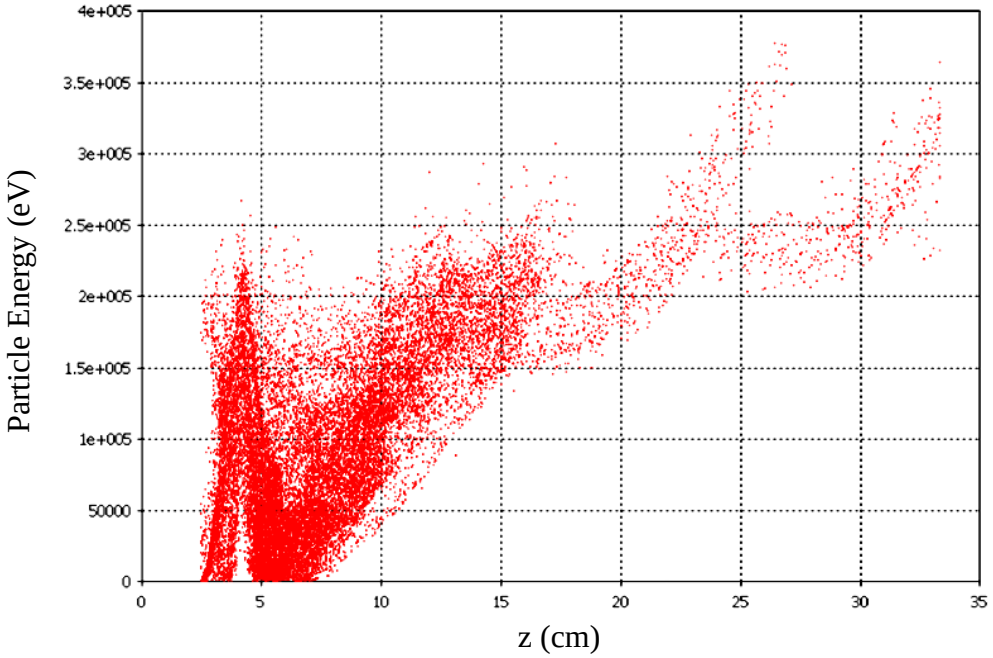

Figure 5.22—Calculated particle energy versus distance at a simulation time of 60 ns for 200 kV input and 1.68 cm AK gap with a calculated dominant frequency of 2.71 GHz

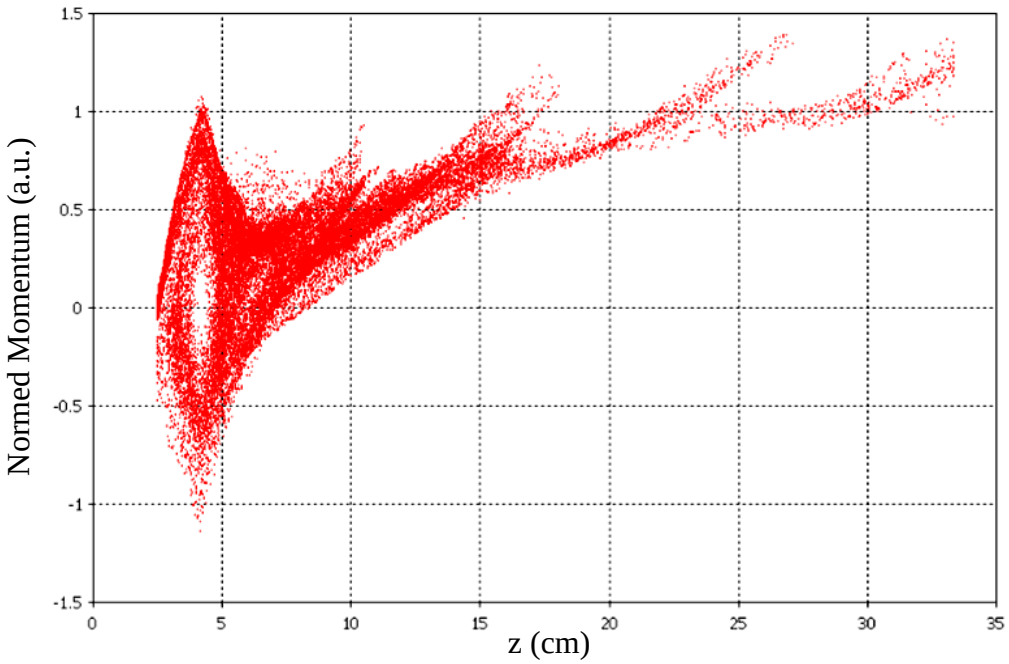

Figure 5.23—Calculated particle momentum versus distance at a simulation time of 60 ns for 200 kV input and 1.68 cm AK gap with a calculated dominant frequency of 2.71 GHz

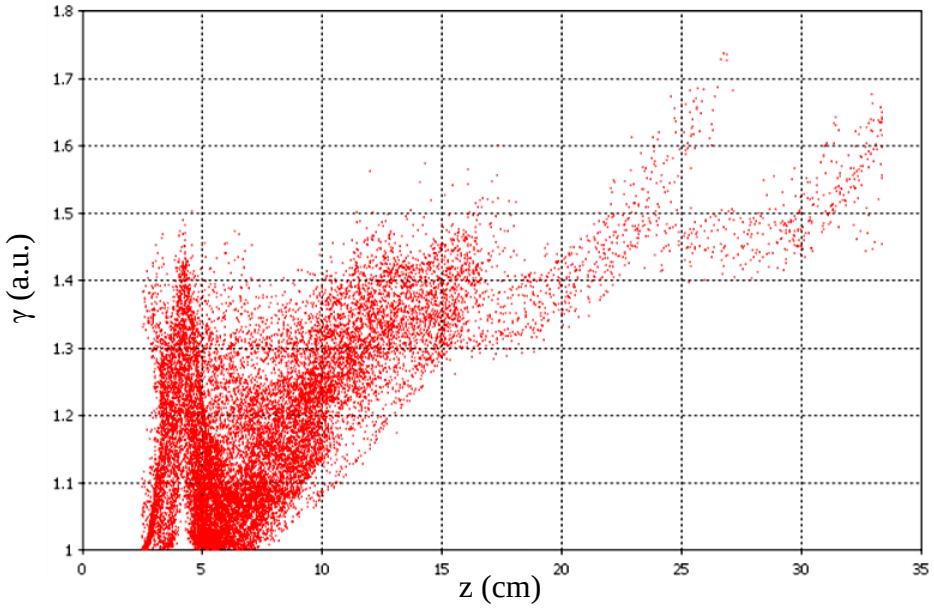

Figure 5.24—Calculated particle relativistic coefficient versus distance at 60 ns for 200 kV input and 1.68 cm AK gap with a calculated dominant frequency of 2.71 GHz

All of the data sets discussed above were recorded during a simulation which iterated the AK gap spacing from 1.00 cm to 2.30 cm to look at the tunability of the vircator as a function of the AK gap spacing as well as the virtual cathode formation at each gap spacing. The voltage for the AK gap parameter sweep was kept constant at 200 kV. The results of a parameter sweep of the AK gap are shown in Figure 5.25. This plot shows the frequency at which the peak occurs for the TE_{10} mode versus the AK gap. The dotted line with the triangular markers is the plot of the data obtained from the simulations, the two solid lines show the boundaries for the range of possible virtual cathode frequencies, and the thin dotted line is the curve fitted to the data. This curve shows a dependence on the AK gap as follows:

$$f_{vc} \propto 1/d^{1.376}$$

This power relation is slightly different than that found from the MAGIC simulations and that predicted in theory, showing a stronger dependence on the gap spacing. Even though

the gap dependence is different, the frequencies obtained from the simulations lie within the theoretical boundaries, and the frequency decreases as the AK gap increases.

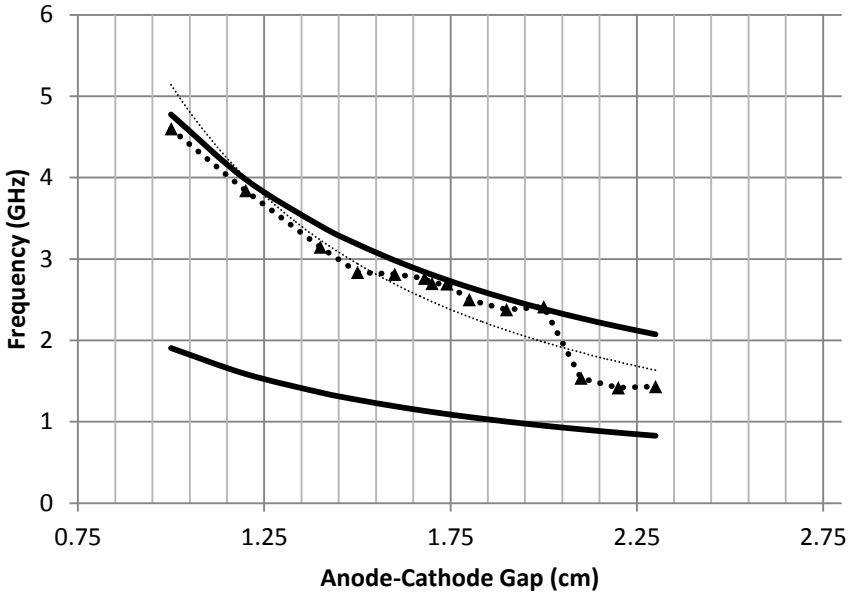

Figure 5.25—Dominant frequency versus AK gap as calculated in CST for 200 kV input

5.3 System Design and Construction

The design specifications for a single vircator are shown in Table 5.1.

Table 5.1—Design specifications for a single vircator

Parameter	Value
Input Voltage	200 kV
Anode-Cathode Gap	1.68 cm
Cathode Diameter	10.16 cm
Drift Tube Diameter	25.4 cm
Input Current	6 kA
Diode Impedance	33.4 Ω
Input Power	1.20 GW
Plasma Frequency	1.13 GHz
Upper Limit of Virtual Cathode Frequency	2.83 GHz
Reflexing Frequency	1.03 GHz

Photographs looking down the drift tube of the vircator can be seen in Figure 5.26 with one showing the vircator without the anode screen and without the cathode emitter

attached to the aluminum base, and the other showing the vircator with the anode and cathode. A photo of the dual vircators fully connected to both the vacuum system and the output waveguides can be seen in Figure 5.27. This figure also shows the output waveguides extending and exiting through the top of the concrete chamber.

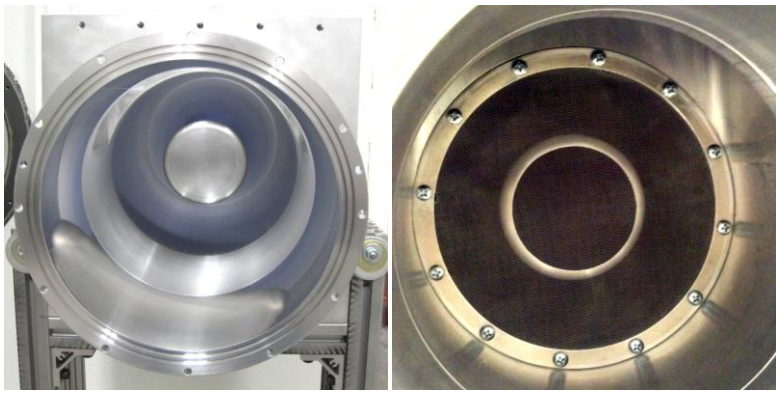

Figure 5.26—Vircator tube without (left) and with (right) anode and cathode emitter

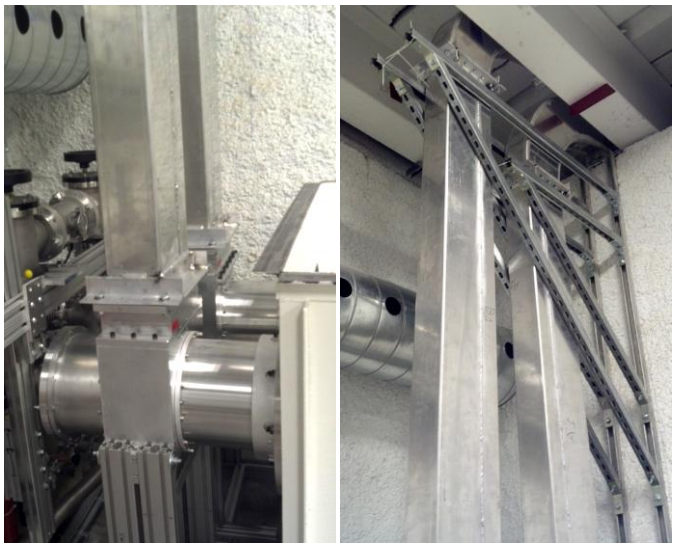

Figure 5.27—Dual vircators connected to output waveguides

Virtual cathode oscillators are vacuum electronic devices. To achieve a vacuum high enough to support an electron beam without breakdown, a vacuum system utilizing a roughing pump and a turbopump is used to obtain vacuum pressures. For all experiments, the vacuum pressure was measured to be between $2.7 * 10^{-6}$ and $6.0 * 10^{-6}$ torr. The system connected to the dual vircators is shown in Figure 5.28.

Figure 5.28—Vacuum system connected to dual vircators

Vacuum flashover is a major concern when dealing with vircators or any other high voltage system that utilizes a vacuum. Under vacuum, in the absence of gas molecules to impede electron motion, there is always a risk of secondary electron emission along the dielectric surfaces. The triple point, which is the point where the vacuum, conductor, and dielectric interfaces all meet at one point, is typically where flashover begins [9], [11], [12]. Keeping the electric field low at this point can drastically reduce the probability of vacuum flashover. Traditionally, decreasing the likelihood of vacuum flashover at the triple point has been accomplished by shaping the electric fields and altering the equipotentials by hiding the triple point with a conductor. The chances of secondary emission and vacuum flashover are reduced by angling the insulator [9]. Using this idea, the cathode portion that comes into contact with the dielectric has been shaped so as to hide the triple point, and the insulator is angled at a 45° angle. The field shaper is also rounded. This minimizes the field enhancement factor created by the corner of the conductor.

As discussed in the background of the vircator sources, the choice of materials is very important. Materials affect the vacuum level from shot to shot, as well as microwave output power and durability during repetitive pulse operation [13], [14], [15], [16]. Typically, fibrous materials such as felt or velvet have higher microwave output power levels although these materials often have larger shot-to-shot variations in frequency or other parameters [14], [16], [17]. Several different anode materials have been tested with particular interest in durability under sustained operation at repetition rates above 10 Hz. In the vircator system at the University of Missouri, the cathode material used was black felt, and several stainless steel wire cloth anode screens have been tested with varying transparencies. An example anode screen with its circular holder and a used black felt cathode are shown in Figure 5.29.

Figure 5.29—Anode screen with holder (left), cathode with black felt emitter (right)

For the system described here, the initial design of the vircator was to allow for the tuning of the plasma frequency to frequencies at or below 800 MHz, assuming a cathode material was used that allowed for the operation at large gap spacings. Because of this, a waveguide capable of transmitting these lower frequencies was necessary. A waveguide was designed and built in-house that was modeled after a WR975 standard

rectangular waveguide for radial microwave extraction. This can be seen in Figure 5.27. The long dimension for this waveguide is 9.75 inches and the short side is 4.875 inches. The cutoff frequency for the dominant mode in this waveguide is approximately 605 MHz.

5.4 Frequency Tuning

In a virtual cathode oscillator, both microwave frequencies created when an electron beam is emitted from the cathode (reflexing frequency and virtual cathode frequency) are related to the spacing between the anode and cathode. Both are inversely proportional to the gap spacing from equation 2.23. Because of this, vircators are tunable over a large range of frequencies as than other HPM sources [1], [18]. This tunability is the key reason for the implementation of a vircator system at the University of Missouri.

Using this relationship between the microwave frequency and the AK gap, the system has been designed to allow for the alteration of this spacing. The AK gap was altered by utilizing different "sleeves" that serve as a section of the cathode stock. Some of these aluminum sleeves can be seen in Figure 5.30.

Figure 5.30—Aluminum sleeves used for setting AK gap

In the future, it would be desirable to alter the system to allow for agile AK gap control. This would allow for the alteration of the AK gap without breaking the vacuum. This would serve two purposes: increased testing speed and providing finer control over the frequency output with finer resolution of gap spacing. The system also operated in such a manner as to only output the virtual cathode frequency. This was done by placing the anode screen at the edge of the waveguide closest to the cathode. An issue with this was that the virtual cathode was not formed in the center of the waveguide, which could reduce coupling to the waveguide. The virtual cathode is formed at a distance past the anode screen that is approximately equal to the spacing between the anode and real cathode [1].

Another element used to control the microwave output is the use of an adjustable "plunger." This plunger allows for the creation and control of the cavity resonance in the drift tube. The plunger in this system is an aluminum plate that is 8 inches in diameter with a variable distance from the anode screen. This plunger is grounded to the vircator's drift tube by a 1.27 cm diameter threaded brass rod. Other experiments using different forms of resonant cavities have shown significant effects on the output bandwidth and power levels [1], [6], [19].

The output frequency of a vircator is subject to variation caused by a chain of small, unpredictable influences: the pulse generator system has variations in the breakdown voltage of the oil-filled switch, and the vircator's plasma frequency changes with this breakdown voltage because of voltage-induced changes in the current density. The plasma frequency tends to increase as the voltage increases because of the increase in current density. This makes predicting the actual output of the vircator somewhat

difficult, but a range of operation can still be formulated. Experimental results describing the voltage variability of the output switch can be seen in Chapter 7. At the electrode spacing of 3.5 mm used in the high pressure oil switch that allows for the output of the high voltage pulse, the percent standard deviation of the breakdown voltage was approximately 11% while the mean output pulse amplitude on the secondary of the inductive voltage adder into a matched load was approximately 200 kV. This means that a majority of the pulse amplitudes into a matched load would be between 180 kV to 220 kV. With an AK gap spacing of about 1.68 cm, the system plasma frequency and reflexing frequencies should lie in the following ranges, respectively:

$$1.08\ GHz \leq f_p \leq 1.18\ GHz$$

$$1.00\ GHz \leq f_r \leq 1.60\ GHz$$

Since the virtual cathode frequency lies in the range of:

$$f_p \leq f_{vc} \leq 2.5 f_p \tag{5.2}$$

the virtual cathode frequency range, depending on the input voltage, is:

$$1.08\ GHz \leq f_{vc} \leq 2.95\ GHz$$

Using the empirical formula given in equation 2.27, the range of frequencies for the virtual cathode frequency is:

$$2.32 GHz \leq f_{vc} \leq 2.55 GHz$$

References for Chapter 5

[1] J. Benford, J. A. Swegle, and E. Schamiloglu, *High Power Microwaves*, 2nd ed.: CRC Press, 2007.

[2] Y. Chen, "Compact, Repetitive Marx Generator and HPM Generation with the Vircator," Texas Tech University, Master's Thesis 2005.

[3] L. E. Thode and C. M. Snell, "Virtual Cathode Microwave Devices - Basics," Los Alamos National Laboratory, Los Alamos, 1991.

[4] W. -Y. Woo, "Two-dimensional features of virtual cathode and microwave emission," *Phys. Fluids*, vol. 30, no. 1, pp. 239-244, January 1987.

[5] D. J. Sullivan, "High power microwave generation from a virtual cathode oscillator (Vircator)," *IEEE Transactions on Nuclear Science*, vol. 30, no. 4, pp. 3426-3428, August 1983.

[6] D. Price, D. Fittinghoff, J. Benford, H. Sze, and W. Woo, "Operational Features and Microwave Characteristics of the Vircator II Experiment," *IEEE Transactions on Plasma Science*, vol. 16, no. 2, pp. 177-184, April 1988.

[7] R. B. Miller, *An Introduction to the Physics of Intense Charged Particle Beams*. New York, United States of America: Plenum Press, 1982.

[8] R. B. Miller, "Mechanism of explosive electron emission for dielectric fiber (velvet) cathodes," *Journal of Applied Physics*, vol. 84, no. 7, pp. 3880-3889, October 1998.

[9] J. P. Shannon, S. F. Philp, and J. G. Trump, "Insulation of High Voltage Across Solid Insulators in Vacuum," *Journal of Vacuum Science and Technology*, vol. 2, no. 5, p. 234, September 1965.

[10] K. S. Woolverton, "High-Power, Coaxial Vircator Geometries," Texas Tech University, PhD Dissertation 1998.

[11] O. Milton, "Pulsed Flashover of Insulators in Vacuum," *IEEE Transactions on Electrical Insulation*, vol. EI-7, no. 1, p. 9, March 1972.

[12] A. Watson, "Pulsed Flashover in Vacuum," *Journal of Applied Physics*, vol. 38, no. 5, p. 2019, April 1967.

[13] J. Walter et al., "Initial anode optimization for a compact sealed tube vircator," in *IEEE Pulsed Power Conference*, 2011, pp. 807-810.

[14] M. Elfsberg, T. Hurtig, A. Larsson, C. Moller, and S. Nyholm, "Experimental Studies of Anode and Cathode Materials in a Repetitive Driven Axial Vircator," *IEEE Transactions on Plasma Science*, vol. 36, no. 3, pp. 688-693, June 2008.

[15] Y. -J. Chen, J. Mankowski, J. Walter, and M. Kristiansen, "Virtual cathode oscillator component optimization," in *Conference Record of the 2006 Twenty-Seventh International Power Modulator Symposium*, 2006, pp. 157-160.

[16] Y. Chen, J. Mankowski, J. Walter, M. Kristiansen, and R. Gale, "Cathode and anode optimization in a virtual cathode oscillator," *IEEE Transactions on Dielectrics and Electrical Insulation*, vol. 14, no. 4, pp. 1037-1044, August 2007.

[17] J. Mankowski, Y. Chen, J. Dickens, and A. Neuber, "A Low-Cost Metallic Cathode for a Vircator HPM Source," in *IEEE Pulsed Power Conference*, Monterey, 2005, p. 66.

[18] Sandia National Laboratories, "SANDIA REPORT SAND2001-1155, A Brief Technology Survey of High-Power Microwave Sources," Available to the public from U.S. Department of Commerce, 2001.

[19] C. Moller, M. Elfsberg, A. Larsson, and S. E. Nyholm, "Experimental Studies of the Influence of a Resonance Cavity in an Axial Vircator," *IEEE Transactions on Plasma Science*, vol. 38, no. 6, pp. 1318-1324, June 2010.

Chapter 6 — System Diagnostics

6.1 Electrical Diagnostics

Multiple diagnostics were in place to monitor the system's electrical operation. These diagnostics were placed throughout the system, measuring voltage and current signals at the modulator, the pulse forming line, the output of the pulse forming line, and, finally, the output of the inductive voltage adder. These diagnostics included resistive and capacitive voltage monitors, current transformers, a D-dot probe, a commercial high voltage probe, and B-dot probes used for measuring current. The diagnostics are discussed by the point in the system at which they are placed.

6.1.1 Modulator Diagnostics

The diagnostics on the modulator included a resistive voltage monitor for measuring the charge voltage on the capacitor bank, a wide bandwidth, high voltage probe used for measuring the pulsed voltage response on the capacitor bank during initial testing, and a current transformer for measuring the current through the thyratron. Figure 3.2 displays the positions of the resistive voltage monitor and the current transformer.

The resistive voltage divider measured the charge voltage of the capacitor bank to allow the operator to monitor and adjust the charge voltage of the modulator capacitor bank. The resistive divider was similar to that which would be found in a Fluke 80K-40 high voltage probe [1]. The voltage division ratio for this monitor was 1000:1 into a DC voltage monitor with an input impedance of 10 MΩ.

Table 6.1—High frequency, high voltage probe specifications

Parameter	Value
Manufacturer	Tektronix
Part Number	P6015B
Input Resistance	100 MΩ
Division Ratio	1000:1
Bandwidth, MHz	75 MHz
Max DC Voltage	20 kV
Max Pulsed Voltage	40 kV

The bandwidth of the resistive divider was not suitable for measuring signals with high frequency components. In order to measure the voltage waveforms of the modulator during pulsed operation, a Tektronix P6015B high frequency, high voltage probe was used. The specifications for this probe are shown in Table 6.1 [2].

Table 6.2—Current transformer specifications

Parameter	Value
Manufacturer	Stangenes Industries, Inc.
Part Number	3-0.002
Sensitivity	2 mV/A
Pulse Droop	0.005 %/μs
Max Current	200 kA
Max RMS Current	1.1 kA

The current through the thyratron was measured with a current transformer in order to ensure that the maximum ratings of the thyratron were not exceeded. The current transformer uses a single turn primary that couples with the secondary to output a voltage proportional to the current through the primary turn. To prevent arcing to the current transformer case, plastic insulation was used to increase the voltage holdoff. The specifications for the current transformer are shown in Table 6.2 [3].

6.1.2 Pulse Forming Line Diagnostics

Diagnostics used for sensing the electrical signals on the pulse forming line included a capacitive divider to measure the charging waveform at the input of the PFL, a D-dot probe for measuring both the charging waveform of the PFL and the discharge waveform of the PFL, and, finally, a capacitive cable probe for sensing the output pulse delivered to the high voltage output cables from the PFL.

The capacitive divider on the pulse forming line measured the charging waveform on the PFL. This allowed for the determination of the voltage to which the line was charged, as well as the energy available in the output pulse to deliver to the load. A diagram of the capacitive divider is shown in Figure 6.1. The capacitive divider is formed by the capacitance between the sensing electrode and the inner conductor and the capacitance between the sensing electrode and the outer conductor. The actual capacitive divider also included external capacitance to further increase the divider ratio and limit the output voltage amplitude from the divider. The output capacitance of the probe was measured to be approximately 12.5 nF. An integrating resistor was included in this monitor, since the time constant of the capacitive divider into a 50 Ω input would include a large percentage of signal droop. Since the voltage reached its maximum at about 2.5 μs, the probe's RC constant had to be much greater than this to prevent significant droop. The RC time constant was chosen to be 20 times the charge time, or 50 μs, making the resistor value equal to 4 kΩ. The output was terminated in 50 Ω on an oscilloscope. The calibration of this probe is discussed later in this section, and the divider ratio was found to be ~1,400,000:1

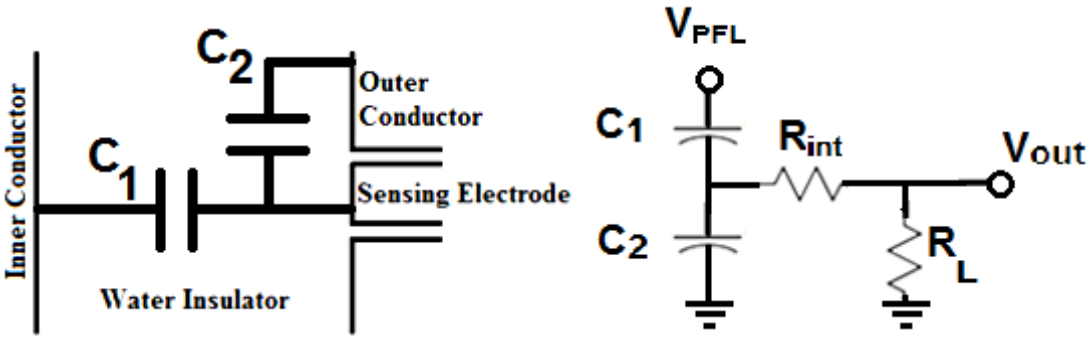

Figure 6.1—Diagram and schematic for capacitive divider

The voltage at the charging side of the oil switch was measured using a D-dot probe. A D-dot probe is an electrical sensor that couples to the electric field generated by the potential of an electrode within its proximity. The probe used here is formed by a small length of PE-047SR 50 Ω semi-rigid cable as shown in Figure 6.2.

Figure 6.2—Mounted D-dot probe

Equation 6.1 relates the output voltage from the probe as a function of a changing electric field:

$$V_0 = \epsilon_r \epsilon_0 R A_p \frac{dE}{dt} \tag{6.1}$$

where V_0 is the output voltage in volts, ϵ_r is the relative dielectric constant of the medium between the probe and the conductor generating the electric field, ϵ_0 is the permittivity of free space in F/m, A_p is the probe area in m^2, R is the impedance being driven by the probe in Ω, and $\frac{dE}{dt}$ is the change in the electric field with respect to time in $V \cdot m^{-1} \cdot s^{-1}$ [4].

In a coaxial geometry, the time derivative of the high voltage is related to the time derivative of the electric field via the equation:

$$\frac{dE}{dt} = \frac{1}{a \ln\left(\frac{r_o}{r_i}\right)} \frac{dv}{dt} \tag{6.2}$$

where dv/dt is the time derivative of the high voltage signal in $V \cdot s^{-1}$, r_o is the radius of the outer conductor of the high voltage coaxial system in meters, r_i is the radius of the inner conductor in meters, and a is the mean of the inner and outer radii in meters [4].

The D-dot probe outputs a signal that is proportional to the time derivative of the high voltage signal. This means that to measure a scaled version of the high voltage signal, the signal must be integrated. To do this, a capacitive integrator with a 2 μs time constant was used. This integrator was a Titan PSD passive integrator, the specifications of which are shown in Table 6.3 [5]. While the time constant of this integrator was smaller than the charge time of the PFL (2.5 μs), the amount of droop can be accounted for in post-processing. The droop at 2.5 μs is calculated to be 72.35%. The attenuation ratio for this probe was found to be 7,700,000:1.

Table 6.3—Capacitive integrator specifications

Parameter	Value
RC Time Constant	2 μs
Input Impedance	50 Ω
Output Impedance	1 MΩ

A capacitive cable monitor measured the output pulse voltage waveform from the PFL. The cable monitor was a Titan PSI voltage monitor with part number PSI-CCM-RG-218. This cable monitor had the same essential operation as the aforementioned voltage probes. It had an electrode which forms a capacitive divide with the center conductor and the cable shielding. It also included an integrating resistor

similar to that used on the capacitive divider. The mounted cable monitor is shown in Figure 6.3.

Figure 6.3—Mounted capacitive cable probe

The probes for the pulse forming line diagnostics were not calibrated initially. To calibrate the other probes in the system, the cable monitor was first calibrated. This was done by using a Tektronix type 109 mercury pulser and a P6015B high voltage probe. The pulser was connected to the high voltage output cable that the cable monitor was mounted to. The high voltage probe was used to measure the input pulse while the output from the cable monitor was simultaneous measured. Using this method, the voltage division ratio of the cable monitor was found to be approximately 5600:1.

To calibrate the other diagnostics, the cable monitor was used as reference. Using the reflection coefficient Γ at the interface between the PFL and the high voltage output cables, the voltage on the line was calculated from the pulse amplitude measured using the cable monitor. The voltage on the line related to the pulse amplitude is:

$$V_{PFL} = \frac{2V_{pulse}}{1+\Gamma}. \tag{6.3}$$

where V_{PFL} is the PFL voltage in kV, V_{pulse} is the output pulse amplitude in kV, and Γ is the reflection coefficient. The scale factors for the capacitive probe on the PFL and the D-dot probe could then be calculated using equation 6.3. The voltage divider ratios for the PFL diagnostic probes are shown in Table 6.4.

Table 6.4—PFL probe calibrated divider ratios

	Probe		
Parameter	**Capacitive Probe (PFL)**	**D-dot Probe**	**Capacitive Probe (Cable)**
Divider Ratio	1,400,000:1	7,700,000:1	5,600:1

6.1.3 Inductive Adder Output Diagnostics

The diagnostics used for the measurement of the electrical signals on the output of the inductive voltage adder included a commercial high voltage probe to measure the load voltage and B-dot probes to measure the current delivered to the load. There were two B-dot probes for measurement of the current into the two branches of the load. This was important, to ensure that current was being shared by the dual vircator load. The current and voltage signals also allowed for the calculation of the input power delivered to the load, which could be used in efficiency calculations.

Figure 6.4—Megaprobe from North Star High Voltage [6]

To measure the high voltage output pulse from the inductive voltage adder, a commercial high voltage probe was used. The high voltage probe was the Megaprobe from North Star High Voltage, a photo of which is shown in Figure 6.4. This probe can only be used with pulsed signals and is designed to be submerged in oil. The probe's specifications can be seen in Table 6.5 [6].

Table 6.5—Megaprobe specifications

Parameter	Value
Manufacturer	North Star High Voltage Probes
Division Ratio	10,000:1
Bandwidth	10 Hz – 50 MHz
Maximum Voltage	1000 kV
Droop	1 %/μs

Initially, two commercial Rogowski coils were going to be used to measure the current pulses delivered to the load. However, spurious electric field coupling resulted in interference that made measurement of the current from the signal nearly impossible. To limit the coupling of the electric field to a current probe, a single-turn B-dot probe was fabricated using an RG-58 coaxial cable. This new probe mitigated much of the noise that was seen in the Rogowski coils. However, the electric field was still coupling to the probe and superimposing a spurious signal on the intended current signal. This was finally removed by placing an electrostatic shield around the single turn. This shield was grounded to the coaxial cable shield which, in turn, was grounded to the system ground. Multiple views of the B-dot probe are shown in Figure 6.5. Using Faraday's Law, the voltage generated and measured on a B-dot probe is related to the changing magnetic flux through the area of the probe. This relation is:

$$v(t) = -NA_p \frac{dB}{dt} \tag{6.4}$$

where $v(t)$ is the probe voltage in volts, N is the number of turns that the probe comprises, A_p is the area of the probe that the magnetic flux passes through in m^2, and dB/dt is the time derivative of the magnetic flux in $T \cdot s^{-1}$ [7]. The magnetic flux is related to the current passing through a conductor in the proximity of the probe. Assuming that the current-carrying conductor is much longer than the area that the probe encompasses, the total output voltage is related to the current through the conductor:

$$v(t) = \frac{\mu_0 N A_p R}{2\pi r L} i(t) \tag{6.5}$$

where R is the resistance of the probe in Ω, $i(t)$ is the time dependent current in amps, μ_0 is the permeability of free space with units of H/m, L is the inductance of the probe in henries, and r is the distance from the conductor in meters [8].

Figure 6.5—Multi-view of B-dot current monitor

In order to determine the current through the load of the inductive voltage adder, the B-dot probes needed to be calibrated. These probes were calibrated using the calibrated Megaprobe high voltage probe which measured the voltage at the output of the adder. The B-dot probe signals were recorded along with the voltage signals for each corresponding pulse. The B-dot signals were digitally processed in MATLAB using filtering techniques to remove digital artifacts such as a slight DC offset in the oscilloscope waveform. The signals were then digitally integrated using trapezoidal integration techniques. To find the scale factor, the theoretical current value derived from Ohm's Law ($I = V/R$) was used as a comparison for both probes where the resistance value was the measured value for the corresponding water load resistor for each branch of the load. The scale factors for each are shown in Table 6.6. The

differences in scale factors are likely the result of a difference in the electrostatic shields, orientations, and differences in distance from the conductor.

Table 6.6—B-dot current probe specifications

Parameter	B-dot Current Probe #1	B-dot Current Probe #2
Area, cm^2	1	1
Turns	1	1
Scaling Factor	$2.46 \cdot 10^{11}$	$4.29 \cdot 10^{10}$

6.2 Microwave Diagnostics

Multiple diagnostics were in place to monitor the virtual cathode oscillator operation. These diagnostics were used to monitor both the output of the inductive voltage adder and the microwave signals in the waveguide. These diagnostic instruments were a commercial high voltage probe for monitoring the vircator voltage, two B-dot probes for monitoring the vircator input current, and two commercial B-dot probes for monitoring the microwave signals in the waveguides.

The diagnostics used to monitor the input signals into the vircators were discussed in the previous section but are reviewed briefly here. To monitor the voltage input to the vircators, a commercial high voltage probe called the Megaprobe from North Star High Voltage was used. This probe is built specifically for pulsed operation at voltages up to 1 Megavolt with a voltage division ratio of 10,000:1.

B-dot probes were used to measure the current delivered to each vircators. Each branch of the inductive adder's output included a B-dot probe for measuring this current. These probes output a voltage proportional to the time-dependent magnetic field generated by the current pulses delivered to the load. Having measurements of the current for both vircators is important for multiple reasons. One significance is that the voltage and current together allow for the determination of the power delivered to the

load. This, coupled with power measurements of the microwave signal, allows for a calculation of the power efficiency. A second significance is that current measurements ensure that both vircators form electron beams and operate properly. Current measurements also provide the opportunity to determine the impedance of the diode, which can permit the matching of impedances from the PFL to the load. The two B-dot probes consisted of RG-58 coaxial cables. The probes were electrostatically shielded to reduce electric field coupling with the probe. To convert from a time-derivative signal to a current pulse, post-processing was performed in MATLAB. This post-processing included filtering to remove both the DC offset inherent in the digital acquisition on the oscilloscope and high frequency noise. The signals were digitally integrated after filtering. The probes were calibrated using the commercial high voltage probe and known resistance values for the water resistor loads.

To measure the high power microwave signals in the waveguides, a commercial B-dot probe, specifically a Beehive 100B (small loop) B-dot probe shown in Figure 6.6, was inserted in the side of the waveguide. The specifications for this probe are shown in Table 6.7 [9].

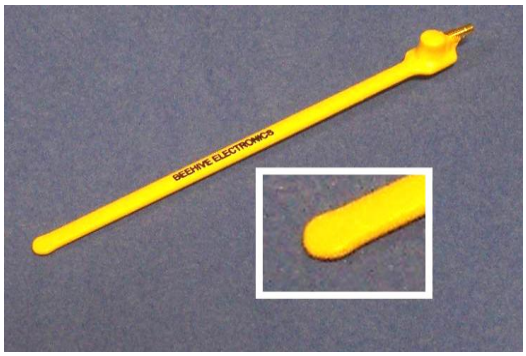

Figure 6.6—Beehive 100B B-dot probe used for microwave signal measurements

Table 6.7—Beehive B-dot probe specifications

Parameter	Value
Manufacturer	Beehive Electronics
Model Number	100B (small loop)
Tip Diameter	0.25 in
Loop Diameter	0.15 in
Upper 3dB Frequency	3100 MHz
First Resonance	>6000 MHz

In a radially extracted vircator using a rectangular waveguide for extraction, less than 10% of the microwave energy is carried in modes other than the TE_{10} mode [10]. In this mode, only three field vectors exist, the H_x, H_z, and E_y vectors, where the x-direction is the long dimension of the waveguide, the y-direction is the short dimension of waveguide, and the z-direction is the direction of propagation through the waveguide [11]. At the center position of the cross section of the waveguide, the H_x and E_y vectors dominate the fields. This relationship is utilized in the positioning of the B-dot probe in the waveguide for measuring the microwave signals. The probe tip is located at the center position of the waveguide oriented so as to measure the H_x vector by aligning the loop such that magnetic field lines pointing in the x-direction pass through the loop.

Initially, the vircators were tested individually. They were tested using a waveguide load that was capped off with a brass plate. The waveguide extension had a length of 58.25 inches, or 1.48 m, as shown in Figure 6.7. At the top, beneath the brass plate, there was anechoic material to both absorb and reduce reflections that might have affected the microwave measurements.

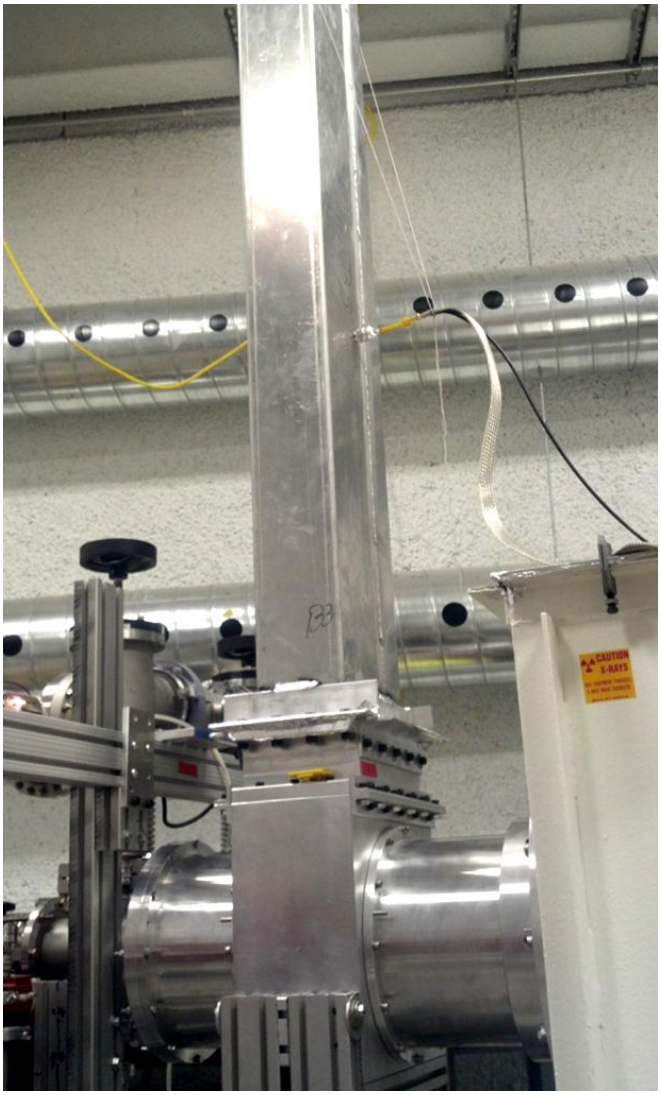

Figure 6.7—Waveguide load connected to single vircator

The B-dot probe used for measuring the microwave signals was connected to a PE2209-20 directional coupler from Pasternack via a 50-foot-long RG223 cable with SMA connectors. This directional coupler has a usable frequency range from 1 GHz to 4 GHz [12]. The directional coupler has a -20 dB output terminal that was connected to a Tektronix DPO70804 oscilloscope. This oscilloscope has a bandwidth of 8 GHz and a sampling rate of 25 GS/s [13]. In order to account for the attenuation of the diagnostic

cable and the directional coupler with respect to frequency in post-processing calculations, the attenuation of the diagnostic connections was measured.

The output of the B-dot probe is related to the frequency of the signal and the magnetic flux density measured by the probe through the equation:

$$P_{out} = X + 20\log_{10} B + 20\log_{10} F \tag{6.6}$$

where P_{out} is the probe output power into 50 Ω in dBm, X is a scale factor dependent on the probe, B is the magnetic flux density in tesla, and F is the frequency in MHz [9]. The actual input into an oscilloscope includes an attenuation term as well:

$$P_{out} = X + 20\log_{10} B + 20\log_{10} F - A(F) \tag{6.7}$$

where $A(F)$ is the attenuation of the diagnostic system in dB as a function of frequency. The scale factor, X, for the B-dot probe used in this system is 42.2 [9].

The peak input of the microwave signal into the oscilloscope could then be used to determine the peak magnetic flux density of the microwave signals. The magnetic field is related to the magnetic flux density via the magnetic permeability, μ:

$$H = \frac{1}{\mu} B \tag{6.8}$$

where H is the magnetic field strength in A/m. The B-dot probe was oriented in such a way as to measure only the H_x vector. This vector in a lossless rectangular waveguide for a TE_{mn} mode is:

$$H_x = \frac{j\beta_g}{k_c^2} H_0 \frac{m\pi}{a} \sin\left(\frac{m\pi x}{a}\right) \cos\left(\frac{n\pi y}{b}\right) e^{-j\beta_g z} \tag{6.9}$$

where β_g is the guided phase constant in rad/m, k_c is the cutoff wave number in rad/m, H_0 is a constant relating all of the field vectors in A/m, m and n are mode numbers, a is the length of the long dimension of the waveguide in meters, b is the length of the short

dimension of the waveguide in meters, and x, y, and z are spatial coordinates in meters [14]. The equations for k_c and β_g are shown below.

$$k_c = \sqrt{\left(\frac{m\pi}{a}\right)^2 + \left(\frac{n\pi}{b}\right)^2} \tag{6.10}$$

$$\beta_g = \sqrt{\omega^2 \mu\epsilon - k_c^2} \tag{6.11}$$

where ω is the angular frequency in rad/s, μ is the permeability of the insulating material in the waveguide in H/m, and ϵ is the permittivity of the insulating material in the waveguide in F/m. Assuming that negligible energy lies in modes other than the TE_{10} mode, the equation for the H_x vector can be further reduced. The B-dot probe is located at $x = \frac{a}{2}$ and $y = \frac{b}{2}$, meaning that the center of the loop on the B-dot probe was located at the center of the cross-sectional rectangle formed by the waveguide. Simplifying the equation gives:

$$|H_x| = \frac{j\beta_g}{k_c^2}\frac{\pi}{a}H_0 \tag{6.12}$$

The value H_0 can be calculated from the amplitude of the H_x vector. Once this value was been determined, the total power in the waveguide could be determined as follows [14]:

$$P(TE_{10}) = \frac{\omega\mu\beta_g H_0^2 a^3 b}{4\pi^2} \tag{6.13}$$

In this way, the peak power of the microwave signal was determined, which also allowed for the calculation of the peak power efficiency.

The microwave signals are carried to an anechoic chamber by the microwave waveguides. These signals were measured at the point where the individual lines of sight of the horn antennas met, approximately 4 meters from the horn antennas. To measure these signals, an electric field probe, namely a Beehive 100D stub probe shown in Figure

6.8, was mounted inside the anechoic chamber. The specifications for this probe are shown in Table 6.8 [9].

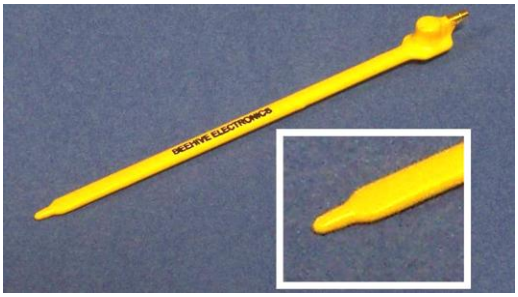

Figure 6.8—Beehive 100D stub probe used for microwave signal measurements in anechoic chamber

Table 6.8—Beehive stub probe specifications

Parameter	Value
Manufacturer	Beehive Electronics
Model Number	100D stub probe
Tip Diameter	0.08 in
3dB Frequency	6000 MHz
First Resonance	>8000 MHz

The output of the electric field probe is related to the frequency of the signal and the electric field measured by the probe through the equation:

$$P_{out} = X + 20\log_{10} E + 20\log_{10} F \tag{6.14}$$

where P_{out} is the probe output power into 50 Ω in dBm, X is a scale factor dependent on the probe, E is the electric field intensity in V/m, and F is the frequency in MHz [9]. The actual input into an oscilloscope includes an attenuation term as well:

$$P_{out} = X + 20\log_{10} E + 20\log_{10} F - A(F) \tag{6.15}$$

where $A(F)$ is the attenuation of the diagnostic system in dB as a function of frequency. The scale factor, X, for the electric field probe used in this system is -113.2 [9]. This probe was calibrated against a commercially calibrated horn antenna and was mounted in a stable position for relative amplitude comparisons.

References for Chapter 6

[1] Fluke, "80K-40 High Voltage Probe," Instruction Sheet 1999.

[2] Tektronix, "P6015 High Voltage Probe," Instruction Manual 1990.

[3] Stangenes Industries, Inc., "SI3-0.002 pulse current transformer," Palo Alto, 2001.

[4] W. R. Edgel, "Electric & magnetic field sensor application," Prodyn, Application Note 192 1997.

[5] Titan PSD, "Fast capacitive integrator," San Leandro, Data Sheet 2003.

[6] North Star High Voltage, "Megaprobe," Data Sheet.

[7] R. B. Lobbia and A. D. Gallimore, "Dynamic Electromagnetic Field Measurements of Clustered Hall Thrusters," in *42nd AIAA/ASME/SAE/ASEE Joint Propulsion Conference and Exhibit*, 2006.

[8] C. Yao et al., "Contactless Measurement of Lightning Current Using Self-integrating B-dot Probe," *IEEE Transactions on Dielectrics and Electrical Insulation*, vol. 18, no. 4, pp. 1323-1327, August 2011.

[9] Beehive Electronics, "100 Series EMC Probes," Data Sheet 2009.

[10] J. Benford, J. A. Swegle, and E. Schamiloglu, *High Power Microwaves*, 2nd ed.: CRC Press, 2007.

[11] C. A. Balanis, *Advanced Engineering Electromagnetics*.: John Wiley & Sons, Inc., 1989.

[12] Pasternack Enterprises, Inc., "PE2209-20 SMA Female Directional Coupler," Irvine, Data Sheet 2011.

[13] Tektronix, "Digital Phosphor Oscilloscopes and Digital Serial Analyzers," Data Sheet 2006.

[14] N. Ida, *Engineering Electromagnetics*, 2nd ed. New York: Springer-Verlag New York, LLC, 2004.

Chapter 7 — Experimental Results

7.1 Overview

The vircator high power microwave system consists of two separate subsystems. One is the pulsed power system discussed in Chapter 3, which included a thyratron-switched modulator, a pulse transformer, a water-filled PFL, an oil switch, and an inductive voltage adder. The second subsystem is the vircator HPM source, which was essentially an electron beam diode with a transparent anode. Both of these systems were tested individually and simultaneously. The experimental results of both are presented in this chapter.

7.2 Pulsed Power System

The hardware used for the pulsed power system had originally been built at LLNL and was used as a high-pressure liquid-dielectric test stand for high pressure switch design and liquid dielectric testing at UMC [1], [2], [3], [4]. This hardware was refurbished and upgraded to be used as the driving source for the vircator HPM source. The upgraded pulsed power system was tested in three phases: the pulse generator with the output delivered into a dummy load, the pulse generator with the addition of the inductive voltage adder into a dummy load, and finally the pulse generator with the inductive voltage adder into the vircator load.

7.2.1 Results into Dummy Load

Before the microwave source was included as a load in the system, the high voltage pulse generator was tested first to verify its output and operation. Multiple diagnostics were used at various points throughout the system, including voltage and

current measurements at the modulator, voltage measurements of the charging waveform on the pulse forming line, and the output voltage pulse delivered to the dummy load via the twelve high voltage transmission lines. These diagnostics of the pulsed power system were discussed in detail in Chapter 6.

The diagnostics used on the modulator portion of the system included a current transformer for monitoring the thyratron current, a low-frequency resistive divider for monitoring the charge voltage, and a high-frequency, high-voltage probe that was used for monitoring the capacitor bank voltage pulse. Initially, the RC snubber was not included at the input of the pulse transformer. An example capacitor bank voltage pulse displaying the voltage on the charge side of the modulator capacitor bank for a charge voltage of 10 kV is shown in Figure 7.1.

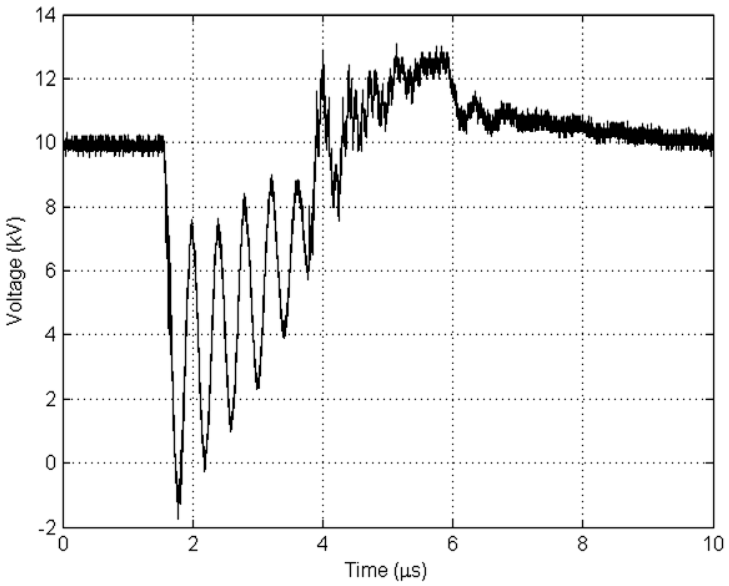

Figure 7.1—Measured modulator charge side voltage with no RC snubber for charge voltage of 10 kV into dummy load

As can be seen, a large amount of ringing is superimposed on the pulse due to the added inductance of the transmission lines that deliver the pulse to the pulse transformer. The

ringing is also visible on leading edge of the thyratron current trace shown in Figure 7.2. The thyratron current shown corresponds to a charge voltage of 20 kV.

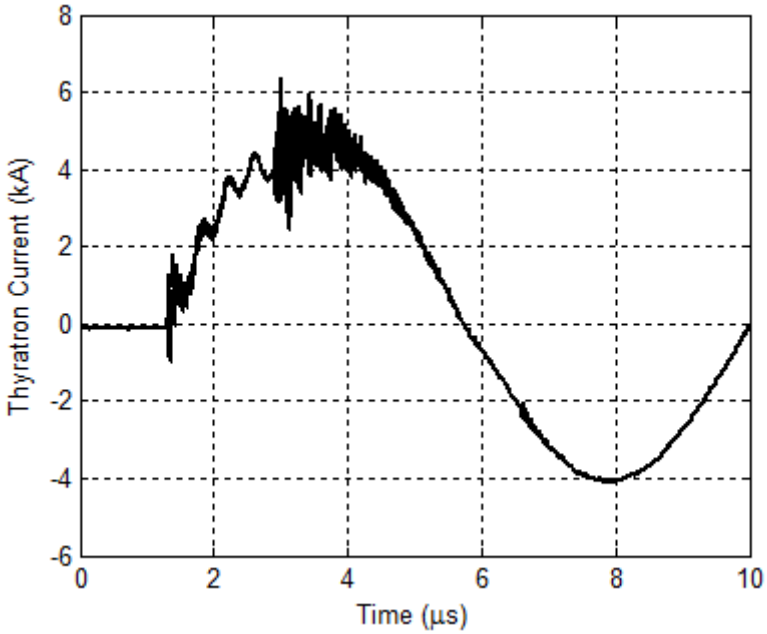

Figure 7.2—Measured thyratron current with no RC snubber for charge voltage of 20 kV into dummy load

An RC snubber was added at the input to the primary of the pulse transformer to reduce the overshoot caused by the inductance of the high voltage transmission lines as well as filter out the ringing in the circuit seen without an RC snubber. The addition and diagram of this circuit was discussed in section 3.1.1. Two thyratron current traces with the addition of the RC snubber are shown in Figure 7.3 to provide examples of repeatability as well as timing jitter. The charge voltage in this case was 25 kV. Higher frequency noise was superimposed on the trace due to reflections occurring when the switch closed on the output of the PFL at about 5 µs. By comparison with Figure 7.2, the ringing of the voltage is greatly reduced by the RC snubber, since no oscillations can be seen on the leading edge of the thyratron current.

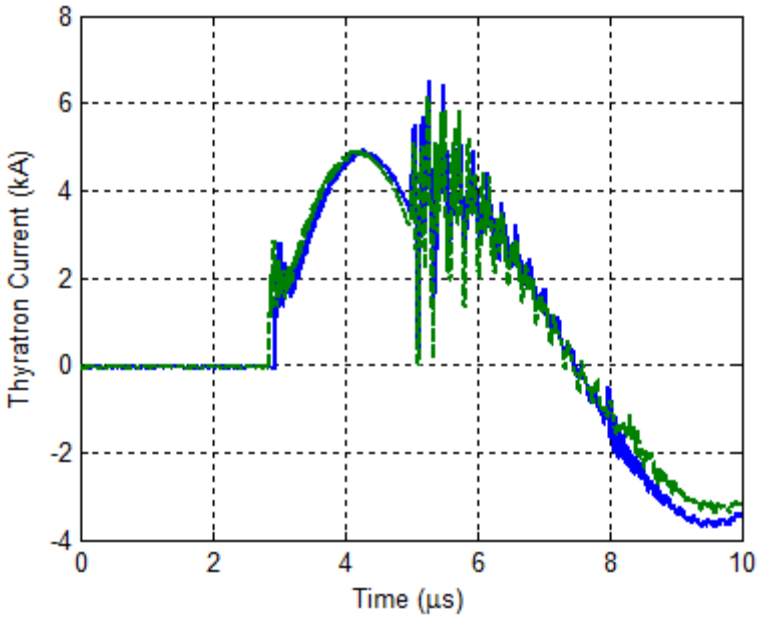

Figure 7.3—Measured thyratron current for two pulses with an RC snubber in place for charge voltage of 25 kV into dummy load

Multiple diagnostics were also incorporated to monitor the voltage on the PFL and its output, including a capacitive divider and a D-dot probe, both used to monitor the charge voltage on the PFL, and a capacitive cable monitor used to monitor the output pulse of the PFL delivered to the load. Sample waveforms of these diagnostics are shown in Figure 7.4 through Figure 7.6 showing the capacitive divider waveforms, D-dot probe waveforms, and the output waveforms for two consecutive pulses, respectively. The capacitive divider and D-dot waveforms were triggered on the oscilloscope by the rising edge of the capacitive divider waveform created when the switch broke down. In these plots, the lines, solid-blue and dashed-green, denote the corresponding pulses. A voltage discrepancy between the two traces exists because of the variability of the switch breakdown voltage. The D-dot probe waveforms are slightly distorted due to the droop created by the analog integrator, which had a time constant of 2 μs.

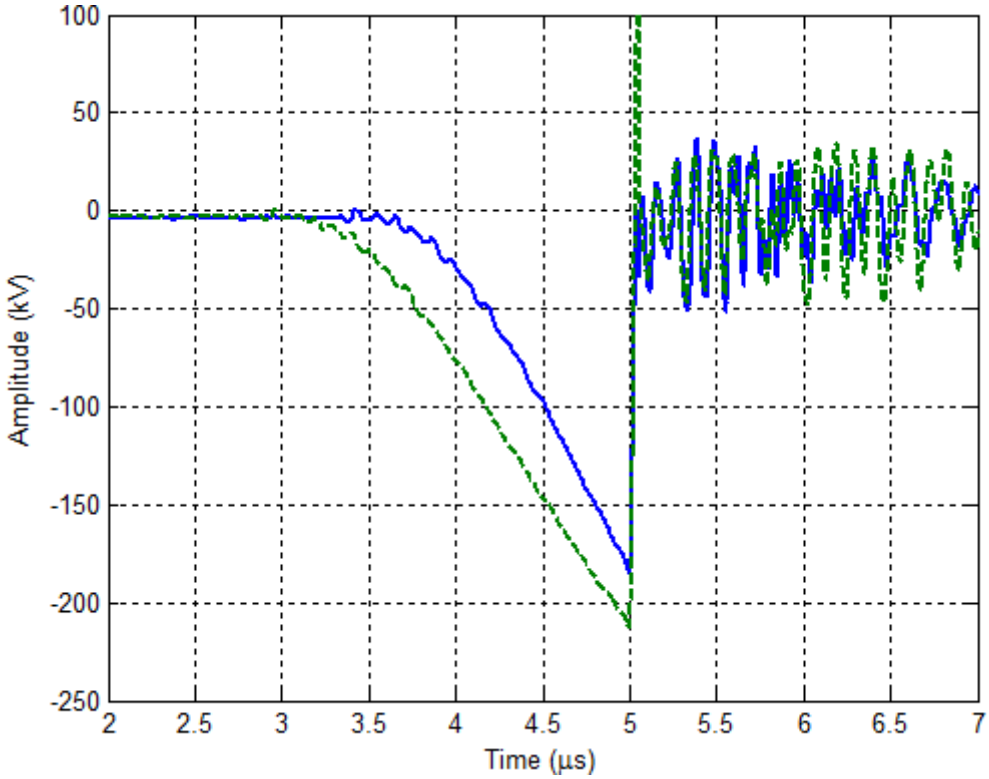

Figure 7.4—Measured PFL capacitive divider waveforms for two pulses for charge voltage of 25 kV, switch gap of 3.5 mm, and oil pressure of 100 psi into dummy load

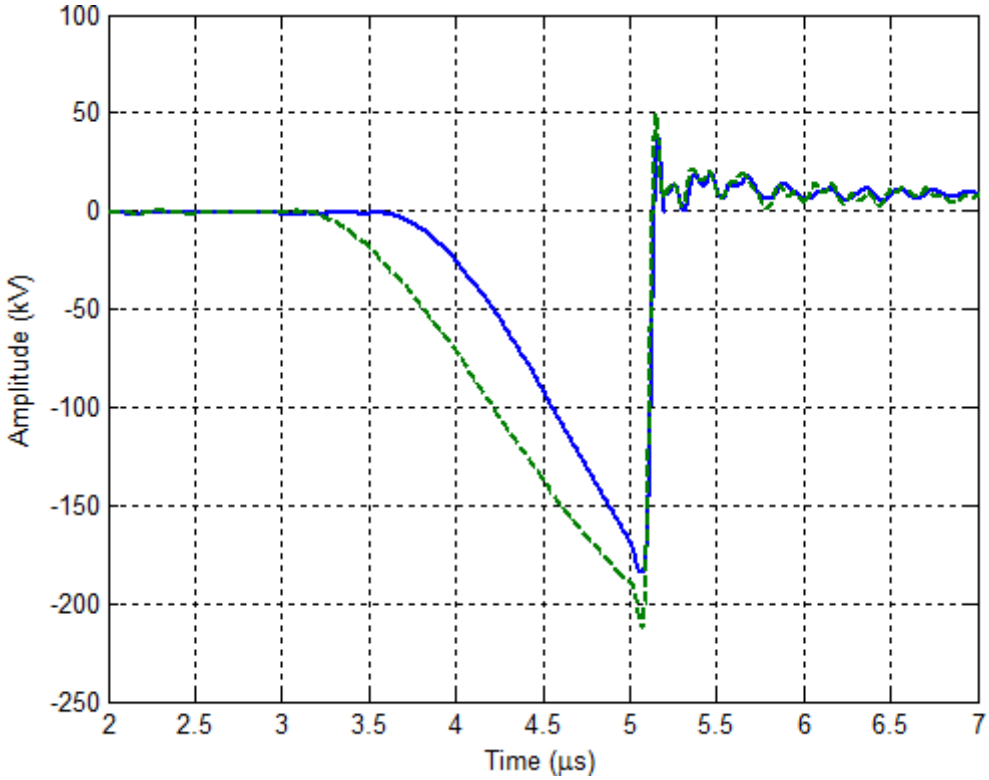

Figure 7.5—Measured PFL D-dot probe waveforms for two pulses for charge voltage of 25 kV, switch gap of 3.5 mm, and oil pressure of 100 psi into dummy load

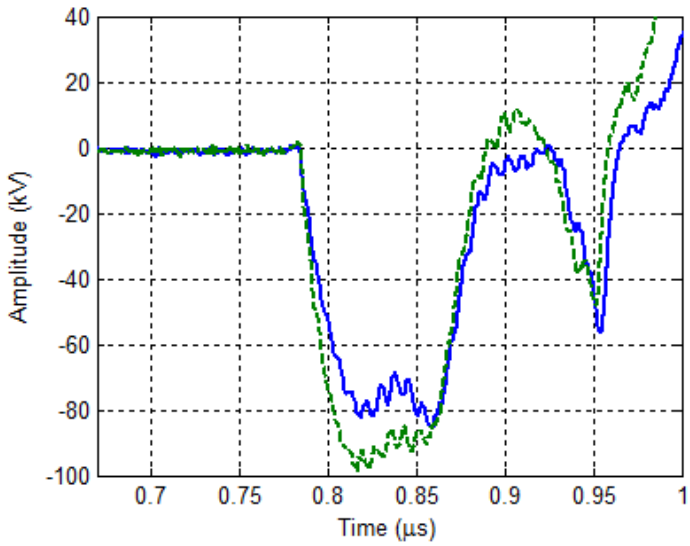

Figure 7.6—Measured PFL output pulses for charge voltage of 25 kV, switch gap of 3.5 mm, and oil pressure of 100 psi into dummy load

The high pressure oil switch was characterized for several different electrode spacings. This not only allowed for the tuning of the output voltage around a particular mean amplitude, but also allowed for the determination of the gap spacing that would be used for testing the vircator load. A curve of the breakdown voltage versus the switch electrode spacing was obtained by acquiring 25 output pulses with a 1 pps repetition rate at each electrode spacing. For each electrode spacing, the switch pressure was adjusted to 100 psi. In the post-processing calculations, the mean voltage minimum, the mean pulse width, the mean pulse fall time, and the breakdown voltage variability were all calculated. An example set of 25 pulses is shown in Figure 7.7. This particular set of data was for an electrode gap spacing of 3 mm. Summary statistics for this set of data is shown in Table 7.1. The mean breakdown voltage versus the gap spacing is plotted in Figure 7.8. A fitted curve for electrode gap spacings varying from 1.00 mm to 3.50 mm is shown in Figure 7.8. This curve has a power relationship of:

$$V_{br} \propto d^{0.551} \tag{7.1}$$

where V_{br} is the breakdown voltage and d is the electrode spacing.

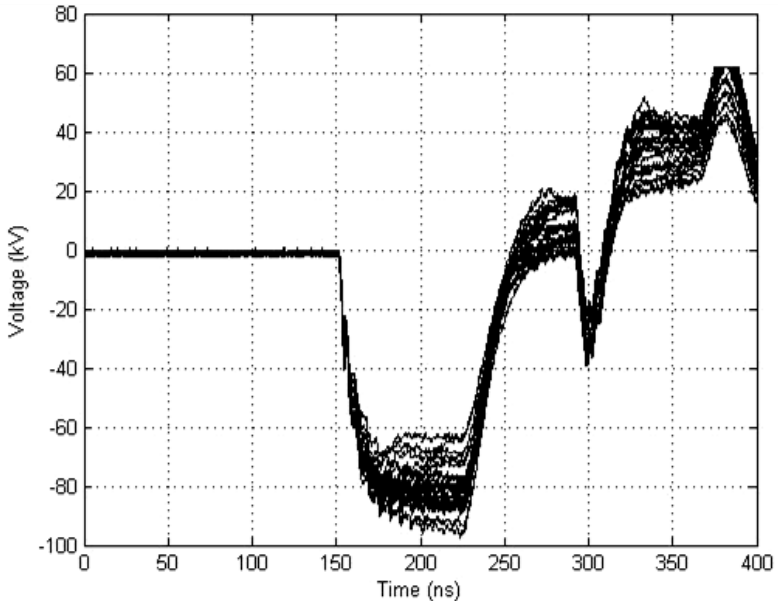

Figure 7.7—Measured output pulses used in determining switch breakdown characteristics with a switch gap of 3 mm and oil pressure of 100 psi

Table 7.1—Statistics of twenty-five output pulses shown in Figure 7.7

Parameter	Value
Mean Pulse Magnitude	-85.0 kV
Percent Standard Deviation	11.87%
Mean Rise Time (10-90)	19.4 ns
Mean Pulse Width (FWHM)	71.7 ns

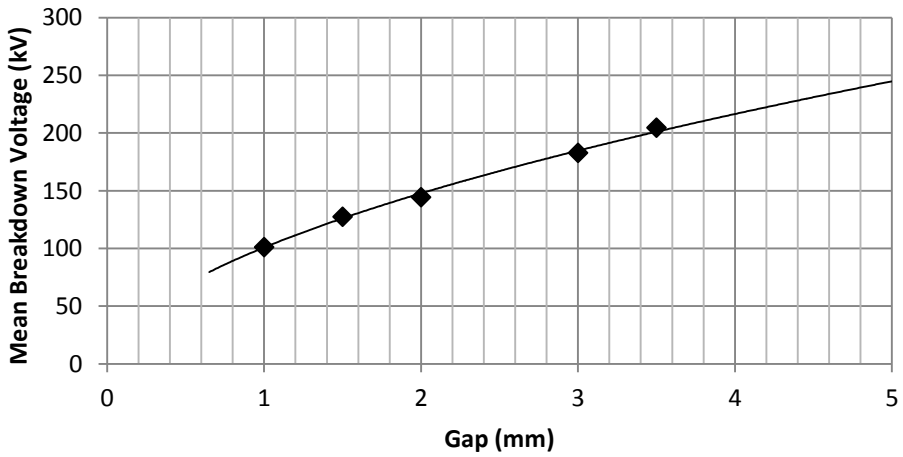

Figure 7.8—Mean breakdown voltage vs. electrode gap spacing for an oil pressure of 100 psi and a charge voltage of 25 kV

Another parameter of the high pressure oil switch that was characterized was the breakdown jitter, or the variability in the breakdown voltage. One way to characterize

this parameter is to examine the percent standard deviation of the breakdown voltage. This parameter can be calculated using the following equation:

$$\%SD = \frac{SD_{br}}{\mu_{br}} \tag{7.2}$$

where $\%SD$ is the percent standard deviation, SD_{br} is the standard deviation of the breakdown voltage, and μ_{br} is the mean breakdown voltage. This provides an unbiased measure of the variation in the breakdown voltage. A plot of the percent standard deviation versus the electrode gap spacing is shown in Figure 7.9. As can be seen, the percent standard deviation decreases as the electrode gap is increased. This curve has a power relationship of:

$$\%SD \propto d^{-0.328}. \tag{7.3}$$

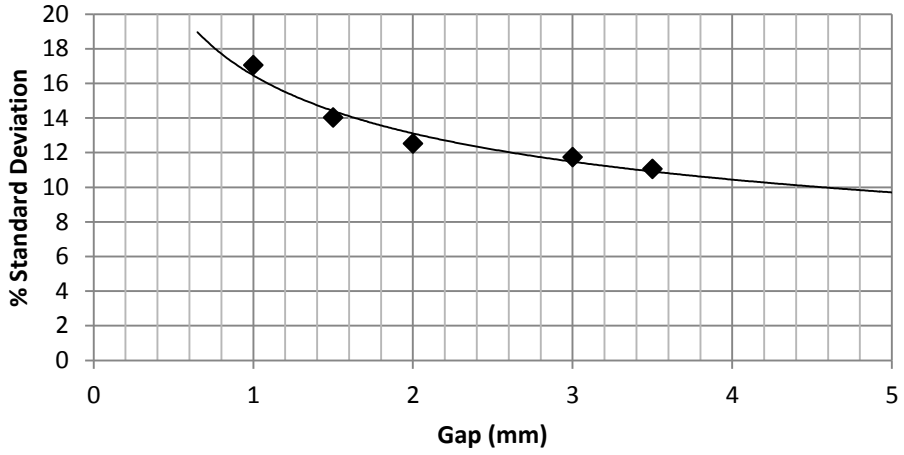

Figure 7.9—Percent standard deviation of breakdown voltage vs. electrode gap spacing for an oil pressure of 100 psi and a charge voltage of 25 kV

7.2.2 Results into Dummy Load with Inductive Voltage Adder

After the pulse generator was characterized, the electrode spacing in the high-pressure oil switch was set to provide reliable breakdown at voltage levels acceptable for operating the HPM sources. The electrode spacing was set to 3.5 mm, which, during testing, had a mean breakdown voltage of approximately 202 kV. The actual breakdown

voltage varied because of switch jitter. This breakdown voltage corresponds with a mean output pulse voltage of approximately 94 kV due to the impedance mismatch at the interface between the PFL and the high voltage output cables (see section 2.2). With a voltage step up of 1:2 produced by the inductive voltage adder, the pulse amplitude would be approximately 188 kV into a matched load. For all data shown, the oil switch electrode spacing was 3.5 mm with an oil pressure of 100 psi and a charge voltage of 25 kV unless otherwise specified.

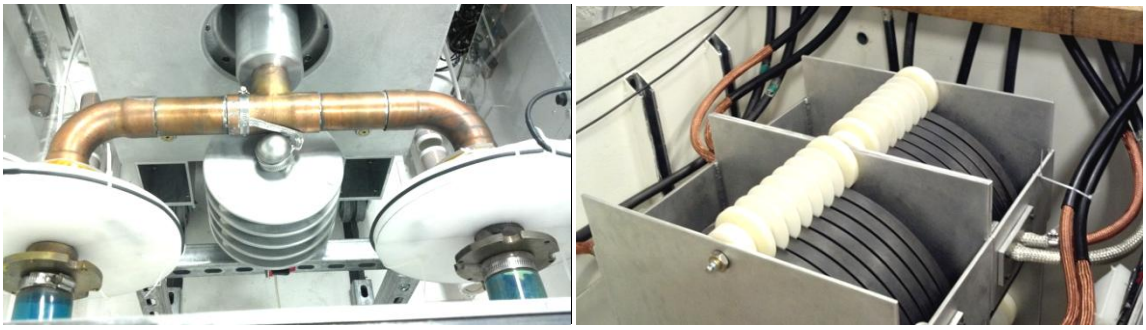

Figure 7.10—Inductive voltage adder output connected to parallel water resistor load (left), high voltage cables connecting to inductive voltage adder (right)

The voltage gain produced by the inductive voltage adder was tested to ensure proper operation. The output of the pulse generator was connected to the adder. The output of the adder was connected to two parallel water resistors, simulating the dual vircators. These water resistors were made using a copper-sulfate and deionized-water solution, one measuring 33 Ω and the other, 35 Ω on an LCR meter. These were discussed in more detail in Chapter 3. A photo showing the inductive voltage adder output connected to the parallel water resistors is shown in Figure 7.10.

Diagnostics were incorporated to measure the output of the inductive voltage adder. These diagnostics included a commercial high voltage probe called the Megaprobe from Northstar High Voltage Probes to measure the load voltage and two B-dot probes built in-house for examining the current through each load. Measuring the

current through each branch in the parallel load was important as this allowed for the study of current sharing between each element of the load.

Sample output waveforms are shown in Figure 7.11 and Figure 7.12. The B-dot probe output signals were integrated digitally. The signals were also digitally filtered to minimize DC components inherent in the oscilloscope trace that would have affected the integrated signal's shape. These digitally integrated signals for the current are the traces shown in Figure 7.12. The current waveforms were very similar to the voltage waveform into the resistive load. The pulse shape was slightly distorted compared to the rectangular pulse that was output by the water-filled PFL. This was likely a combination of the cable inductance, the leakage inductance in the inductive voltage adder, and the bandwidth limitations of the probes.

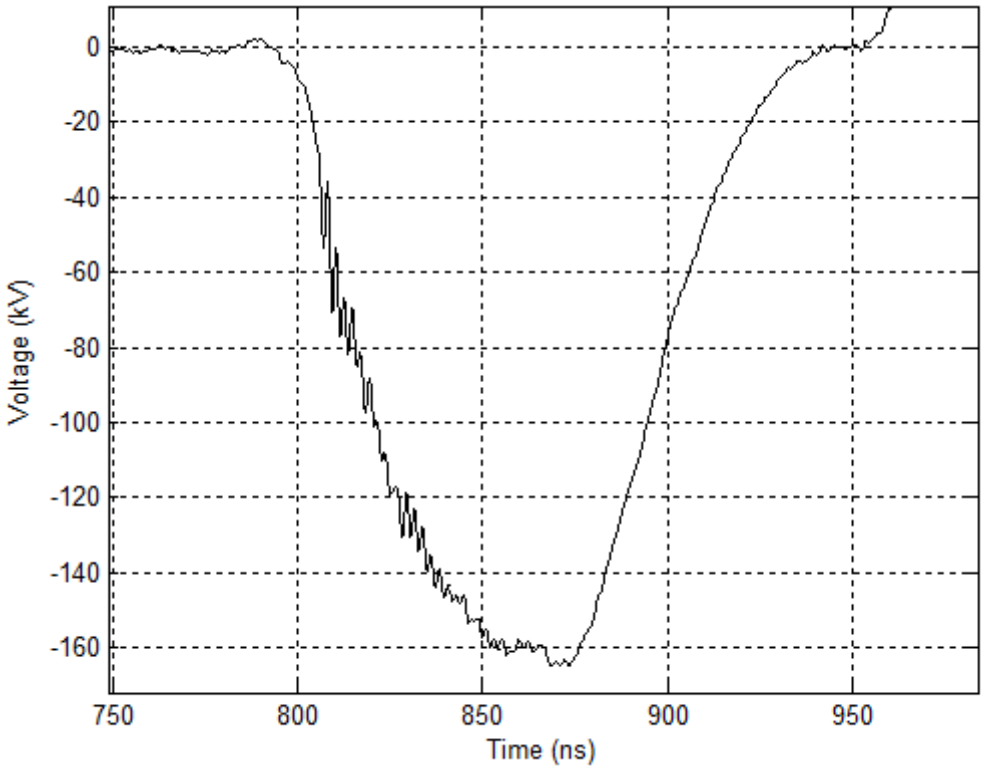

Figure 7.11—Measured voltage trace at the output of the inductive adder for charge voltage of 25 kV, switch gap of 3.5 mm, and oil pressure of 100 psi with inductive voltage adder output connected to dummy load

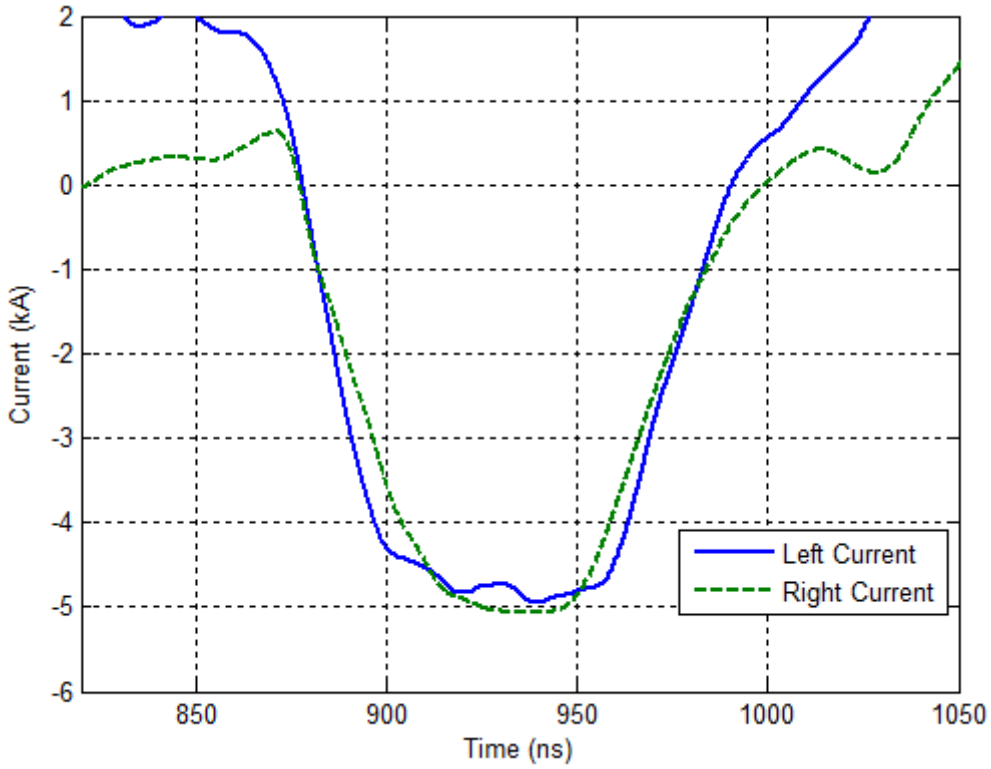

Figure 7.12—Measured current traces out of the inductive voltage adder for charge voltage of 25 kV, switch gap of 3.5 mm, and oil pressure of 100 psi with inductive voltage adder output connected to dummy load

7.2.3 Results into Vircator Load with Inductive Voltage Adder

After the inductive voltage adder operation was verified, the vircators were tested. Initially, only one vircator was connected at a time. This was done mainly to determine the tunability and other characteristics of each vircator. This ensured that the two vircators were not influencing each other by making unwanted alterations to the microwave signals. A MATLAB script was written to analyze the data files saved on the oscilloscopes. This script included the plotting of the raw data signals that were captured, the filtering and integration to obtain the current through each branch of the inductive adder output, the determination of both the impedance and the power versus time of each output branch, and the ratio of the measured current to the predicted Child-Langmuir current [5], [6], [7], [8]. This script also read from and wrote to a Microsoft Excel

spreadsheet that was populated with data values, including the minimum voltage of the input pulse, the minimum current values, and the peak input power for both sides of the inductive voltage adder load. Figure 7.13 through Figure 7.16 display example output waveforms created by the MATLAB script for one pulse with only one branch of the inductive voltage adder connected to a vircator. The other branch of the inductive voltage adder was terminated with a water resistor. The vircator was connected to the "right" side of the output with an AK gap of 1.74 cm with the water resistor connected to the "left" side. Figure 7.13 shows an example driving voltage pulse at the output of the inductive voltage adder, Figure 7.14 shows the corresponding current traces, Figure 7.15 shows the instantaneous power dissipation for each branch of the load, and Figure 7.16 shows the time-resolved impedance for each branch of the load.

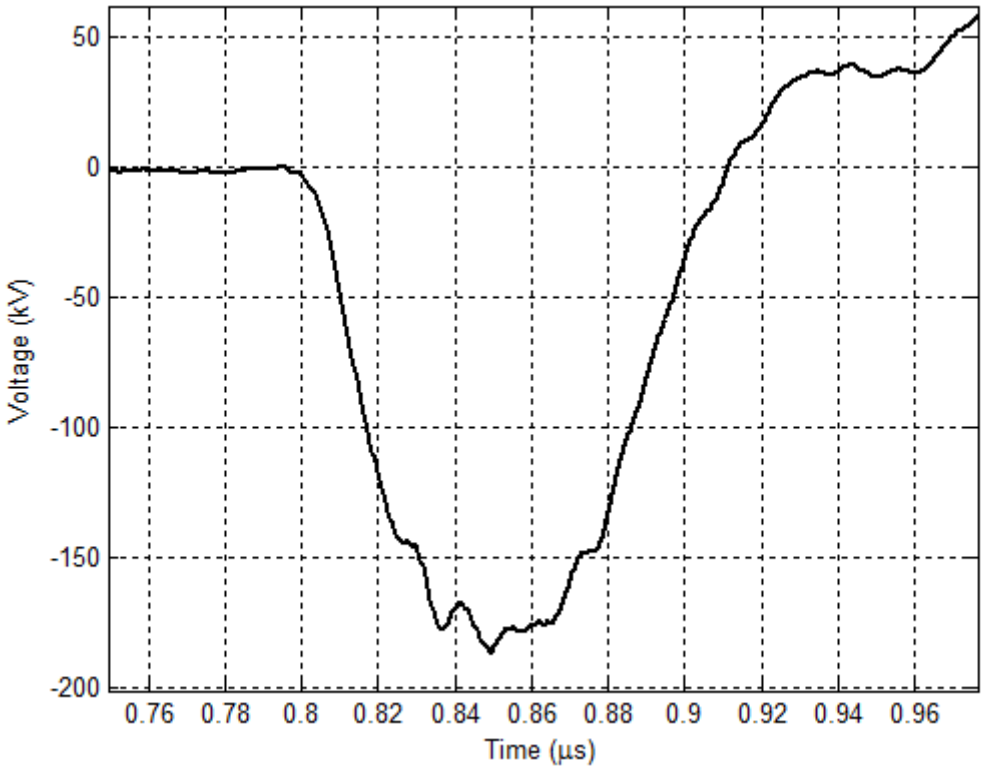

Figure 7.13—Measured input voltage pulse with single vircator with AK gap of 1.74 cm and water resistor load

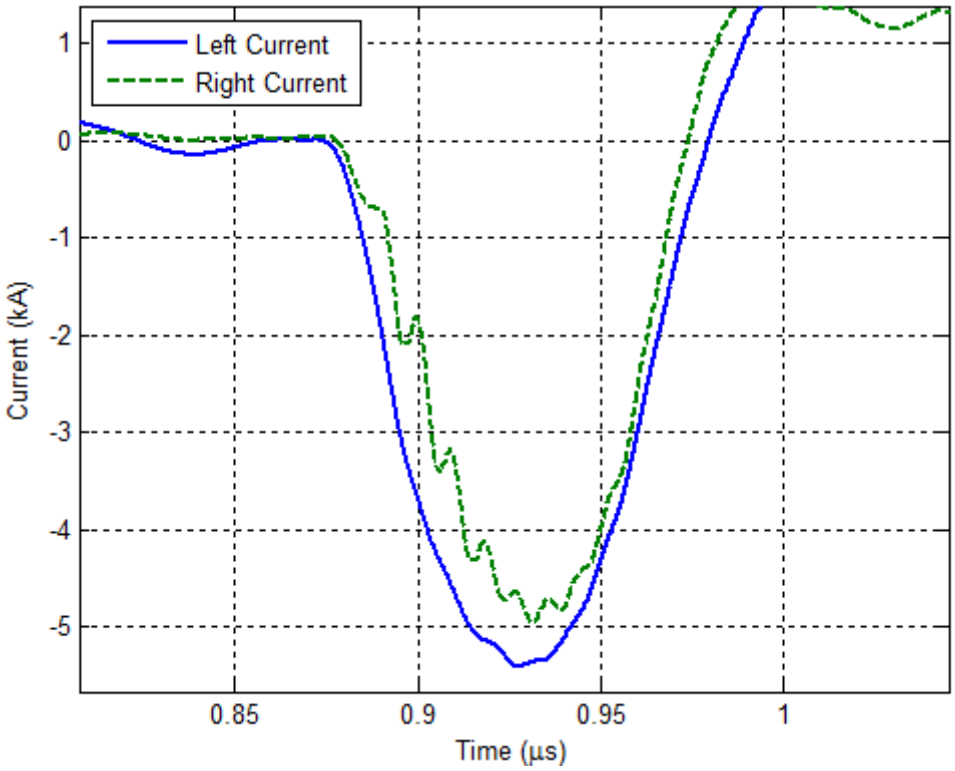

Figure 7.14—Measured input current, right connected to vircator with AK gap of 1.74 cm, left to water resistor

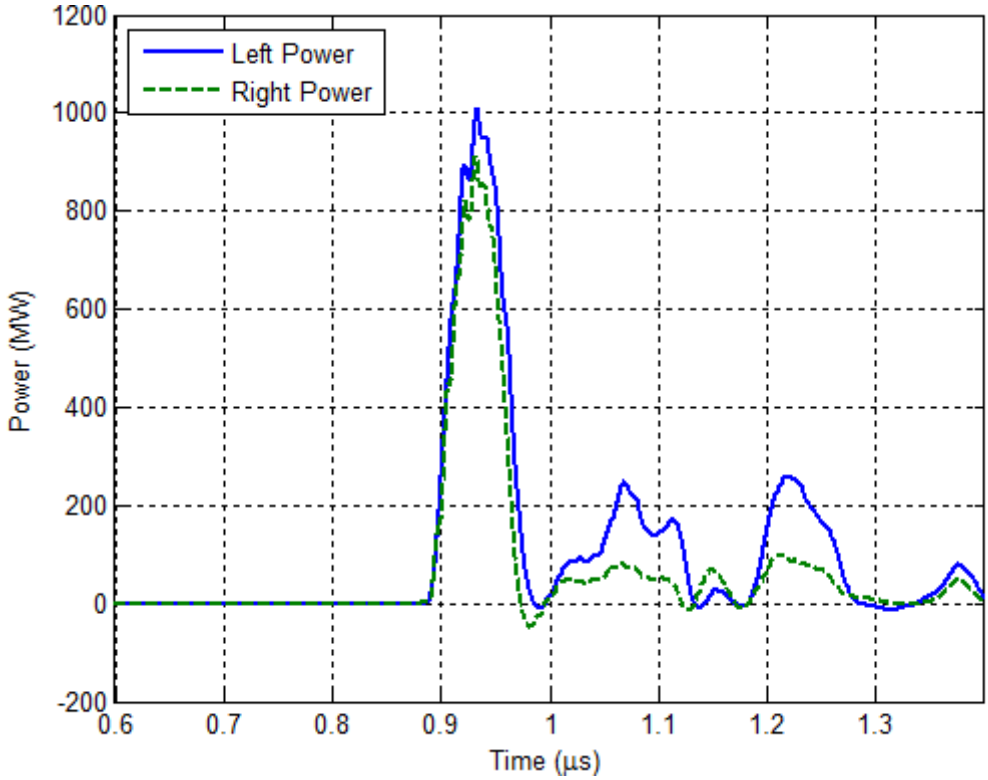

Figure 7.15—Input power calculated from measurements, right branch connected to vircator with AK gap of 1.74 cm, left to water resistor

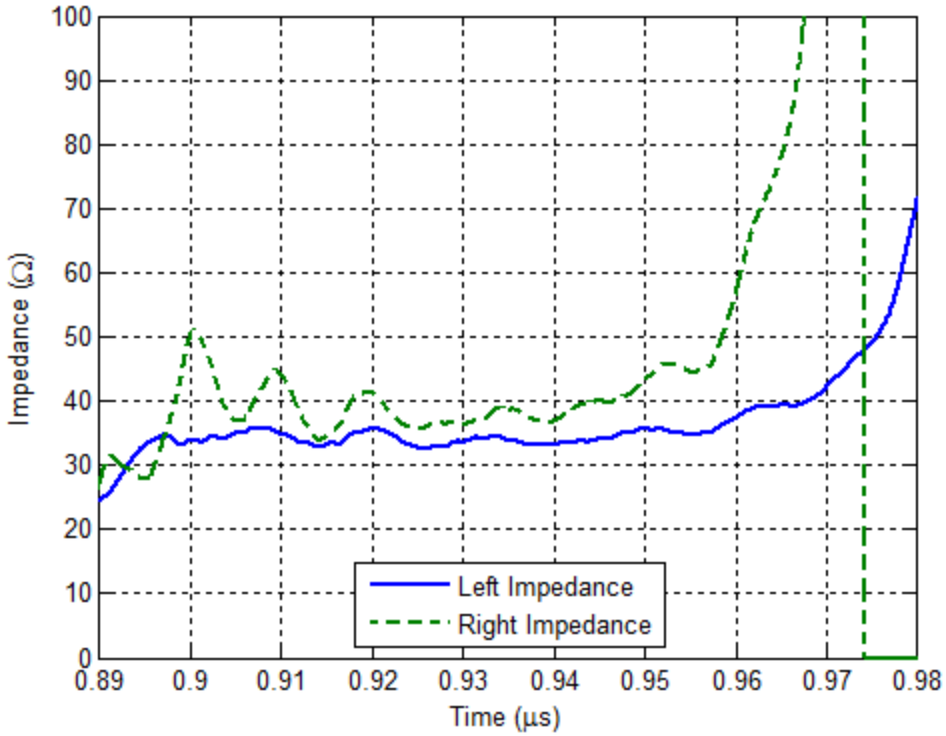

Figure 7.16—Impedance calculated from measurements, right branch connected to vircator with AK gap of 1.74 cm, left to water resistor

The dominant frequency of a vircator is largely dependent on the AK gap. To determine the frequency tunability of each of the vircators, the gap was varied across a range from 1.50 cm to a maximum of 2.54 cm. At the same time, the diode impedance of each vircator for each gap spacing and pulse was calculated. The impedances versus the AK gap for each vircator are shown in Figure 7.17 and Figure 7.18. This data corresponds to a single vircator being tested with a water resistor in parallel. The impedance varied for a given gap spacing largely because of the variation in the voltage across the AK gap created by the switch jitter. Regardless, the impedance increase with the AK gap was as expected. Also, the impedance for one vircator matched the other very closely for a given AK gap. This allowed for the determination of how the gaps could be adjusted to reliably form a particular equivalent impedance.

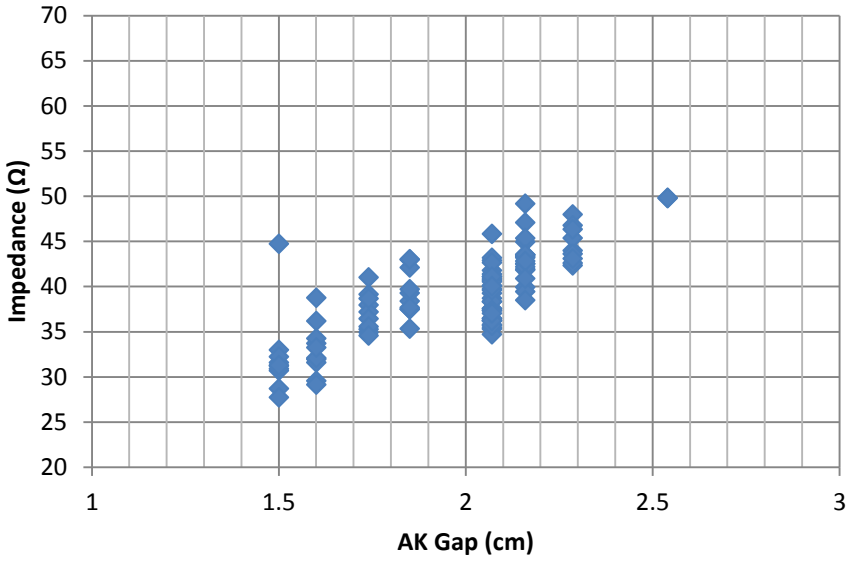

Figure 7.17—Impedance vs. AK gap for "right" vircator

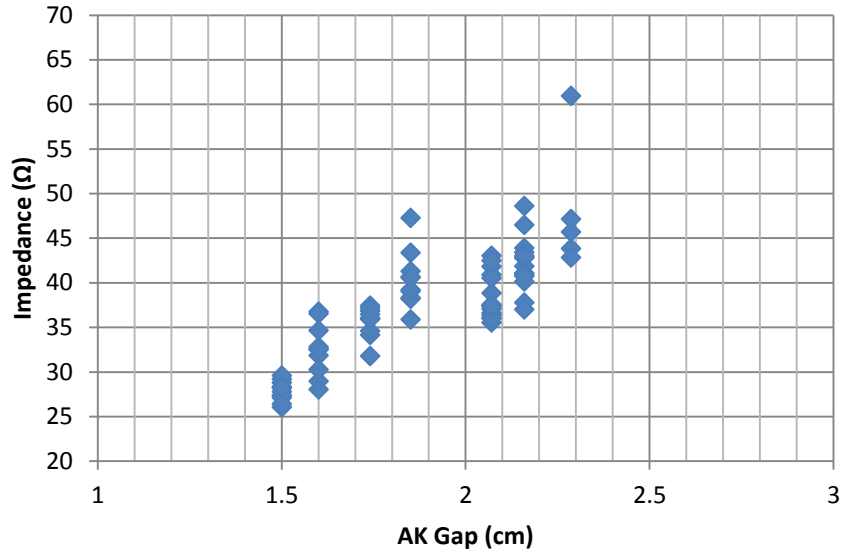

Figure 7.18—Impedance vs. AK gap for "left" vircator

After the vircators were characterized individually, they were tested in tandem. To accomplish this, the vircators were connected in parallel to the output of the inductive voltage adder. The vircators were initially connected to waveguide loads as they were when testing the vircators individually. These loads consisted of waveguide sections that

were capped off with brass plates. Anechoic material was used to absorb the microwaves. These loads are shown in Figure 7.19.

Figure 7.19—Dual vircators with waveguide loads

Similar measurements were taken as for the single vircator case. Example waveforms for a dual vircator load are shown in Figure 7.20 through Figure 7.23. The right vircator in these plots had an AK gap of 2.29 cm (0.90 inches) and the left vircator had an AK gap of 1.50 cm. Each vircator formed an electron beam with current very nearly equal to the space-charge-limited current predicted by the Child-Langmuir equation. It was shown that the input power into the vircator with the larger gap spacing was much lower than the vircator with the smaller gap. Because of this, it is likely that the microwave power produced at larger gaps would be less than the smaller gaps.

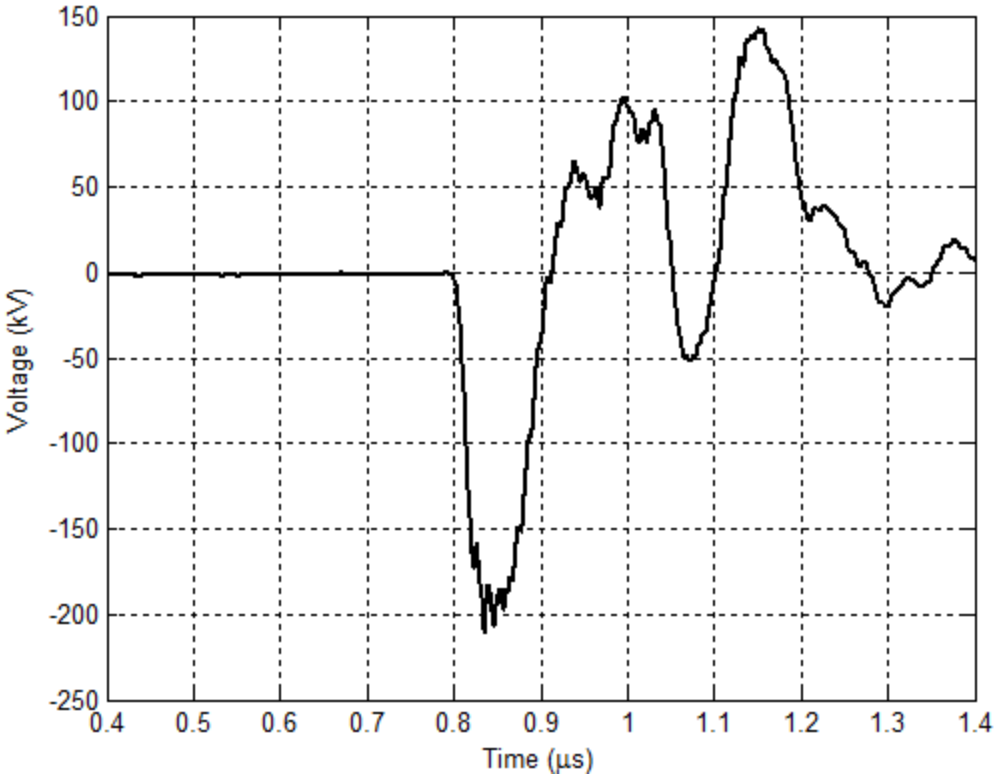

Figure 7.20—Measured input voltage pulse to dual vircator load, left AK gap 1.50 cm, right 2.29 cm

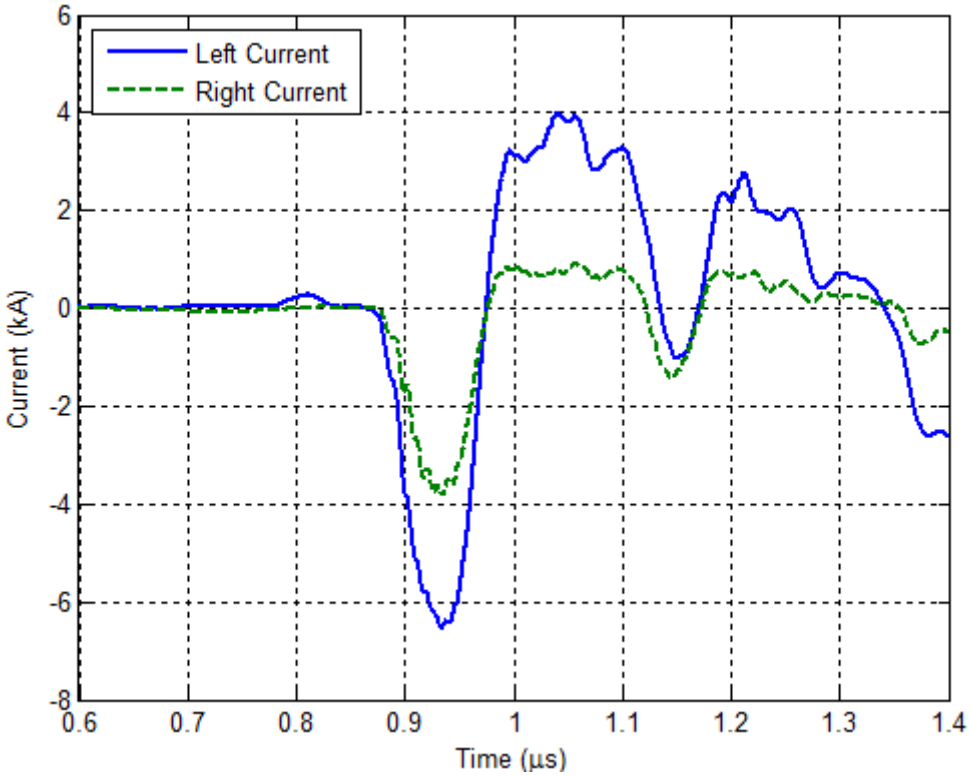

Figure 7.21—Measured input current to dual vircator load, left AK gap 1.50 cm, right 2.29 cm

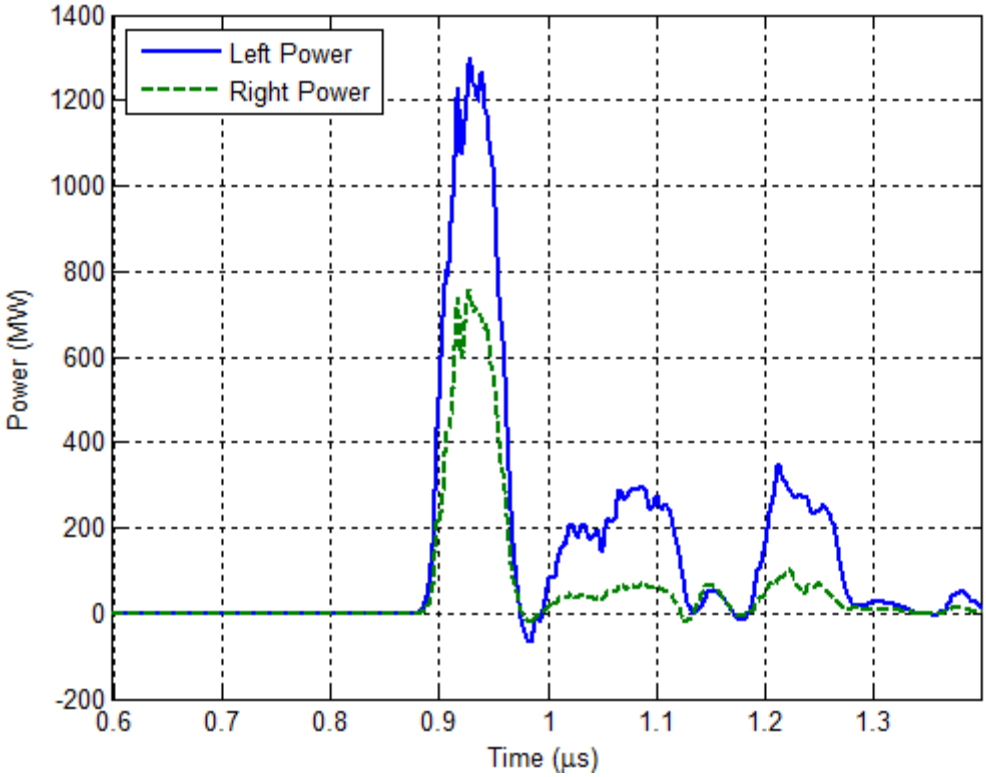

Figure 7.22—Input power calculated from measurements to dual vircator load, left AK gap 1.50 cm, right 2.29 cm

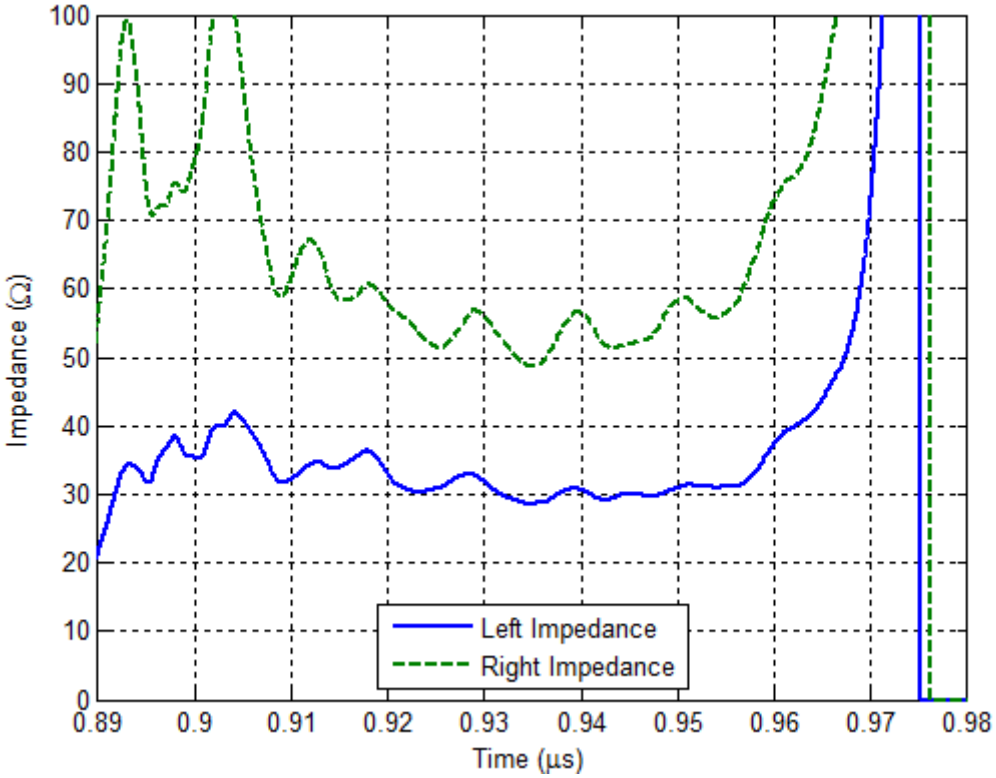

Figure 7.23—Impedance calculated from measurements of dual vircator load, left AK gap 1.50 cm, right 2.29 cm

Using the parallel load impedances and the voltage amplitude of the input pulse to the load, the voltage variability was determined to provide a metric to compare the frequency variability against. The output impedance of the high voltage transmission lines transferred to the secondary of the inductive voltage adder, assuming a 1:2 voltage step-up ratio, was 16.7 Ω. The reflection coefficient Γ at the interface between the inductive voltage adder output and the load is:

$$\Gamma = \frac{Z_L - Z_0}{Z_L + Z_0} \tag{7.4}$$

where Z_L is the equivalent load impedance of the parallel loads in Ω, and Z_0 is the output impedance of the high voltage transmission lines in Ω. The equivalent load impedance was calculated from the left and right branch impedances by:

$$Z_L = \frac{Z_{left} Z_{right}}{Z_{left} + Z_{right}} \tag{7.5}$$

where Z_{left} and Z_{right} are the left and right impedances in Ω, respectively. Using the reflection coefficient Γ at the load, the pulse amplitude delivered to the inductive voltage adder from the water PFL was calculated:

$$V_{in} = \frac{V_L}{1 + \Gamma} \tag{7.6}$$

where V_{in} is the input voltage into the load without reflections in volts and V_L is the load voltage in volts. Using these relationships, the mean voltage amplitude delivered to the load without reflections and the percent standard deviation of the input pulse voltage was determined. For all of the voltage pulses delivered to a load utilizing a vircator as a part of the load, the mean voltage pulse was 183 kV with a percent standard deviation of 11.07% at a switch electrode spacing of 3.5 mm and an oil pressure of 100 psi. After

accounting for the impedance mismatch at the load, the average input amplitude of all of the pulses into a matched load would be approximately 191 kV.

7.3 Vircator HPM Output

Aside from the input diagnostics measuring the voltage and current delivered to the vircators, the microwave signals created were also measured. Initially, the vircators were operated with rectangular waveguide loads, which were capped off with a brass plate. This was done to verify their operation and characterize the operational frequencies of the vircators. The vircators were first tested individually to disallow coupling effects between the vircators. The experimental results of the vircators' microwave outputs are presented in the following sections, including the results of the tests performed with single and dual vircator loads, frequency tunability, and microwave power output of the system.

7.3.1 Microwave Measurements

The microwave signals in the rectangular waveguide were measured with a commercial B-dot probe, specifically a Beehive 100B (small loop) B-dot probe, that was inserted in the side of the waveguide. The loop of the probe was located at the center of the waveguide, oriented so as to capture the H_x vector where the x-direction was the direction parallel to the long dimension of the waveguide. The B-dot probe was connected to a PE2209-20 directional coupler from Pasternack via a 50 foot long RG223 cable with SMA connectors. This directional coupler had a usable frequency range from 1 GHz to 4 GHz [9]. The directional coupler was used because it had a -20 dB output terminal that was connected to a Tektronix DPO70804 oscilloscope for measuring the

output signals from the B-dot probes. This oscilloscope had a bandwidth of 8 GHz and a sampling rate of 25 GS/s [10].

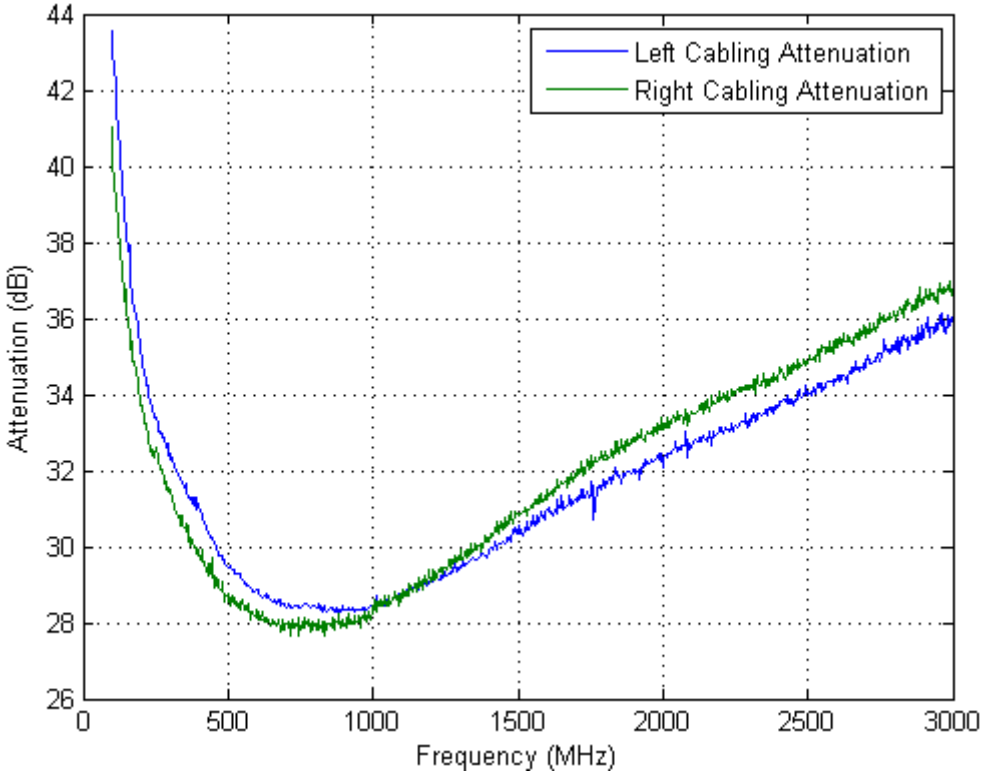

Figure 7.24—Measured diagnostic attenuation versus frequency

To account for the attenuation of the diagnostic cable and the directional coupler with respect to frequency in post-processing calculations, the attenuation of the diagnostic connections was measured. Figure 7.24 shows the combined attenuation of the coaxial cable and the directional coupler's -20 dB output terminal from 100 MHz to 3 GHz measured using an Agilent E5071C Network Analyzer. With the amplitude of the input signal, the attenuation of the cable and directional coupler, and the frequency of the signal known, the magnetic flux density and magnetic field intensity could be calculated. With these values, the power in the waveguide was calculated as discussed in Chapter 6.

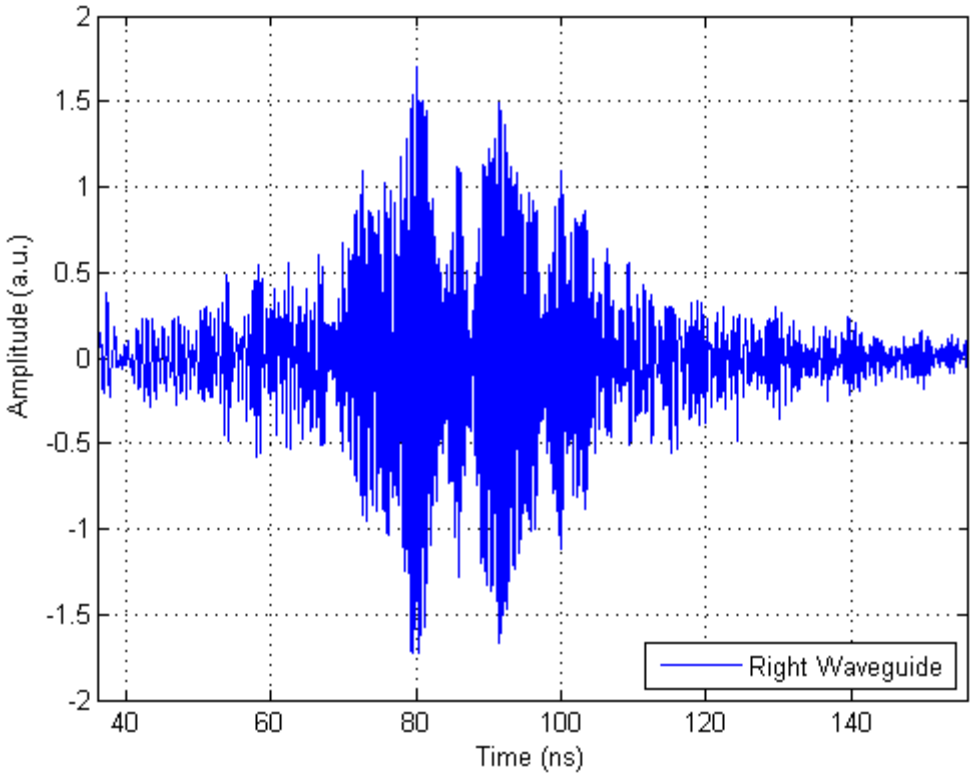

Figure 7.25—Example measured microwave pulse from right vircator, AK gap of 1.74 cm

An example microwave pulse recorded on the oscilloscope is shown in Figure 7.25. The vircator in this case was the right vircator with a gap spacing of 1.74 cm. The anode screen was stainless steel with an 84.6% transparency. The cathode emitter was black felt. The dominant frequency of the microwave signal was found by applying a fast Fourier transform (FFT) to the signal. The magnitude at each frequency in the frequency domain was corrected by accounting for the attenuation loss versus frequency in the diagnostic cabling system. The frequency response of the B-dot probe itself was also accounted for in order to determine the actual frequency that dominated the microwave signal. The corrected spectrum for the microwave pulse is shown in Figure 7.26. The corrected spectrum includes frequencies from 600 MHz, the cutoff of the waveguide, to 3.1 GHz, the upper limit of the calibrated range of the B-dot probe [11].

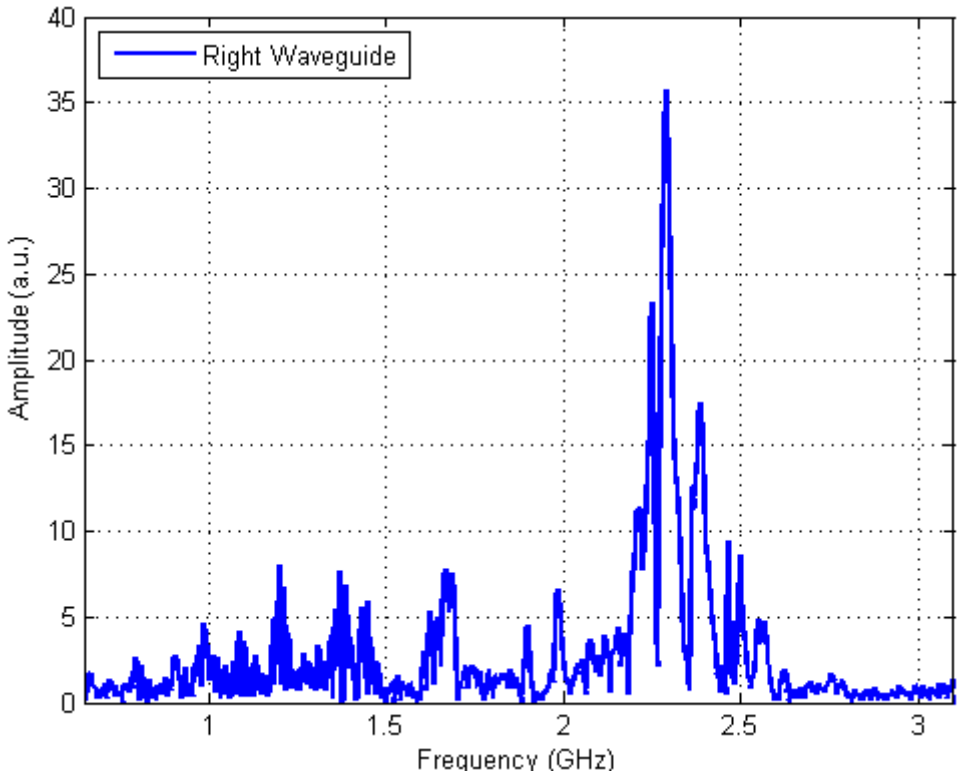

Figure 7.26—Example corrected microwave pulse spectrum of right vircator, AK gap of 1.74 cm

The MATLAB script also produced a spectrogram plot to observe the time-resolved frequency of the microwave signal. The spectrogram for this example microwave pulse is shown in Figure 7.27. The magnitude for each spectrum time step was normalized. The normalization took place after the magnitudes at each frequency were corrected by accounting for the diagnostic system attenuation and probe frequency response. The color represents the magnitude where dark blue is near zero and dark red is near a value of one. While the frequency content and microwave signal lasts much longer, the full-width half-max (FWHM) of this particular pulse was approximately 35 ns lasting from 70 ns to 105 ns as seen in Figure 7.25. In the spectrogram, this is the time range where the frequency content at approximately 2.3 GHz dominates.

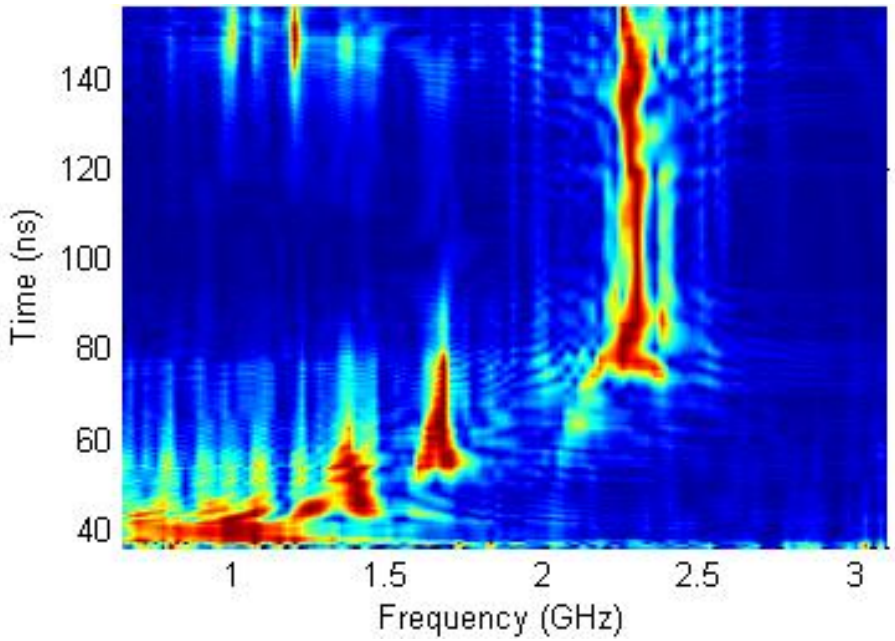

Figure 7.27—Example microwave pulse spectrogram of right vircator, AK gap of 1.74 cm

7.3.2 Single Vircator Operation

The vircators were initially tested individually to analyze the frequency and the output power as a function of the AK gap. Restricting operation to one vircator at a time avoided any influence of the other vircator on the frequency measurement. The results of dual vircator operation are analyzed separately and are discussed later in this chapter.

The anode was initially a stainless steel woven screen with a transparency of 51.7%. However, after firing two shots in this setup, no microwave signal was measured. An electron beam was being formed in this setup with a current exceeding the geometrical limit necessary for virtual cathode creation but no microwave signals were measured. The screen was then changed to a stainless steel woven screen with a transparency of 69.7%. The two screens can be seen in Figure 7.28 with the 69.7% transparent screen on the right. After this alteration, the system was tested again with successful microwave signal production. The anode screen was then changed to a

stainless steel woven screen with a transparency of 84.6% and a wire diameter of 0.1 mm (0.004 inches). This was done to increase the maximum power output from the vircator based upon the results of a linear relationship between the output power and screen transparency [12]. Microwave signals were then consistently seen for every successive pulse after this change was made.

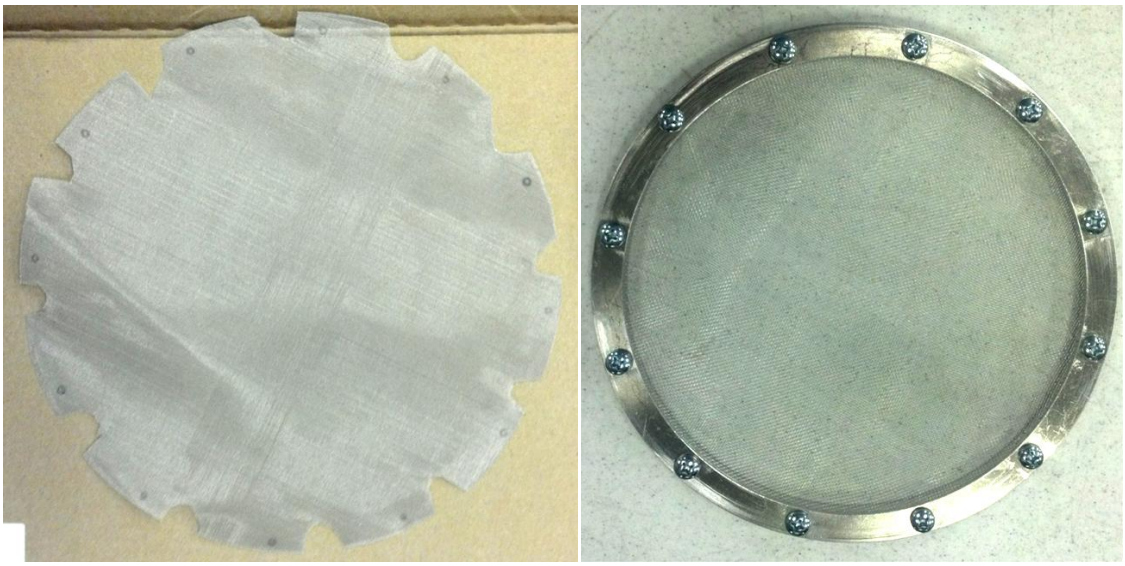

Figure 7.28—Two anode screens with transparencies of 51.7%, left, and 69.7%, right

Material degradation and outgassing is a major concern in vircators, especially when operated for sustained periods of repetitive pulse operation [13], [14], [15], [16], [17]. The vircators described here used a felt emitter to enhance the electric field at the tips of the fibers. The felt surface became noticeably faded after several pulses and this degradation was most discernable after smaller gap spacings were tested, since more current was emitted. An example of this cathode degradation is shown in Figure 7.29.

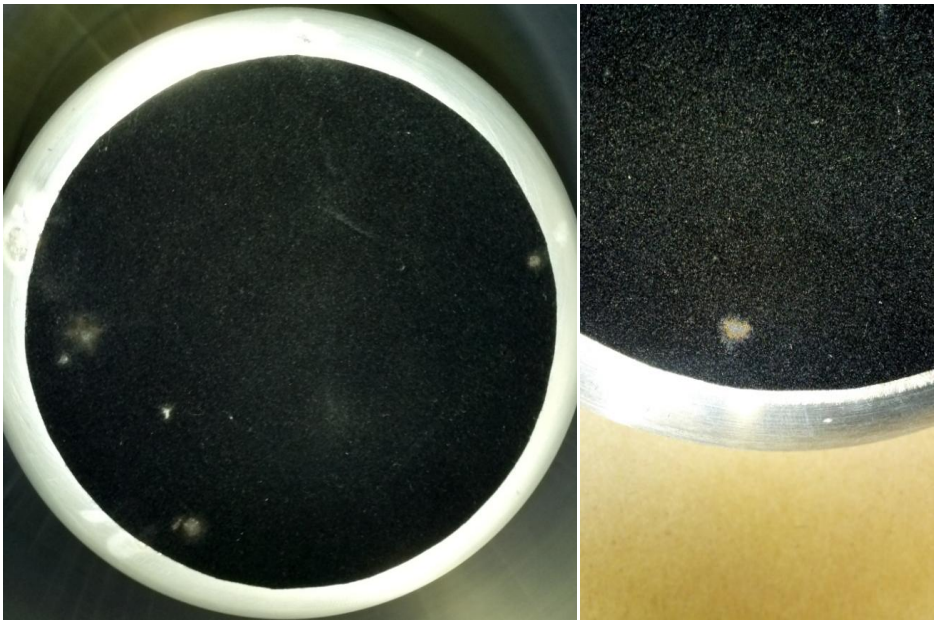

Figure 7.29—Cathode degradation evidence after 100 single-shot pulses

Each vircator was characterized by determining the dominant frequency of operation for a series of AK gaps. The peak microwave power at each of these AK gaps was also determined in the post-processing MATLAB routine. At each gap spacing, at least 10 microwave pulses were acquired. The dominant frequency was determined for each pulse after accounting for the probe's frequency dependence and system attenuation as discussed in Chapter 6. The mean frequency for each gap spacing was calculated along with the standard deviation of the dominant frequency. The results are plotted in the graphs for the right and left vircators in Figure 7.30 and Figure 7.31, respectively, with error bars depicting one standard deviation of the dominant frequency. These graphs show that the variability of the microwave frequency increased with gap spacing. It is unsure why this occurred, but it is thought to be the result of plasma nonuniformity on the cathode due to lower electric fields at these larger gap spacings. Nonetheless, the mean frequency was inversely proportional to the AK gap as expected.

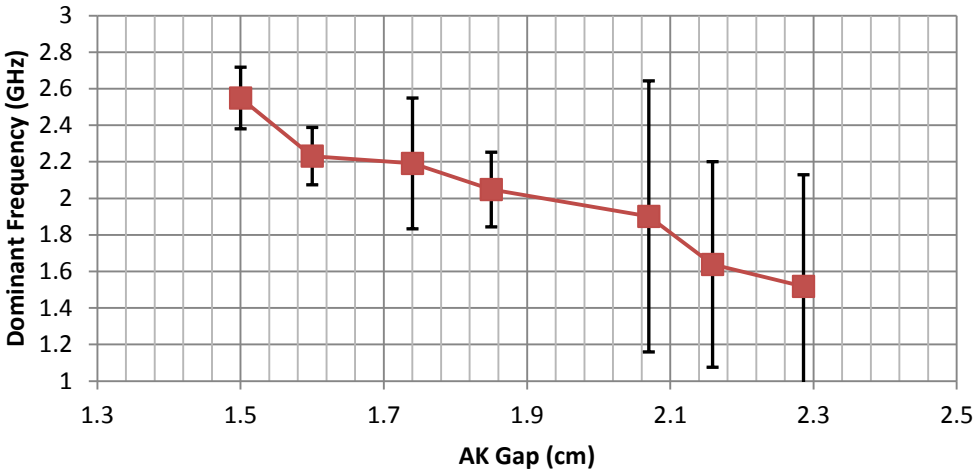

Figure 7.30—Measured dominant frequency over 10 pulses versus AK gap for right vircator

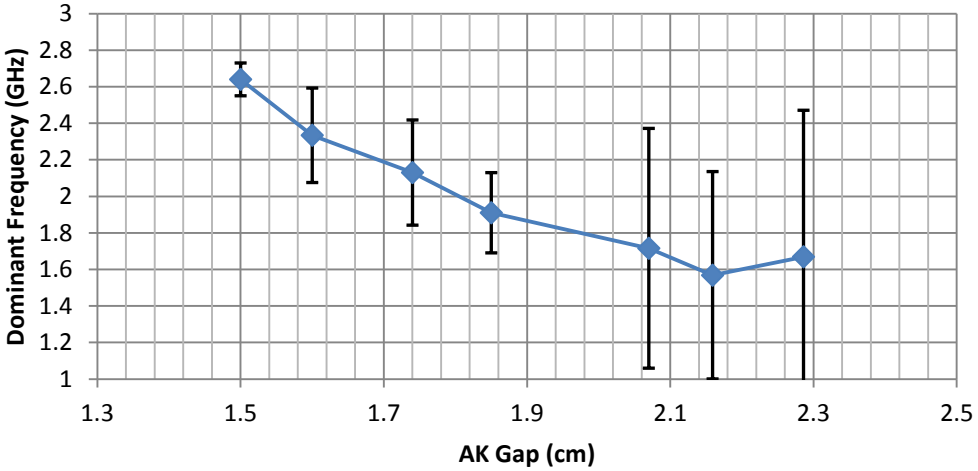

Figure 7.31—Measured dominant frequency over 10 pulses versus AK gap for left vircator

The peak power in the waveguide of the microwave signals at each gap spacing was also calculated using rectangular waveguide equations discussed in Chapter 6 [18], [19]. The peak power values for each gap spacing were averaged and the standard deviation was calculated. The results are plotted in the graphs for the right and left vircators in Figure 7.32 and Figure 7.33, respectively, with error bars depicting one standard deviation of the peak power. The mean peak power and the variability of the power increased with decreasing AK gaps. Both vircators showed a power increase at a gap spacing of 1.74 cm

relative to the power seen at 1.60 cm. The reasoning for this is not fully understood but it could be related to voltage variations from the pulsed power system or some sort of resonance effect in the vircator's design. Other reasons these two plots might differ is that the cathode and anode may have not been perfectly parallel in some cases.

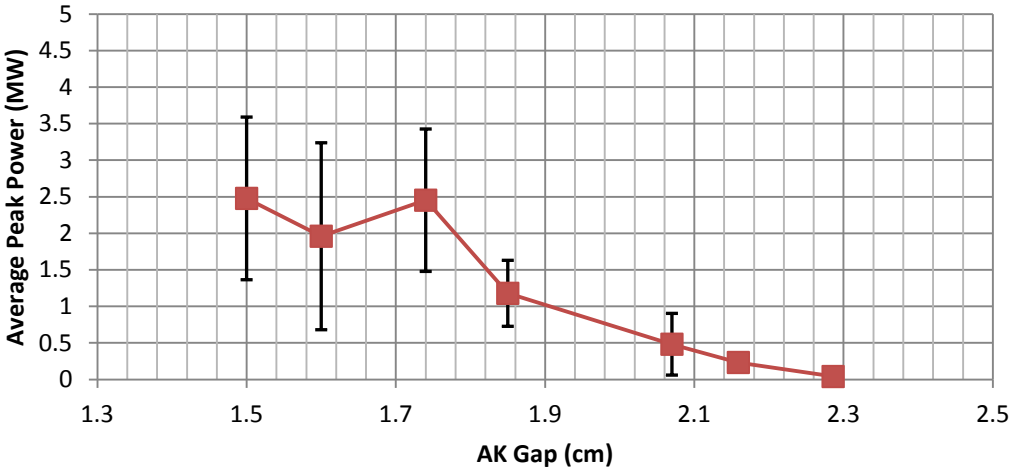

Figure 7.32—Measured peak power averaged over 10 pulses versus AK gap for right vircator

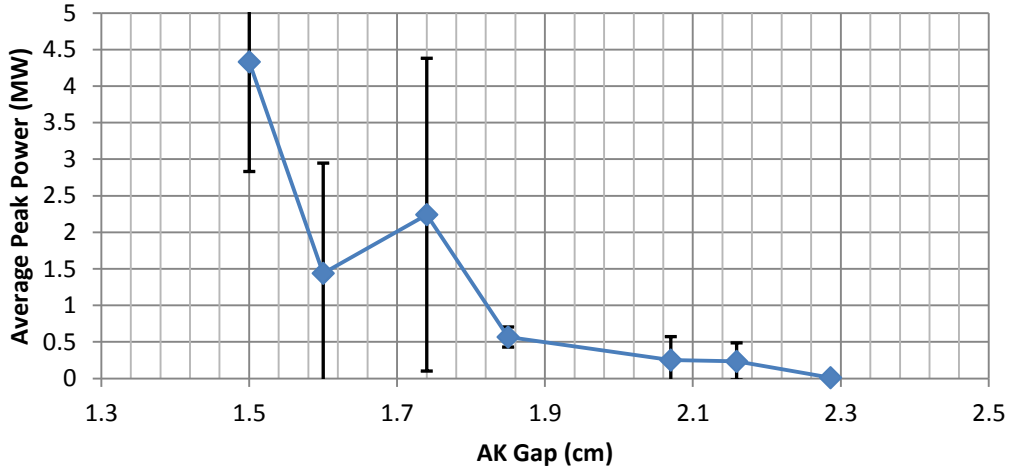

Figure 7.33—Measured peak power averaged over 10 pulses versus AK gap for left vircator

The previous plots show the peak power averaged over 10 microwave pulses. The peak powers measured for each AK gap during both single vircator and dual vircator testing are shown in Figure 7.34 for the right and left vircators. The peak powers in both

vircators were obtained at an AK gap of 1.5 cm with the peak power from the left vircator being 21.6 MW and from the right vircator being 17.25 MW. The maximum peak power efficiencies are shown in Figure 7.35 where the efficiency is the peak microwave power divided by the peak input power. The peak power efficiencies in both vircators were obtained at an AK gap of 1.5 cm with the peak efficiency from the left vircator being 1.58% and from the right vircator being 1.45%. These peak values were measured during dual vircator operation.

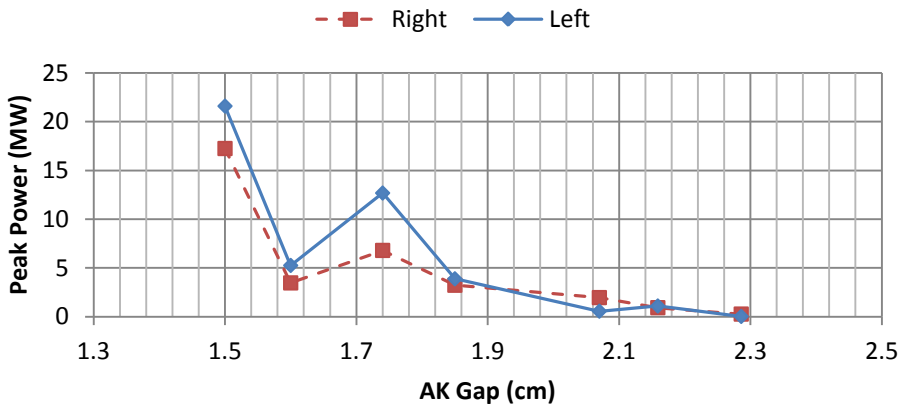

Figure 7.34—Maximum peak power measured versus AK gap for both vircators

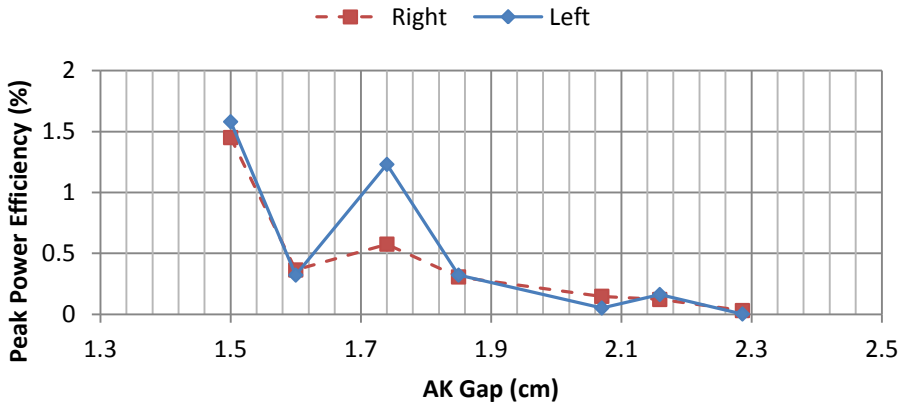

Figure 7.35—Maximum peak power efficiency measured versus AK gap for both vircators

The high voltage pulse generation system discussed in Chapter 3 inherently has a statistical variation in the output voltage pulse amplitude determined by the oil switch. In

the microwave signal analysis, the voltage difference between pulses was accounted for by using the relationship between the output frequency and voltage of $f \propto V^{1/2}$ [5], [20]. The frequencies were adjusted to correspond with a voltage of 200 kV. For example, for a pulse with a peak voltage of 185 kV, a correction factor of $\sqrt{\frac{200\ kV}{185\ kV}} = 1.04$ was multiplied by the measured dominant frequency. The corrected dominant frequencies are plotted versus the AK gap in Figure 7.36. In this graph, the dominant frequencies for the tested AK gaps of the right vircator are marked with red square markers and of the left vircator are marked with blue diamond markers. Both vircators operated at near the same frequency for a given AK gap, showing that the results were repeatable with the design of the vircators presented. The graph also shows an inverse relationship between the dominate frequency and the AK gap as expected.

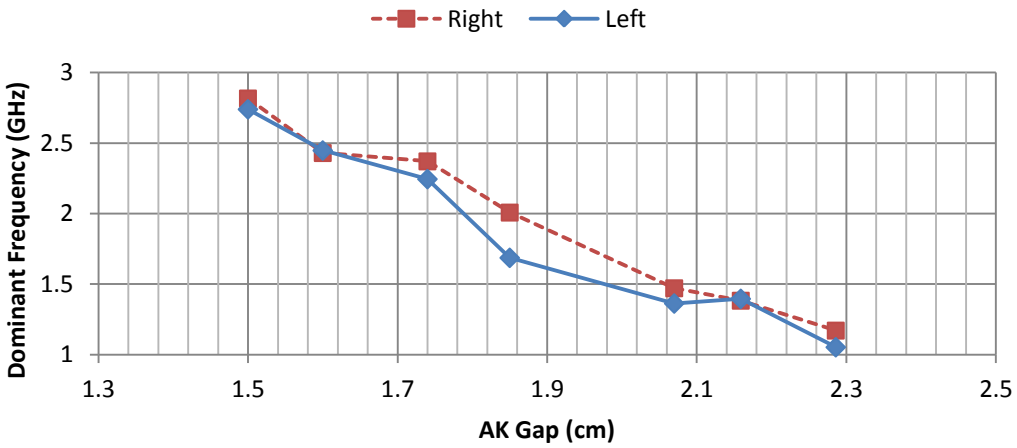

Figure 7.36—Corrected measured dominant frequency over 10 pulses versus AK gap for both vircators

The microwave output power versus the AK gap was also analyzed. The peak microwave power for all of the pulses for a particular gap spacing was averaged after accounting for the input power variability created by the driving voltage. The power variability was corrected by multiplying the measured power by a factor equal to the

square of the ratio of 200 kV to the measured minimum voltage for a given shot number. The corrected, averaged peak power for each gap spacing is shown in Figure 7.37. From this graph, the power output decreases as the AK gap increases. This is mostly due to the decreased current emitted in the electron beam at larger gap spacings. The power increase at 1.74 cm relative to the power at 1.60 cm is no longer seen, pointing to the conclusion that the voltage variation of the pulsed power system was the cause of this observation. The peak power would likely increase to an extent if the gap were decreased; this would also lead to a higher output frequency.

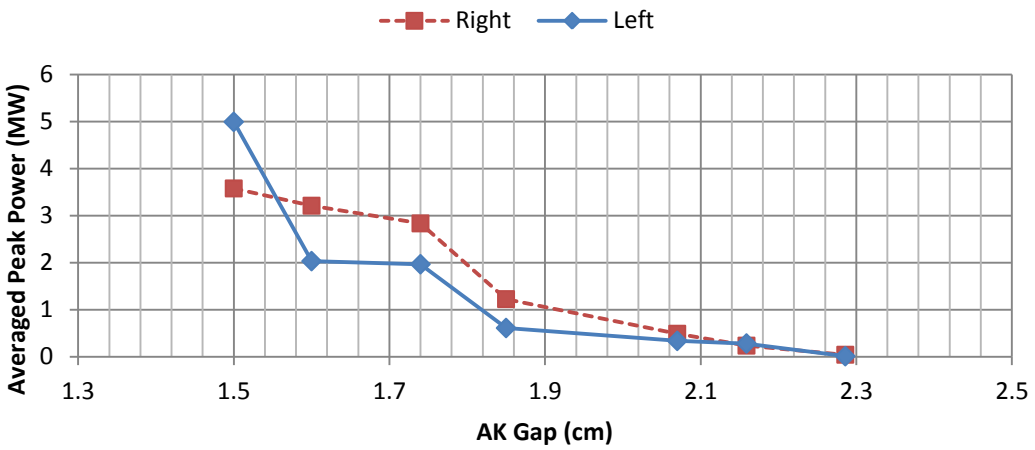

Figure 7.37—Corrected measured averaged peak output power over 10 pulses versus AK gap for both vircators

The peak power of the microwave signal was used to calculate the peak power efficiency of the system for each gap spacing by taking the ratio of the peak microwave power to the peak input power. The calculated efficiencies for each gap spacing are shown in Figure 7.38. For single vircator operation, the highest peak microwave power for the left vircator was 8.20 MW with an efficiency of 0.55% at an AK gap of 1.50 cm while the peak microwave power for the right vircator was 4.86 MW with an efficiency of 0.45% at an AK gap of 1.50 cm. The efficiency at 1.74 cm is higher than that at 1.60 cm, likely

because the mean voltage amplitude for the 1.60 cm series for both vircators was lower, leading to less emission, and thus, less microwave production. Nonetheless, the calculated efficiencies were on the same order as previous vircator research for radial extraction (~0.5%) [5]. In most cases, the diode voltage used in vircator experiments is typically higher than 200 kV making direct comparison difficult. Nonetheless, the measured efficiencies lie within reason when comparing the efficiencies to efficiencies reported in other published results with best case efficiencies lying between 1-2%. In the results described in this report, the peak efficiency measured on the left vircator was 1.58% and on the right vircator was 1.45%.

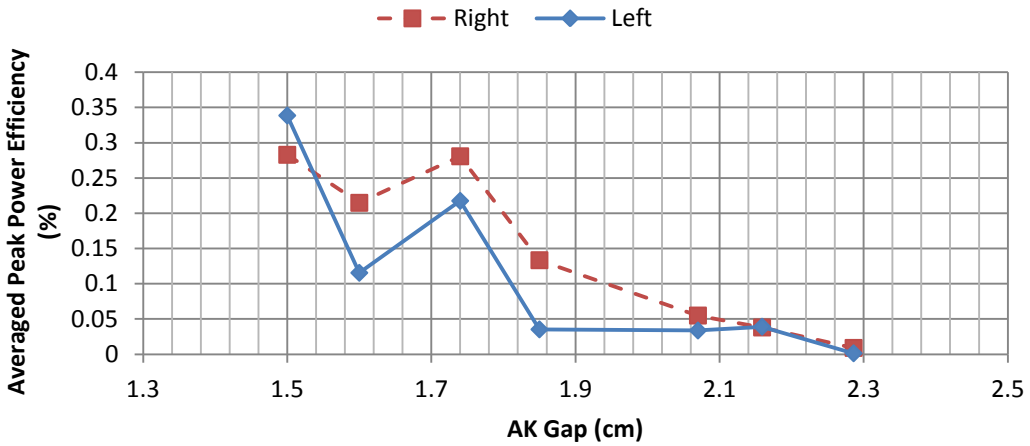

Figure 7.38—Averaged peak power efficiency over 10 pulses versus AK gap for both vircators

Another finding during the testing of the individual vircators was a frequency dependence on the position of the plunger in the drift tube section. The plunger was an aluminum plate with a diameter of 8 inches. The plunger was electrically connected to the system ground and was in place to act as a device to tune the drift tube cavity. The frequency dependence was particularly noticeable for larger gaps where lower frequencies should have been seen in the output signals. An example of this frequency

dependence can be seen in Figure 7.39, showing the spectra for an AK gap of 2.16 cm and two different plunger positions for the left vircator. In the figure, the dashed-green trace represents a plunger position of approximately 9.9 cm from the anode screen, and the solid-blue trace represents a plunger position of approximately 20 cm from the anode screen. The reasons for this discrepancy are that the resonance of the cavity affects the frequency and the short plunger position likely absorbed some of the emitted electrons that had passed through the anode screen, altering the virtual cathode oscillations.

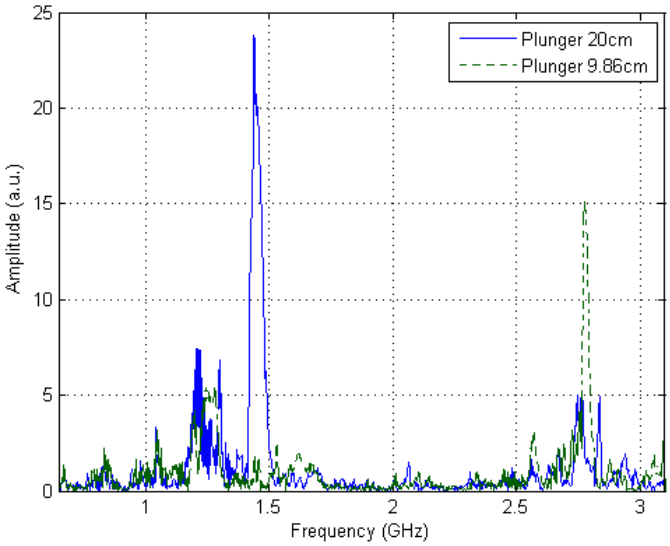

Figure 7.39—Spectra of two pulses with differing plunger positions at 2.16 cm AK gap

7.3.3 Dual Vircator Operation Results

After the vircators were characterized individually, they were connected in parallel. The reason for using two vircators in parallel was to have a combined microwave signal that was made up of two distinct frequencies. The operation of the vircators needed to show, then, that the frequencies of the two vircators were not only consistent with those obtained in the individual vircator tests, but that the frequencies of each could be tuned independently of the other. The first experiment was performed with both vircators having an AK gap of 1.74 cm with the plungers positioned 14.6 cm from

the anode screen. From the individual vircator tests, the dominant frequency of the high power microwave signals should be around 2.2 GHz, varying with the input voltage amplitude. The spectra from a single pulse with this dual vircator setup is shown in Figure 7.40 with both having a peak at approximately 2.3 GHz.

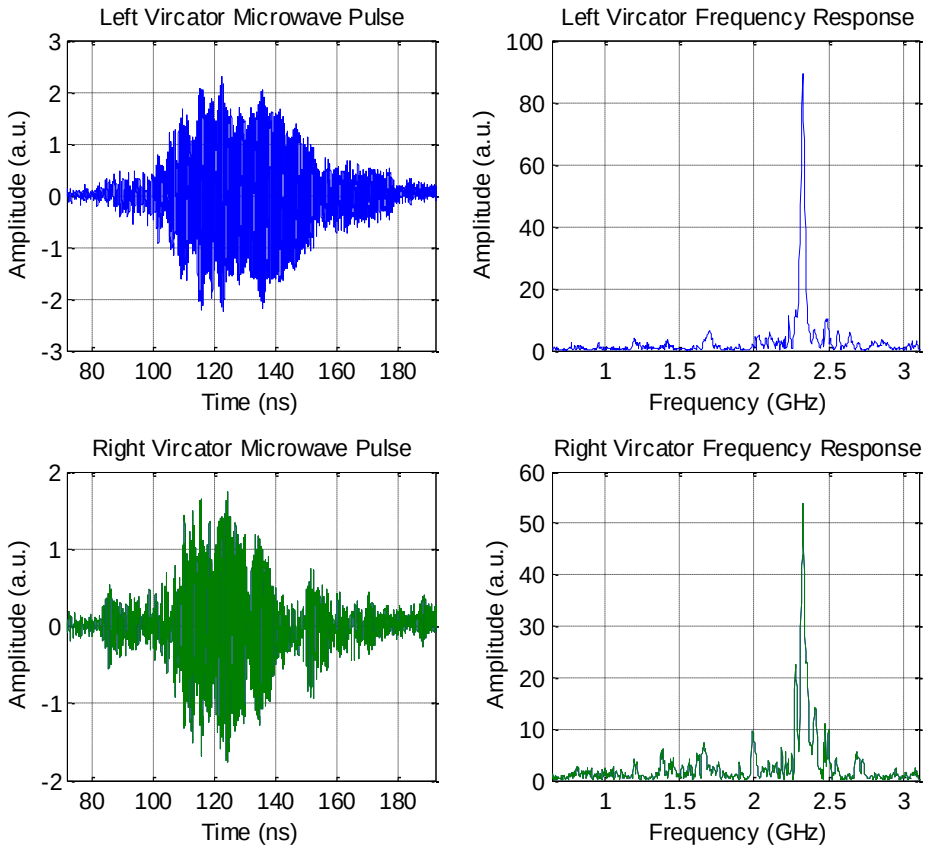

Figure 7.40—Microwave pulses and spectra for dual vircator load, AK gap 1.74 cm on left vircator, AK gap 1.74 cm on right vircator

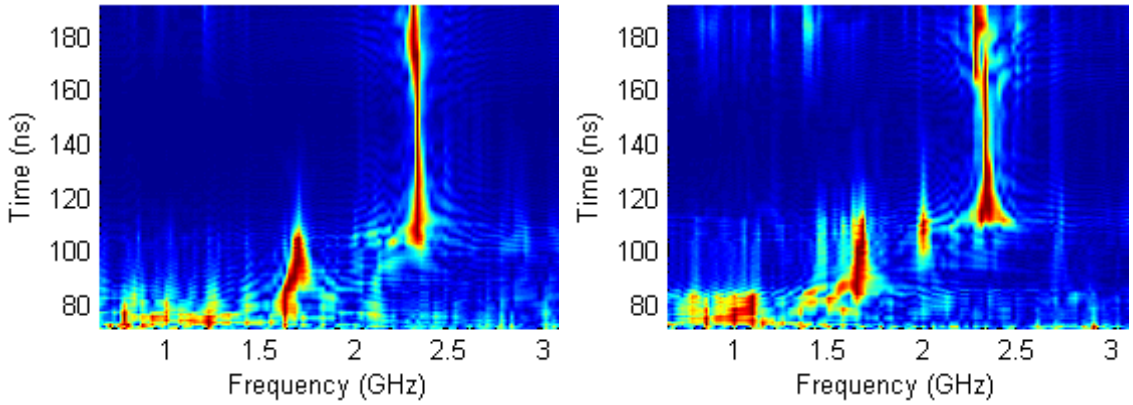

Figure 7.41—Microwave spectrogram for dual vircator load, AK gap 1.74 cm on left vircator, AK gap 1.74 cm on right vircator

In this case, the power output in the right vircator was lower than in the left, but the dominant frequencies were very nearly identical. The power output discrepancy could have many explanations including one cathode emitting in a different way than the other, e.g. more uniformly or earlier caused by one cathode being more conditioned than the other. These differing emission characteristics might be supported by the spectrogram plots shown in Figure 7.41. Both plots are on the same scale, and it is shown that the right vircator reached its dominant frequency of 2.3 GHz at a slightly later time than the left vircator. The peak power levels for the left and right vircator were 4.55 MW and 3.24 MW, respectively, for this pulse.

After testing the vircators at the same gap to verify that the vircators would operate in parallel, the vircators were tested with staggered AK gaps to fully verify the frequency tunability that was seen in the individual vircator experimental results. A multitude of AK gap combinations were explored and the results are shown in Figure 7.42 through Figure 7.55. The parameters and results of each combination are discussed in the following.

In all proceeding spectrogram plots, the spectrogram of the left vircator is shown on the left with the right vircator's shown on the right. Figure 7.42 and Figure 7.43 show the spectra and spectrograms, respectively, for the dual vircator setup with the left vircator having an AK gap of 1.74 cm and a plunger position of 14.6 cm from the anode screen while the right vircator had an AK gap of 2.16 cm and a plunger position of 29.4 cm from the anode screen. The expected dominant frequencies were 2.3 GHz and 1.4 GHz for the left and right vircators, respectively. The magnitudes differ greatly, but this is expected as the output power was shown to decrease with the AK gap in Figure

7.37. From the microwave pulse, the microwave pulse frequency is detectable from about 90 ns to 175 ns. The reason that the microwave pulse seemed to be detectable for a longer period of time than the driving voltage pulse, which was 70 ns, was likely the result of attenuated reflections. The peak power levels for the left and right vircator were 4.59 MW and 0.92 MW, respectively, for this pulse.

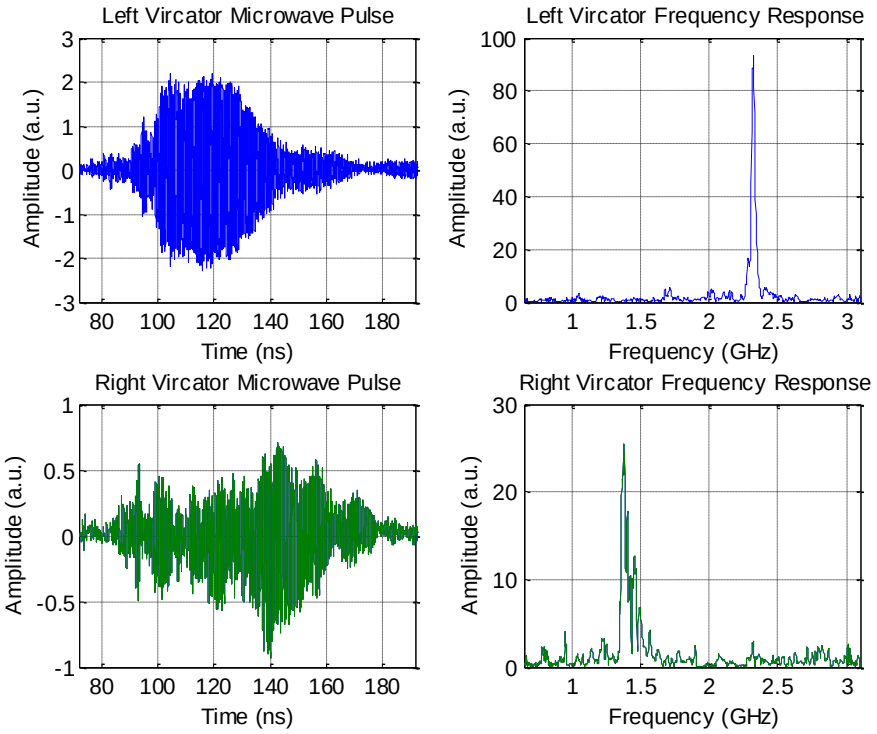

Figure 7.42—Microwave pulses and spectra for dual vircator load, AK gap 1.74 cm on left vircator, AK gap 2.16 cm on right vircator

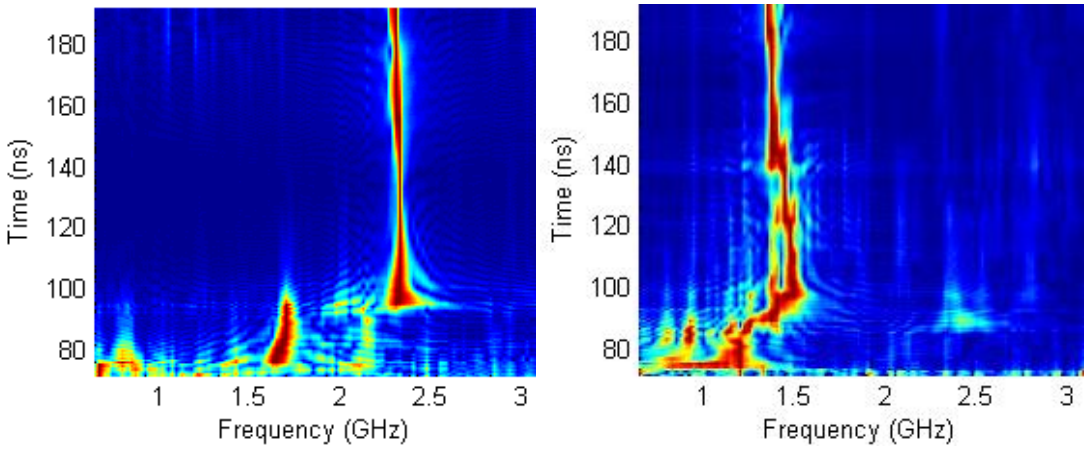

Figure 7.43—Microwave spectrogram for dual vircator load, AK gap 1.74 cm on left vircator, AK gap 2.16 cm on right vircator

Figure 7.44 and Figure 7.45 show the spectra and spectrograms, respectively, for the dual vircator setup with the left vircator having an AK gap of 2.16 cm and a plunger position of 29.4 cm from the anode screen while the right vircator had an AK gap of 1.74 cm and a plunger position of 14.6 cm from the anode screen. The peak power levels for the left and right vircator were 1.09 MW and 2.89 MW, respectively, for this pulse.

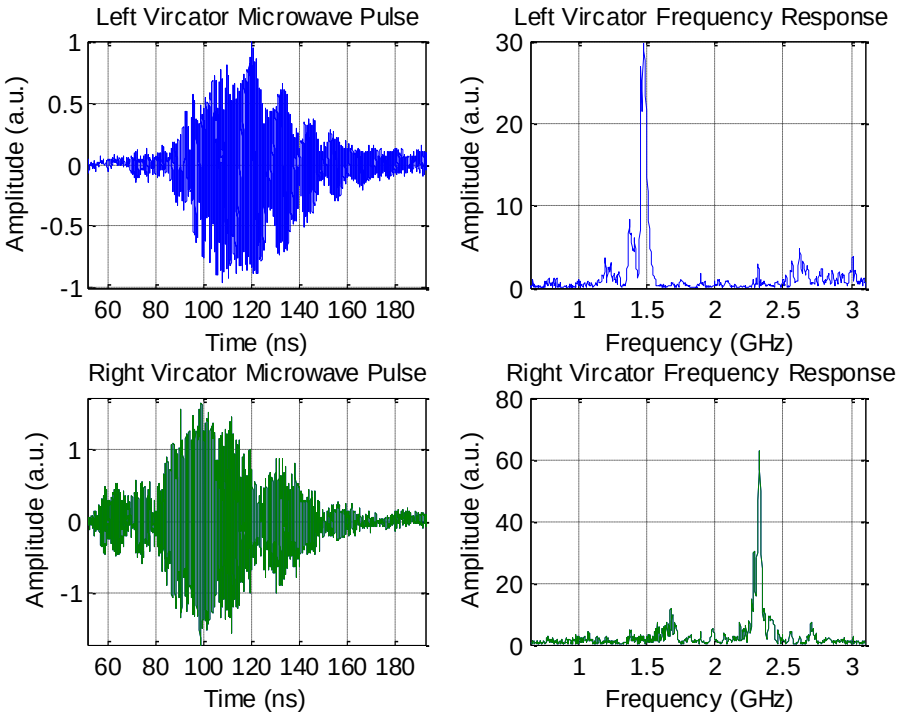

Figure 7.44—Microwave pulses and spectra for dual vircator load, AK gap 2.16 cm on left vircator, AK gap 1.74 cm on right vircator

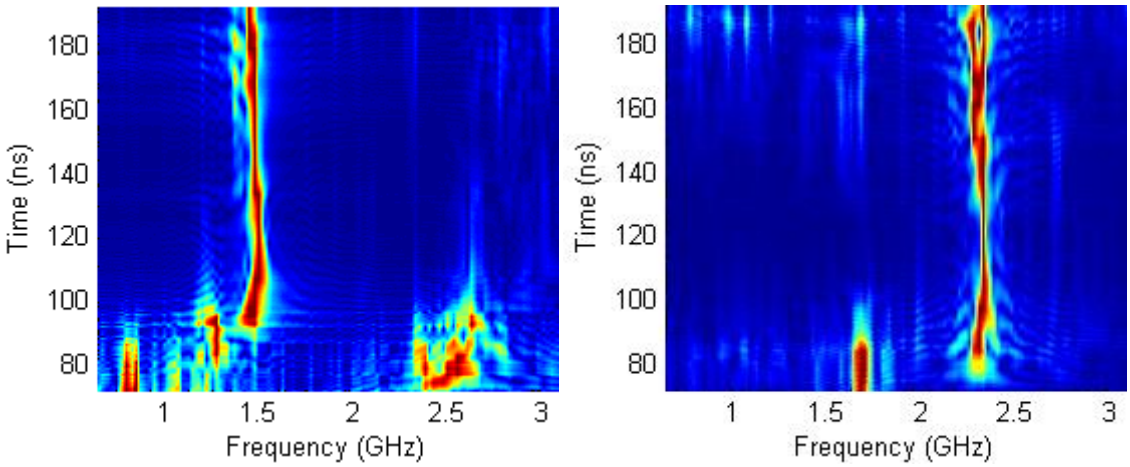

Figure 7.45—Microwave spectrogram for dual vircator load, AK gap 2.16 cm on left vircator, AK gap 1.74 cm on right vircator

Figure 7.46 and Figure 7.47 show the spectra and spectrograms, respectively, for the dual vircator setup with the left vircator having an AK gap of 1.50 cm and a plunger position of 13.3 cm from the anode screen while the right vircator had an AK gap of 1.85 cm and a plunger position of 14.6 cm from the anode screen. The left vircator produced a signal higher than expected and exceeded the limits of the oscilloscope. The peak power levels for the left and right vircator were 13.05 MW and 3.22 MW, respectively, for this pulse.

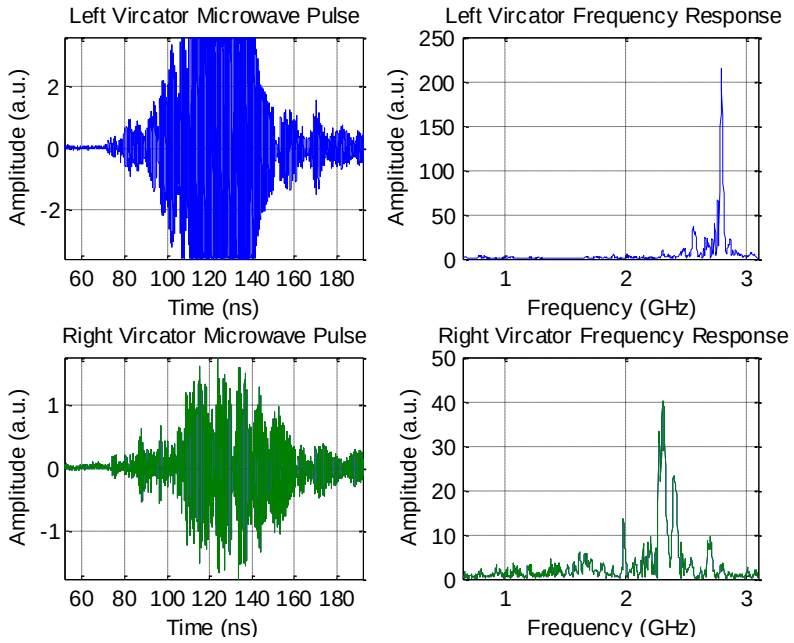

Figure 7.46—Microwave pulses and spectra for dual vircator load, AK gap 1.50 cm on left vircator, AK gap 1.85 cm on right vircator

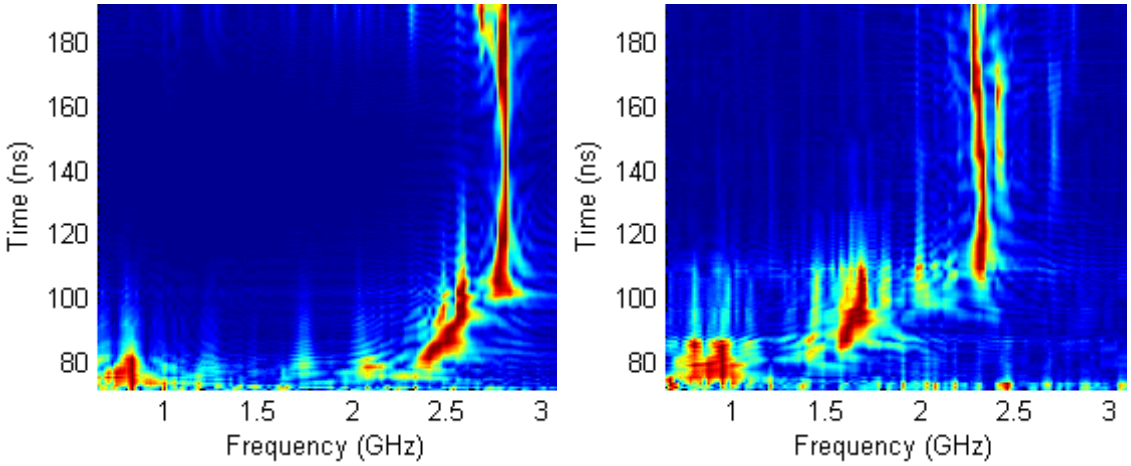

Figure 7.47—Microwave spectrogram for dual vircator load, AK gap 1.50 cm on left vircator, AK gap 1.85 cm on right vircator

Figure 7.48 and Figure 7.49 show the spectra and spectrograms, respectively, for the dual vircator setup with the left vircator having an AK gap of 1.50 cm and a plunger position of 13.3 cm from the anode screen while the right vircator had an AK gap of 2.29 cm and a plunger position of 29.4 cm from the anode screen. The peak power levels for the left and right vircator were 21.60 MW and 0.26 MW, respectively, for this pulse.

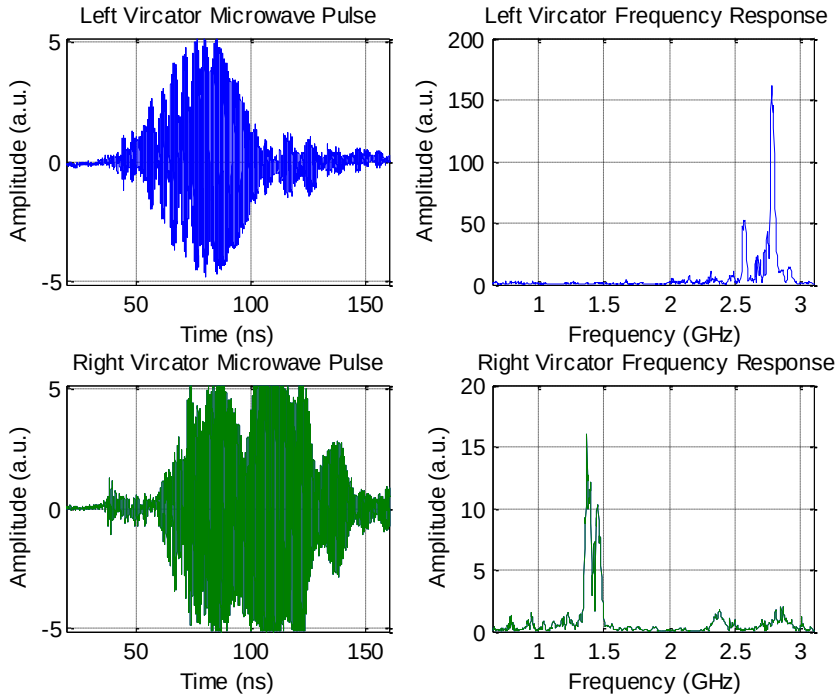

Figure 7.48—Microwave pulses and spectra for dual vircator load, AK gap 1.50 cm on left vircator, AK gap 2.29 cm on right vircator

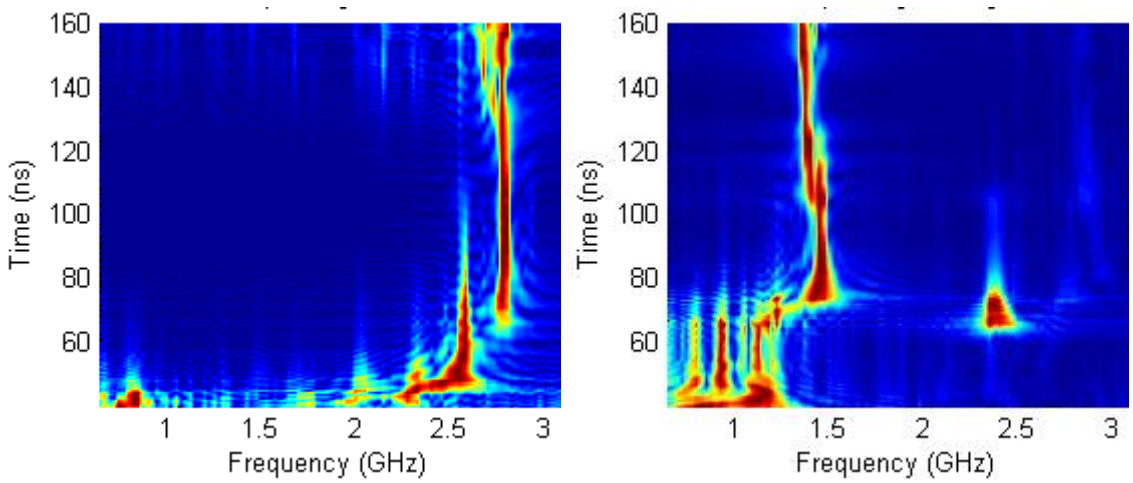

Figure 7.49—Microwave spectrogram for dual vircator load, AK gap 1.50 cm on left vircator, AK gap 2.29 cm on right vircator

Figure 7.50 and Figure 7.51 show the spectra and spectrograms, respectively, for the dual vircator setup with the left vircator having an AK gap of 1.85 cm and a plunger position of 14.6 cm from the anode screen while the right vircator had an AK gap of 1.74 cm and a plunger position of 14.6 cm from the anode screen. The peak power levels for the left and right vircator were 3.06 MW and 4.17 MW, respectively, for this pulse.

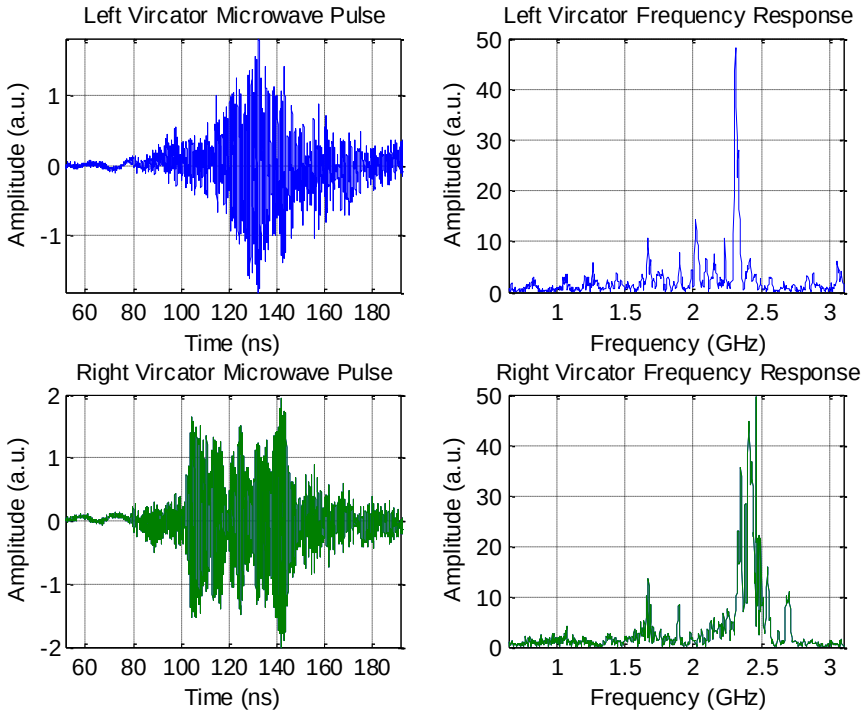

Figure 7.50—Microwave pulses spectra for dual vircator load, AK gap 1.85 cm on left vircator, AK gap 1.74 cm on right vircator

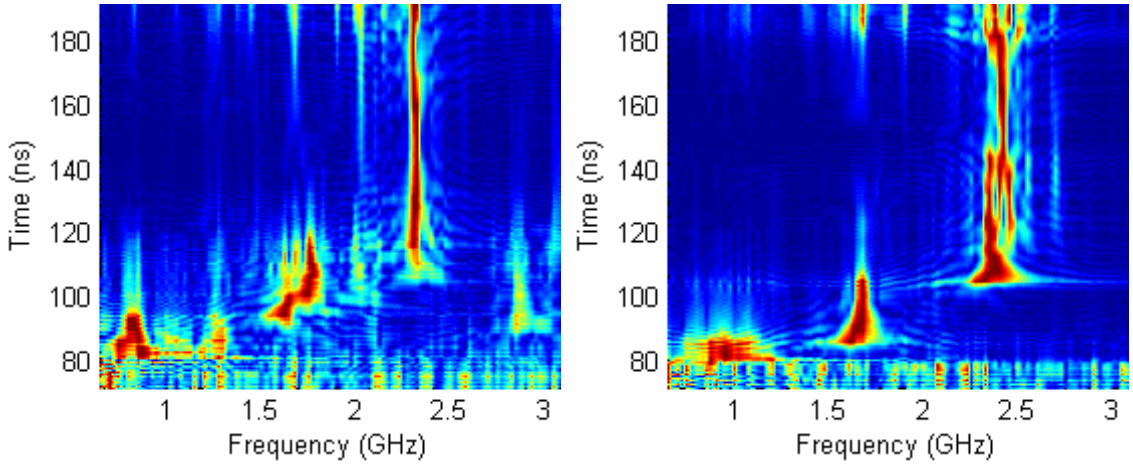

Figure 7.51—Microwave spectrogram for dual vircator load, AK gap 1.85 cm on left vircator, AK gap 1.74 cm on right vircator

Figure 7.52 and Figure 7.53 show the spectra and spectrograms, respectively, for the dual vircator setup with the left vircator having an AK gap of 1.60 cm and a plunger position of 14.6 cm from the anode screen while the right vircator had an AK gap of 1.74 cm and a plunger position of 14.6 cm from the anode screen. The peak power levels for the left and right vircator were 2.02 MW and 0.92 MW, respectively, for this pulse.

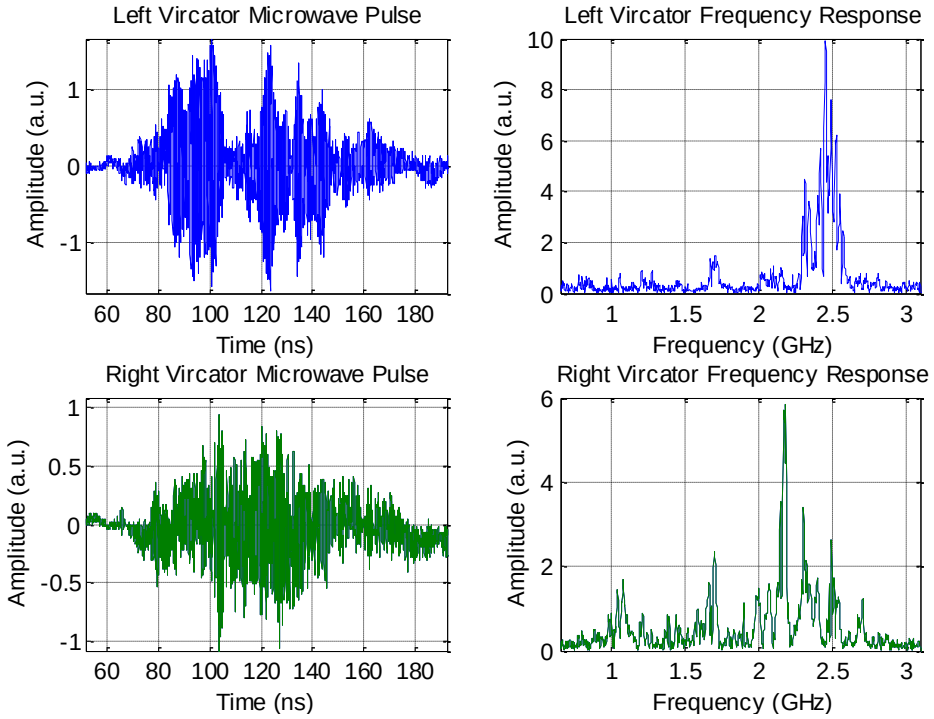

Figure 7.52—Microwave pulses and spectra for dual vircator load, AK gap 1.60 cm on left vircator, AK gap 1.74 cm on right vircator

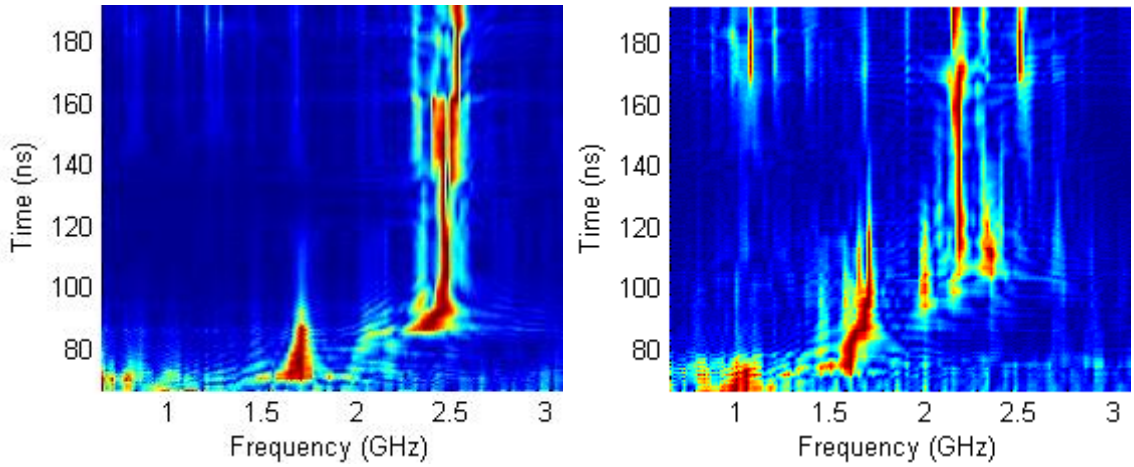

Figure 7.53—Microwave spectrogram for dual vircator load, AK gap 1.60 cm on left vircator, AK gap 1.74 cm on right vircator

Figure 7.54 and Figure 7.55 show the spectra and spectrograms, respectively, for the dual vircator setup with the left vircator having an AK gap of 1.74 cm and a plunger position of 14.6 cm from the anode screen while the right vircator had an AK gap of 1.50 cm and a plunger position of 14.6 cm from the anode screen. The peak power levels for the left and right vircator were 2.75 MW and 11.55 MW, respectively, for this pulse.

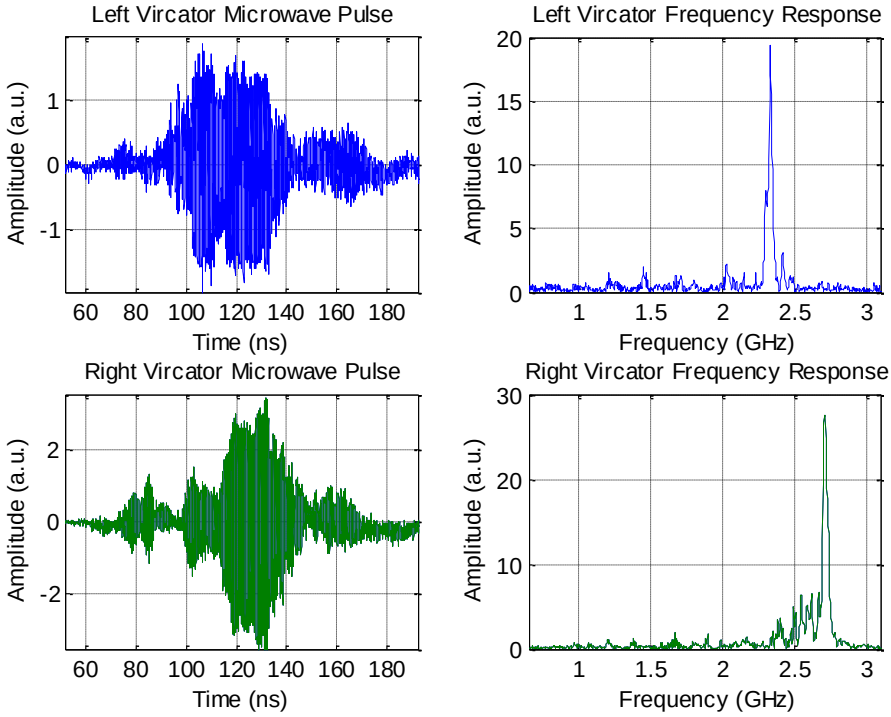

Figure 7.54—Microwave pulses and spectra for dual vircator load, AK gap 1.74 cm on left vircator, AK gap 1.50 cm on right vircator

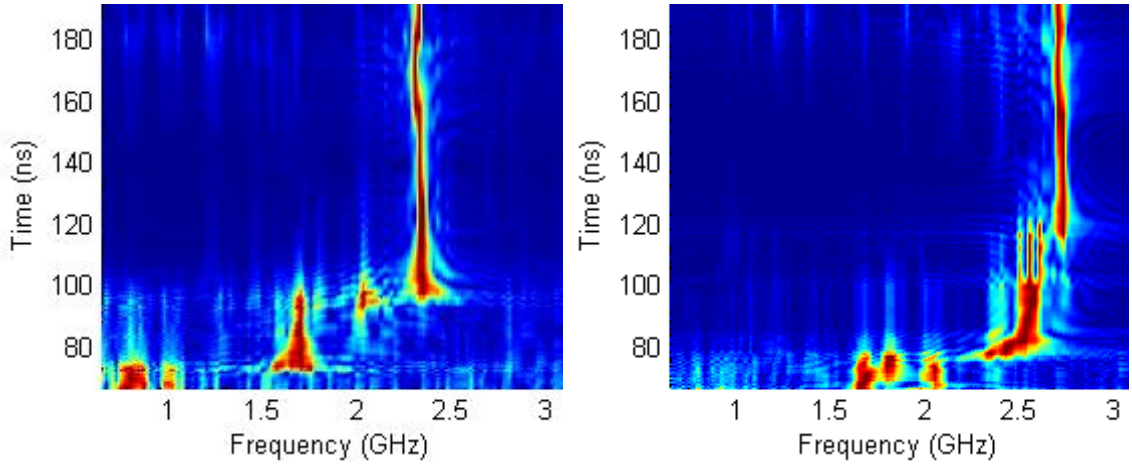

Figure 7.55—Microwave spectrogram for dual vircator load, AK gap 1.74 cm on left vircator, AK gap 1.50 cm on right vircator

From all of the results shown in the spectra and spectrograms, it is clear that the vircators are independently tunable and show similar characteristics to the results found during single vircator testing. Some discrepancies do exist between vircators. The most significant difference between the two is a result of emission onset and microwave frequency settling. This is most prevalent in the spectrogram plots where, in most cases, it is clear that one vircator stabilizes at a particular frequency before the other, although it is not the same vircator in every case. There are also instances where the spectrogram plots reveal that the microwave energy is not necessarily isolated at one single frequency but is distributed among a multitude of frequencies. This varies from pulse to pulse, pointing to a variation in electron emission from pulse to pulse. However, the spectrogram plots show that the microwave frequency is quite stable after the voltage and current waveforms reach their peak values. The dominant frequencies seen in dual vircator operation coincide with those found during individual vircator operation.

The effect of dual vircator operation on the peak microwave output power was also analyzed. In the single vircator experiments, the vircators were placed in parallel with a water resistor whose impedance was constant for all tests. Because of this, the equivalent impedance was fully dependent on the AK gap for the single vircator. The resistors used in these tests were on the order of 33 Ω, which, from Figure 7.17 and Figure 7.18, corresponds to an AK gap of about 1.50 cm or 1.60 cm. Due to this, the equivalent impedance of the water resistor and the single vircator at the smaller gap spacings would be much lower than the equivalent impedance for dual vircators operating with simultaneous gaps differing by a large margin, e.g. a 1.50 cm gap in combination with a 2.29 cm gap. This increased impedance for staggered AK gaps in a dual vircator

load would then increase the voltage seen at the AK gap due to the impedance mismatch. For example, in the case that one vircator's AK gap was 1.50 cm and the other was 1.74 cm, the average peak voltage of the input pulse was 182 kV. The vircator with the 1.50 cm AK gap outputs an average microwave peak power of 7.34 MW and an average peak power efficiency of 0.832%. When the AK gap combination is changed to 1.50 cm and 2.29 cm, the average peak voltage of the input pulse was 192 kV. The average microwave peak power for the vircator with the 1.50 cm AK gap was 13.57 MW with an average peak power efficiency of 1.15%. From this relationship, it is not surprising that the peak microwave power was measured with the latter AK gap combination (1.50 cm and 2.29 cm, the smallest and largest gap spacings tested). This peak microwave power was measured to be approximately 21.60 MW with a peak power efficiency of 1.58%.

The microwave signals produced by the vircators were carried by microwave waveguides to an anechoic chamber. Connected to the waveguides were pyramidal aperture horn antennas used to produce a directional beam of microwave radiation at a target position in the chamber. At this target position, an electric field probe (100D stub probe from Beehive Electronics) was mounted to measure the electric field intensity. An example output pulse is shown in Figure 7.56. The left vircator had an AK gap of 1.74 cm, and the measured peak power of the signal in the waveguide was 3.22 MW. The right vircator had an AK gap of 1.50 cm, and the measured peak power of the signal in the waveguide was 9.44 MW. The FWHM of the microwave pulse measured in the anechoic chamber was approximately 70 ns. This pulse width was slightly larger than that seen in each vircator's microwave pulse. This was likely due to a time discrepancy between the times that the independent pulses reached the target position. This time

discrepancy was created by the differing overall lengths in the microwave waveguides. The right waveguide has an overall length of approximately 7.23 m, and the left waveguide has an overall length of approximately 10.19 m, both measured along the waveguide at the center point of the waveguide cross section. Assuming that the microwave frequency is high enough above the cutoff frequency, the propagation velocity in the waveguide is near the speed of light. This would mean that the right horn antenna would receive its microwave signal approximately 9.87 ns before the left horn would. If both microwave pulses are equal in pulse width, this would cause an overall pulse width extension of nearly 20 ns. The microwave signals measured at the microwave source typically had pulse widths around 50 ns, which would correspond to the 70 ns overall pulse width seen in Figure 7.56. This would also mean that the two microwave pulses are seen simultaneously for approximately 40 ns. The spectrograms for the left and right vircator outputs are shown in Figure 7.57.

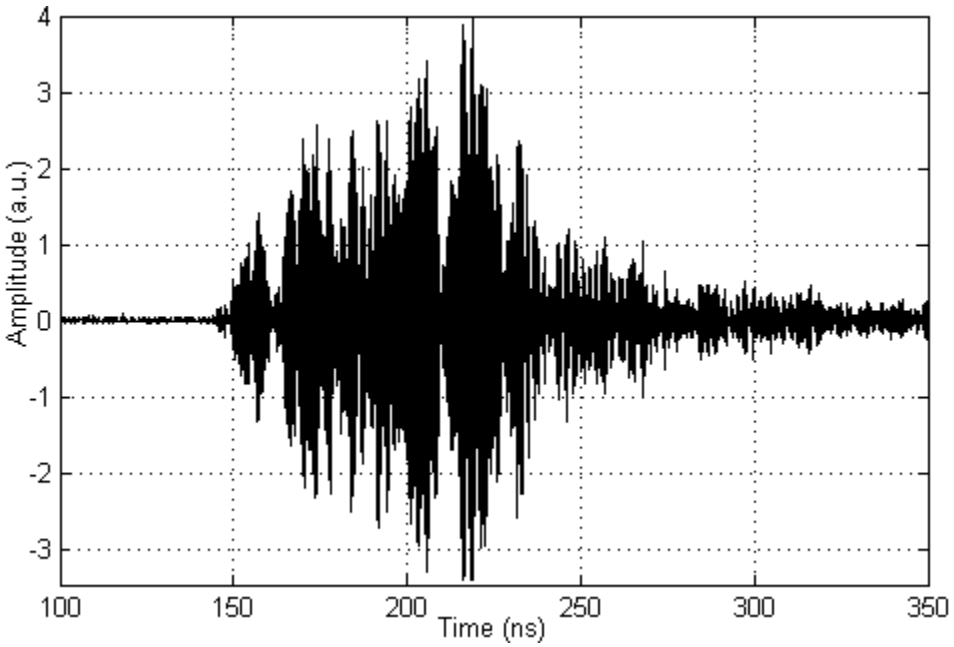

Figure 7.56—Combined microwave pulse measured in anechoic chamber for AK gap spacings for the left vircator of 1.74 cm, and for the right of 1.50 cm

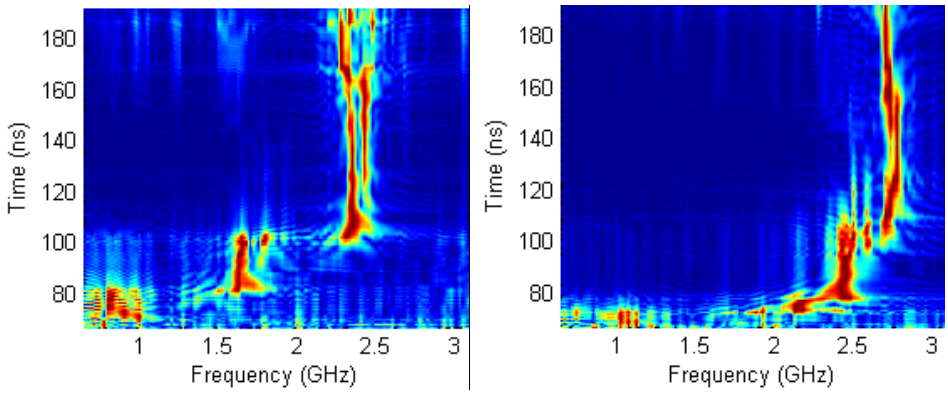

Figure 7.57—Normalized microwave spectrogram for AK gap spacings for the left vircator of 1.74 cm, and for the right of 1.50 cm

The left vircator settles at two frequencies of approximately 2.35 GHz and 2.42 GHz with 2.35 GHz having the larger amplitude, and the right settles at a frequency of approximately 2.78 GHz. From this then, the microwave signal measured in the chamber should contain the same frequency content. The normalized spectrogram of the combined microwave signal measured in the anechoic chamber is shown in Figure 7.58. In this figure, the amplitude is plotted as a normalized linear value from 0 to 1. It would almost see as though the signal was hopping back and forth between two frequencies, but this is just an effect of the normalized scaling. It is clear that two frequencies existed simultaneously at the frequencies of 2.35 GHz and 2.78 GHz. The peak electric field measured for this pulse was found to be approximately 9 kV/m at a distance of 6 m.

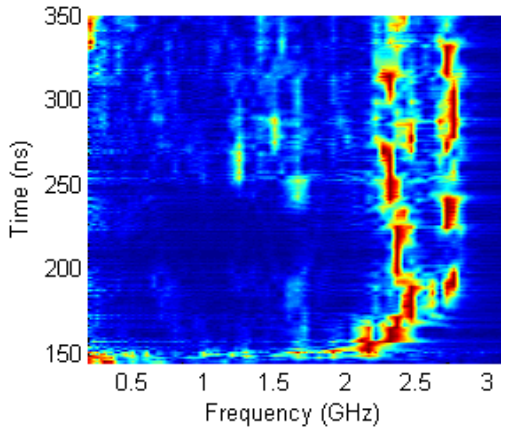

Figure 7.58—Normalized microwave spectrogram of signal measured in anechoic chamber, linear amplitude on the left, logarithmic amplitude on the right

7.3.4 Waveguide Attenuation Measurements

Previously mentioned power measurements were acquired near the microwave source. The B-dot probes used to measure this output power were placed at a distance of approximately seven feet from the microwave source in the waveguide. In order to determine the attenuation of the microwave signal caused by the bends and length of the two waveguides, B-dot probes were also placed at a distance of approximately one foot before the point where the waveguides delivered the microwave signals to the horn antennas inside the anechoic chamber. These waveguides and their connection to the anechoic chamber are shown in Figure 7.59.

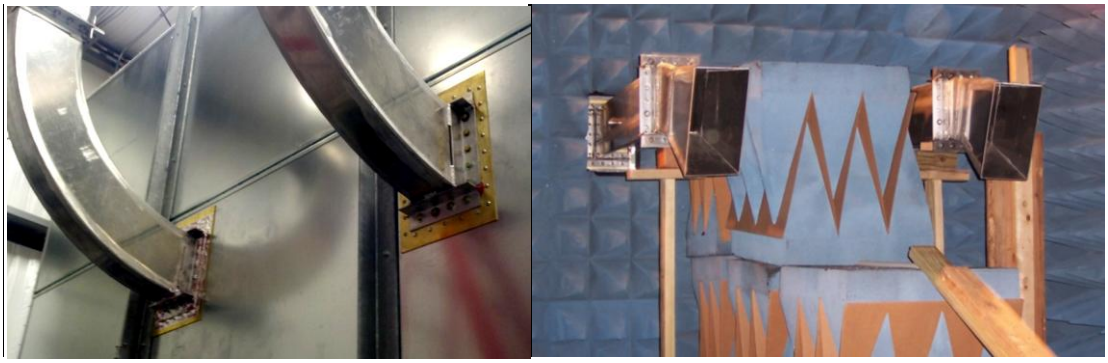

Figure 7.59—Waveguides carrying microwave signal to horn antennas inside anechoic chamber

To measure the attenuation, the B-dot probes both near the microwave source and near the horn antenna output were used to capture the microwave signals for five microwave pulses. The peak powers at the microwave source and at the horn antenna were calculated using the same technique discussed in Chapter 6. The ratio of these peak powers allowed for the calculation of the dB difference, or attenuation, caused by the waveguides. This same process was performed across a wide frequency range by varying the AK gap on both vircators. This allows for the calculation of the attenuation at various frequencies. To form a curve, the attenuation was interpolated from point to point.

These attenuation curves for both waveguides is shown in Figure 7.60. Both waveguides vary in attenuation across this frequency range from approximately 4 dB up to 12 dB. This curve is used to optimize the choice of output frequencies from each vircator to provide maximum power to the horn antennas.

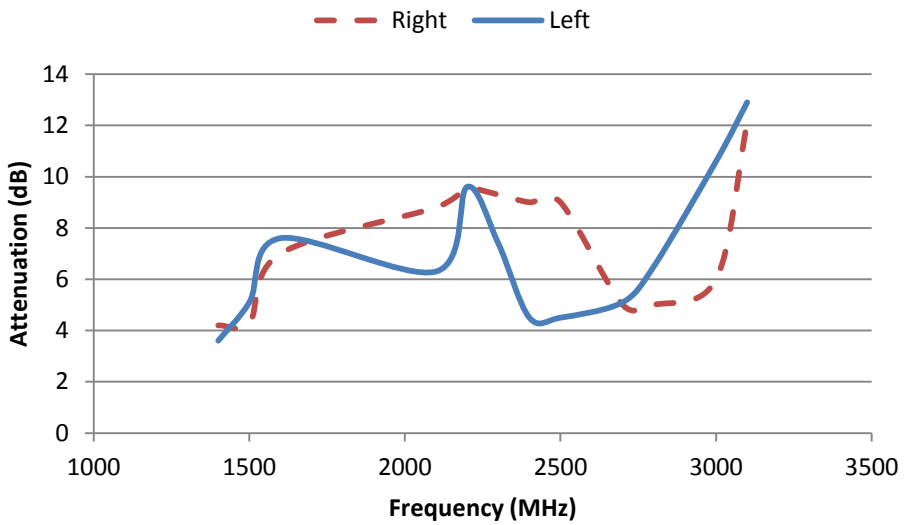

Figure 7.60—Measured waveguide attenuation from 1400 MHz to 3100 MHz

References for Chapter 7

[1] D. L. Birx, S. A. Hawkins, S. E. Poor, L. L. Reginato, and M. W. Smith, "Technology of Magnetically Driven Accelerators," *IEEE Transactions on Nuclear Science*, vol. 32, no. 5, pp. 2743-2747, October 1985.

[2] P. Norgard and R. D. Curry, "An In-Depth Investigation Into the Effect of Oil Pressure on the Complete Statistical Performance of a High Pressure, Flowing Oil Switch," in *IEEE Pulsed Power Conference*, 2009, pp. 844-849.

[3] P. Norgard, "Development of a Gigawatt Repetitive Pulse Modulator and High-Pressure Test Stand and Results from High-Pressure Switch Tests," University of Missouri - Columbia, Master's Thesis 2006.

[4] J. Leckbee et al., "Design and testing of a high pressure, rep-rate, liquid dielectric switch for directed energy applications," in *Proc. IEEE 26th Int'l Power Modulator Conf.*, 2004, pp. 193-196.

[5] J. Benford, J. A. Swegle, and E. Schamiloglu, *High Power Microwaves*, 2nd ed.:

CRC Press, 2007.

[6] I. Langmuir, "The effect of space charge and residual gases on thermionic currents in high vacuum," *Phys. Rev.*, no. 2, p. 450, 1913.

[7] C. D. Child, *Phys. Rev.*, no. 32, p. 492, 1911.

[8] R. B. Miller, *An Introduction to the Physics of Intense Charged Particle Beams*. New York, United States of America: Plenum Press, 1982.

[9] Pasternack Enterprises, Inc., "PE2209-20 SMA Female Directional Coupler," Irvine, Data Sheet 2011.

[10] Tektronix, "Digital Phosphor Oscilloscopes and Digital Serial Analyzers," Data Sheet 2006.

[11] Beehive Electronics, "100 Series EMC Probes," Data Sheet 2009.

[12] Y. Chen, J. Mankowski, J. Walter, M. Kristiansen, and R. Gale, "Cathode and anode optimization in a virtual cathode oscillator," *IEEE Transactions on Dielectrics and Electrical Insulation*, vol. 14, no. 4, pp. 1037-1044, August 2007.

[13] See for example M. Elfsberg, T. Hurtig, A. Larsson, C. Moller, and S. Nyholm, "Experimental Studies of Anode and Cathode Materials in a Repetitive Driven Axial Vircator," *IEEE Transactions on Plasma Science*, vol. 36, no. 3, pp. 688-693, June 2008.

[14] J. Mankowski, Y. Chen, J. Dickens, and A. Neuber, "A Low-Cost Metallic Cathode for a Vircator HPM Source," in *IEEE Pulsed Power Conference*, Monterey, 2005, p. 66.

[15] Y. -J. Chen, J. Mankowski, J. Walter, and M. Kristiansen, "Virtual cathode oscillator component optimization," in *Conference Record of the 2006 Twenty-Seventh International Power Modulator Symposium*, 2006, pp. 157-160.

[16] Y. Chen, "Compact, Repetitive Marx Generator and HPM Generation with the Vircator," Texas Tech University, Master's Thesis 2005.

[17] J. Walter et al., "Initial anode optimization for a compact sealed tube vircator," in *IEEE Pulsed Power Conference*, 2011, pp. 807-810.

[18] C. A. Balanis, *Advanced Engineering Electromagnetics*.: John Wiley & Sons, Inc., 1989.

[19] N. Ida, *Engineering Electromagnetics*, 2nd ed. New York: Springer-Verlag New

York, LLC, 2004.

[20] L. E. Thode and C. M. Snell, "Virtual Cathode Microwave Devices - Basics," Los Alamos National Laboratory, Los Alamos, 1991.

Chapter 8 — Conclusion

8.1 Summary of Project and Results

The design and construction of a pulsed power driving system, a dual vircator HPM source, and the accompanying suite of system diagnostics have been described in detail in this report. The pulsed power system was used to drive the vircator microwave source and was capable of providing over 3 GW of peak power. This system consisted of a thyratron-switched modulator, a pulse transformer, a water-filled PFL, and a high-pressure oil switch. The modulator was used to pulse charge the PFL through a step-up pulse transformer. A square pulse was created through the discharge of the high-pressure oil switch. This output pulse was then stepped up through an inductive voltage adder and used to power the dual vircator load.

This system used an array of diagnostics to monitor the performance. Among these were a voltage and current monitor on the modulator measuring the voltage that the capacitor bank was charged to and the current through the thyratron during a pulse. Voltage monitors were included to measure the charging waveform on the water-filled PFL and the output pulse voltage. A commercial high voltage probe was used to measure the voltage out of the inductive voltage adder. Two B-dot probes were built using coaxial cables to monitor the current delivered to either side of the parallel load. The voltage and current provided a way to determine the input power into each side of the load and the impedance of each side of the load.

Initially, the voltage discharge pulse delivered to the primary of the pulse transformer at the output of the modulator capacitor bank had an impedance mismatch

effect created by the inductance of the transmission cables. This caused severe overshoot on the discharge pulse. To alleviate this overshoot, an RC snubber circuit was built and inserted into the system. This snubber removed the resonant overshoot.

Before the inclusion of the vircator HPM load and the inductive voltage adder, the pulse generator system was tested. In particular, the breakdown voltage of the high-pressure oil switch was examined for a number of different electrode gaps. The gap was set such that the switch would break down at a mean voltage of approximately 200 kV for an oil pressure of 100 psi. The percent standard deviation of the breakdown voltage for all of the pulses driving the HPM sources for which data was reported was approximately 10%.

The inductive voltage adder was then introduced into the system and tested. It was shown that the inductive voltage adder doubled the pulse amplitude. The commercial high voltage probe was used to calibrate the B-dot probes used for measuring the current. This was done simply by using Ohm's law relating the known voltage and resistance values to the current signal obtained from the B-dot probes.

The vircators were tested individually after verifying the operation of the high voltage pulsed power system. To test the vircators, a section of rectangular waveguide was used as a load and attached to the radial extraction port on the vircator. This waveguide was capped off with a brass plate to contain the microwaves. Anechoic material was placed in the end of the waveguide to absorb the microwaves and reduce reflections. A commercial B-dot probe was used to measure the microwave signal. To determine the frequency of the signal, an FFT was performed on the time-domain waveform captured by the probe. This probe also allowed for the determination of the

magnetic field strength in the waveguide, which permitted the calculation of the microwave signal's power. For all of the reported results, the cathode emitter was black felt while the anode screen was a stainless steel woven screen with a transparency of 84.6%. The dominant frequency, peak microwave power, and microwave efficiency were all determined for a multitude of AK gaps. It was shown that all three parameters tended to decrease with an increase in the AK gap.

After the tunability was verified for each vircator, they were connected in parallel. It was shown that the tunability of the microwave frequency remained the same for a given AK gap as the tunability of the frequency from single vircator testing. The microwave signals were carried via a rectangular waveguide to an anechoic chamber. Horn antennas were connected to the waveguide to provide directionality to the microwave radiation.

The microwave outputs from the vircators were compared to the simulations. The frequency dependence on the AK gap was explored in both CST Particle Studio® and MAGIC. The results from these simulation packages were discussed in section 5.2. A plot comparing the simulation dominant frequencies to the measured dominant frequencies for a range of AK gaps is shown in Figure 8.1. The two black, dashed-line curves show the dominant frequency versus the AK gap from the simulations with the dotted-line representing the MAGIC simulations and the dashed-line representing the CST simulations. The red and blue curves represent the measured dominant frequencies from the right and left vircators, respectively. It would seem from these results that MAGIC provides a very good estimation of the microwave frequency output by the vircator. The CST simulation results do not match the experimental results quite as well,

but the offset between the CST results and experimental results is somewhat stable except for larger gap spacings where the two curves match closely. The discrepancy between the MAGIC and CST predicted frequencies could possibly be due to differences in emission models or calculation techniques.

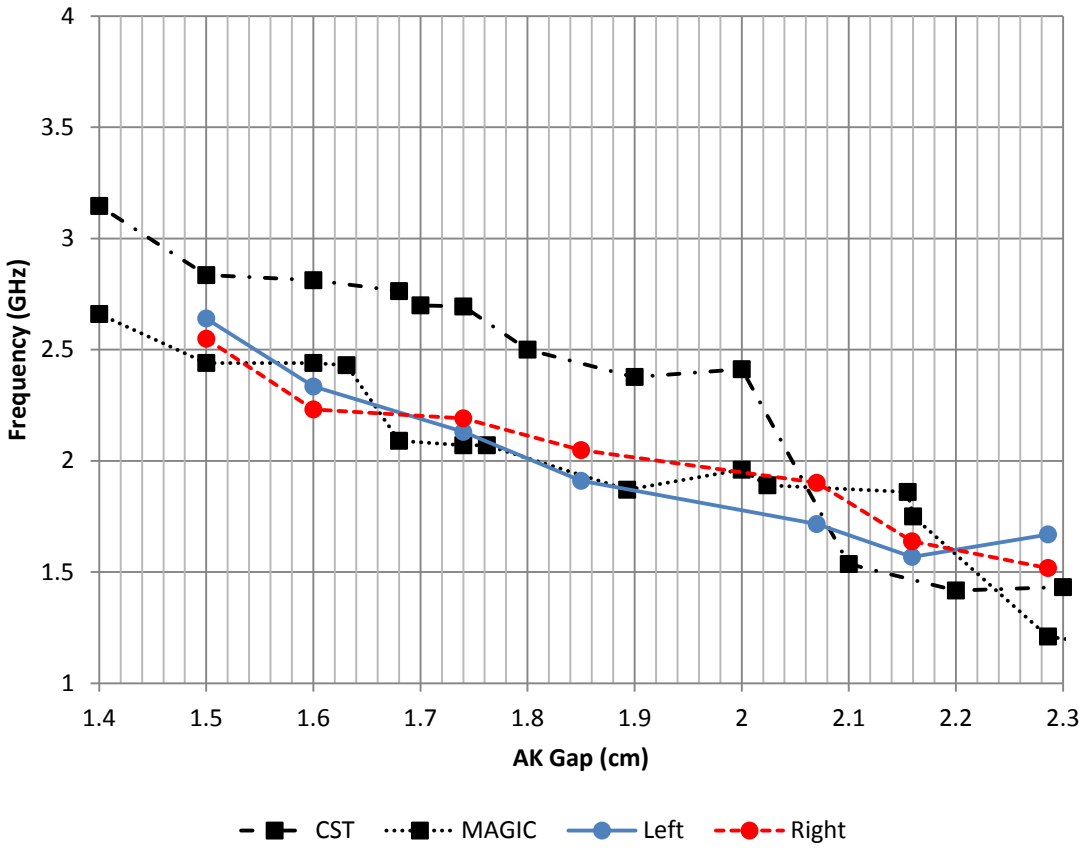

Figure 8.1—Comparison of dominant output frequency from simulations and from measured microwave signals

8.2 Future Work

The dual vircator test stand makes it possible to explore multiple system parameters in parallel. There are several items that should be explored in the future. Among these plans are in-depth materials testing, system modifications for increasing the voltage of the driving signal, the implementation of components to stabilize the voltage amplitude, a design modification of the vircators to allow for the external alteration of the

AK gap, and the implementation of other diagnostics for system measurement verification.

One system parameter that has been the focus of numerous research studies is diode materials used in a vircator, primarily the materials used for the cathode emitter and the anode screen. The primary concern with these materials has been durability and lifetime particularly when operating in sustained repetitive pulse mode [1], [2]. Gas evolution has also been a focus of previous research studies [3]. Various materials should be tested in repetitive pulse mode including different emitter materials on the cathode and various screens and wires for the anode. An issue seen in the results presented in this report is the frequency variability of the output microwave signal, particularly at larger AK gaps. It is proposed that the reason for this variability is that the plasma formation across the cathode surface is both non-uniform and inconsistent from pulse to pulse. Carbon fibers doped with cesium iodide have been shown to have lower electric field threshold values for emission, more uniform emission characteristics, and better reproducibility from pulse to pulse [4], [5], [6]. Carbon fiber emitters alone have also been shown to produce higher frequency stability characteristics in vircators [7]. Both carbon fiber emitters and cesium doped carbon fibers should be tested in the future to determine whether more uniform electron emission allows for less variation in the microwave output.

In the results presented, the pulsed power system was operated at approximately 66% of its maximum voltage capabilities. To increase the power of the driving signals, the system should be modified so as to produce higher voltage pulses. Initially, this should be achieved by increasing the oil pressure in the high-pressure oil switch. It has

been shown that the breakdown strength of a liquid dielectric increases with pressure [8], [9], [10]. This can increase the voltage by as much as 10%-15% [11]. The system's mean output voltage can also be increased by a larger proportion by increasing the electrode spacing in the high-pressure oil switch and increasing the charge voltage on the capacitor bank to ensure that breakdown occurs.

Another issue affecting the variability of the microwave output is the variability in the input voltage. As discussed, with any system reliant on a high voltage dielectric switch for discharging an output pulse, the voltage amplitude varies from pulse to pulse. This voltage jitter affects the output frequency due to the relation between the diode voltage and the plasma frequency [12], [13]. To address this problem and reduce the output pulse voltage variation, the use of a metal-oxide varistor (MOV) stack should be explored to clamp the voltage. The use of MOVs has been researched in pulsed power systems for pulse shaping and clamping [14], [15].

The current system design requires the vacuum to be broken to alter the AK gap for frequency tuning. Experiments in which the AK gap is varied would be made much less complicated and allow for quicker testing with a system modification permitting the alteration of the AK gap through some sort of external control. This would also negate the necessity of breaking vacuum to tune the vircator's output frequency. Designs for this external tuning alteration should be examined.

Finally, other system modifications that could be made are diagnostic modifications. A commercial B-dot probe measures a magnetic field vector dominated by the TE_{10} mode in the rectangular waveguide in the current method for characterizing the microwave output from the vircators. In the future, a directional coupler should be

added to the waveguide for power measurements of the microwave signal. A diode detector would be used for measuring the pulse envelope. This would allow for a more accurate measurement of the microwave power and would also include all waveguide modes that the microwaves operate in. Another diagnostic that could be improved is the measurement of the current delivered to the load. The current measurements are obtained using B-dot probes built and calibrated in-house. A commercial current probe should be incorporated into the system. A commercial current probe would allow for a more precise calibration of the B-dot probes rather than the simple calibration performed using the measured voltage from the high voltage probe and the measured resistance values of the water resistor loads. These diagnostic modifications would allow for the verification of measurements presented in this report.

References for Chapter 8

[1] M. Elfsberg, T. Hurtig, A. Larsson, C. Moller, and S. Nyholm, "Experimental Studies of Anode and Cathode Materials in a Repetitive Driven Axial Vircator," *IEEE Transactions on Plasma Science*, vol. 36, no. 3, pp. 688-693, June 2008.

[2] J. Mankowski, Y. Chen, J. Dickens, and A. Neuber, "A Low-Cost Metallic Cathode for a Vircator HPM Source," in *IEEE Pulsed Power Conference*, Monterey, 2005, p. 66.

[3] J. Vara, "Anode Material Testing in a Vacuum Diode," Texas Tech University, Lubbock, Master's Thesis 2011.

[4] J. N. Benford, D. Price, and W. DeHope, "Extension of HPM Pulse Duration by Cesium Iodide Cathodes in Crossed Field Devices," AFRL, 1998.

[5] D. A. Shiffler et al., "Comparison of carbon fiber and cesium iodide coated cathodes," *IEEE Transactions on Plasma Science*, vol. 28, no. 3, pp. 517-522, June 2000.

[6] D. Shiffler, J. Heggemeier, M. LaCour, K. Golby, and M. Ruebush, "Low level plasma formation in a carbon velvet cesium iodide coated cathode," *Physics of*

Plasmas, vol. 11, no. 4, pp. 1680-1684, April 2004.

[7] L. Li et al., "A study on frequency stabilities of microwave emission from a reflex triode vircator," in *17th Int'l Conference on High Power Particle Beams (BEAMS)*, 2008, pp. 1-4.

[8] J. Leckbee, R. Curry, K. McDonald, R. Cravey, and A. Grimmis, "An advanced model of a high pressure liquid dielectric switch for directed energy applications," in *Proc. IEEE 14th Int'l Pulse Power Conf.*, 2003, pp. 1389-1393.

[9] J. Leckbee et al., "Design and testing of a high pressure, rep-rate, liquid dielectric switch for directed energy applications," in *Proc. IEEE 26th Int'l Power Modulator Conf.*, 2004, pp. 193-196.

[10] P. Norgard, "Development of a Gigawatt Repetitive Pulse Modulator and High-Pressure Test Stand and Results from High-Pressure Switch Tests," University of Missouri - Columbia, Master's Thesis 2006.

[11] P. Norgard and R. D. Curry, "An In-depth Investigation of the Effect of Oil Pressure on the Complete Statistical Performance of a High-pressure Flowing Oil Switch ," *IEEE Transactions on Plasma Science*, vol. 38, no. 10, pp. 2539-2547, October 2010.

[12] J. Benford, J. A. Swegle, and E. Schamiloglu, *High Power Microwaves*, 2nd ed.: CRC Press, 2007.

[13] L. E. Thode and C. M. Snell, "Virtual Cathode Microwave Devices - Basics," Los Alamos National Laboratory, Los Alamos, 1991.

[14] M. C. Clark, "A new, compact pulsed power system based on surge arrestor technology," in *IEEE Pulsed Power Conference*, 2009, pp. 938-943.

[15] M. Giesselman et al., "Simulation, design and test of a MOV pulse shaping device for high power microwave generators," in *IEEE International Pulsed Power Conference*, 1999, pp. 1433-1436.

Appendix A: MAGIC Simulation Code

Two PIC simulation software packages were used for modeling the vircators. One was CST Particle Studio® which uses a CAD-based three-dimensional structure for simulations. The other was MAGIC. MAGIC is a 2½ -dimensional simulation software package that requires writing code with a particular syntax for performing a simulation. The code shown in this Appendix is an example simulation code used to simulate a vircator with an AK gap of 1.68 cm, a voltage signal with an amplitude of 200 kV and a rise time of 20 ns, and an anode transparency of 90%. In this code, the AK gap can be changed by altering the value for "CATHODE.ANODE.GAP., and the voltage amplitude can be changed by altering the value for "VOLTAGE_MAX."

This particular code outputs several plots for visualizing various aspects of the simulated vircator. The input voltage and current into the vircator are both calculated and displayed. These two parameters are used to determine a time dependent impedance of the diode. The electric field and magnetic field are both calculated at a given point in the waveguide simulated waveguide. An FFT is performed on each of these measured signals so that the output microwave frequency can be resolved to allow for the prediction of the experimental output frequencies. Several particle plots are also calculated and displayed. The particles are tracked in 1 ns steps for the whole simulation time. This is shown as the calculations are performed. After the simulation has completed, the energy, momentum, and relativistic coefficient of each of the particles at the last time step of the simulation are recorded and plotted in phase space plots versus the axial direction, z.

```
!-----------------------------------------------------------
! ===========================================================
! ===========================================================
  HEADER AUTHOR "KELTON CLEMENTS" ;
  HEADER ORGANIZATION "CPPE" ;
  HEADER DEVICE "VIRCATOR" ;
! ===========================================================
! ===========================================================
!-----------------------------------------------------------

!graphics pauseon tsys$last;
!graphics pause ;
graphics pauseOn Tsys$last ;

kpush  = 1 ;   ! particle-to-field time step ratio.
kfreq  = 1 ;   ! creation-to-particle time step ratio.
TimingOption = "TIMING" ;
!-----------------------------------------------------------

SYSTEM CYLINDRICAL ;

DR = 2mm ;
DZ = 2mm ;

CATHODE.ANODE.GAP =  1.68cm;

CATHODE.RADIUS = 4.3CM ;
CATHODE.LENGTH = 3CM ;
AREA Cathode Conformal 0, 0, Cathode.Length,
            Cathode.Radius ;
mark CATHODE x2 min size +2*dr ;
mark CATHODE x1 size DZ ;

ANODE.EXT = 16.51CM ;
ANODE.RADIUS.INNER = 12.7CM ;
ANODE.RADIUS.OUTER = ANODE.RADIUS.INNER + DR ;
WAVE.LENGTH = 12.3825cm;
ANODE1.LENGTH = CATHODE.LENGTH + CATHODE.ANODE.GAP + DZ;
ANODE2.START = ANODE1.LENGTH + WAVE.LENGTH ;
ANODE2.END = ANODE2.START+ANODE.EXT+DZ;
AXIAL.VOLTAGE.END = CATHODE.LENGTH + CATHODE.ANODE.GAP ;

Area  ANODE1 Conformal 0.0,ANODE.radius.INNER,
            Anode1.length, ANODE.RADIUS.OUTER ;

mark ANODE1 x2 max size dr;
mark ANODE1 x1 size DZ ;

Area  ANODE2 Conformal ANODE2.START,ANODE.radius.INNER,
            Anode2.END, ANODE.RADIUS.OUTER ;

mark ANODE2 x2 max size dr;
mark ANODE2 x1 size DZ ;
```

```
ANODECAP.RADIUS = ANODE.RADIUS.OUTER ;
ANODECAP.END = ANODE2.END + DZ;

Area ANODECAP CONFORMAL  ANODE2.END,0, ANODECAP.END ,
        ANODECAP.radius;

mark ANODECAP x2  ;
mark ANODECAP x1 size DZ ;

ANODEFOIL.THICKNESS = .02032CM ;
AXIAL2.WFOIL = AXIAL.VOLTAGE.END + DZ ;
AXIAL3.WFOIL = AXIAL2.WFOIL + 0.5*WAVE.LENGTH ;
WAVE.HEIGHT = 160.6CM;
WAVEPOS = ANODE.RADIUS.OUTER + (wave.height - 30.5cm)/2 ;

AREA WAVE1 CONFORMAL
        -DZ+ANODE1.LENGTH,ANODE.RADIUS.OUTER,ANODE1.LENGTH,
        WAVE.HEIGHT;
MARK WAVE1 X1 SIZE DZ;
MARK WAVE1 X2 SIZE DR;

WAVE2.END = ANODE2.START+DZ;
AREA WAVE2 CONFORMAL ANODE2.START,ANODE.RADIUS.OUTER,
        WAVE2.END,WAVE.HEIGHT;
MARK WAVE2 X1 SIZE DZ;
MARK WAVE2 X2 SIZE DR;

WAVECAP.TOP = WAVE.HEIGHT+DR;
AREA WAVECAP CONFORMAL -DZ+ANODE1.LENGTH,WAVE.HEIGHT,
        WAVE2.END,WAVECAP.TOP;
MARK WAVECAP X1 SIZE DZ;
MARK WAVECAP X2 SIZE DR;

AREA WAVE.INS CONFORMAL
        NODE1.LENGTH,ANODE.RADIUS.INNER,ANODE2.START,
        ANODE.RADIUS.OUTER;
MARK WAVE.INS X1 SIZE DZ;
MARK WAVE.INS X2 SIZE DR;

AREA ANODEFOIL CONFORMAL AXIAL.VOLTAGE.END,0, AXIAL2.WFOIL,
        ANODE.RADIUS.INNER ;
mark ANODEFOIL x2 ;
mark ANODEFOIL x1 size DZ ;

!PLUNGER.RADIUS = 10.16cm;
!PLUNGERROD.RADIUS = 0.635cm;
!AREA PLUNGER CONFORMAL ANODE2.START,0, WAVE2.END,
!       PLUNGER.RADIUS;
!mark PLUNGER x2 size DR;
!mark PLUNGER x1 size DZ ;

!AREA PLUNGER.ROD CONFORMAL WAVE2.END,0, ANODE2.END,
!       PLUNGERROD.RADIUS;
!mark PLUNGER.ROD x2 size DR;
!mark PLUNGER.ROD x1 size DZ ;
```

```
LINE INCIDENT.WAVE CONFORMAL 0.0, CATHODE.RADIUS,0.0,
        ANODE.RADIUS.INNER ;
LINE VOLTAGE.PORT  CONFORMAL 0.0, CATHODE.RADIUS,0.0,
        ANODE.RADIUS.INNER ;
LINE VOLTAGE.AXIAL CONFORMAL Cathode.Length,0,
        AXIAL.VOLTAGE.END,0 ;
POINT EFIELD.AXIAL AXIAL3.WFOIL, 0.0;
POINT EFIELD.WAVE AXIAL3.WFOIL, WAVEPOS ;
VCPOS1 = AXIAL2.WFOIL + CATHODE.ANODE.GAP ;
VCPOS2 = VCPOS1 + DZ ;
LINE VOLT.VC CONFORMAL AXIAL2.WFOIL,0, VCPOS2,0 ;

EX.Z = CATHODE.LENGTH + DZ ;
XNOTEMITTER.I = 0.0 ;
XNOTEMITTER.F = CATHODE.LENGTH -0.2*DZ ;
AREA NOTEMITTER  CONFORMAL XNOTEMITTER.I,0,XNOTEMITTER.F,
        ANODE.RADIUS.INNER;

EMITTER.I = CATHODE.LENGTH -0.2*DZ ;
EMITTER.F = CATHODE.LENGTH +0.2*DZ ;
AREA EMITTER  CONFORMAL EMITTER.I,  0, EMITTER.F,
        ANODE.RADIUS.INNER;

GAP_Z   = CATHODE.ANODE.GAP ;
EMITTER_AREA = 1PI*CATHODE.RADIUS**2 ;

autogrid ;

SPECIES BLUEELECT CHARGE 1 MASS 1 ELECTRON COLOR BLUE ;

  SPECIES REDELECT CHARGE 1 MASS 1 ELECTRON COLOR RED ;
FOIL ANODEFOIL X1 ANODEFOIL.THICKNESS MO
   EXIT_SPECIES REDELECT
   TRANSMISSION FRACTION 0.846 ;

TKMAX = 70NANOSECOND ;
DURATION TKMAX ;

conductor CATHODE  MATERIAL ALUMINUM ;
conductor ANODECAP MATERIAL ALUMINUM ;
conductor ANODE1    MATERIAL ALUMINUM ;
conductor ANODE2    MATERIAL ALUMINUM ;
conductor WAVE1    MATERIAL ALUMINUM ;
conductor WAVE2    MATERIAL ALUMINUM ;
conductor WAVECAP    MATERIAL ALUMINUM ;
!conductor PLUNGER    MATERIAL ALUMINUM ;
!conductor PLUNGER.ROD    MATERIAL ALUMINUM ;
DIELECTRIC WAVE.INS PLEXIGLASS ;

DISPLAY ;

VRISE = 20.0NANOSECOND ;
TRISE = 5NANOSECOND ;
PTOP = 50.0NANOSECOND ;
VOLTAGE_MAX = 200 KILOVOLTS ;
```

```
 FUNCTION FTEMPORAL(T) = 0.5*VOLTAGE_MAX*RAMP(T/Trise) ;
 FUNCTION FDESIRED(T)  = VOLTAGE_MAX*Smooth_RAMP(T/Trise) ;

 FUNCTION Gr(z,r) = 1/R ;
 FUNCTION Gphi(z,r) = .0 ;

 PORT INCIDENT.WAVE POSITIVE
    INCOMING FTEMPORAL
          FUNCTION E2 Gr E3 Gphi
          NORMALIZATION VOLTAGE VOLTAGE.PORT
          CIRCUIT TRISE FDesired obS$In_volt
         ;
OBSERVE FIELD_INTEGRAL E.DL VOLTAGE.PORT SUFFIX IN_VOLT;

! ============================================================;

 NpCell = 1 ;   ! Number of particles per cell.
 THRESHOLD_FIELD = 1e5 ;

EMISSION EXPLOSIVE THRESHOLD THRESHOLD_FIELD MODEL
         EXPLOSIVE NUMBER NpCell
         TIMINGOption Kfreq SURFACE_SPACING RANDOM ;

 EMIT EXPLOSIVE CATHODE EXCLUDE  NOTEMITTER  INCLUDE  EMITTER ;

LORENTZ TIMING KPUSH ;
TS = 20*Kpush*KFreq*sys$dtime ;

EPS0 = 8.8544E-12 ;
EBYM = 1.7588E+11 ;
CJCONST = 4/9*EPS0*SQRT(2*EBYM) ;

OBSERVE EMITTED   CATHODE  ALL CURRENT
         FILTER STEP TS Suffix I_actual;
OBSERVE COLLECTED ANODECAP ALL CURRENT
         FILTER STEP TS ;
OBSERVE COLLECTED ANODEFOIL ALL  CURRENT
         FILTER STEP TS ;
OBSERVE COLLECTED  ALL     ALL  CURRENT
         FILTER STEP TS  Suffix I_actual2;

OBSERVE FIELD_INTEGRAL E.DL VOLTAGE.AXIAL
         Filter Step TS suffix Vgap;

Function Z_Diode(xo,t) =
         MIN(200,OBS$Vgap/Max(10,ABS(OBS$I_Actual))) ;
OBSERVE Transform Z_Diode Filter Step TS ;

TIMER PHS PERIODIC REAL 1NANOS TKMAX 1NANOS ;

PHASESPACE AXES X1 X2 PHS AXIS X 0 ANODECAP.END
         AXIS Y 0 ANODE.RADIUS.OUTER
         MOVIE PNG MOVIE_NAME AKGap168cm ;
PHASESPACE AXES X1 KE tsys$last ;
PHASESPACE AXES X1 P1 tsys$last ;
PHASESPACE AXES X1 GAMMA tsys$last ;
```

```
OBSERVE FIELD E1 EFIELD.WAVE SUFFIX Eyvec
     FILTER STEP TS
     FFT MAGNITUDE
     WINDOW
     FREQUENCY 500MHZ 6000MHZ
     WRITE_TABLE ;

OBSERVE FIELD B3 EFIELD.WAVE SUFFIX Hxvec
     FILTER STEP TS
     FFT MAGNITUDE
     WINDOW
     FREQUENCY 500MHZ 6000MHZ
     WRITE_TABLE ;

TIMER STATS PERIODIC 25 9999 25 ;
STATISTICS STATS ;
DUMP TYPE ALL;

start ;
stop;
```

Appendix B: MATLAB Code for Analyzing Data

To analyze the data acquired during testing, MATLAB was used to process the data files, present the data in a form that could be analyzed and understood, and to capture and output important measurement parameters. The MATLAB code displayed in this Appendix processes data captured by the Megaprobe used to measure the diode voltage, the two B-dot probes used to measure the diode current, and the two B-dot probes used for measuring the microwave signals produced by the dual vircators.

The code is broken into two separate processing sections. The first section processes the data for the diode voltage and current. For processing the diode voltage, a smoothing, or filtering, technique is used to remove noise that is coupled into the signal. The diode currents are found by digitally filtering and digitally integrating the waveforms captured by the B-dot probes. A calibrated scale factor is applied to this integrated waveform to obtain the final processed waveform.

The second section processes the data for the measured microwave pulses. Two parameters are of definite interest with regards to the microwave pulses. One is the dominant frequency seen during the pulse. This is found by performing an FFT and determining at which frequency the peak occurs. The second important parameter is the peak power seen during the pulse. This is calculated using the relationship between the output signal and the magnetic flux density. Once the magnetic field at the measurement point in the waveguide is determined, waveguide equations are used to calculate the power in the waveguide assuming that a majority of the microwave power travels in the TE_{10} mode.

This MATLAB code also reads from and writes to an Excel spreadsheet file. This spreadsheet file includes the following parameters: the shot number, the AK gaps on the left and right vircators, the maximum voltage measured, the maximum current measured for each vircator, the peak input power for each vircator, the peak microwave output power for each vircator, the peak power efficiency for each vircator, and the dominant frequency for each vircator.

In order to visualize the data, the MATLAB code produces plots of the voltage, current, impedance, input power, and microwave signals as functions of time. The frequency domain plots of the microwave signals are also produced as a visualization of the output spectrum. Finally, a time-resolved frequency plot, or spectrogram, is also produced for analyzing how the frequency changes with time for a given microwave pulse.

Five saved files from the oscilloscopes contain the data to be processed. In the following file names, XXXX represents the shot number with zeros padding the first numbers where necessary.

File Names	Measurement
VXXXX	Diode voltage
RBXXXX	Current into right branch of the load
LBXXXX	Current into left branch of the load
RBwavXXXX	Microwave measurement in right waveguide
LBwavXXXX	Microwave measurement in left waveguide

```
%%%%%%%%%%%%%%%%%%%%%%%%%%%%%%%%%%%%%%%%%%%
% The following program is the copyright of Kelton R. Clements.
%%%%%%%%%%%%%%%%%%%%%%%%%%%%%%%%%%%%%%%%%%%
% The program will execute in Matlab to analyze and plot waveforms captured in
% the Dual Vircator setup with corresponding file names of waveforms saved on
% Tektronix TDS5054B-NV-T and Tektronix DPO70804 oscilloscopes.  Critical
% parameters are both read and written to an Excel spreadsheet.
%%%%%%%%%%%%%%%%%%%%%%%%%%%%%%%%%%%%%%%%%%%

clear all;
close all;

% Obtain user inputs of the pulse number to plot and analyze and whether to
% save the produced figures
prompt={'Input the shot number to examine: ',...
    'Do you want to save (y or n)?: '};
dlg_title = 'Inputs';
num_lines = 1;
def = {'221','y'};
param = inputdlg(prompt,dlg_title,num_lines,def);
shot = param{1};
qsav = param{2};

% Convert the inputs into parameters used to import data and label plots
shotnum = str2double(shot);
shoti = sprintf('%04.0f',shotnum);
path = ['Shot ' shot];
[spread txthead] = xlsread('ShotData.xlsx');

% Change the directory to corresponding pulse number and import data
cd([path '\']);

% Obtain samping interval and number of samples from oscilloscope file
testparam = importdata(['LB' shoti '.hdr']);
len = testparam(1);
Ts = testparam(2);

% Build a time vector for plotting the voltage and current waveforms
t = (0:Ts:(len-1)*Ts)';

% Import the B-dot probe and voltage waveforms
LB = importdata(['LB' shoti '.dat']);
RB = importdata(['RB' shoti '.dat']);
V = importdata(['V' shoti '.dat']);

% Create high pass filter to remove the slight DC offset in the oscope's output
fcV = 35e6;
tauV = 1/(2*pi*fcV);
aV = Ts/tauV;

% Filter the voltage waveform and read the peak voltage
V = filter(aV,[1 aV-1],V);
[Vmin VI] = min(V);

% Plot the raw data waveforms of voltage and B-dot probe
figure;
```

```
subplot(2,1,1);
plot(t*1e6,LB,t*1e6,RB)
grid on
title(['B-dot Probe Raw Traces-Shot ' shot])
xlabel('Time (\mus)')
xlim([0.4 1.4]);
ylabel('Voltage (V)')
legend('Left B-Dot','Right B-dot','Location','northwest')
subplot(2,1,2);
plot(t*1e6,V/1e3);
grid on
title('Megaprobe Raw Trace')
xlabel('Time (\mus)')
xlim([0.4 1.4]);
ylabel('Voltage (kV)')
if qsav == 'y'
   saveas(gcf,['Raw Data-Shot ' shot '.tif']);
end

% Obtain mean values from initial portion of B-dot waveform to filter out
avgL1 = mean(LB(1:15000));
avgR1 = mean(RB(1:15000));

% Remove DC offset created by oscilloscope
LBa = LB;
LBa = LBa-avgL1;
fcBdot = 5e5;
tauBdot = 1/(2*pi*fcBdot);
aBdot = Ts/tauBdot;
LBa = filter([1-aBdot aBdot-1],[1 aBdot-1],LBa);

fcBdotR = 1e5;
tauBdotR = 1/(2*pi*fcBdotR);
aBdotR = Ts/tauBdotR;
RBa = RB;
RBa = RBa-avgR1;
RBa = filter([1-aBdotR aBdotR-1],[1 aBdotR-1],RBa);

% Integrate the B-dot probe signal to get the current waveform
LBI = cumtrapz(t,LBa);
Lscale = 2.46512404e+11;
LBI = LBI*Lscale;

RBI = cumtrapz(t,RBa);
Rscale = 4.2938931e+10;
RBI = RBI*Rscale;

% Filter current signal for high frequency noise
fcIl = 35e6;
tauIl = 1/(2*pi*fcIl);
aIl = Ts/tauIl;
LBI = filter(aIl,[1 aIl-1],LBI);
[ILmin ILI] = min(LBI(1:0.6*length(LBI)));

RBI = filter(aIl,[1 aIl-1],RBI);
[IRmin IRI] = min(RBI(1:0.6*length(RBI)));
```

```
% Determine the peak input power from peak voltage and current
PLmax = Vmin*ILmin;
PRmax = Vmin*IRmin;

% Write peak voltage, current and power to spreadsheet array
spread(shotnum,10) = Vmin/1e3;
spread(shotnum,11) = ILmin/1e3;
spread(shotnum,12) = PLmax/1e6;
spread(shotnum,16) = IRmin/1e3;
spread(shotnum,17) = PRmax/1e6;

% Plot Integrated Current signals
figure;
plot(t*1e6,LBI/1e3,t*1e6,RBI/1e3,'LineWidth',2);
grid on
title(['Integrated B-dot Signals-Shot ' shot])
legend('Left Current','Right Current','Location','northwest')
xlabel('Time (\mus)')
xlim([0.6 1.4]);
ylabel('Current (kA)')
if qsav == 'y'
   saveas(gcf,['Current-Shot ' shot '.tif']);
end

% Set delay between voltage and current due to differing cable lengths
VILdelay = 0.0818e-6;
VIRdelay = 0.082e-6;
Idelay = round(max(VILdelay,VIRdelay)/Ts);
IRdelay = round(VIRdelay/Ts);
ILdelay = round(VILdelay/Ts);

% Create padded arrays to align voltage and current to obtain power and
% impedance time traces
Vpad = [zeros(Idelay,1); V];
if VILdelay > VIRdelay
   LBIpad = [LBI; zeros(ILdelay,1)];
   RBIpad = [zeros(Idelay-IRdelay,1); RBI; zeros(IRdelay,1)];
else
   LBIpad = [zeros(Idelay-ILdelay,1); LBI; zeros(ILdelay,1)];
   RBIpad = [RBI; zeros(IRdelay,1)];
end

% Build new padded time vector
[l k] = size(Vpad);
tpad = 0:Ts:(l-1)*Ts;

% Read in the AK gap and determine theoretical current from voltage waveform
% using Child-Langmuir law
gapL = spread(shotnum,2);
gapR = spread(shotnum,3);
conL = 4/9*8.854e-12*sqrt(2*1.6e-19/9.11e-31)/gapL^2*5.08^2*pi;
conR = 4/9*8.854e-12*sqrt(2*1.6e-19/9.11e-31)/gapR^2*5.08^2*pi;
IRchild = zeros(l,1);
ILchild = IRchild;
```

```
for i = 1:l
   if Vpad(i)<-500
      IRchild(i) = -conR.*(abs(Vpad(i)).^1.5);
      ILchild(i) = -conL.*(abs(Vpad(i)).^1.5);
   end
end

% Calculate the impedance versus time and power versus time
ZL = min(200,max(Vpad./LBIpad,0));
ZR = min(200,max(Vpad./RBIpad,0));
RatL_child = min(20,max(abs(LBIpad./ILchild),0));
RatR_child = min(20,max(abs(RBIpad./IRchild),0));
PL = Vpad.*LBIpad;
PR = Vpad.*RBIpad;

% Plot the synchronized current and voltage traces
figure;
plot(tpad*1e6,LBIpad/abs(min(LBIpad(1:0.6*length(LBIpad)))),...
   tpad*1e6,RBIpad/abs(min(RBIpad(1:0.6*length(RBIpad)))),...
   tpad*1e6,Vpad/abs(min(Vpad)),'LineWidth',2);
grid on
title(['Normalized & Synchronized Signals-Shot ' shot])
legend('Left Current','Right Current','Voltage','Location','northwest')
xlabel('Time (\mus)')
xlim([0.6 1.4]);
ylabel('Normalized Signals')
if qsav == 'y'
   saveas(gcf,['Synchronized-Shot ' shot '.tif']);
end

% Plot the ratio of the current to the Child-Langmuir current
figure;
plot(tpad*1e6,RatL_child,tpad*1e6,RatR_child,'LineWidth',2);
xlim([.89 0.98]);
ylim([0 5]);
grid on
title(['Ratio of Current to Child-Langmuir Current vs. Time-Shot ' shot])
legend('Left Ratio','Right Ratio','Location','northeast')
xlabel('Time (\mus)')
ylabel('Ratio')
if qsav == 'y'
   saveas(gcf,['Ratio of Current to CL Current-Shot ' shot '.tif']);
end

% Plot the Impedance vs. Time
figure;
plot(tpad*1e6,ZL,tpad*1e6,ZR,'LineWidth',2);
xlim([.89 0.98]);
ylim([0 100]);
grid on
title(['Impedance vs. Time-Shot ' shot])
legend('Left Impedance','Right Impedance','Location','south')
xlabel('Time (\mus)')
ylabel('Impedance (\Omega)')
if qsav == 'y'
   saveas(gcf,['Impedance-Shot ' shot '.tif']);
```

```
end

% Plot the Power vs. Time
figure;
plot(tpad*1e6,PL/1e6,tpad*1e6,PR/1e6,'LineWidth',2);
grid on
title(['Power vs. Time-Shot ' shot])
legend('Left Power','Right Power','Location','northwest')
xlabel('Time (\mus)')
xlim([0.6 1.4]);
ylabel('Power (MW)')
if qsav == 'y'
   saveas(gcf,['Power-Shot ' shot '.tif']);
end

%% Microwave Diagnostics Section

% Obtain samping interval and number of samples from oscilloscope file from
% microwave waveforms
testparamHF = importdata(['RBwav' shoti '_hdr.dat']);
TsHF = testparamHF(2);
lengthHF = testparamHF(1);

% Find the sampling frequency and build the time and frequency vectors for the
% microwave signals
Fs = 1/TsHF;
tHF = (0:TsHF:(lengthHF-1)*TsHF)';
f = (0:Fs/lengthHF:(Fs/2-Fs/lengthHF))';
[lenf d] = size(f);

% Determine the time the oscope was triggered for plotting the signals
trigI = testparamHF(3);
trigt = TsHF*trigI*1e9;

% Build the attenuation vector versus frequency from measured attenuation
% No Directional Coupler was used in the case that the AK gap was bigger
% than 2.2cm
aL1 = -1.0723468e-18;
aL2 = 1.1302179e-14;
aL3 = -4.8161884e-11;
aL4 = 1.0667404e-7;
aL5 = -1.3059861e-4;
aL6 = 8.1012826e-2;
conL = -47.808915;

f1 = f./1e6;

if gapL>2.2
   attenL = .0046*f1;
else
   attenL = -1*(aL1*f1.^6 + aL2*f1.^5 + aL3*f1.^4 + aL4*f1.^3 +...
   aL5.*f1.^2+aL6.*f1+conL);
end

aR1 = -7.0645394e-19;
aR2 = 7.6101905e-15;
```

```
aR3 = -3.3698383e-11;
aR4 = 7.9069493e-8;
aR5 = -1.0387964e-4;
aR6 = 6.7521775e-2;
conR = -44.357927;

if gapR>2.2
   attenR = .0046*f1;
else
   attenR = -1*(aR1*f1.^6 + aR2*f1.^5 + aR3*f1.^4 + aR4*f1.^3 +...
   aR5.*f1.^2+aR6.*f1+conR);
end

for i = 1:length(f1);
   if and(f1(i)>=1e2,f1(i)<=3.1e3)
   else
      attenL(i) = 0;
   end
end

for i = 1:length(f1);
   if and(f1(i)>=1e2,f1(i)<=3.1e3)
   else
      attenR(i) = 0;
   end
end

% Import the microwave signal waveforms
LBwav = importdata(['LBwav' shoti '.dat']);
RBwav = importdata(['RBwav' shoti '.dat']);

% Perform FFT to obtain magnitude spectra of microwave signals
LBwavfft = abs(fft(LBwav-mean(LBwav))/lengthHF);
LBwavfft = LBwavfft(1:lenf,1);
RBwavfft = abs(fft(RBwav-mean(RBwav))/lengthHF);
RBwavfft = RBwavfft(1:lenf,1);

% Correct the magnitudes in the frequency domain for the probe frequency
% response and the system attenuation
X = 42.2;
probe = (X+20*log10(f1));
probe = max(probe)-probe;
LBwavfftcorr = LBwavfft;
RBwavfftcorr = RBwavfft;

for i = 1:length(LBwavfft);
   if and(f1(i)>=650,f1(i)<=3100)
      LBwavfftcorr(i) = LBwavfft(i)*10^(probe(i)/20)*10^(attenL(i)/20);
      RBwavfftcorr(i) = RBwavfft(i)*10^(probe(i)/20)*10^(attenR(i)/20);
   end
end

% Plot the microwave signals in time domain
figure;
plot(tHF*1e9,LBwav,tHF*1e9,RBwav);
grid on
```

```
title(['Microwave Time Domain Traces-Shot ' shot])
xlabel('Time (ns)')
xlim([trigt trigt+120])
ylabel('Amplitude')
legend('Left Waveguide','Right Waveguide','Location','southeast')
if qsav == 'y'
   saveas(gcf,['Microwave Signals-Shot ' shot '.tif']);
end

% Plot the microwave spectra without correction factors
figure;
plot(f/1e9,LBwavfft,f/1e9,RBwavfft,'LineWidth',1);
grid on
title(['Raw Microwave Frequency Domain Traces-Shot ' shot])
xlabel('Frequency (GHz)')
ylabel('Amplitude')
xlim([0 5]);
legend('Left Waveguide','Right Waveguide','Location','northwest')
if qsav == 'y'
   saveas(gcf,['Microwave Frequency (Raw)-Shot ' shot '.tif']);
end

% Plot the microwave spectra with correction factors
figure;
plot(f/1e9,LBwavfftcorr,f/1e9,RBwavfftcorr,'LineWidth',1);
grid on
title(['Corrected Microwave Frequency Domain Traces-Shot ' shot])
xlabel('Frequency (GHz)')
ylabel('Amplitude')
xlim([0.65 3.1]);
legend('Left Waveguide','Right Waveguide','Location','northwest')
if qsav == 'y'
   saveas(gcf,['Microwave Frequency (Corrected)-Shot ' shot '.tif']);
end

% Filter out the DC signal of the microwave signals
fc = 200e6;
tau = 1/(2*pi*fc);
a = TsHF/tau;

RBwavfilt = filter([1-a a-1],[1 a-1],RBwav);
LBwavfilt = filter([1-a a-1],[1 a-1],LBwav);

for i = 1:3
   RBwavfilt = filter([1-a a-1],[1 a-1],RBwavfilt);
   LBwavfilt = filter([1-a a-1],[1 a-1],LBwavfilt);
end

% Calculate the peak power using waveguide equations
omegac = 3e8*pi/(9.75*.0254);
fc = omegac/(2*pi);
[C Imaxwav] = max(abs(RBwavfilt));
lengthwavmax = 50e-9/TsHF;
RBwavmax = RBwavfilt(Imaxwav-lengthwavmax/2+1:Imaxwav+lengthwavmax/2);
RBwavmaxfft = abs(fft(RBwavmax))/length(RBwavmax);
fwavmaxR = 0:1/(TsHF*lengthwavmax):(1/(2*TsHF)-1/(TsHF*lengthwavmax));
```

```
attenwavmaxR = zeros(length(fwavmaxR),1);
[C Ifatten] = min(abs(fwavmaxR-200e6));
fwavmaxR1 = fwavmaxR/1e6;
probe = (X+20*log10(fwavmaxR1));
probe = max(probe)-probe;

aR1 = -7.0645394e-19;
aR2 = 7.6101905e-15;
aR3 = -3.3698383e-11;
aR4 = 7.9069493e-8;
aR5 = -1.0387964e-4;
aR6 = 6.7521775e-2;
conR = -44.357927;
if gapR>2.2
   attenwavmaxR = .0046*fwavmaxR1;
else
   attenwavmaxR = -1*(aR1*fwavmaxR1.^6 + aR2*fwavmaxR1.^5 + ...
      aR3*fwavmaxR1.^4 + aR4*fwavmaxR1.^3 +...
   aR5.*fwavmaxR1.^2+aR6.*fwavmaxR1+conR);
end

for i = 1:length(fwavmaxR1);
   if and(fwavmaxR1(i)>=1e2,fwavmaxR1(i)<=3.1e3)
   else
      attenwavmaxR(i) = 0;
   end
end

RBwavmaxfft = RBwavmaxfft(1:length(fwavmaxR));
RBwavmaxfftcorr = RBwavmaxfft;
for i = 1:length(RBwavmaxfft);
   if and(fwavmaxR1(i)>=600,fwavmaxR1(i)<=3100)
      RBwavmaxfftcorr(i) = RBwavmaxfft(i)*10^(probe(i)/20)...
         *10^(attenwavmaxR(i)/20);
   end
end
[C Ifatten] = min(abs(fwavmaxR-600e6));
[C fImaxwav] = max(RBwavmaxfftcorr(Ifatten:length(RBwavmaxfftcorr)));
fImaxwav = fImaxwav+Ifatten-1;
RBwavmaxamp = max(abs(RBwavfilt))/sqrt(2);
fwavmaxRval = fwavmaxR(fImaxwav);
[C attenI] = min(abs(fwavmaxRval/1e6-fwavmaxR1));
Pbdot = 10*log10(RBwavmaxamp^2/50*1000)+attenwavmaxR(attenI);
Brms = 10^((Pbdot-X-20*log10(fwavmaxRval/1e6))/20);
Hrms = Brms*1e7/4/pi;
betag = 2*pi*fwavmaxRval*sqrt(4*pi*1e-7*8.8542*1e-12)*...
   sqrt(1-(fc/fwavmaxRval)^2);
kc = pi/(9.75*.0254);
H0rms = Hrms*kc^2*9.75*.0254/(betag*pi);
PavgR = 2*pi*fwavmaxRval*4*pi*1e-7*betag*H0rms^2*(.0254^2*9.75*4.875)/...
   (2*kc^2);
effR = PavgR/PRmax*100;

[C Imaxwav] = max(abs(LBwavfilt));
lengthwavmax = 50e-9/TsHF;
LBwavmax = LBwavfilt(Imaxwav-lengthwavmax/2+1:Imaxwav+lengthwavmax/2);
```

```
LBwavmaxfft = abs(fft(LBwavmax))/length(LBwavmax);
fwavmaxL = 0:1/(TsHF*lengthwavmax):(1/(2*TsHF)-1/(TsHF*lengthwavmax));
attenwavmaxL = zeros(length(fwavmaxL),1);
[C Ifatten] = min(abs(fwavmaxL-200e6));
fwavmaxL1 = fwavmaxL/1e6;
probe = (X+20*log10(fwavmaxL1));
probe = max(probe)-probe;

aL1 = -1.0723468e-18;
aL2 = 1.1302179e-14;
aL3 = -4.8161884e-11;
aL4 = 1.0667404e-7;
aL5 = -1.3059861e-4;
aL6 = 8.1012826e-2;
conL = -47.808915;

if gapL>2.2
   attenwavmaxL = .0046*fwavmaxL1;
else
   attenwavmaxL = -1*(aL1*fwavmaxL1.^6 + aL2*fwavmaxL1.^5 + ...
      aL3*fwavmaxL1.^4 + aL4*fwavmaxL1.^3 +...
   aL5.*fwavmaxL1.^2+aL6.*fwavmaxL1+conL);
end
for i = 1:length(fwavmaxL1);
   if and(fwavmaxL1(i)>=1e2,fwavmaxL1(i)<=3.1e3)
   else
      attenwavmaxL(i) = 0;
   end
end

LBwavmaxfft = LBwavmaxfft(1:length(fwavmaxL));
LBwavmaxfftcorr = LBwavmaxfft;
for i = 1:length(LBwavmaxfft);
   if and(fwavmaxL1(i)>=600,fwavmaxL1(i)<=3100)
      LBwavmaxfftcorr(i) = LBwavmaxfft(i)*10^(probe(i)/20)...
         *10^(attenwavmaxL(i)/20);
   end
end

omegac = 3e8*pi/(9.75*.0254);
fc = omegac/(2*pi);
[C Ifatten] = min(abs(fwavmaxL-600e6));
[C fImaxwav] = max(LBwavmaxfftcorr(Ifatten:length(LBwavmaxfftcorr)));
fImaxwav = fImaxwav+Ifatten-1;
LBwavmaxamp = max(abs(LBwavfilt))/sqrt(2);
fwavmaxLval = fwavmaxL(fImaxwav);
[C attenI] = min(abs(fwavmaxLval/1e6-fwavmaxL1));
Pbdot = 10*log10(LBwavmaxamp^2/50*1000)+attenwavmaxL(attenI);
Brms = 10^((Pbdot-X-20*log10(fwavmaxLval/1e6))/20);
Hrms = Brms*1e7/4/pi;
betag = 2*pi*fwavmaxLval*sqrt(4*pi*1e-7*8.8542*1e-12)*...
   sqrt(1-(fc/fwavmaxLval)^2);
kc = pi/(9.75*.0254);
H0rms = Hrms*kc^2*9.75*.0254/(betag*pi);
PavgL = 2*pi*fwavmaxLval*4*pi*1e-7*betag*H0rms^2*(.0254^2*9.75*4.875)/...
   (2*kc^2);
```

```
effL = PavgL/PLmax*100;

% Write the dominant frequency, peak microwave power, and microwave efficiency
% to spreadsheet array
spread(shotnum,15) = fwavmaxLval/1e6;
spread(shotnum,20) = fwavmaxRval/1e6;

spread(shotnum,13) = PavgL/1e6;
spread(shotnum,14) = effL;
spread(shotnum,18) = PavgR/1e6;
spread(shotnum,19) = effR;

% Acquire time-resolved frequency of the microwave signal
div = 10;
window = ceil(length(LBwav)/div);
noverlap = window - 1;
nfft = window;

z = zeros(window-1,1);
LBwava = [z; LBwav; z];
RBwava = [z; RBwav; z];
SL = zeros(length(LBwav)/div,window);
SR = SL;
Tssp = TsHF*div;
tsp = 0:Tssp:(length(SL(:,1))-1)*Tssp;
delfsp = Fs/window;
fsp = 0:delfsp:(Fs/2-delfsp);

f1 = fsp./1e6;
attenL = -1*(aL1*f1.^6 + aL2*f1.^5 + aL3*f1.^4 + aL4*f1.^3 +...
   aL5.*f1.^2+aL6.*f1+conL);
attenR = -1*(aR1*f1.^6 + aR2*f1.^5 + aR3*f1.^4 + aR4*f1.^3 +...
   aR5.*f1.^2+aR6.*f1+conR);
probe = (X+20*log10(f1));
probe = max(probe)-probe;

for i = 1:length(LBwav)/div
   SL(i,:) = abs(fft(LBwava(div*(i-1)+1:window+div*(i-1))))...
      /(window+div*(i-1));
end
SL = SL(:,1:length(fsp));
ScorrL = SL;
ScorrLnorm = SL;
for k = 1:length(SL(:,1))
   for i = 1:length(fsp);
      if and(f1(i)>=650,f1(i)<=3100)
         ScorrL(k,i) = SL(k,i)*10^(probe(i)/20)*10^(attenL(i)/20);
      end
   end
   ScorrLnorm(k,:) = ScorrL(k,:)/max(ScorrL(k,:));
end
ScorrLdb = 20*log10(ScorrL);
for k = 1:length(ScorrLdb(:,1))
   for i = 1:length(ScorrLdb(1,:))
      if ScorrLdb(k,i)<=-30
         ScorrLdb(k,i)=-30;
```

```
        end
    end
end

for i = 1:length(RBwav)/div
    SR(i,:) = abs(fft(RBwava(div*(i-1)+1:window+div*(i-1))))...
        /(window+div*(i-1));
end
SR = SR(:,1:length(fsp));
ScorrR = SR;
ScorrRnorm = SR;
for k = 1:length(SR(:,1))
    for i = 1:length(fsp);
        if and(f1(i)>=650,f1(i)<=3100)
            ScorrR(k,i) = SR(k,i)*10^(probe(i)/20)*10^(attenR(i)/20);
        end
    end
    ScorrRnorm(k,:) = ScorrR(k,:)/max(ScorrR(k,:));
end
ScorrRdb = 20*log10(ScorrR);
for k = 1:length(ScorrRdb(:,1))
    for i = 1:length(ScorrRdb(1,:))
        if ScorrRdb(k,i)<=-30
            ScorrRdb(k,i)=-30;
        end
    end
end

% Plot the spectrograms
figure;
surf(fsp/1e9,tsp*1e9,ScorrLnorm,...
    'LineStyle', 'none','FaceColor','interp',...
    'FaceLighting','phong')
xlim([0.65 3.1])
ylim([trigt trigt+120])
view(2)
title(['Microwave Pulse Spectrogram Left Side-Shot ' shot])
ylabel('Time (ns)')
xlabel('Frequency (GHz)')
zlabel('Amplitude (dB)')
if qsav == 'y'
    saveas(gcf,['Microwave Pulse Spectrogram Left Side-Shot '...
        shot '.tif']);
end

figure;
surf(fsp/1e9,tsp*1e9,ScorrRnorm,...
    'LineStyle', 'none','FaceColor','interp',...
    'FaceLighting','phong')
xlim([0.65 3.1])
ylim([trigt trigt+120])
view(2)
title(['Microwave Pulse Spectrogram Right Side-Shot ' shot])
ylabel('Time (ns)')
xlabel('Frequency (GHz)')
zlabel('Amplitude (dB)')
```

```
if qsav == 'y'
   saveas(gcf,['Microwave Pulse Spectrogram Right Side-Shot '...
      shot '.tif']);
end

% Write the acquired parameters to the Excel spreadsheet
raw = [txthead; num2cell(spread)];

cd('..');
xlswrite('ShotData.xlsx',raw);
```

Appendix C: B-Dot Probe Design

Magnetic field probes were used to measure the current delivered to the vircators. They were built using RG-58 coaxial cables and were built with a single turn. Assuming that the magnetic flux through the area of the probe is approximately constant over the whole area, the voltage induced on the probe by the magnetic flux density is:

$$V = -AN\frac{dB}{dt}$$

where A is the area of the probe in meters, N is the number of turns, and $\frac{dB}{dt}$ is the time-derivative of the magnetic flux density. The magnetic flux at the center of the probe can be calculated assuming the conductor is a wire:

$$B = \frac{\mu_0 I}{2\pi r}$$

where μ_0 is the permeability of free space in H/m, I is the current in amperes, and r is the radial distance from the current carrying wire.

Both probes were made with a single turn and a probe area of approximately 1 cm^2. The center of the probe was approximately 15.24 cm, or 6 inches, away from the conductor. Using a current value of 6 kA with a rise time of 20 ns, the approximate voltage induced on these probes should have been approximately 39.4 V at its peak.

In actuality the cables carrying the pulse to the oscilloscope attenuated this signal. The probes also included an electrostatic shield around the probe to remove capacitively-coupled noise. These shields, the cables' attenuation, and other factors reduced the measured voltage to a peak between 5 V and 25 V depending on the diode current and the probe. These signals were digitally integrated, filtered, and scaled to determine the actual current pulse amplitude.

Appendix D: Inductive Voltage Adder Core Specifications

Ceramic Magnetics, Inc.—CN20 Magnetic Material

Typical Properties

Initial Permeability	925
Maximum Permeability	5000
Saturation Flux Density	4000 Gauss
Remanent Flux Density	2600 Gauss
Coercive Force	0.20 Oersted
Curie Temperature	185°C
dc Volume Resistivity	10^{10} ohm-cm
Bulk Density	5.24 g/cc

Unless otherwise specified, all tests were performed at 10 KHz, 22°C

Bs tested at 1 KHz, 20 Oersted • Br, Hc at 1 KHz, 5 Oersted

Initial Permeability vs. Temperature at 500 KHz

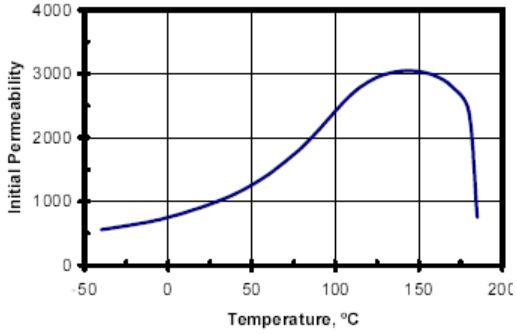

Permeability vs. Flux Density

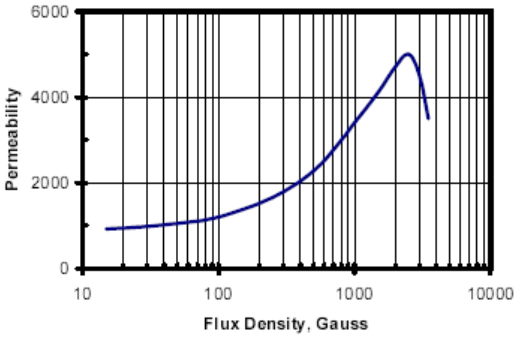

Quality Factor vs. Frequency

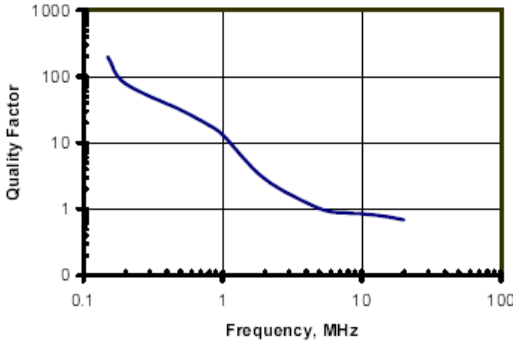

Complex Permeability vs. Frequency

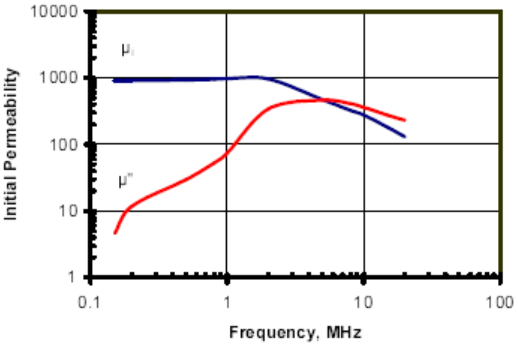

BH Loop Parameters vs. Temperature